Simulating Earthquake-triggered Runout using Higher-order Hydromechanical MPM and PM4Sand.

Abdelrahman Munther Khalil Alsardi

Dissertation submitted to the Faculty of the
Virginia Polytechnic Institute and State University
in partial fulfillment of the requirements for the degree of

Doctor of Philosophy
in
Civil Engineering

Alba Yerro Colom, Chair
Christopher Curtis Long
Russell A. Green
Adian Rodriguez-Marek
Jorge Macedo Escudero

December 1, 2025
Blacksburg, Virginia

Keywords: MPM, Higher-order, Isogeometric, PM4Sand, Earthquake

Simulating Earthquake-triggered Runout using Higher-order Hydromechanical MPM and PM4Sand.

Abdelrahman Munther Khalil Alsardi

ABSTRACT

Earthquake-triggered landslides pose a significant risk to society and infrastructure. Despite the catastrophic consequences, significant questions remain regarding their manifestation and have rarely been analyzed in large-strain numerical frameworks. There is a need to simulate earthquake-triggered landslides within a unified framework that can incorporate geometrical and material nonlinearities, while having the capability to simulate the runout process, from triggering to post-failure cyclic mobility. The Material Point Method (MPM) is a particle-based computational technique that has achieved significant success in simulating geotechnical problems; however, it suffers from numerical errors that have prevented it from realizing its full potential in geotechnical earthquake engineering. The aim of this research is to develop and validate an MPM framework that facilitates a deeper understanding of earthquake-triggered landslides. To achieve this goal, a higher-order multiphase isogeometric MPM framework is proposed. Non-zero kinematic and periodic boundary conditions are developed to simulate shaking table loading and free-field modes. Finally, the PM4Sand constitutive model is implemented in the hydromechanical MPM to enable the model to capture the cyclic behavior of sand, including liquefaction triggering and cyclic mobility. Verification and validation of the framework are performed by comparing the results with those obtained using the Finite Element Method (FEM), analytical solutions including Newmark-type techniques, and shaking table tests. A centrifuge test of a clay embankment overlying saturated sand is simulated using the computational framework. The accelerometer and pore wa-

ter pressure trends are satisfactorily matched with experimental data, and the deformation mechanism is well captured. The MPM framework proposed in this dissertation presents promising advancements toward a stable hydromechanical large-strain methodology that can capture material and geometric nonlinearity, simulating the entire runout process from triggering to post-failure stabilization to ultimately better understand earthquake-triggered landslide manifestations.

Simulating Earthquake-triggered Runout using Higher-order Hydromechanical MPM and PM4Sand.

Abdelrahman Munther Khalil Alsardi

GENERAL AUDIENCE ABSTRACT

Earthquake-triggered landslides pose a significant risk to downstream communities due to their runouts. It is essential to understand how these landslides develop, as the ground shaking exerts additional loading to mobilize a sliding mass. Mathematical algorithms have been developed to incorporate accurate soil behavior. However, most contributions have been limited to small deformations and are unable to capture the evolution of the landslide. As such, advancements in these mathematical algorithms are necessary to simulate hazardous runouts. The Material Point Method (MPM) has gained popularity due to its practicality in simulating large deformations; however, it has rarely been applied to earthquake-triggered loadings. In this dissertation, we propose and validate an enhanced MPM framework to simulate earthquake-triggered landslides. Specifically, we address the application of seismic loading to simulate the shaking in experimental shaking table tests and symmetric geometries in the field. Soil is simulated as a saturated material that can naturally transition from undrained to drained, considering accurate cyclic soil behavior. The model can also capture soil liquefaction with the use of advanced constitutive models. Trends from experimental data are accurately captured. This research presents a promising tool that geotechnical engineers can use to assess runout hazards considering ground shaking due to earthquakes.

Dedicated to

my dad, Munther, my mum, Nariman,

my sisters, Layan and Lujain, and my brother, Moataz.

I love you deeply and infinitely.

Acknowledgments

I am greatly indebted and thankful to have worked under the supervision of Dr. Alba Yerro Colom to pursue my PhD studies. Dr. Yerro was very generous in mentoring me. She went above and beyond to meticulously work with me to meet tight deadlines while always reminding me of the broad vision of our project. She was also extremely patient in allowing me to solo dive head-first into the details of computational problems knowing how much fun I find theoretical details to be. Dr. Yerro acted as a firm mentor who pushed to help me become an independent researcher while also treating me as her colleague. She listened (often times more than she should), processed, and guided me in the most professional and graceful manner. I cannot express how grateful I am to have worked with her. Thank you for being a guiding light when it felt too dark in this PhD.

My time in Los Alamos, New Mexico, has shaped my vision and introduced me to a broad array of scientific disciplines that have expanded the horizons of my career. From small talks on walks to Hot Rocks cafè to incredible seminars at the Center of Nonlinear Studies (CNLS), the amount of passion for science expressed by my Los Alamos supervisors and colleagues is not lost on me. Most importantly, Dr. Christopher Curtis Long has extensively supervised my work and was instrumental in building my understanding in Isogeometric Analysis. Also, Dr. Duan Zhang was an invaluable resource who introduced me to new concepts in multiphase analysis and significantly expanded my then-shallow knowledge in the Material Point Method (MPM). I am eternally thankful to have worked with Dr. Long and Dr. Zhang in the Los Alamos National Laboratory. It was also so fun to be in Los Alamos alongside my Fishbowl and CNLS colleagues. I apologize in advance in case I miss a name. I am grateful to Dr. Anton Goertz, Dylan Weatherred, Dr. Hunor Csala, Rylan Paye, Jessica

Williams, Dr. Quincy Huhn, Dr. Kelsey Lund, Dr. Mithun Goutham, Connor Woodsford, Gwendolyn Galleher, and Facundo Airaudo for many (hilarious) technical discussions and hikes.

I am very grateful to the Virginia Tech faculty for teaching me fundamentals and advanced details of Geotechnical Engineering. I aspire to be as disciplined, knowledgeable, and detail-oriented as Professor Russell Green. I have thoroughly enjoyed interacting with Professor Green to learn Geotechnical Earthquake Engineering. Thank you for the detailed notes and the thought-provoking classes. I am grateful to Professor Adrian Rodriguez-Marek for his tremendously clever geotechnical insights and for all the effort he puts in to build a sense of community in the geotechnical department. I am also grateful to Dr. Sherif Abdelaziz and Dr. Nina Stark for their mentorship when I worked as their Graduate Teaching Assistant. My graduate student colleagues at Virginia Tech have played an important role in making my PhD fun. I am grateful to Dr. Luis Zambrano, Dr. Veronica Girardi, Dr. Kaleigh Yost, Jonathan Moore, Dr. Varsha Swamy, Dr. Kristen Ulmer, Dr. Sneha Upadhyaya, Dr. Grace Huang, Dr. Tyler Quick, Dr. Reem Jaber, Dr. Nicolai Brilli, Tat Shing Thum, Behrooz Daneshian, Balakumar Anbazaghan, Justin Ward, Carole Karam, Jasleen Bheora, Francis Li, Shijun Wei, Ian Pierce, John Murphy, and Sukrit Samanta. I apologize if I have missed people in that list of names. I thank you from the bottom of my heart for listening to me ramble about bugs in my MPM code.

I thank the Anura3D community members for their support. They were a invaluable resource to discuss the development of the MPM throughout my PhD. I would also like to thank faculty members from my previous university affiliations (UC Berkeley and University of Bristol) who have played a corner-stone role in my education. I am grateful to Professor Kenichi Soga, Dr. Elliot James Fern, Dr. Dimitris Karamitros, Professor George Mylonakis, Professor Flavia De Luca, Dr. Liz Holcombe, Professor Andrea Diambra, Professor James

Norman, Professor Erdin Ibraim, and Professor Shawn Shadden. I thank my jiu jitsu mentor, Professor Tim Mannon, who often helped me get out of the academic rut through sparing competitions. I also want to thank my Bristol friends who have always been there for me since the very start of my Geotechnical Engineering journey. I am grateful to Arfon Irish, Joe Camfield, Joe McFarlane, Alasdair Cavaye, and Ben Petty.

I am grateful to have a supportive family. I thank my parents, siblings, and nephews for calling me every single day to make sure I am on top of my research work. Honestly, the academic road look even more treacherous than how it started. Although, I have no doubt I shall overcome it all with my family by my side. I could possibly write a whole another dissertation about how thankful I am to my family, but for now I shall stop. I love you all to my very core.

Contents

List of Figures

List of Tables

Chapter 1

Introduction

Consequences of coseismic slope failures can be catastrophic (Figure 1.1). Procedures adopted in geotechnical engineering practice for computing permanent displacements of coseismic slope failures are highly idealized. Underlying theories often assume one-dimensional response with several restrictive assumptions that prevent the simulation of site-specific geometric complexities, large deformations, and accurate soil-water interaction when subject to dynamic earthquake loading. In particular, aspects of fundamental soil mechanics, including softening, cyclic mobility, and flow due to liquefaction, are completely neglected in these simplified procedures. Fully-controlled experimental models are often conducted to simulate these complex phenomena at a prototype scale and in centrifuge tests (e.g., [1, 2, 3]). However, conducting centrifuge or shaking table tests in the laboratory requires experimental facilities that are not widely available in practice and are extremely expensive. As such, the ability to perform accurate numerical simulations of coseismic landslide hazards, from failure initiation to final runout, is vital for assessing the associated economic risk and disaster management of the natural environment, human population, and critical infrastructure. Towards this end, there is a dire need to advance predictive coseismic hazard simulation tools to incorporate large deformations and contribute to the development of more resilient communities. The overarching goal of this dissertation is to advance the understanding of the triggering and post-failure kinematics of coseismic slope instabilities, considering geometric and material complexities, by developing advanced computational tools.

In this chapter, the motivation for this research is described, which primarily stems from real-scale coseismic landslides and their corresponding detrimental consequences. Second, a background overview of fundamental aspects relevant to this research is presented, including soil behavior under cyclic loading, displacement prediction tools, numerical methods, and non-linear constitutive modeling. Third, the objective is highlighted to outline the scope of this dissertation. Fourth, specific research tasks are listed to achieve the dissertation objective. Finally, the dissertation structure is outlined to describe the content of each chapter and appendix.

Figure 1.1: (a) Mejia embankment failure, 2016 M_w 7.8 Pederndales, Ecuador [4]; (b) Coseismic landslide disruption, 2014 M_w 5.0 Misca, Peru [5]; (c) Coseismic landslide in Bingham Canyon Mine, 2014 M_w 2.5 Salt Lake County, Utah [6]; (d) Coastal landslide, 2017 M_w 3.5 Big Sur, California [7]. Permission was granted from each author for the use of these photos in this dissertation.

1.1 Motivation.

The ultimate motivation of this research is to provide a better comprehension of the increasing risk associated with coseismic landslide hazards. The accomplishment of this goal involves the development of a novel numerical framework capable of simulating the overall failure mechanism, from failure triggering to large deformations during post-failure, caused by earthquake excitation within a dynamic framework that incorporates hydromechanical formulations and advanced constitutive models to capture the soil-porous water interactions and complexities of soil behavior during cyclic loading.

Earthquake-triggered slope instabilities play a detrimental role in recursive economic and life losses incurred by communities located in seismically-active regions. Advancements in lifeline and natural disaster management infrastructure are hindered by the lack of standardized coseismic slope analysis techniques that can accurately predict these landslide catastrophes while still taking into account site-specific geometric complexities such as topography and stratigraphy [8, 9]. This is because fundamental questions regarding the connection between mechanics of failure initiation, post-failure mobility, and the role of pore fluid, especially in these complex sites, remain unanswered. Current predictive empirical techniques typically rely on extensive simplifications and, thus, are incapable of reasonably simulating the post-failure behavior and large deformations associated with coseismic landslides. In practice, performance-based engineering has been widely adopted within the earthquake engineering community as the basis for a sustainable and economical approach to designing infrastructure and mitigating risk from natural hazards [10, 11, 12]. This often involves establishing a level of risk tolerance for damage that is deemed acceptable for a particular infrastructure design. For critical infrastructure located in seismically active regions, such as flood-defense levees, nuclear facilities, tailing dams, and water-retention structures, damage tolerance becomes very low and more sophisticated analyses are necessary to identify, quantify, and mitigate

the risk of earthquake-triggered large deformations. A few examples of such failures and their detrimental consequences are described herein.

The earthquake-triggered disruption of slopes and earth embankments occurs in approximately 46% of earthquakes [13], often constructed to serve as water-retention structures, bridge foundations, or roadways (Figure 1.1). A recent case study of such a devastating instability is the Mejia embankment failure in Manabi, Ecuador, which occurred during the M_w 7.8 megathrust earthquake on 16 April, 2016 [4] (Figure 1.1a). The peak ground acceleration (PGA) recorded at the nearest strong motion station was $0.32g$, which caused an underlying 7 m layer of loose silty sand to liquefy [4]. The Mejia bridge embankment exhibited catastrophic rotational failure, with maximum horizontal displacements of 5 m. The corresponding direct cost of repairing the damage attributed to liquefaction-induced coseismic landslides is estimated to be over US$1 billion [4], more than 5% of Ecuador's GDP. Besides the direct repair costs, coseismic landslides due to transportation embankment instabilities cause severe disruption and delay, leading to low disaster management efficiency, longer infrastructure downtime, and ultimately significant indirect economic losses to most businesses in the area. The seismic vulnerability of the Sacramento-San Joaquin Delta earthen levees is also a significant example that should be analyzed in a large-strain framework to better understand potential failure consequences. Failure of such levees jeopardizes California's water, electric, and natural gas transmission systems, which serve approximately 23 million citizens and all nearby farmlands. With the increasing floodwater levels resulting from climate change, the risk of breaches of these levees due to seismic activity is also increasing [14]. The seismic vulnerability of the levees in the Delta is primarily associated with the catastrophic loss of freeboard due to the liquefaction of the sand foundation soils or soils comprising the levee itself.

Additionally, with the recent expansion of the mining industry, the rate of kilometer-scale

tailings dam construction has significantly increased in recent years. Many seismically active countries in South America and Asia, such as Chile, Peru, China, and Japan, rely on their mining industries as one of the main pillars of their economies [15]. Apart from the environmental threat posed by these large-scale retaining structures, there are no universally-accepted regulations for tailings dam construction, with seismic stability often crudely estimated using simplified approaches [16]. Moreover, the retained tailings mass is often extremely stratified, which results in geometric complexities that should be taken into account to understand their potential instability mechanism (Figure 1.1(c)). One example is the El Cobre mining facility, Chile, which catastrophically failed during the M_w 7.5 earthquake in 1965 and caused a series of other dam failures, killing approximately 500 people and leaving over 100 thousand people homeless and an estimated damage of approximately US$1 billion [15]. The tailing dam failure was attributed to seismic liquefaction and subsequent flow failure, which was triggered by the generation of excess pore water pressures during the earthquake shaking [15]. Ishihara et al. [17] highlighted the need to numerically analyze tailing dams in a large deformation framework and emphasized the importance and effects of the water table levels and channel drainage on the tailing mobility and post-failure runout.

In summary, earthquake-triggered slope failures have a significant adverse impact on social, economic, and environmental aspects. State-of-the-art simplified predictive tools cannot reasonably account for the combined effects of site-specific geometric and material complexities, particularly because they neglect soil-porous water interactions, which often leads to catastrophic large deformations such as flow liquefaction of sandy soils. This dissertation addresses this important necessity by developing and validating a general numerical framework that can simulate the entire deformation process of earthquake-triggered failures in complex sites.

1.2 Background.

This section provides general background information and highlights current state-of-the-art limitations in the study of coseismic landslides. The brief background herein describes (a) fundamentals of cyclic soil loading, (b) existing simplified permanent displacement techniques, (c) numerical methods to simulate large deformations, and (d) constitutive models to simulate cyclic soil behavior.

1.2.1 Fundamentals of soil behavior under cyclic loading.

During earthquakes, soils are subjected to irregular and cyclic vibrations. Depending on the site characteristics, seismic waves can be either amplified or attenuated at specific frequencies. The secondary waves (S-waves) result in the rotation of the in-situ principal stresses [18]. Vertically propagating pressure waves (P-waves) result in a series of compression/dilation loads inducing volumetric deformations. The S-waves can also result in volumetric change tendencies. For example, sands exhibit densification in drained conditions or pore water pressure generation in constant-volume undrained conditions. An accurate understanding of the loading imposed on the soil is crucial for understanding the response the soil can exhibit during earthquake events. Upon large deformations, it is generally well-accepted that a critical stress locus exists for soils whereby shear strain can be accumulated at constant stress, volume, and velocity, known as the 'critical state' [18, 19, 20, 21, 22]. The fundamental characteristics of cyclic soil response are described in this section.

Firstly, the dissipation of energy in soils due to wave propagation away from the system subject to shaking is known as radiation damping. The magnitude of radiation damping depends on the excitation frequency, the system's geometry, the mode of oscillation, and the impedance contrast between the system's base and the underlying half space. Secondly, the

dissipation of energy due to non-linear material hysteresis caused by the friction between granular particles and the strain-rate-dependent viscous pore fluid flow is known as material damping. In undrained conditions, the former is more predominant and is approximated to be frequency independent [23]. It is conventional to define material damping solely due to hysteresis as the ratio of dissipated energy to the elastic stored energy in a cycle of loading, with a proportionality constant of $\frac{1}{4\pi}$ [23]. Hysteretic damping increases with strain amplitude due to the increase in the non-linear response of the soil [23, 24, 25, 26]. The relationship between secant shear modulus and strain amplitude is typically characterized by a normalized modulus reduction curve versus shear strain. The non-linearity in the stress-strain relationship results in an increase in energy dissipation, and therefore an increase in material damping ratio with increasing strain amplitude.

It is well known that the cyclic stress paths of soils are different from those for monotonic loading. For example, in drained conditions, loose soils or all soils at lower levels of vibration exhibit densification, which is a net contractive strain accumulation irrespective of the initial stress state relative to the critical state line. Sandy soils tend to cyclically harden to reach a minimum possible void ratio [27]. For a given relative density, shear strain amplitude, and number of loading cycles, experimental strain-controlled element tests showed that final net contraction is independent of normal effective stress [28]. In undrained conditions, pore water pressure increases, resulting in a reduction of the mean effective stress. The pore pressure generation per cycle is dependent on plastic volumetric strain and undrained stiffness of the soil. Eventually, mean effective stresses can approach zero, triggering soil liquefaction. Saturated sandy soils can exhibit liquefaction phenomena such as cyclic mobility and earthquake-triggered flow liquefaction [23]. Cyclic mobility is a strain hardening phenomenon in cyclically softened dense-of-critical soils, due to the inertial and static driving shear stresses resulting in incremental deformations during earthquakes. Conversely, flow

liquefaction is the strain-softening phenomenon that occurs in loose-of-critical soils when the driving static shear stresses exceed the residual strength of soils, which brings the soil to a state where it becomes intrinsically unstable. Flow liquefaction due to seismic action has rapid and detrimental consequences. A post-liquefaction residual shear strength (S_r) is reached, which is important to understand the ultimate effects on geotechnical structures. The definition of the state parameter concept [18, 20, 29], which separates the sand's behavior based on its initial mean effective stress and relative density, is important in understanding the constitutive response and potential liquefaction consequences that occur in soils. In addition to this, inherent fabric anisotropy and principal stress rotations (i.e., load reversal) play an important role in quantifying the earthquake-induced pore water pressure that can induce liquefaction hazards in sands [30, 31, 32].

1.2.2 Methods to predict permanent displacements due to seismic loading.

The state-of-the-practice procedures that address landslide triggering and runout (i.e., permanent displacement) involve the synthesis of theoretical and empirical considerations that have emerged over the past five decades. These are easy and rapid to apply. However, they are not applicable to complex sites, and when soil liquefaction is expected. The oldest and most widely used seismic slope stability method is the pseudo-static method [33], whereby earthquake forces are simulated as body forces that are integrated within the free-body limit equilibrium methods of slices to calculate a combined factor of safety for the system, albeit neglecting any assessment of slope performance. Newmark [34] assessed the performance of a slope under earthquake loading in a simplified manner. The slope's slip surface is modeled as a block on an inclined plane that is subjected to an acceleration. When the acceleration exceeds the yield acceleration, relative velocities are induced. The relative velocity results in

the sliding block incurring permanent displacements. The implementation of the Newmark [34] involves integrating the relative acceleration twice to calculate permanent displacements. The sliding block re-stabilizes when the relative velocities return to zero. However, Newmark's method is highly idealized, enforcing crude assumptions to simulate the dynamic loading and the geology of complex scenarios. This includes adopting a single rigid perfectly plastic slip surface, rigid sliding mass movement, and no shear modulus reduction or pore pressure generation [2, 35]. The use of Newmark's method was primarily developed for rigid earth embankments with a natural period close to zero, often justified by considering the uncertainty to be majorly in the seismological ground motion selection. However, these simplifying assumptions violate the geotechnical understanding of dynamic loading stress paths and stress-strain rheology, resulting in the abandonment of the notion that stress-history-dependent localization of slip surfaces within slopes, staged construction in-situ stresses, natural soil layering, and non-linear pore water generation and consolidation are relevant. The current state-of-the-practice relies on simplified Newmark-type regressions, which have been widely used for assessing slope permanent displacement due to dynamic loading. The framework of these simplified Newmark-type approaches is based on a multi-random variable statistical analysis that can incorporate accumulated uncertainty in a probabilistic manner. Various researchers employed Newmark's approach to propose simplified regression equations which facilitate the calculation of permanent displacement, although they retained all of Newmark's crude assumptions (e.g., [36, 37, 38, 39]). Several improvements were also introduced within the simplified regression analysis to overcome some of the limitations. First, the 'decoupled approach' was developed to overcome the rigid sliding mass assumption and to take into account the effect of dynamic response due to S-wave propagation upon permanent slip of the sliding mass (e.g., [40, 41, 42, 43, 44, 45, 46]. The most important limitation of the decoupled procedure is that the computation of the seismic response of the potential sliding mass is decoupled from the subsequent slip with no consideration of pore water pres-

sure generation due to shaking and mass sliding. In addition, the internal mass response is approximated solely for S-wave shearing-type deformations, neglecting earthquake-induced S-wave and P-wave coupled volumetric deformations. Second, the 'coupled approach' was developed to consider the role of internal shear deformation of the sliding mass upon the permanent displacement accumulation (e.g., [44, 46, 47]). The coupled approach solves the equation of motion using simplified viscoelastic-perfectly-plastic elements, which simulate the one-dimensional deformation of the flexible sliding mass during the landslide. Besides the dynamic site response, the coupled approach inherits the aforementioned limitations of the Newmark and decoupled approaches.

1.2.3 Numerical methods to simulate large deformations

Geotechnical engineers often resort to numerical models to overcome the aforementioned limitations of the Newmark, decoupled, and coupled approaches to understand the mechanism of instability initiation and subsequent progressive movement. The most commonly used numerical approaches are the Finite Element Method (FEM) (e.g., [48, 49, 50, 51]) and the Finite Difference Method (FDM) (e.g., [52, 53, 54]). These mesh-based methods are conceptually simple and are capable of modeling history-dependent materials and complex geometries. In both cases, a nodal computational mesh discretizes the continuum and represents its deformation. As a result, these methods exhibit severe element distortion when large deformations are incurred, leading to significant errors and an unstable numerical solution (e.g., [55, 56, 57]). An effort has been made to improve these techniques to extend their applicability to large strain problems with rezoning, remeshing, and remapping algorithms. However, these techniques are computationally very expensive and interpolate the history state variables at the nodes, reducing the model's accuracy [55]. To overcome these limitations, particle-based methods are being developed, with the Material Point Method (MPM)

being one of the most popular for geotechnical applications because of its close resemblance to the FEM formulation and its ability to incorporate continuum-based constitutive models [56]. The MPM [58] discretizes the continuum body into a finite number of mobile Lagrangian points (i.e., material points) that move to represent the deforming material carrying the updated variables (e.g., density, strain, state parameters). The main governing equations (i.e., dynamic momentum balances) are solved at the nodes of a computational mesh, which usually remains undeformed and stores no permanent information. The MPM prevents mesh distortion and overcomes the difficulty of tracking history-dependent materials in fully Eulerian methods. Moreover, the boundary conditions in MPM can be applied on the nodes (i.e., similar to mesh-based methods) or on the material points [56, 59]. Due to these promising numerical features, this proposal focuses on the development of MPM to advance the understanding of the triggering and post-failure runout kinematics of co-seismic landslides.

Some of the numerical limitations of the MPM framework, especially relevant in the application of coseismic failures, include the generation of numerical noise due to (a) cell-crossing instability, (b) limitations of time integration schemes, and (c) volumetric locking. 'Cell-crossing' instability corresponds to the high-frequency noise that is generated when material points cross the elements of the background mesh, particularly when lower-order elements are used [60]. This noise disrupts the stress solution at each material point (MP) as it transitions from one element to another, causing the accumulation of errors, especially when constitutive models involve history-dependent state variables. Several techniques, such as the mixed MPM integration scheme [61], generalized interpolation material point (GIMP) [60, 62], and convected particle domain interpolation (CPDI) have been introduced to mitigate cell-crossing noise. However, existing numerical limitations in the aforementioned limitations. For example, the mixed MPM integration scheme is often used with Gaus-

sian stress smoothing to achieve stable solutions, which erases the material's stress history. Additionally, GIMP-type techniques are susceptible to spurious tensile separation of the MPs, particularly when large deformations occur [63, 64]. The Dual Domain Material Point (DDMP) method was developed to mitigate cell-crossing errors by modifying the interpolation function derivatives within the lower order framework [64]. The local stress different (LSD) approach was incorporated within the DDMP variant of the MPM to reformulate the internal force calculation [65]. The use of LSD and DDMP has presented significant stability improvement to the traditional MPM [65]. However, the DDMP implementation can be complex while still retaining lower-order stress distributions. More recently, the B-spline higher-order MPM has garnered attention in the literature due to its ability to intrinsically eliminate cell-crossing [66, 67]. Despite the potential of higher-order MPM frameworks [68], a multipatch isogeometric analysis has never been implemented in the MPM framework, which would enable the mitigation of cell-crossing noise while accurately capturing complex geometries. The second source of error in traditional MPM schemes is the use of the Forward Euler-Cromer time integration scheme, which is conditionally stable and may result in spurious high-frequency numerical oscillation and inconvergence when simulating coseismic landslides. Recent advancements offer user-controlled high-frequency numerical noise elimination and time step selection [69, 70, 71, 72, 73, 74]. Notably, the generalized-α implicit time integration scheme [69] recently adapted for MPM by Tran and Solowski [74], presents a family of self-starting numerically dissipative algorithms and is a more general implementation of the commonly employed Newmark-β scheme in numerical earthquake engineering. The scheme achieves an optimal combination of maximum dissipation of high-frequency noise and minimum low-frequency dissipation. Han et al. [73] showed that the generalized-α scheme is consistent in its desirable numerical features when using it in multi-phase coupled formulations in FEM. Finally, the third source of numerical noise mainly relevant in this study is that MPM suffers from volumetric mesh-locking when simulating incompressible

undrained shearing conditions. This limitation has recently been mitigated using pressure operator splitting and Chorin's projection technique in a $u-p$ hydromechanical formulation [75, 76, 77].

Although MPM has been successfully applied in a wide array of applications, it has been rarely used for the study of earthquake-triggered failures. Most of the current state-of-the-art relies on small-scale shaking table experiments where fully reflective boundaries are generally accepted and simple constitutive models are used [57, 78, 79, 80]. It is well known that simulating wave propagation problems requires considering unbounded domains to prevent artificial reflection at the boundaries. Even when advanced free-field boundary conditions are implemented in the MPM, the two-phase single-point formulation has never been used to simulate coseismic liquefaction [81, 82]. Free-field boundary conditions usually assume simple viscoelastic constitutive behaviors to capture the radiation damping. Elastoplastic constitutive model selection can be incompatible with underlying boundary condition assumptions. As such, the use of advanced bounding surface elastoplasticity models can necessitate simplification of the boundary conditions to achieve stable stress integration [83]. The higher-order MPM has never been used to simulate the detrimental large-strain effects of earthquake-triggered liquefaction.

1.2.4 Constitutive modeling of soil subjected to earthquake loading

During low-intensity shaking, soil behavior can be approximated as linear, and for long-period soil profiles, the corresponding material damping can have negligible effects on the site response [84]. One-dimensional wave propagation closed-form transfer functions were derived for these small-strain wave propagation problems [23]. For short-period soil profiles,

non-linear effects can have significant effects on the site response even at small strains [84]. Under more intense shaking, soil behavior can generally be extremely nonlinear. As such, the equivalent-linear approach was developed as a simple way to handle nonlinear soil behavior whereby the stiffness modulus and damping ratio are varied in an iterative manner to obtain the approximate average or 'effective' strain induced in a soil layer using the linear closed-form solutions (e.g., [23, 85, 86, 87]). Although this approach is computationally very efficient compared to other numerical techniques, the secant stiffness modulus and damping ratio are implicitly assumed to remain constant for the entire duration of shaking, which represents a significant limitation of the method because it fails to reflect accurate soil behavior.

Masing's rules [88] have been introduced in numerical models to capture the functional form of the elastic nonlinear cyclic behavior (e.g., [51, 89]). The dependency of the shear modulus on the deformation observed in laboratory tests can be effectively reproduced by this type of model. Additional rules in conjunction with the Masing's rules were introduced to address irregular cyclic loading and cyclic behavior of clay [90, 91]. Various simplified stress-based, strain-based, and energy-based pore pressure generation models have also been developed, which can be used in tandem with Masing's rules (e.g., [92, 93, 94, 95]). These models extend the use of this type of constitutive relationship to the simulation of liquefaction-related problems. Although being robust and relatively easy to implement, Masing's rules do not explicitly consider the initial stiffness modulus degradation [96], and hysteresis damping is generally overestimated [97]. It was also shown by Taborda et al. [51] that the use of Masing's rules in FEM results in erroneous material damping at large strains. Camilo and Hashash [89] introduced an improved damping formulation that can be incorporated to enhance Masing's rules to better match measured modulus reduction and damping curves. However, Masing's rules are only applicable within the framework of elasticity. Therefore, they are unsuitable to simulate large deformations.

Simple conventional elastoplastic models, such as the isotropic Mohr-Coulomb and Drucker-Prager employ a single yield surface and often include softening/hardening laws (e.g., [56, 57, 72, 98]). However, these simple models fail to capture seismic softening, liquefaction-triggering, cyclic mobility, and flow liquefaction mechanisms [51, 99]. The straightforward modification of the Mohr-Coulomb model to include stiffness non-linearity was proposed by Jardine et al. [100]. However, it was observed that inconsistent stress paths were obtained due to the inability of the model to capture anisotropy due to seismic loading effects. Advancements of these conventional constitutive models included the use of cycle-counting algorithms (e.g., [101]) that can incorporate liquefaction-triggering and subsequent strength loss in an empirical and highly simplified manner (e.g., [102]). However, cycle-counting algorithms do not enable such constitutive models to capture pore water pressure generation and key stress-strain behaviors, including cyclic mobility and flow liquefaction [103].

Elastoplastic constitutive models with advanced yield surface treatments are considered the most suitable techniques for simulating accurate stress paths in numerical models. They can include nonlinear hysteresis behavior through multiple nested yield surfaces (e.g.,[104]), general plasticity (e.g., [105, 106, 107]), and bounding surface plasticity theories (e.g., [32, 108, 109, 110, 111]), among other concepts which have been employed in the modeling of liquefaction (e.g., hypo-plasticity and hyper-plasticity, etc.). The improvement in accuracy and modeling capabilities through the use of multiple yield surfaces can result in a significant increase in the number of material parameters and in the required computational effort. Cyclic behavior of a soil can be determined by obtaining high-quality field samples and then testing them in an appropriate laboratory device. However, experience has shown that sand samples obtained by conventional sampling techniques are sufficiently disturbed to render the resulting measurements of cyclic strength unreliable and impractical in most situations. Consequently, recourse is generally sought through in-situ testing techniques such as the

Standard Penetration Test (SPT) or Cone Penetration Test (CPT). Recent advancements in constitutive modeling introduced effective stress models that have been adapted to enable users to calibrate constitutive models from these in-situ testing techniques for use in a fully hydro-mechanically coupled manner. Among others, given their less tedious calibration procedure and their extensive documentation, UBCSAND [105, 107], PM4Sand [111], and PM4Silt [112] serve as a good trade-off and represent the state-of-the-practice constitutive models that capture most features of liquefaction-triggering and cyclic mobility [103] based on soil mechanics principles. UBCSAND is an effective stress plasticity model developed primarily for sand-like soils. The model predicts the shear stress-strain behavior of the soil using an assumed hyperbolic relationship, and estimates the associated volumetric response of the soil skeleton using a flow rule that is a function of the current stress ratio. PM4Sand is a stress-ratio controlled, critical state compatible, bounding surface plasticity model for sands based on the SANISAND model [32]. PM4Sand has grown in popularity to become the state-of-the-practice model to simulate earthquake-triggered liquefaction in sand [110, 111]. Finally, PM4Silt is an enhancement of PM4Sand that was developed for low-plasticity silts and clays.

1.3 Research objectives

Driven by the motivation and limitations in the research literature, the following objectives are outlined to define the scope of the work in this dissertation:

- Develop kinematic prescribed velocity and periodic boundary conditions to assess the capabilities of the MPM framework to simulate coseismic landslides.

- Implement the generalized-α time integration in the MPM framework to assess its

efficiency in mitigating high-frequency noise and its practicality for use in coseismic landslides applications.

- Develop a stabilized higher-order hydromechanical MPM numerical framework for simulating large deformations while taking into account geometric complexities.
- Verify and validate the developed higher-order MPM for large-scale geotechnical applications, including slope instabilities and penetration problems.
- Implement PM4Sand state-of-the-practice bounding surface constitutive model in MPM to capture the cyclic soil behavior more accurately to simulate the full instability process, from the application of the seismic motion to the final runout.
- Validate the stabilized higher-order hydromechanical MPM framework using PM4Sand with laboratory centrifuge tests, considering different slope configurations.

1.4 Dissertation structure

This dissertation comprises a series of manuscripts that build up in numerical complexity and collectively serve to meet the research objective. Each manuscript is either published, submitted, or will be submitted for publication in a peer-reviewed journal. The chapters are organized as follows:

- Chapter 2 proposes a methodology to impose kinematic Dirichlet boundary conditions in MPM to simulate the seismic loading by means of an input ground motion. The background computational mesh, typically kept constant in MPM simulations, is adjusted to follow the ground motion, enabling the strong enforcement of boundary conditions and reducing cell crossing for MPs that exhibit relative deformation. An

undrained large deformation shaking table test by Wartman et al. [26] is simulated using the classic linear MPM framework. This is simulated using the single-phase formulation in a total stress analysis. The numerical results are validated against experimental observations in terms of slip surface location, evolution of permanent displacement at control points, and overall final geometry. Finally, the capabilities of the MPM framework to capture large deformations and post-failure runout are assessed by comparing the MPM results with those provided by the Finite Element Method (FEM), Finite Difference Method (FDM), Newmark [34], and simplified Newmark-type techniques.

- Chapter 3 proposes the implementation of periodic boundary conditions in MPM to capture the modal site response as the seismic loading propagates through the soil column. A particle relocation technique is employed to ensure that the MPs remain within the background computational mesh when large deformations occur. Additionally, the explicit generalized-α time integration scheme is implemented to suppress high-frequency noise resulting from cell-crossing and quadrature errors. The effectiveness of the new MPM features is assessed by analyzing the coseismic response of a horizontal soil column, and the results are compared with those from FEM. The capability of the mixed Gauss-point-MPM spatial integration scheme is also assessed. Finally, a coseismic slope instability of an embankment resting on a foundation is simulated. A parametric analysis is performed to assess the effect of Arias intensity, geometry, and constitutive model on the embankment runout. Simple constitutive models are considered (i.e., Mohr-Coulomb and Mohr-Coulomb with strain softening).

- Chapter 4 proposes a further enhanced higher-order multipatch isogeometric MPM framework that intrinsically eliminates cell-crossing error in the MPM. This framework is a multi-purpose numerical tool capable of simulating saturated porous media

in a stable, higher-order isogeometric formulation. An incremental strain smoothing algorithm is also proposed to mitigate volumetric locking. The framework using B-splines is verified using simple and general benchmarks, including pressure wave propagation and viscoelastic column compression under gravity. The Non-Uniform Rational B-splines (NURBS) are used within the isogeometric framework to simulate deformations in complex circular geometries. The multipatch framework is developed to hydromechanically simulate the penetration of footings in saturated soils. The cubic interpolation function presents the most stable solutions to combat cell-crossing and volumetric locking errors.

- Chapter 5 assesses the stability of the hydromechanical higher-order B-spline MPM framework within the context of real-scale geotechnical applications. This includes simulating a large-strain oedometer problem, the Selborne brittle slope failure, and hydromechanical footing penetration under various penetration velocities and hydraulic conductivities. The implication of the use of higher-order interpolation functions is investigated on the manifestation of slip surfaces, sliding mass mobilization, kinematic response, and stress path evolution. Convergence is achieved using cubic interpolation functions, with no additional practical value seen in the use of quartic interpolation functions.

- Chapter 6 implements PM4Sand within the hydromechanical higher-order MPM framework for the first time, and the new MPM framework is fully deployed and validated in dynamic loading conditions. The aim is to bridge the gap between state-of-the-practice constitutive models developed using small strain and particle-based techniques that enable large strains. As such, we capture the cyclic sand behavior including liquefaction-triggering and subsequent cyclic mobility. This framework can enable the investigation of the accuracy of emerging constitutive model beyond failure. The PM4Sand

implementation is verified against Opensees [113, 114]. The overall framework is used to simulate a centrifuge experiment from the VELACS program where the deformation of a clay embankment resting on saturated sand is instrumented. The proposed MPM framework presents a promising tool to analyze earthquake-triggered failures and runout while capturing material nonlinearity in a unified framework.

- Chapter 7 presents the dissertation's conclusion, providing the main findings and recommendations for future work to extend this research.

Appendices are also included in this dissertation, which contain peer-reviewed conference publications and supplementary material related to this research as follows:

- Appendix A presents MPM runout modeling of a shaking table test by Hiraoka et al. [115]. This includes the assessment of the seismic shaking application on the nodes versus the MPs. The contact algorithm is also used to simulate the soil-structure interaction. Parametric analyses are conducted to investigate the impact of unsaturated soil conditions on the runout.

- Appendix B presents a comparison of the MPM with the one-dimensional site response solution using a real ground motion. Linear-elastic behavior is assumed to simplify the problem. Comparison of the MPM is also performed with FEM.

- Appendix C presents a study on the simulation of fluid column collapses using the higher-order B-spline MPM. This includes large-strain free-surface flows with downstream barrier interaction. The effect of rigid versus flexible barrier on the fluid runout is also explored. Comparison with experiments and data from other numerical models in the literature is included for reference.

- Appendix D presents the implementation details of the higher-order isogeometric MPM. This includes computational cycle details of the two-phase single-point formulation, NURBS interpolation function algorithm, local position calculation, and pertinent simplified benchmarks.

- Appendix E presents the formulation of the PM4Sand constitutive model including details regarding the bounding, dilatancy, critical state and yield surfaces. The model is stress-ratio controlled and captures pertinent characteristics of the cyclic behavior of sand. This includes stress reversal, nonlinear elastic modulus, kinematic hardening, calibrated response for contraction and dilation, and stress-induced anisotropy through tracking the fabric.

Chapter 2

Modeling Earthquake Triggered Slope Runout using the MPM

Published in the Proceedings of the Institution of Civil Engineers - Geotechnical Engineering, with the following reference: Alsardi, A., Copana, J. and Yerro, A., 2021. Modelling earthquake-triggered landslide runout with the material point method. Proceedings of the Institution of Civil Engineers-Geotechnical Engineering, 174(5), pp.563-576.

The following authors contributed to this manuscript, as follows:

- Abdelrahman Alsardi
  - Conceptualized and implemented the kinematic prescribed velocity boundary condition while moving the mesh corresponding to the ground motion.
  - Researched the literature and obtained experimental data by Wartman et al. [26]
  - Performed all numerical simulations from pre-processing to post-processing and analysis.
  - Prepared all figures and wrote the original draft of the manuscript.
- Julio Copana
  - Performed the Newmark [34] and simplified Newmark-type analyses for the theoretical slope geometry.
- Dr. Alba Yerro
  - Introduced the idea of simulating coseismic slope instabilities using MPM.
  - Discussed feedback, results, and troubleshooting strategies to perform successful numerical simulations.
  - Obtained research funds to enable the development of the framework.
  - Edited and revised the manuscript.

2.1 Abstract

Landslides triggered by earthquakes cause devastating consequences to downstream infrastructure. The simulation and prediction of these large-strain events remain challenging. The

objectives of this paper are i) to validate the Material Point Method (MPM) framework for the study of coseismic landslides; and ii) to compare the capabilities of MPM with mesh-based methods and simplified Newmark-type methods to simulate post-failure runouts. To achieve these objectives, the MPM framework is presented whereby nodal kinematic boundary condition is employed with a moving mesh. Secondly, the framework is validated with a shaking-table laboratory test of a saturated clay slope. Thirdly, a parametric analysis is conducted using 25 real ground motions on a simple theoretical slope. The MPM results are compared to those obtained with mesh-based methods and three state-of-the-art Newmark-type approaches. It is concluded that mesh-based methods are consistent with MPM predictions for small-strain instabilities associated with low energy ground motions (i.e. Arias intensity lower than 4 m/s). When using ground motions with energy above this threshold, mesh-based methods accumulate significant errors associated with bad geometry. MPM results consistently matched permanent displacements predicted with the Newmark-type methods employed in this analysis.

2.2 Introduction

Coseismic landslides are considered as one of the most catastrophic large-strain manifestations of earthquakes. A recent example of such problem was in January 2020, whereby an earthquake in Puerto Rico (M_w 6.4) triggered more than 120 landslides, and mobilised soil mass up to 40 km from the initial epicenter [116]. Consequently, the lives of 7,500 residents were disrupted due to these events [117]. Despite the socio-economic impacts associated with coseismic landslides, it is still challenging to predict the relationship between the triggering factors (e.g., intensity measures of the earthquake) and the final runout of these events. The mechanisms controlling the kinematics of these failures involve soil non-linearity, large

deformation, and multiphase interaction, all in one dynamic framework.

Traditional seismic slope stability analyses include several methods. In the pseudostatic limit equilibrium analysis [33], the slope stability is crudely represented as a factor of safety, which is only valid when there is low crest accelerations and less than 15% soil strength degradation due to pore pressure build up [118]. The rigid sliding block analytical solution was proposed by [34] to predict permanent displacements resulting from seismic loading. [34] assumes that soil behaves in a rigid-perfectly plastic manner across a well-defined slip surface, with no strength loss due to shaking. The block exhibits relative sliding episodes when the factor of safety goes below unity, and accumulates permanent displacement as it moves downstream. This model provides a simple framework with only two input parameters, namely yield acceleration, a_y as proxy for its threshold dynamic resistance, and the acceleration-time history of the basal ground. Practitioners often employ the pseudostatic limit equilibrium analysis to quantify the value of a_y. However, this ultimately restricts the scope of [34] method to simple constitutive behaviours and geometries. Many researchers modified the [34] approach to include internal volumetric straining as a mechanisms of slope deformation. Makdisi and Seed [40] developed charts to semiempirically estimate Newmark-type permanent displacements considering one-dimensional acceleration amplification from the slope base to crest using the Finite Element Method (FEM), producing the so-called "decoupled approaches". Further subsequent advancements such as the "fully coupled approaches" were developed to accomplish a simultaneous analysis of deformations caused by the dynamic response and the sliding response [44]. Newmark-type sliding block methods can be simplified to data-driven procedures where the results are correlated to the slope's dynamic characteristics and ground motions parameters to develop generalised semiempirical equations known as the "simplified Newmark-type methods" to estimate permanent displacements.

Advancements in understanding the large-strain mechanics of coseismic landslides often re-

sort to controlled shaking-table experiments or centrifuge models (e.g., [26]). However, these laboratory facilities are extremely expensive and challenging. For this reason, the validation of numerical methods capable of modelling large strains, multiphase problems, advanced constitutive behavior, and time-dependent boundary conditions play an important role for evaluating shaking effects on the triggering and post-failure deformations of coseismic landslides. Mesh-based formulations, such as FEM or Finite Difference Method (FDM), are among the most commonly used tools for conducting dynamic numerical analyses (e.g., [48]). They use a Lagrangian formulation whereby the continuum is discretised into a computational mesh that deforms to represent the material behaviour. At large strains, element distortion leads to extreme error accumulation leading to mesh tangling. Efforts to extend these techniques to large-strain problems include rezoning, remeshing, and remapping algorithms. However, these algorithms are computationally expensive and interpolate the history variables at the nodes, which ultimately reduces the accuracy of the stress calculation [55]. To overcome the distortion of the computational mesh, particle-based numerical tools are used for the modelling of landslides, such as the Material Point Method (MPM) and the Smoothed Particle Hydrodynamics (SPH). In the MPM computational cycle, the state variables are mapped back and forth between the material points and the nodes which significantly increases the computational cost compared to traditional mesh-based approaches (e.g., FEM, FDM). Numerical oscillations may arise in the MPM computation due to cell-crossing error [60]. Expensive computational cost is also seen with SPH as a result of the use of particle search functions. SPH suffers from difficulties when defining boundary conditions and numerical instabilities when insufficient neighboring particles are found [55]. This research focuses on MPM; validation is necessary to build confidence in the MPM as an emerging tool for the analysis of coseismic landslides.

The objectives of this study are i) to present and validate the MPM framework for the

modelling of earthquake-induced shaking using a time-dependent boundary condition in a moving mesh approach; and ii) to evaluate the performance of MPM in comparison with other existing approaches for the prediction of runout such as mesh-based methods (i.e. FEM and FDM) and simplified Newmark-type methods. To achieve these goals, the paper is organized as follows. First, the MPM numerical framework is introduced with particular emphasis on advancements to model earthquake-induced shaking. Secondly, the capabilities of the MPM in modelling large-strain coseismic landslides are validated against a laboratory test [26] whereby a saturated clay slope was tested on a shaking table apparatus. The results and sensitivity of the MPM to mesh refinement is discussed. Thirdly, parametric analysis is performed on a theoretical slope geometry using 25 real strong-motions records from the Pacific Earthquake Engineering Research (PEER) center database. The MPM results are compared with predictions from the rigid sliding block method, simplified Newmark method, and the mesh-based methods (FEM and FDM). The limitations of the mesh-based numerical methods are demonstrated in the context of error accumulation due to large-strain runout.

2.3 The Material Point Method

MPM is a hybrid Lagrangian-Eulerian numerical procedure capable of modelling large-strain deformations in history-dependant materials. The spatial discretisation consists of an Eulerian discretisation of the entire domain using a background mesh and a Lagrangian discretisation of the material domain (i.e., continuum body) using a set of integration points. Each point, so-called a Material Point (MP), moves attached to the material carrying state variables including the mass of the represented subdomain. Limitations of the MPM include noise due to cell-crossing instabilities, particularly when using lower-order shape functions [60]. Higher order and B-spline shape functions provide continuity of gradients of the shape

functions which eliminate cell-crossing error. However, the construction of the mass matrix and force vectors become more challenging. Negative values of the shape functions in the element can lead to a singular mass matrix [67]. In addition, higher order shape functions are computationally expensive when considering high number of degrees of freedom. Trade off between the overall stability and the computational cost limit the application of higher order shape functions in MPM. Noise reduction techniques include the use of mixed MPM-Gauss-Point integration, which allows the computation of an averaged incremental stress using optimally positioned Gauss points [119]. In this paper, the mixed MPM-Gauss-Point integration scheme is adopted to compute the nodal internal forces, but the constitutive equation is evaluated at each individual MP to retain the history of the MP state variables. Least squares volumetric strain-smoothing algorithm is also employed, as implemented in previous works (e.g.,[120]), to overcome element locking and prevent over-stiffening effects in undrained incompressible material modelling. Further details of the MPM basis, formulation and implementation is presented in [59] as employed in the Anura3D software. Recently, MPM has demonstrated promising capabilities for the simulation of landslides, including advanced hydro-mechanical coupling [119, 121, 122]. Considering an explicit time integration scheme, the MPM computational cycle, can be summarized as follows [59, 123]:

- Interpolate state variables from MPs to nodes using shape functions to calculate nodal mass, nodal external forces, and nodal internal forces.
- Solve discretised linear momentum governing equation to compute nodal acceleration.
- Compute MP velocity using the explicit time integration scheme.
- Compute MP and nodal linear momentum. Subsequently, evaluate the nodal velocity.
- Compute incremental MP strain rate using the nodal velocity.

- Solve constitutive equation at the MP, and update stresses and state variables.
- Update MP displacement and discard nodal variables to reinitiate a non-distorted mesh for the next computational cycle.

2.3.1 Developments of MPM for the modelling of coseismic landslides

Earthquake loading in MPM can be prescribed as velocity, displacement, or stress-time history. Although the specification of input ground motion using stress-time history could be attractive for use with viscous boundary conditions, Green et al. [52] found that the use of stress-time input is least accurate when comparing the nonlinear numerical dynamic numerical response of a viscoelastic column with its equivalent linear solution. Since displacement-time histories are less commonly available for real ground motions, this study specifies the input ground motion in the MPM as a velocity-time history.

Few attempts exist in the literature that model earthquake shaking with MPM [78, 124, 125]. All of them apply a time-dependent kinematic velocity boundary condition on the MPs. This approach requires the definition of a 'basal' material (e.g., shaking table box or bedrock frame) that moves within the mesh according to a prescribed velocity-time history. As such, the basal MPs move back-and-forth within the computational domain. In these boundary conditions, when the conventional MPM approach (i.e., fixed background mesh) is employed, the nature of the shaking increases the cell-crossing (i.e., MPs crossing element boundaries) as most of the MPs move back and forth with respect to the mesh. This may lead to numerical instabilities cell-crossing instability is not prevented. Very recently, the authors of this paper, proposed a more computationally efficient non-zero kinematic velocity boundary condition to overcome some of these drawbacks in [80]. This boundary condition

applies the prescribed velocity on the boundary nodes of the background mesh of the MPM model. A moving mesh technique [119] is also incorporated to reduce the cell-crossing to only those MPs that move with respect to the seismic motion (i.e., MPs in the sliding mass). In this manner, the computational mesh moves following the input velocity-time history of the ground motion. Therefore, the noise possibly generated from cell-crossing in the coseismic landslide simulation is considered comparable to the one generated in the accepted MPM models for non-seismically triggered landslides (e.g., [56]). Additionally, this approach provides more flexibility in the geometry of the problem, as the definition of the basal MPs is not mandatory. The work presented here is implemented in an internal version of the Anura3D software (http://www.anura3d.com) within the framework of the one-phase formulation.

Figure 2.1 summarizes the implementation of the nodal kinematic boundary condition within the MPM computational cycle [80]. The prescribed nodal velocity is applied along the boundary domain Ω_u of the mesh (Figure 2.1a). Consistent with the presented computational cycle, step 1 to 4 are identical whereby the information is mapped to the nodes and thereof solved to obtain the nodal velocity, v_i, as shown in Figure 2.1b. To specify the shaking criteria in the MPM system along the boundaries of the mesh, the nodal velocity solution is overwritten with the velocity-time history, v^{input}, at the beginning of each computational cycle, as shown in Figure 2.1c. The MP velocity is updated using shape functions particularly for those MPs in the elements which contain a prescribed velocity node to ensure solution consistency in both Lagrangian and Eulerian domains (Figure 2.1d). Finally, as opposed to discarding the nodal displacement in step 7, the mesh is incrementally rigidly moved by Δu^{mesh}, following the ground motion input and ensuring that the MPs remain within the computational domain (Figure 2.1e).

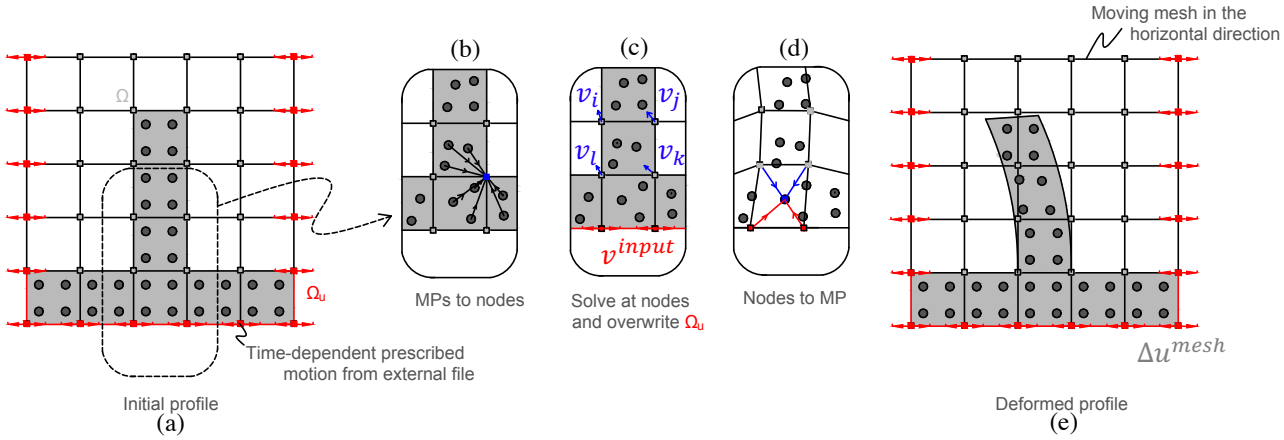

Figure 2.1: MPM computational cycle using the time-dependent kinematic nodal prescribed velocity boundary condition in a moving mesh approach: (a) Initial configuration whereby the prescribed velocity is applied on the nodes; (b) information is mapped from MPs to nodes; (c) velocity is overwritten on the nodal solution of the momentum balance equation; (d) velocity of the MPs is corrected to be consistent with the nodal solution; (e) final deformed configuration.

Table 2.1: Parameters of the synthetic Kaolinite-Bentonite clay material used in the MPM model

Parameter	Soft Clay	Stiff Clay
Saturated unit weight, γ [kN/m^3]	13.6	13.6
Peak undrained strength, $S_{u,peak}$ [kPa]	2.68	5.90
Residual undrained strength, $S_{u,resd}$ [kPa]	1.77	4.03
Undrained poisson ratio, ν_u [-]	0.485	0.485
Undrained small-strain stiffness, E_u [kPa]	615	4190

2.4 Numerical validation using shaking table test on model-scale clay slope

The objective of this section is to validate the MPM framework for earthquake-induced motion using experimental data from a shaking table test on a clay slope conducted by [26] at the University of California, Berkeley. This section focuses on modelling the translational/rotational deformation mechanism observed in the largest slope model built in the testing

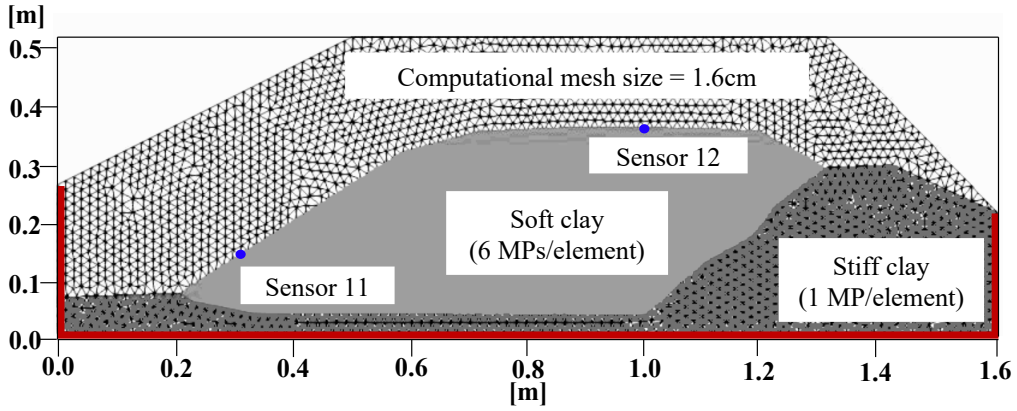

Figure 2.2: Plane-strain MPM model of the shaking table experiment by Wartman et al. [26]

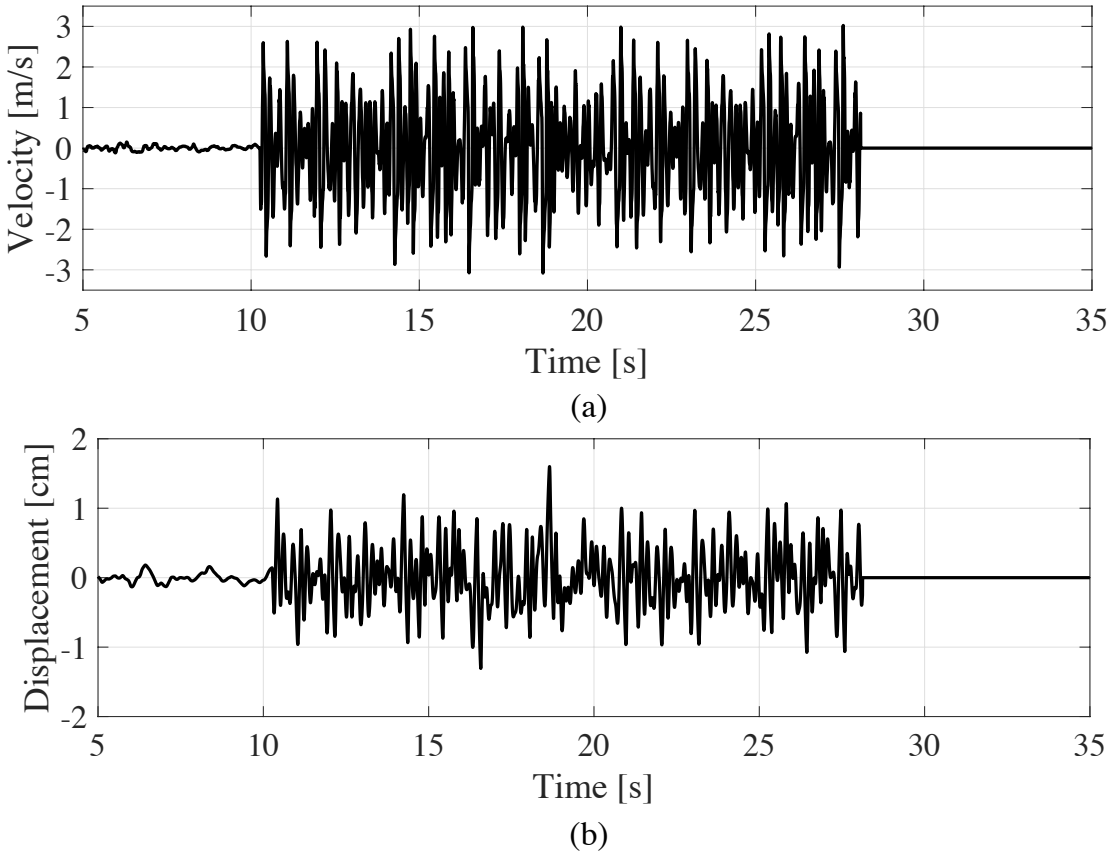

Figure 2.3: Results from processing the synthetic acceleration-time history used in Wartman et al. [26]: (a) velocity-time history. (b) displacement-time history.

program by Wartman et al. [26].

2.4.1 Physical testing

The physical testing program by Wartman et al. [26] involved building, 30 cm high, saturated slopes made from synthetic clay mixture, placing each slope in a rigid box container, and shaking them by means of a shaking table apparatus. The geometry and strength parameters used to construct the slope were not based on a real prototype, albeit Wartman et al. [26] used approximate model scaling for mimicking a tall natural embankment. The cross-section of the considered slope used is depicted in Figure 2.2, which was comprised of a soft clay deposited over a stiff clay base. Both materials were made from a synthetic mixture of identical mineralogy, consisting of 75% kaolinite and 25% bentonite by dry weight, with different initial water content to control their strength and stiffness. Potentiometers, labelled sensor 11 and 12 in Figure 2.2, were used to measure the displacements across the surface of the slope during the shaking table test. The shaking table box (highlighted in red in Figure 2.2), made from rigid fully-reflective Plexiglass, plays no effect on the experimental results as it is not in direct contact with the soft clay. The undrained strength of the soft clay was characterized using a miniature vane shear test to an average confining depth of 18 cm [26]. The mobilised undrained shear strength for a reference sample was presented against peripheral displacement along the circumference, as shown in Figure 2.4. The in-situ small-strain stiffness was calculated by measuring the shear wave velocity from striking a hammer on the constructed clay slope. The acceleration response of the slope was also analysed using the shaking table prior to the actual test, whereby gentle sweep tests were applied using low-amplitude ground motion without causing permanent deformation. The clay surface was marked and surveyed before and after the shaking table test to measure the final displacement caused by the failure mechanism of the slope.

The behaviour of the synthetic clay was seen to be complex, including strain-softening behaviour, moderate strain-rate effects, and shear modulus degradation [26, 126]. Since the shear strain rates were more than 100 times larger than that of the hammer blow tests, the measured shear wave velocities were required to be corrected by calibrating the simulated and recorded acceleration response spectra from the sweep test [127]. Consistently, Chen and Qiu [128] performed nonlinear dynamic analysis of the same slope with the SPH method. They showed that the shear wave velocity required to reproduce the slope response during the sweep test needs to be increased with respect to those measured from the hammer strike by approximately 65% and 80%, for soft clay and stiff clay, respectively.

2.4.2 Ground motion correction scheme

The strong ground motion input used to shake this slope in the experiment was created synthetically to cover a frequency content ranging from 1 Hz to 20 Hz, with PGA of 3.46g. In the present work and as recommended by Wartman et al. [26], a linear baseline trend correction is applied to remove the drift in the acceleration-time record. Additionally, high-pass filtering at 0.5 Hz and low-pass filtering at 60 Hz, is considered to eliminate significant long period noise contamination. The acceleration-time history filtering is conducted using Obspy, an open-source Python package by Beyreuther et al. [129]. The filter is applied in the forward and backward direction to prevent any phase-shifts. The acceleration-time history is numerically integrated, using the trapezoidal rule, to obtain the velocity-time history (Figure 2.3a) for use as an input in the kinematic boundary condition in the MPM. The velocity-time history is integrated in a similar way to obtain the displacement-time history (Figure 2.3b), which confirms the elimination of long period noise and baseline drift, while ensuring negligible amplitude difference of less than 10% when comparing with the displacement-time history without the correction scheme.

2.4.3 Constitutive model

In this paper, the strength of the synthetic clay is modelled by means of an associated Tresca constitutive model that incorporates an additional strain-softening law based on Yerro [120] to account for the material brittleness. Strain-rate effects and stiffness degradation are not modelled here for simplification. The employed softening law (Equation 2.1) reduces the undrained shear strength, S_u, exponentially as a function of the accumulated equivalent plastic strain, ϵ^p_{eq}. The peak undrained shear strength, $S_{u,peak}$, and the residual shear strength, $S_{u,resd}$ are input properties. Also, the shape factor, η, is required to calibrate the exponential functional form of this softening law against experimental data. Large values of η correspond to greater strength decrease with plastic strain accumulation (i.e., more brittle nature). Table 2.1 presents a summary of the total stress material parameters based on Wartman et al. [26], with exception to the undrained small-strain stiffness, E_u, which is based on the aforementioned calibration performed by Chen and Qiu [128].

$$S_u = S_{u,resd} + (S_{u,peak} - S_{u,resd})e^{-\eta\epsilon^p_{eq}} \tag{2.1}$$

Besides the basic mesh h-type refinement associated with reducing the element size to ensure better failure localisation, it is known that the use of a softening law in continuum-based constitutive models adds extra complexity [56, 130]. The energy dissipation across each element in the MPM is dependent on the mesh size and a mesh convergence analysis is required to calibrate η with laboratory testing. The goal is to ensure an equivalent dissipated energy between the numerical model and the physical experiment. Yerro [120] proposed to use the 'smeared-crack' fracture approach defined by Oliver and Huespe [130] to calibrate the factor η. Following Yerro [120], the strength mobilised in strain-controlled single-element tests needs to be calibrated (i.e. using different values of η) to be consistent with the one

observed in the vane shear laboratory test [26]. Wroth [131] showed that the stress path of the soil in a vane shear test is partly mechanically equivalent to a reoriented direct simple shear test (DSS) such that the vertical and horizontal confining stresses of a soil element near the shear blade are reversed. Inspired by Morris and Williams [132] and Wroth [131], two-dimensional (2D) plane-strain DSS are modelled using a single row of elements. Assuming K_0=0.5 at an average blade depth of 18 cm, the in-situ total vertical stress is applied to confine the elements horizontally, and the in-situ lateral total stress is applied on the simulation vertically. Prescribed velocity of 12 cm/min, consistent with the circumferential speed of vane shear test, is applied at the top of the row of elements to generate the DSS total stress path. The results from the vane shear test presented by Wartman et al. [26] from a representative clay sample are used here for reference. The value of η is varied by increments of 0.05 until the area under the stress-displacement graph is approximately the same for the MPM simulation and the vane shear laboratory test, to ensure an equivalent energy dissipation in all the simulations. The calibration was conducted for element length, h, of values associated with a coarse-medium (3 cm), medium (2.3 cm), and fine mesh (1.6 cm) as shown in Figure 2.4.

2.4.4 Numerical model and calculation stages

The MPM model consists of a plane-strain analysis. Triangular elements with first order (linear) shape functions are considered in the MPM model. The initial configuration is depicted in Figure 2.2. Each element of the soft clay material is initiated with the minimum number of MPs to prevent sporadic empty elements at large strains. Six MPs per element is determined to be the minimum for the soft clay material. One MP per element is sufficient for the elements of the stiff clay as its MPs are close to the boundary and do not exhibit cell-crossing. First, the stresses due to gravity are initiated in quasi-static conditions, assuming

a fully fixed base and rollers in the vertical boundaries. Then, horizontal fixities are removed and the shaking is applied on the boundary nodes (highlighted in red in Figure 2.2) with the velocity-time history shown in Figure 2.3a to represent the rigid, fully-reflective shaking table box. Artificial local damping of 5% is applied to the computational system during the shaking stage. The background mesh is moved in a rigid manner with the box to minimize cell-crossing noise. The MPs at locations corresponding to sensors 11 and 12 are tracked to plot the displacement-time history for quantitative validation with the physical experiment.

2.4.5 Results and discussion

The relationship of the strain-softening calibration with the employed mesh refinement is highlighted in Figure 2.5, that shows the effect of mesh size, h, in the results. It is observed that the use of a single value of η produces inconsistent displacement values at sensor 11, whereby finer meshes result in larger displacements. Contrarily, after calibrating η for each value of h, the accumulated total displacement is consistent for all mesh sizes. This highlights the importance of calibrating the constitutive model at a single-element level, which is of paramount importance in ensuring the consistency of the results. The final geometry of the slope is shown for different mesh refinements in Figure 2.6. Although the shear band thickness was observed to decrease with smaller element size, this qualitative comparison of the displacement profile shows that the mesh dependency is reduced when the value of η of the constitutive model is calibrated. In this conditions, the computational cost increases with mesh refinement (as shown in CPU times in Figure 2.5). Similar results were also reported by [56] using the MPM for modelling strain-softening progressive failure in natural scale slopes. To optimise the computational cost, the coarse-medium mesh size (h=3.0 cm) with its calibrated shape factor (η=4.35) is sufficient for practical purposes. However, in this paper, the model with fine mesh is presented for better visualisation of the slope profile.

Figure 2.7a and 2.7b depicts the displacement (magnitude) and final deviatoric strain profiles of the slope, respectively, and compares them with the outline of the final experimental profile. It is clear that the interface between the soft and stiff clay plays a major role in the development of the shear band, whereby the soft clay develops a translational/rotational mechanism at this interface. The deformed MPM profile is in acceptable match with the experimental profile, particularly at the toe and the upper surface of the embankment, whereby a maximum displacement magnitude of 12 cm is observed (Figure 2.7a). The experimental runout value was approximated by [26] to be 12-13 cm which is consistent with the MPM results. It is noted that the numerical profile at the crest scarp does not match the physical experiment. This is due to the continuum-scale nature of the MPM model which prevents free-separation between the MPs and requires advanced constitutive contact algorithms to reproduce the scarp transition. As such, the vertical settlement observed in MPM near the slope scarp (i.e., 1-1.3 m from the front of model container) is underestimated as shown in Figure 2.7c. In Figure 2.7, the MPM results are also compared with those presented by [128], who simulated the same slope using SPH employing an advanced Drucker-Prager constitutive model. Despite that the SPH model incorporates cyclic shear modulus degradation and strain rate-dependent strength, the SPH results are almost identical to the MPM model. Similar to MPM, the SPH model shows inconsistency at the scarp due to its continuum approach.

Finally, Figure 2.8 presents the horizontal displacement of sensors 11 and 12, located near the toe and the crest, respectively (Figure 2.2). An acceptable match between the MPM results and the experimental data is observed. This includes movement initiation at 11 seconds, which corresponds to the beginning of the strong motion shaking, and the subsequent general displacement trend. Note that the experimental runout results were cut short at 25 seconds due to the failure of the potentiometer sensor at large-strain. From these results, it is

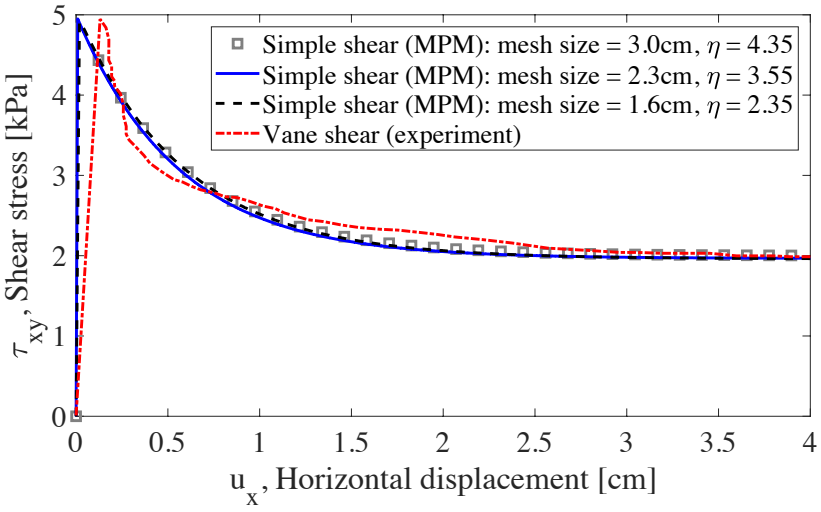

Figure 2.4: Calibration of the strain-softening exponential fitting factor, η

arguable that the strain-softening behaviour dominates in capturing the failure mechanism and the runout of the slope. Further investigation of the advanced constitutive model can provide insights into the compensating nature of the strain-rate strength increase and the shear modulus degradation on cumulative runout.

2.5 Comparative overview of the MPM against mesh-based and Newmark-type methods

The objective of this section is to investigate the capabilities of the MPM to model coseismic slope failure runouts compared to other available methods. In particular, two mesh-based methods (i.e., FEM and FDM) and three Newmark-based sliding block analyses are considered. A parametric analysis on a model-scale theoretical slope, in a shaking table set-up, is conducted using 25 ground motions. The ground motions correspond to 14 different earthquakes from the PEER strong motion database [133] as summarised in Table 2.2, covering a range of moment magnitudes, M_w from 6.0 to 8.0. Arias intensity, I_A, is computed for

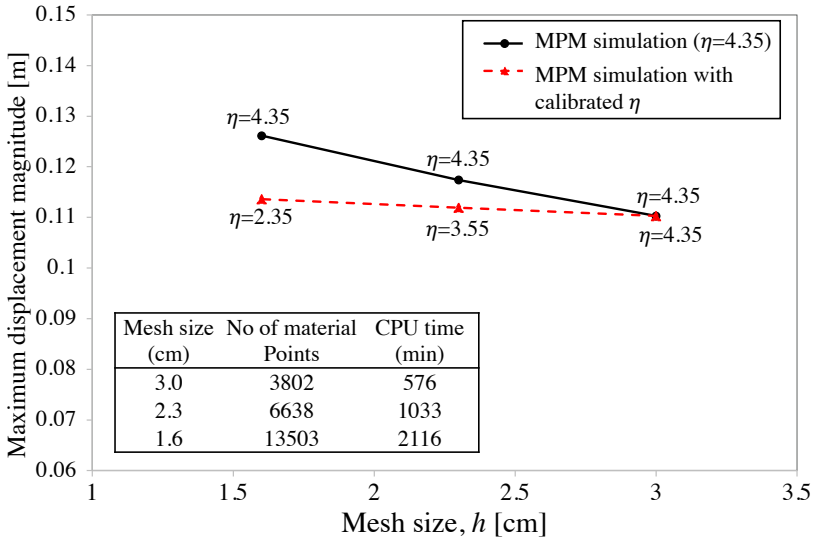

Mesh size (cm)	No of material Points	CPU time (min)
3.0	3802	576
2.3	6638	1033
1.6	13503	2116

Figure 2.5: Final runout (t = 30 s) mesh sensitivity analysis of the MPM model to the strain-softening constitutive model calibration.

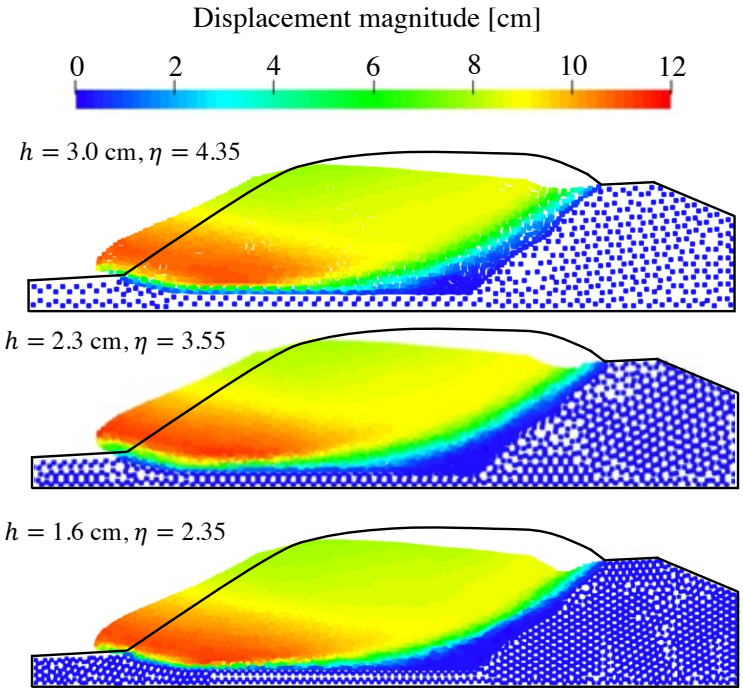

Figure 2.6: MPM displacement profile at t = 30 s for different mesh sizes using the calibrated constitutive factor, η.

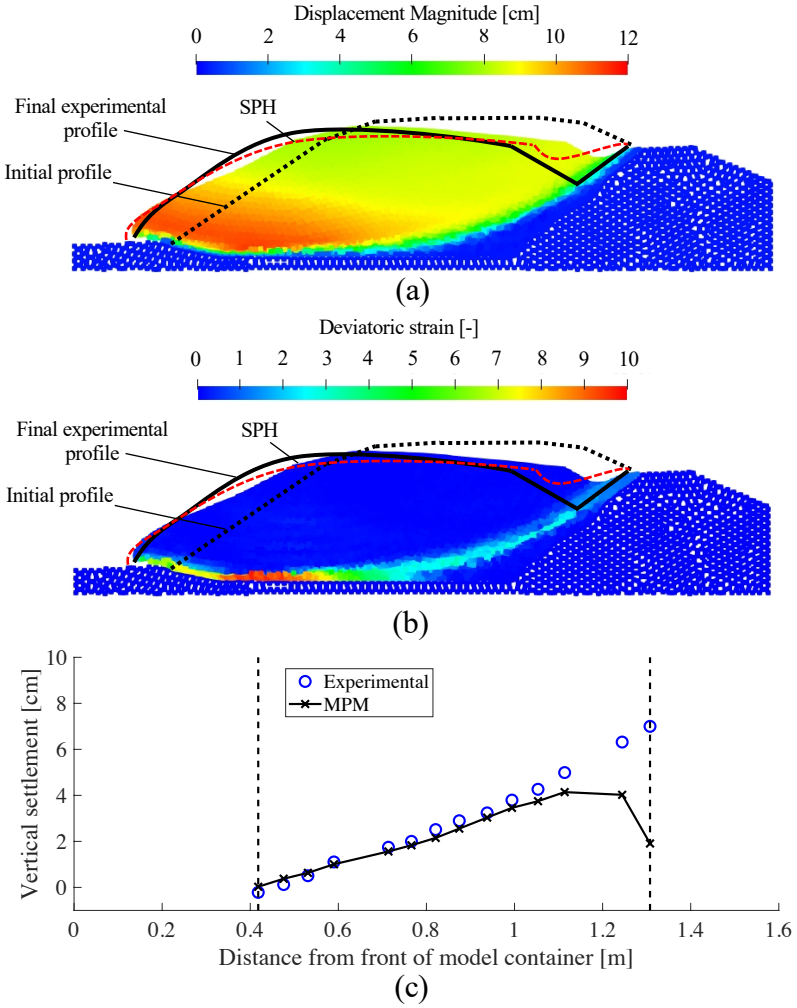

Figure 2.7: Experimental and numerical deformed profile of the slope; (a) displacement magnitude, (b) deviatoric strain, (c) final vertical displacement of the ground surface (t = 30 s).

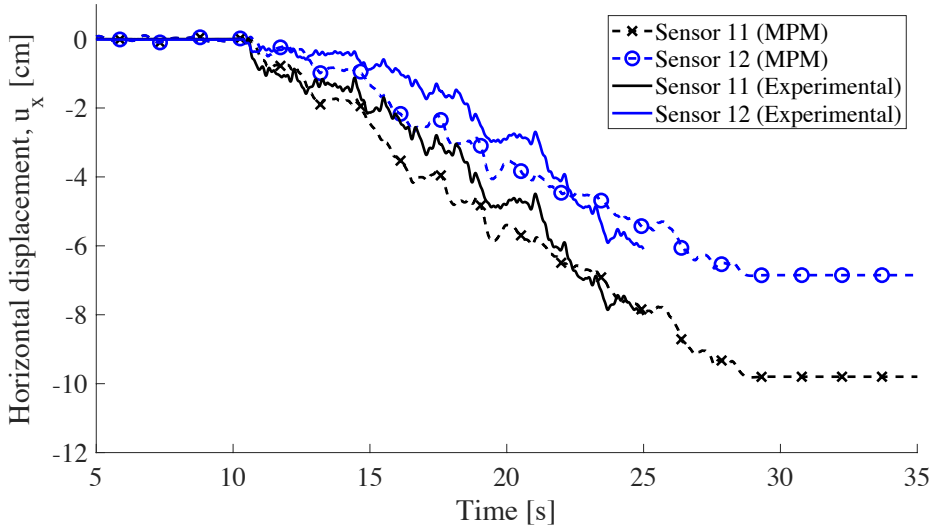

Figure 2.8: Horizontal displacement recorded at the toe (sensor 11) and top (sensor 12) of the slope. Comparison between MPM and experimental data recordings.

each ground motion as defined in Equation (3.16). The value of I_A provides an intensity measure of the energy delivered by the input ground motion as a function of its acceleration, a_t, across the overall duration, d, whereby g is the gravitational acceleration. This I_A intensity measure was selected as it holistically captures the amplitude, duration, and frequency characteristics of the input motion employed in the analysis [134]. For each station, the horizontal ground motion component that generated higher I_A was considered in the analysis. The relationship between the slope toe runout and I_A is investigated.

$$I_A = \frac{\pi}{2g} \int_0^d {a_t}^2 dt \tag{2.2}$$

The geometry of the homogeneous theoretical slope used in the parametric analysis is schematically depicted in Figure 2.9. The shaking boundary conditions (highlighted in red) correspond to a rigid box in a similar shaking table setup to the one discussed in the previous section. The unit weight, γ, of the soil was selected as 17 kN/m^3. A non-associated

Mohr-Coulomb constitutive model is employed to model the strength of a clayey sand soil with the following parameters: friction angle, ϕ'=25°; dilatancy angle, ψ=0°; cohesion, c'=1 kPa; Young's modulus, E'=3000 kPa; Poisson's ratio, ν'=0.33. Another important dynamic parameter is the fundamental period of the slope, T_n, which is a measure of the slope's rigidity as a function of the geometry and shear wave velocity. Equation (3.18) is employed to obtain the fundamental period of the adopted model-scale theoretical slope, consistent with [44]. This is considered as an acceptable approximation of the slope period when the potential sliding mass of crustal homogeneous slope is expected to be approximately shaped as a segment of a circle and the acceleration response throughout the depth of the model is approximated to be one-dimensional [44, 135]. The adopted model-scale theoretical slope has T_n=0.13 s, as calculated using Equation (3.18), whereby H is the vertical height of the slope and V_s is the shear wave velocity as computed from (2.4). The calculated value of T_n is used to guide whether the slope is characterised as 'rigid' or 'flexible'. For this study, a threshold value of T_n=0.2 s is adopted as the limit of rigid behaviour, consistent with [136]. Thus, the slope analysed here can be characterised as rigid.

$$T_n = \frac{4H}{V_s} \tag{2.3}$$

$$V_s = \sqrt{\frac{E'}{\frac{\gamma}{g}2(1+\nu')}} \tag{2.4}$$

2.5.1 Parametric analysis

The numerical analysis was conducted using FEM, FDM, and MPM. Details regarding the numerical implementation are summarized in Table 2.3. Note that the numerical damping schemes for each method were default, as recommended by the respective software develop-

ers to ensure stability and smoothness of the dynamic solution according to the employed time integration scheme. The initial configurations of the MPM, FEM, and FDM numerical models are presented in Figures 2.10a, 2.10b and 2.10c, respectively. Mesh size (h-type) convergence analysis was conducted for each model, and the largest mesh size, whereby convergence was achieved, was subsequently selected for further investigation in the parametric analysis. The calculation stages in FEM, FDM, and MPM are identical to those considered in the previous example. The MP at the toe was tracked for investigating the displacement-time history kinematics using MPM. Similarly, the node at the toe is tracked for the FEM and FDM analyses.

The state-of-the-art engineering practice relies on empirical simplified regressions based on the Newmark [34] framework. Taking into account that the slope is characterized as rigid, the Newmark [34] rigid sliding block method and two other simplified rigid Newmark-type methods (i.e., [36, 137]) are selected for comparison with MPM. The Jibson [36] model in Equation (2.5) was developed from an exhaustive regression of 875 sliding rigid-block displacements for yield pseudostatic coefficient, k_y, values between 0.2 and 0.8, and recommended for slopes that exhibit shallow landslides and rigid behavior. Similarly, the Hsieh and Lee [137] model in Equation (2.6) corresponds to a global ground motion data set (form 2) correlation. Both semiempirical models consider the displacements D in cm and I_A in m/s. Note that other well-known decoupled and coupled simplified Newmark-type methods (e.g., [118, 127]) were developed for large-scale geometries and high V_s values to account for the one-dimensional ground response, rendering their model assumptions inconsistent for comparison with the theoretical slope adopted here. The [34] rigid sliding block method was implemented considering only the positive side of the accelerations for integration, so up-slope displacements are neglected. Using this approach, earthquake-induced deviatoric permanent displacements are computed at a predefined slip surface. To determine k_y, pseu-

dostatic analyses using the [138] limit equilibrium framework were performed to identify the failure surface with yield pseudostatic coefficient k_y that provides a factor of safety equal to one, resulting in k_y=0.20.

$$\log(D) = 2.401 \log(I_A) - 3.481 \log(k_y) - 3.230 \tag{2.5}$$

$$\log(D) = 0.847 \log(I_A) - 10.62 k_y + 6.587 k_y \log(I_A) + 1.84 \tag{2.6}$$

2.5.2 Parametric analysis results and discussion

The effects of strong ground motions from earthquakes on slopes vary from minimal displacement to failure. For comparison, two representative ground motion cases with I_A values equal to 2.5x10$^-$3 and 11.8 m/s are analysed to assess the numerical models' performance at small-strain and large-strain, respectively. Figure 2.11a shows that shaking with low I_A induces small strains and the displacement-time history obtained with FEM, FDM, and MPM match perfectly. All methods, including the [34] rigid sliding block method, consistently predict zero permanent displacement. For large-strain runouts (Figure 2.11b), the FDM simulation crashes at 6 second due to bad element geometry at the toe. Similarly, the mesh of the FEM simulation accumulates error, entangles, and the mobilised mass interpenetrates the base platform downstream at 11 seconds. The erroneous behavior of the mesh-based models at large-strain are depicted for the FEM and FDM models in Figure 2.10e and Figure 2.10f, respectively. By contrast, the MPM successfully models the entire slope instability process until stabilization at 33 seconds with final deformed profile shown in Figure 2.10d. The toe displacement predicted with MPM is consistent with the permanent displacement calculated using [34]. Note that while the displacement-time history trends obtained with FEM, FDM

and MPM are sensitive to the direction of the dynamic load, the Newmark approach predicts a monotonic increase of the permanent displacement because only the downward slide motion is accounted. Figure 2.12 presents the final runouts (i.e., horizontal displacement recorded at the toe) obtained with the different methodologies correlated with the I_A from the 25 ground motions. For reference, a quadratic trend of the MPM results is also included. Figure 2.12a compares the results obtained with the numerical simulations (FEM, FDM, and MPM). Note that only successful simulations are plotted in this figure (i.e., no entanglement and no crashing). The capabilities of the mesh-based and particle-based methods are similar only for small-strain slope instabilities ($0< I_A <4$ m/s). For large-strain instabilities associated with high energy ground motions ($I_A >4$ m/s), the particle-based MPM is necessary to model the entire slope instability mechanism. Figure 2.12b shows the comparison between the MPM runout results and the permanent displacement predicted by the sliding block analyses [34, 36, 137]. In general, the [36] and [137] simplified methods are in good match, exhibiting less scatter than the [34] rigid sliding block solution. A threshold value of $I_A =4$ m/s is observed. Below that threshold, the Newmark-type methods slightly underpredict the permanent displacement with respect to the MPM. Conversely, they estimate higher displacements than the MPM above that threshold. Since the permanent displacement outputs of the simplified Newmark-type methods are merely seen as an order of magnitude indices, the general variation of the runout with the I_A value of the input groundmotion in Figure 2.12b is deemed consistent with the MPM. This parametric analysis successfully confirms that the advancements in the large-strain numerical framework of the MPM are consistent with state-of-the-art simplified Newmark-type methods presented in this paper.

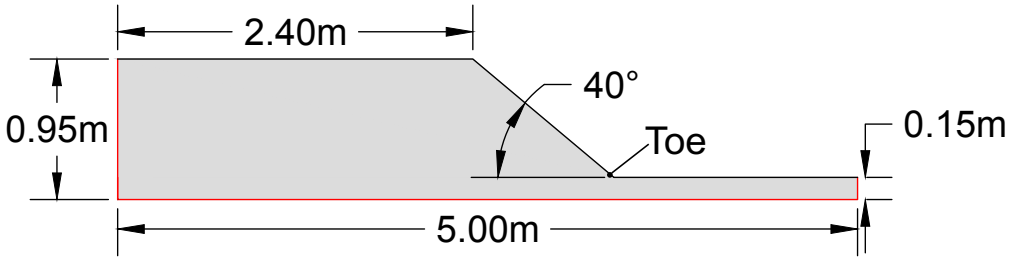

Figure 2.9: Slope geometry with shaking boundary conditions (highlighted in red)

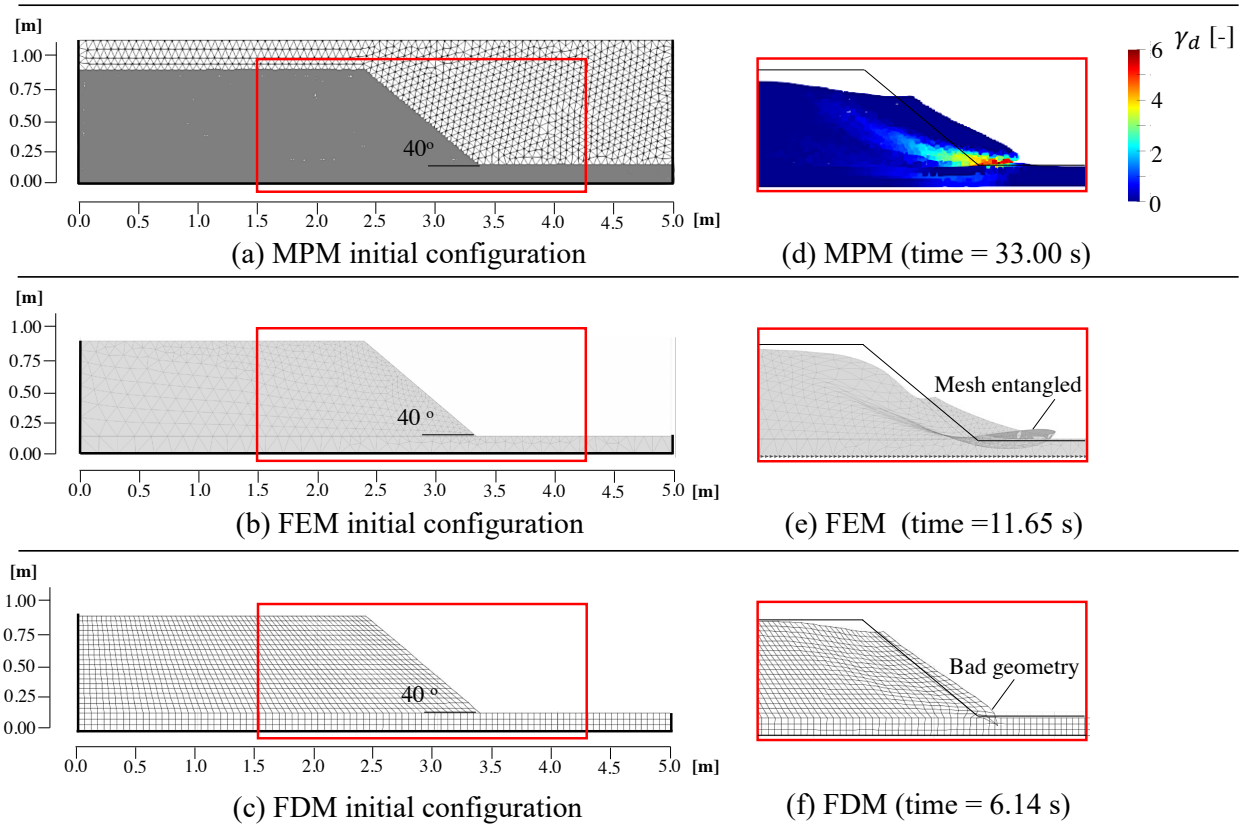

Figure 2.10: Initial configurations of the numerical models as part of the parametric analysis, and the deformed profiles associated with the Tabas earthquake, Iran (I_A=11.8 m/s). (a) MPM, (b) FEM, (c) FDM.

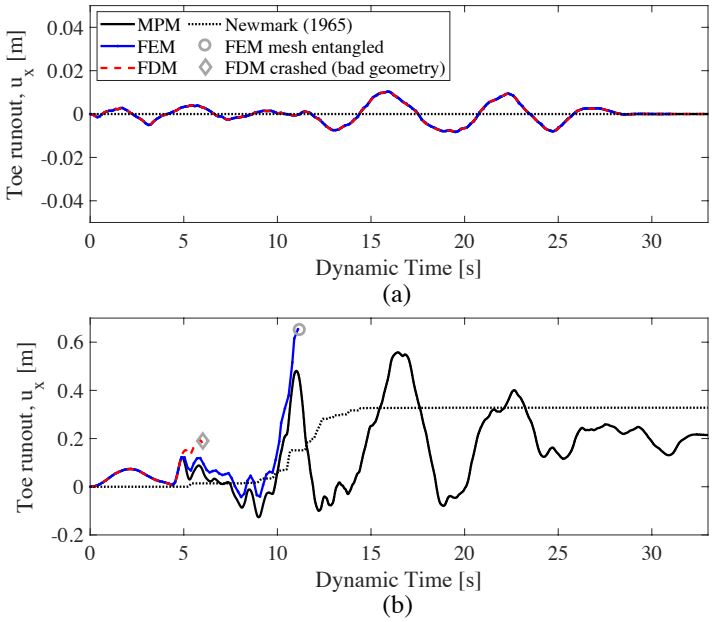

Figure 2.11: Toe runout at (a) low Arias intensity (i.e., I_A=2.5x10^{-3} m/s). Note MPM, FEM, and FDM results lie on top of each other; (b) high Arias intensity (i.e., I_A=11.8 m/s)

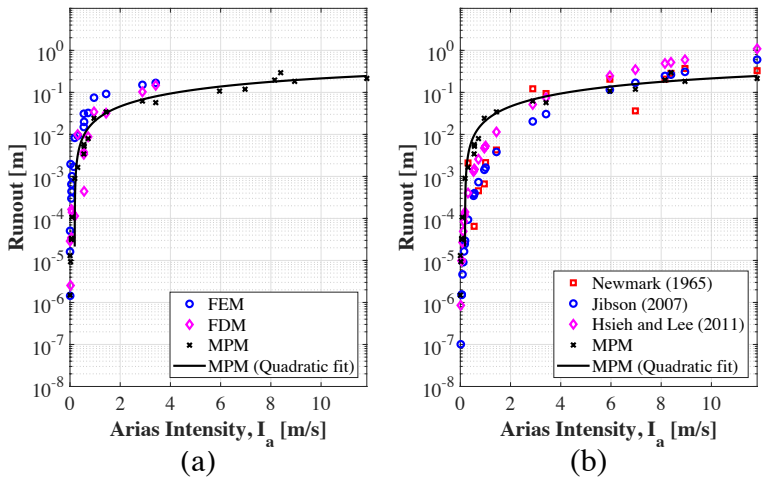

Figure 2.12: Permanent displacements obtained from 25 ground motions using (a) MPM, FEM, FDM and (b) MPM and selected Newmark-type sliding block methods.

Table 2.2: Summary of the ground motions.

Event	Date	Region	M_w	Number of records
Morgan Hill	April 24, 1984	California	6.19	1
Whittier Narrows	October 1, 1987	California	5.99	1
Palm Springs	July 8, 1986	California	6.06	1
Northridge	January 17, 1994	California	6.69	1
Chalfant Valley	July 21, 1986	California	6.19	1
Landers	June 28, 1992	California	7.28	2
San Fernando	February 02, 1971	Califronia	6.61	3
Cape Mendocino	April 25, 1992	California	7.01	4
Mammoth lakes	May 25, 1980	California	6.06	1
Parkfield	September 28, 2004	California	6.19	2
Helena	October 18, 1935	California	6.00	1
Kobe	January 17, 1995	Japan	6.90	1
Izmit	August 17, 1999	Turkey	7.51	1
Tabas	September 06, 1978	Iran	7.35	5

Table 2.3: Summary of the numerical analyses conducted in the parametric investigation.

Numerical method	Material Point Method (MPM)	Finite Element Method (FEM)	Finite Difference Method (FDM)
Software	Anura3D (plane-strain)	Plaxis2D (plane-strain)	Flac2D (plane-strain)
Elements	3-noded triangular element with 3 material points	15-noded triangular element with 12 gauss points	4-noded quadilateral element
Time integration scheme	Explicit Forward-Euler	Implicit Newmark Beta	Explicit Forward-Euler
Numerical damping scheme	5% artificial local damping	10% Newmark Beta damping ($\alpha = 0.3025$, $\beta = 0.6$)	5% artificial local damping
Dynamic boundary conditions	Rigid nodal prescribed velocity	Rigid nodal prescribed velocity	Rigid nodal prescribed velocity

2.6 Conclusions

The MPM formulation was outlined and discussed for earthquake-induced shaking, employing a nodal time-dependent boundary condition in a moving mesh approach. Subsequently, a slope failure on a shaking table based on [26] was successfully modelled using MPM, and a Tresca with strain-softening constitutive model. The numerical results in terms of the slope displacement and runout match well the physical experiment. Mesh-dependency effects were discussed, highlighting the importance of constitutive model calibration on the runout result of the slope. To understand the capabilities and limitations of the mesh-based, particle-based, and simplified Newmark approaches, a parametric analysis was conducted for a theoretical 'rigid' slope in a shaking table setup, using 25 real ground motions from the PEER database. The parametric analysis highlighted the limited capabilities of the mesh-based approaches at large-strain, whereby a maximum Arias intentsity of 4 m/s was identified as the energy threshold limit of the input ground motion in mesh-based models of the slope. Good match was seen between MPM results and selected state-of-the-art simplified Newmark-type methods. It is concluded that the validated MPM framework offers a promising numerical tool for modelling coseismic landslides and has good potential to simulate more complex large-strain scenarios.

Chapter 3

Coseismic site response and slope instability using periodic boundary conditions in MPM

Published in Journal of Rock Mechanics and Geotechnical Engineering, with the following reference: Alsardi, A. and Yerro, A., 2023. Coseismic site response and slope instability using periodic boundary conditions in the material point method. Journal of Rock Mechanics and Geotechnical Engineering, 15(3), pp.641-658.

The following authors contributed to this manuscript, as follows:

- Abdelrahman Alsardi
  - Conceptualized periodic boundary conditions in the MPM to capture the large-strain site response of a level-ground soil column.
  - Implemented periodic boundary conditions and the dissipative generalized-α time scheme in the MPM.
  - Performed all numerical simulations from pre-processing to post-processing and analysis.
  - Prepared all figures and wrote the original draft of the manuscript.
- Dr. Alba Yerro
  - Introduced the idea of the MP relocation technique to ensure that it remains within the background computational mesh when large deformations occur.
  - Discussed feedback, results, and troubleshooting strategies to perform successful numerical simulations.
  - Obtained research funds to enable the development of the framework.
  - Edited and revised the manuscript.

3.1 Abstract

This paper proposes the use of periodic boundary conditions and the explicit generalized-α time scheme in the Material Point Method (MPM) for the simulation of coseismic site response. The proposed boundary condition uses an intuitive particle-relocation algorithm that ensures that material points always remain within the mesh. The explicit generalized-α time scheme is implemented in MPM to enable the damping of spurious high frequency oscillations. Firstly, the MPM is verified against Finite Element Method (FEM). Secondly, ability of the MPM in capturing the analytical transfer function is investigated. Thirdly, a symmetric embankment is adopted to investigate the effects of ground motion arias intensity, I_A, geometry dimensions, and constitutive models. The larger the model size, the higher the crest runout and settlement for the same ground motion. When using a Mohr-Coulomb model, the crest runout increases with I_A. However, if the strain-softening law is activated, the results are less influenced by the ground motion. Finally, the MPM results are compared with the Newmark sliding block solution. The simplified analysis herein highlights the capabilities of MPM to capture the full deformation process for earthquake engineering applications, and the importance of geometry characterization and the selection of appropriate constitutive models when simulating coseismic site response and subsequent large deformations.

3.2 Introduction

During earthquakes, soils are subject to irregular and multi-directional cyclic vibrations, and depending on the site characteristics, seismic waves can be either amplified or attenuated at specific frequencies. The reliable evaluation of wave propagation is important to under-

stand manifestations in soils and infrastructure. During low intensity earthquake shaking, soil behavior can be approximated to be linear and material damping is approximated to be negligible. One-dimensional wave propagation closed-form transfer functions are available for these small-strain wave propagation problems [23]. However, under more intense shaking, soil behavior can be extremely nonlinear. As such, the equivalent-linear approach was developed as a simple way to handle nonlinear soil behavior. The stiffness modulus and damping ratio are varied in an iterative manner to obtain an 'effective' strain induced in a soil layer using the linear elastic closed-from solutions (e.g., [85, 86]). Although this approach is computationally efficient compared to other numerical techniques, the secant stiffness modulus and damping ratio are implicitly assumed to remain constant for the entire duration of the shaking. This particularly represents an important limitation of the method because it fails to reflect accurate soil behavior. Additionally, the equivalent-linear approach is incapable of considering case scenarios that involve soil-water-structure interaction, staged construction, and complex geometries.

The rigid sliding block solution was proposed by Newmark [34] to assess slope performance and to obtain the runout incurred due to seismic loading. Newmark [34] assumes that soil behaves in a rigid-perfectly plastic manner across a well-defined slip surface, with no dynamic site response or strength loss due to shaking. The sliding mass exhibits permanent displacements when the relative velocity between the sliding mass and the underlying base is greater than zero. This model provides a simple method that requires only two input parameters, namely (a) yield coefficient, k_y, as proxy for the threshold of dynamic resistance in units of $g = 9.81 m/s^2$, and (b) the acceleration-time history of the ground foundation. Practitioners often employ the pseudo-static limit equilibrium analysis to quantify the value of k_y. For these reasons, the scope of the Newmark [34] method is restricted to simple constitutive behaviors and geometries. Various researchers employed Newmark's approach to propose

simplified regression equations which facilitate the calculation of permanent displacement, although retain all of Newmark's crude assumptions (e.g., [36, 37, 38, 39]). To overcome some of the limitations, the 'decoupled' approach was developed to overcome the rigid sliding mass assumption and to take into account the effect of dynamic response due to shear wave (S-wave) propagation upon permanent slip of the sliding mass (e.g., [40, 41, 42, 43, 44, 45, 46]). The most important limitation of the decoupled procedure is that the computation of the seismic response of the potential sliding mass is decoupled from the subsequent slip. Second, the 'coupled' approach was developed to consider the role of internal shear deformation of the sliding mass upon the permanent displacement accumulation (e.g., [44, 46, 47]). The coupled approach solves the equation of motion using simplified viscoelastic-perfectly-plastic elements which simulate the one-dimensional deformation of the flexible sliding mass during the landslide. Besides the dynamic site response, the coupled approach inherits the other limitations of the Newmark and decoupled approaches (i.e., simple geometries and soil behavior). In contrast to Newmark's original approach, the decoupled and coupled simplified regressions provide only the final magnitude of permanent displacement with no indication of the time of sliding initiation or final mass stabilization.

Alternatively, numerical methods are often employed in geotechnical engineering to simulate coseismic site response using nonlinear constitutive models and complex geometries. Advancements in numerical mesh-based techniques incorporate nonlinear soil behavior that can successfully model small-strain boundary value problems associated with site response. However, these mesh-based techniques have limited capabilities in simulating large strains associated with post-failure deformations induced by strong-motion shaking [57]. This is because of excessive mesh entanglement and distortion. Examples of such large strain applications include coseismic landslides, tunnel collapses, and liquefaction. To address large deformation in multi-phase problems, in the last decade, the geotechnical engineering community

has widely adopted the material point method (MPM) (e.g., [56, 76, 98, 121, 139, 140, 141]). However, the MPM has been rarely used for the study of earthquake-triggered failures. This primarily because of challenges associated with the stability of the MPM when involving dynamic time-dependent boundary conditions and advanced constitutive models. Most of the current state-of-the-art modeling of coseismic large deformations rely on simulating small-scale shaking table experiments where fully reflective boundaries are generally accepted (e.g., [78, 80]). When using fully-reflective boundary conditions, there are inherit numerical limitations which prevent the study of coseismic site response. This is because of the artificial wave reflections across the boundaries of the numerical domain. One-dimensional wave propagation solution using periodic boundary conditions plays an important role in simulating in-situ free-field conditions in numerical simulations [83]. This setup is schematically depicted in Figure 3.1, whereby a free-field soil layer overlies bedrock. Periodic boundary conditions simulate a representative unit of the free-field soil layer. Recently, Feng et al. [81] extended the use of MPM with free-field boundary conditions to simulate the Lower San Fernando Dam case study albeit there was no verification conducted to assess the implemented periodic conditions that serve to calculate the one-dimensional free-field wave propagation solution. It should be noted that results from numerical models that use free-field boundary conditions are highly dependent on the accuracy of the used one-dimensional wave propagation solution using periodic boundary conditions [142]. As such, rigorous element-level verification of periodic boundary conditions in MPM are required to ensure that performance of the free-field columns is consistent with analytical and other numerical techniques.

The MPM is well suited to simulate large deformations, but it is more computationally expensive than mesh-based approaches such as Finite Element Method (FEM). This is due to the back-and-forth information mapping between the nodes from the computational mesh and the material points (i.e., integration points). Also, the use of the MPM is traditionally

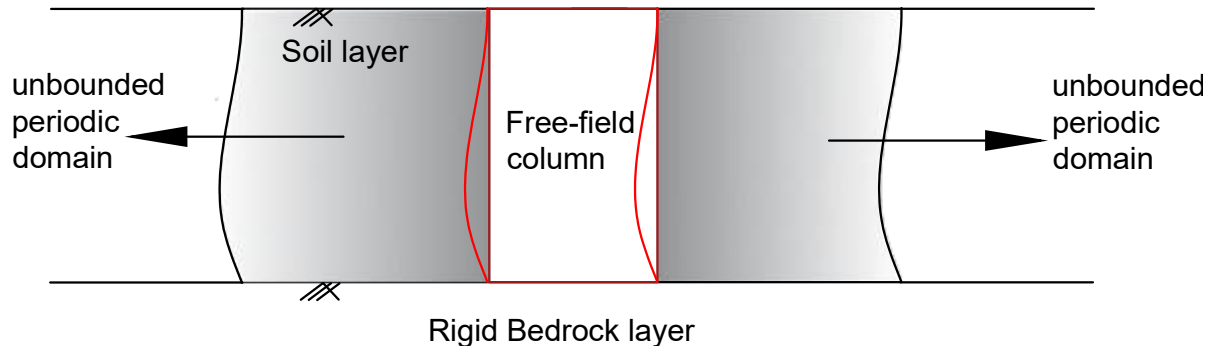

Figure 3.1: Schematic of in-situ conditions to be simulated using periodic boundary conditions in a numerical model.

accompanied with the explicit Forward Euler-Cromer (MPM-EC) time integration scheme which may result in spurious high-frequency numerical oscillation when simulating earthquake engineering problems such as coseismic landslides [72, 74]. Recent advancements in time integration schemes offer user-controlled high frequency numerical noise elimination to stabilize these oscillations [69, 72, 143]. Notably, the explicit generalized-α time integration scheme was developed by Hulbert and Chung [143] and was recently adapted for MPM by Tran and Solowski [74]. This time scheme is second order accurate, self-starting and enables user-controlled damping. The generalized-α scheme is a more general implementation of the commonly employed Newmark-β scheme in earthquake dynamics (e.g., [144]). Based on the authors' knowledge, the use of periodic boundary conditions and generalized-α time scheme in MPM has never been verified for site response against element-level FEM soil column and the linear analytical site response solution. This is a crucial step to simulate free-field earthquake engineering problems accurately.

The objective of this paper is to propose a verified MPM framework capable of accurately simulating the full deformation process of earthquake-triggered failures. To achieve this

goal, periodic boundary conditions together with the explicit generalized-α time integration scheme are implemented. Contrary to the implementation of Feng et al. [81], the periodic boundary conditions proposed herein are attached to a moving mesh and are equipped with a particle relocation algorithm to improve the accuracy of the solution. The paper is organized as follows. Firstly, the implementation of the periodic boundary conditions is presented. The MPM computational cycle in the explicit generalized-α time scheme (MPM-GA) is also presented. Secondly, the numerical model of a linear-elastic column is used to verify the MPM-GA implementation with periodic boundary conditions against the FEM using Plaxis software [145]. The MPM results are also compared with an analytical linear site response solution in the frequency domain. Thirdly, the periodic boundary conditions are leveraged to conduct a parametric analysis to investigate the effect of the ground motion intensity, model dimensions, and material brittleness on the coseismic slope instability of a symmetric slope embankment. Finally, the numerical results are compared against Newmark rigid sliding-block solution [34]. Conclusions are drawn at the end of this paper.

3.3 Advancements in MPM for earthquake-triggered site response

The MPM is a particle-based numerical tool whereby a continuum is discretized into a set of Lagrangian points, each so-called a material point (MP) [58]. The MPs move within an Eulerian computational mesh and represent the deformation of the continuum. Figure 3.2 summarizes the MPM computational cycle, which is usually integrated explicitly in time and involves (a) interpolating state variables from MPs to nodes, (b) solving the governing dynamic momentum balance equations at the nodes, (c) remapping the nodal solution back to the MPs, and (d) updating final MP positions and state variables. The computational

mesh does not usually store any information and can be moved or regenerated after each time step. In the MPM framework, the boundary conditions can be applied on the nodes or on the MPs. Some of the numerical limitations of the original MPM framework include the generation of spurious noise when integrating upon the mobile MPs that cross from one element to another (i.e., cell-crossing noise) [60, 146]. This is because of the discontinuity in the shape function derivatives when using lower-order elements. Several MPM variations have been proposed to alleviate the cell-crossing noise errors (e.g., [60, 68, 147]), including the use of mixed MPM-Gauss-Point integration, which allows the computation of an averaged incremental stress using optimally positioned Gauss points [148]. Another limitation of the use of advanced absorbing boundary conditions in MPM when the deformations are large can be the sporadic incidents of MPs leaving the background computational mesh which often terminates the numerical simulations. Recent developments for earthquake-induced shaking include the advancement of boundary conditions to prescribe seismic action in terms of acceleration, velocity, displacement (e.g., [57, 78, 79, 80]) or traction (e.g., [81]). In particular, for this research, an in-house version of the Anura3D open-source software is used ([149]). Details of the MPM one-phase formulation and implementation in Anura3D can be found in Fern et al. [59]. Recent advancements in the simulation of seismic shaking implemented within the Anura3D framework are described by the authors in Alsardi et al. [57]. They propose to prescribe the ground motion as a time-dependent Dirichlet boundary condition which is applied at the nodes of a moving background computational mesh (i.e., the mesh rigidly moves following the input ground motion). This approach, also used in this paper, is seen to minimize cell-crossing to only the MPs that exhibit relative movement with respect to the seismic motion.

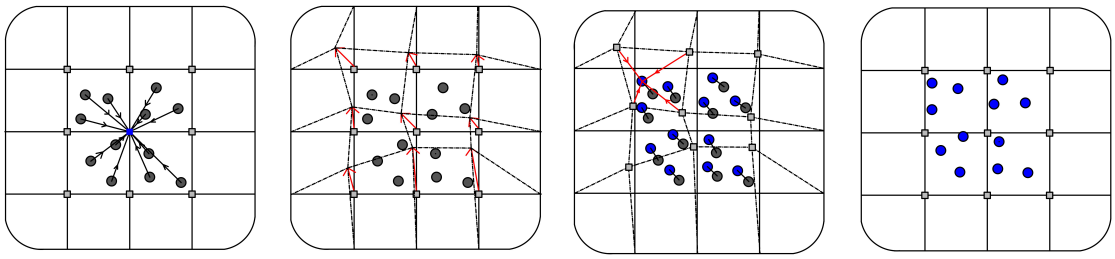

(a) Material point to node (b) Nodal solution (c) Node to material point (d) Update material points and reinitialize mesh

Figure 3.2: MPM computational cycle: (a) Map information from MPs to background mesh. (b) Solve dynamic momentum balance equation to obtain nodal accelerations. (c) Update velocity and momentum balance at the MPs from nodal acceleration. (d) Update state variables at MPs using constitutive equations and mass balance equations. Discard nodal values.

3.3.1 Periodic boundary conditions in MPM

One-dimensional site response analysis due to shear wave propagation in a soil column is commonly adopted to understand free-field soil amplification response. This analysis is often considered as an element-level verification approach for numerical and constitutive models [113, 150, 151]. In this paper, periodic boundary conditions are implemented in the MPM framework to simulate one-dimensional site response in a two-dimensional problem. The main objective of the periodic boundary condition is to ensure that identical displacements (i.e., solution in Figure 3.2b) for the nodes at the same spatial level from both lateral sides of the model. This constrains the model to simulate a free-field domain through the effect of periodicity. Similar to mesh-based methods, periodic boundary conditions can be implemented in the MPM framework by overwriting the degrees of freedom of the corresponding nodes to obtain the same nodal solution. The implementation enables the sharing of information between the tied nodes. Effectively, the mass and the forces of these tied nodes are summed so that they are identical. A single acceleration, velocity, and ultimately

displacement value is obtained for each set of nodes. The nodal solution is mapped to the MPs within the computation cycle (Figure 3.2c).

Under large deformations due to strong-motion shaking in level ground conditions, the MPs may leave the computational domain which terminates the simulation. An initial intuitive approach used by others (e.g., [81]) is to increase the element size to provide more space for the MPs to move. However, spatial discretization refinement can impose an element size restriction based on the maximum frequency content of the ground motion [152]. Also, the use of coarse mesh compromises the accuracy of the solution. In the implementation herein, a novel and intuitive particle relocation technique is incorporated to ensure that the MPs remain within the computational domain. This technique is schematically illustrated in Figure 3.3. When the MP moves out of the computational domain due to deformation, such as shown in Figure 3.3b, the MP is relocated to its corresponding periodic position by subtracting the repeating unit width.

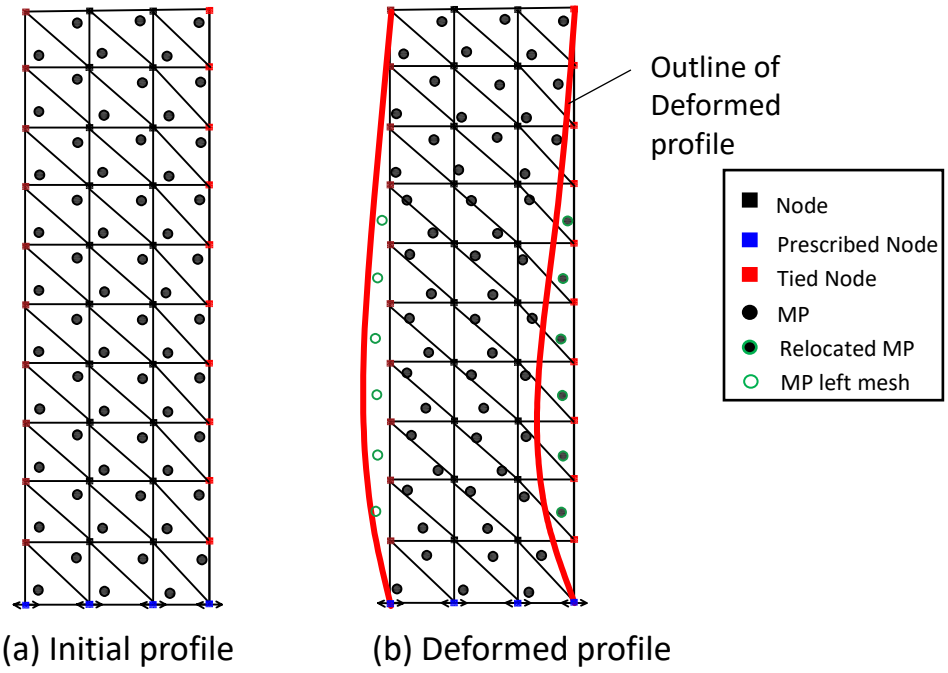

Figure 3.3: Schematic of the particle relocation technique employed with the periodic boundary conditions.

3.3.2 Explicit generalized-α time integration scheme

Given the suitable selection of time scheme parameters, the generalized-α time scheme [69] is capable of achieving an optimal combination of maximum dissipation of high frequency numerical noise but minimum low frequency dissipation. The fundamental idea of this time scheme is the evaluation of the various terms of the equation of motion at different points within the time step. Hulbert and Chung [143] proposed this conditionally-stable explicit version of the generalized-α time scheme by setting the numerical parameter corresponding to the internal forces computation, α_f, to zero. The explicit scheme is recommended to be used for problems where the time step, Δt, needed for sampling accuracy is of the same order of the critical time step, Δt_c (e.g., wave propagation problems in compressible and

drained media). Tran and Solowski [74] adopted the explicit algorithm for use in MPM, and their work forms the basis for the MPM-GA implementation presented herein. In this explicit time scheme, the user can control the damping by varying the values of the time step, Δt, and minimum spectral ratio, ρ_b. Kontoe et al. [72] recommends the use of the $\rho_b = \frac{9}{11}$ with a time step of $\Delta t = 0.01$ sec which achieves 18.2% of damping and prevents excessive dissipation of physical high frequencies. However, this recommendation is oriented towards the implicit generalized-α scheme and it is not strictly applicable to the explicit version herein.

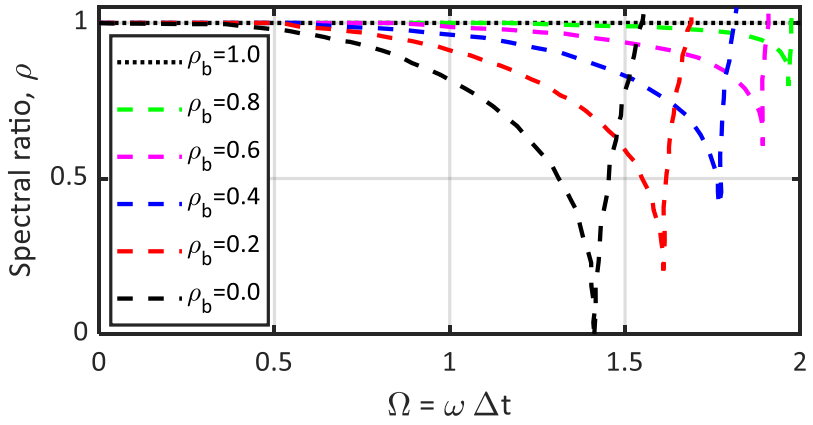

Figure 3.4: Spectral ratio variation with non dimensional frequency, Ω $(= \omega \Delta t = 2\pi f \Delta t)$ [143]. The plot is shown for different bifurication spectral ratios.

Figure 3.4 shows the variation of the spectral ratio, ρ, versus the value Ω, which equals the product of the generated angular frequency, ω, and the chosen time step, Δt. When ρ is equal to 1, it corresponds to no damping. By contrast, when ρ is zero, complete damping of the corresponding frequency is achieved. Maximum damping associated with the minimum spectral ratio, ρ_b, occurs at the bifurication limit, Ω_b. The value of ρ increases after reaching Ω_b experiencing a reduction in the damping beyond the bifurication limit. The stability limit, Ω_s, is the limit at which ρ equals 1 beyond the Ω_b limit. The existence of frequencies beyond the Ω_s limit results in amplification of those frequencies which ultimately might

lead to an unstable numerical model. The stability of the model using MPM-GA scheme is conditional on the selection of Δt and ρ_b such that the frequencies beyond Ω_b limit are kept to minimum. Since this is an explicit scheme, the time step increment, Δt, must also satisfy the critical time step, Δt_c using the Courant-Friedrichs-Levy (CFL) condition [61, 120, 153] ($\Delta t \leq \Delta t_c$). Note that the Ω_b and Ω_s are both a function of the ρ_b and do not depend on the chosen time step as presented in their closed form in Equations 3.1 and 3.2, respectively. All other numerical parameters, α_m, β, and γ, in the time scheme can be calculated as a function of ρ_b using Equations 3.3, 3.4, and 3.5, respectively. The reader is referred to Chung [154] for details regarding the derivation of Equations 3.1-3.5.

$$\Omega_b = (1 + \rho_b)\sqrt{2 - \rho_b} \tag{3.1}$$

$$\Omega_s = \sqrt{\frac{12(1 + \rho_b)^3(2 - \rho_b)}{10 + 15\rho_b - \rho_b^2 + \rho_b^3 - \rho_b^4}} \tag{3.2}$$

$$\alpha_m = \frac{2\rho_b - 1}{1 + \rho_b} \tag{3.3}$$

$$\beta = \frac{5 - 3\rho_b}{(1 + \rho_b)^2(2 - \rho_b))} \tag{3.4}$$

$$\gamma = \frac{3}{2} - \alpha_m \tag{3.5}$$

Overall, the advantage of this explicit MPM-GA formulation is that it does not require expensive iteration to keep a desired high frequency damping. The drawback is that it requires calibration to ensure the stability of the solution for the level of damping required. The MPM-GA algorithm is primarily based on storing the accelerations at the nodes to obtain an initial acceleration, $\vec{a}_i^t$, at time, t. The initial acceleration, $\vec{a}_i^t$, is assumed to be zero in the first time step. The dynamic momentum balance is then solved at the nodes to compute an intermediate acceleration, $\vec{a}_i^{\Delta t(1-\alpha_m)}$, at $t = \Delta t(1 - \alpha_m)$. This algorithm

linearly interpolates the initial and intermediate solution to obtain the final acceleration, $\vec{a}_i^{t+\Delta t}$, at $t = t + \Delta t$. In the implementation herein and contrary to Tran and Solowski [74], the acceleration-to-velocity integration is done at the MP-level similar to the fluid implicit particle (FLIP) scheme [155]. This approach is recommended by Brackbill et al. [155] because it reduces numerical diffusion when the nodal solution is remapped to the MPs. The computational cycle of the MPM-GA is presented as follows (noting that the subscripts denote node or MP index, and superscripts denote the time of the evaluated term).

- Compute nodal mass by mapping MP mass, m_{MP}, using basis functions, $\vec{N}_i$, and looping across the number of active elements associated with the node, n_{el}, and the number of MPs located within these elements, n_{MP} (Equation 3.6).

$$M_i^t = \Sigma_{n_{el}} \Sigma_{n_{MP}} \vec{N}_i m_{MP} \tag{3.6}$$

- Compute the the rate of change of momentum, $\vec{f}_i^t$ (Equation 3.7).

$$\vec{f}_i^t = \vec{f}_i^{ext,t} - \vec{f}_i^{int,t} \tag{3.7}$$

- Compute intermediate nodal acceleration, $\vec{a}_i^{t+\Delta t(1-\alpha_m)}$, at the nodes by dividing the rate of change of momentum by the mass (Equation 3.8).

$$\vec{a}_i^{t+\Delta t(1-\alpha_m)} = \frac{\vec{f}_i^t}{M_i^t} \tag{3.8}$$

- Compute final nodal accelerations, $\vec{a}_i^{t+\Delta t}$, through linear interpolation (Equation 3.9).

$$\vec{a}_i^{t+\Delta t} = \frac{(\vec{a}_i^{t+\Delta t(1-\alpha_m)} - \alpha_m \vec{a}_i^t)}{(1-\alpha_m)} \tag{3.9}$$

- Compute MP velocity, $\vec{v}_{MP}^{t+\Delta t}$, at time $t+\Delta t$ using basis functions, N_i, of active element nodes, $n_{n,el}$ (Equation 3.10).

$$\vec{v}_{MP}^{t+\Delta t} = \vec{v}_{MP}^{t} + \Sigma_{i=1}^{n,el}\vec{N}_i[(1-\gamma)\vec{a}_i^t + \gamma\vec{a}_i^{t+\Delta t}]\Delta t \tag{3.10}$$

- Compute nodal velocity, $\vec{v}_i^{t+\Delta t}$, by dividing nodal momentum by nodal mass (Equation 3.11).

$$\vec{v}_i^{t+\Delta t} = \frac{\Sigma_{n_{el}}\Sigma_{n_{MP}} m_{MP}\vec{v}_{MP}^{t+\Delta t}}{M_i^t} \tag{3.11}$$

- Compute incremental nodal displacements, $\Delta\vec{u}_i^{t+\Delta t}$, (Equation 3.12) and subsequently multiply by the basis function gradients, $\vec{B}$, to obtain MP incremental strain, $\Delta\vec{\varepsilon}_{MP}$ (Equation 3.13).

$$\Delta\vec{u}_i^{t+\Delta t} = \vec{v}_i^{t+\Delta t}\Delta t \tag{3.12}$$

$$\Delta\vec{\varepsilon}_{MP} = \vec{B}\Delta\vec{u}_i^{t+\Delta t} \tag{3.13}$$

- Compute final MP displacement, $\vec{u}_{MP}^{t+\Delta t}$, (Equation 3.14).

$$\vec{u}_{MP}^{t+\Delta t} = \vec{u}_{MP}^{t} + \vec{v}_{MP}^{t+\Delta t}\Delta t + \Sigma_{i=1}^{n,el}\vec{N}_i[(1/2-\beta)\vec{a}_i^t + \beta\vec{a}_i^{t+\Delta t}](\Delta t)^2 \tag{3.14}$$

- Store the nodal accelerations, $\vec{a}_i^{t+\Delta t}$, for use in the subsequent time step.

In this paper, we adopt a Courant number of 0.95 for all simulations, which means that $\Delta t = 0.95\Delta t_c$ according to the CFL condition. The value of ρ_b can be varied for each simulation with the goal of damping out high frequencies (above 35 Hz consistent with

Kontoe et al. [72]) while ensuring that the bifurication limit Ω_b is not reached. In cases where that this is not possible due to the CFL critical time step restriction, a reduced value of ρ_b is adopted (note that the value of $\rho_b = 0.0$ is always avoided to prevent a very low value for the bifurcation and stability limits). The frequency where dissipation starts to occur is calculated using Equation 3.15. In each example herein, the value of the used ρ_b and Δt is documented with the corresponding damped out frequency range.

$$f = \frac{\Omega}{\Delta t \cdot 2\pi} \tag{3.15}$$

3.4 Ground motions considered in this paper

Three ground motions from the PEER database [156] are adopted in this paper as plotted in Figure 3.5. These recordings are selected because of their rich frequency content (primarily up to 30 sec^{-1} as shown in Figure 3.6) which is expected to engage a range of modes in the soil column to enable the numerical back calculation of the transfer function [72]. Reference will be made to these ground motions (I, II, III) throughout the following sections. Note that the goal is to compare against an analytical solution and not to reproduce a particular site response case study. As such, specific ground motion characteristics, and their site class and place of occurrence are not relevant herein but are documented in Table 3.1 for the reader to facilitate their retrieval from the PEER database if desired. Arias intensity, I_A, is computed for each ground motion as defined in Equation 3.16. In addition to the PEER recordings, a Gabor wavelet [157] acceleration load, a_w, defined by Equation 3.17 is also considered in one the examples presented herein. The wavelet shape parameters (β_w, α_w, t_w, γ_w) used in the analysis are documented in Table 3.2. The trapezoidal rule is used to integrate the acceleration of all time histories and obtain the velocity time histories to be applied in the

simulation. Additionally, a linear baseline correction check is applied to ensure there is no displacement drift in the ground motion.

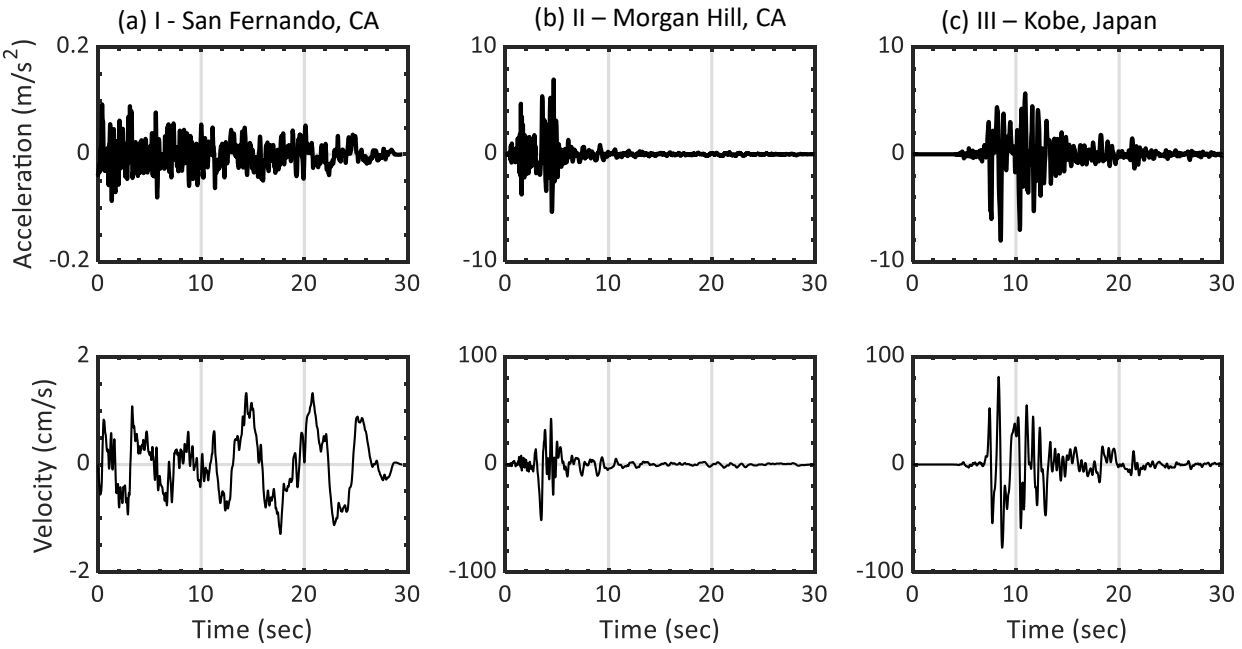

Figure 3.5: Plot of ground motion acceleration and velocity time histories used as input in the analysis.

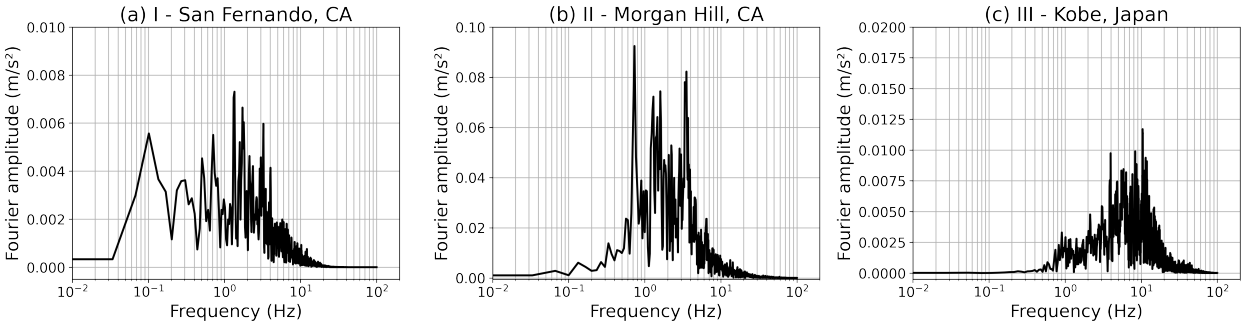

Figure 3.6: Plot of acceleration Fourier amplitude versus frequency for the ground motions used in the analysis.

$$I_A = \frac{\pi}{2g} \int_0^d {a_t}^2 dt \tag{3.16}$$

$$a_w = \sqrt{\beta_w \cdot exp(-\alpha_w t) \cdot t^{\gamma_w}} \cdot sin(2\pi t f_0) \tag{3.17}$$

Table 3.1: Summary of ground motions details used in the analysis.

Number	Region	Station	Component	Date	Moment magnitude	Arias intensity (m/s)	PGA (g)	PGV (cm/s)	D_{5-95} (sec)
I	San Fernando, California	Maricopa Array #2	H1	2 Feb 1971	6.61	5.51 x 10^{-2}	9.51 x 10^{-3}	1.33	26.5
II	Morgan Hill, California	Coyote Lake Dam Southwest Abutment	H1	24 Apr 1984	6.19	3.95	0.711	51.6	7.02
III	Kobe, Japan	KJMA	H1	17 Jan 1995	6.90	8.39	0.821	81.3	9.36

3.5 Coseismic response of horizontal ground with MPM

The goal of this section is to verify the performance of the proposed MPM formulation in horizontal ground profiles.

3.5.1 Numerical model.

A plane-strain 10 m soil column (labeled herein 'SC') is considered to simulate site response of an infinitely horizontal and homogeneous ground surface due to one-dimensional wave propagation using MPM (Figure 3.7a). This model is also generated in FEM with Plaxis (Figure 3.7b). The MPM model employs linear triangular elements, and the FEM model employs quadratic triangular elements. The effect of the basis function order is not significant in this problem since a linear-elastic constitutive model is used. Parameters of all the soil column models are documented in Table 3.2). A fine element size of 0.25 m is used equal to one-tenth times the minimum wavelength of the shear wave generated by the ground motions (Table 3.1) in the considered materials (Table 3.2) . This spatial discretization approach is

consistent with Kuhlemeyer et al. [158], and is commonly adopted in mesh-based numerical techniques (e.g., [71, 159]).

Natural frequency modes of the soil column are calculated using Equation 3.18, as a function of the column height, H=10 m, unit weight, γ=18.5 kN/m^3, and the linear-elastic material parameters. The value of n corresponds to the natural frequency mode. As such, setting n = 0, 1, and 2 corresponds to calculating the fundamental, first and, second natural frequency mode, respectively.

$$f_n = \frac{\sqrt{\frac{E}{2\frac{\gamma}{g}(1+\nu)}}}{4H}(2n+1) \tag{3.18}$$

The geo-static stresses in the soil column are generated using the $K0$-procedure assuming the at-rest lateral earth pressure, K_0, equal to 0.5. The ground motion is prescribed as a time-dependent Dirichlet condition [57] at the base of the model to generate vertically-polarized shear (SV) waves. Also, periodic boundary conditions are specified at the lateral sides. The background computational mesh is moved after every time step to follow the input ground motion according to Alsardi et al. [57]. Similar to MPM, the Dirichlet boundary condition is applied at the base of the FEM model and the periodic boundary conditions are specified at the lateral edges of the mesh. For all the FEM models, the implicit Newmark time scheme (FEM-N) is employed with parameters set as $\alpha_N = 0.3025$ and $\delta_N = 0.6$, consistent with the a dissipative version of the scheme commonly used in the literature (e.g., [50, 72]).

In total, four different soil column models are considered herein for verification purposes using different combinations of input motions and Young's modulus. Table 3.2 provides a summary the models' characteristics, including the elastic material properties, input ground motion, ground motion scaling factor, time step, calibrated MPM-GA parameters, and FEM-N parameters.

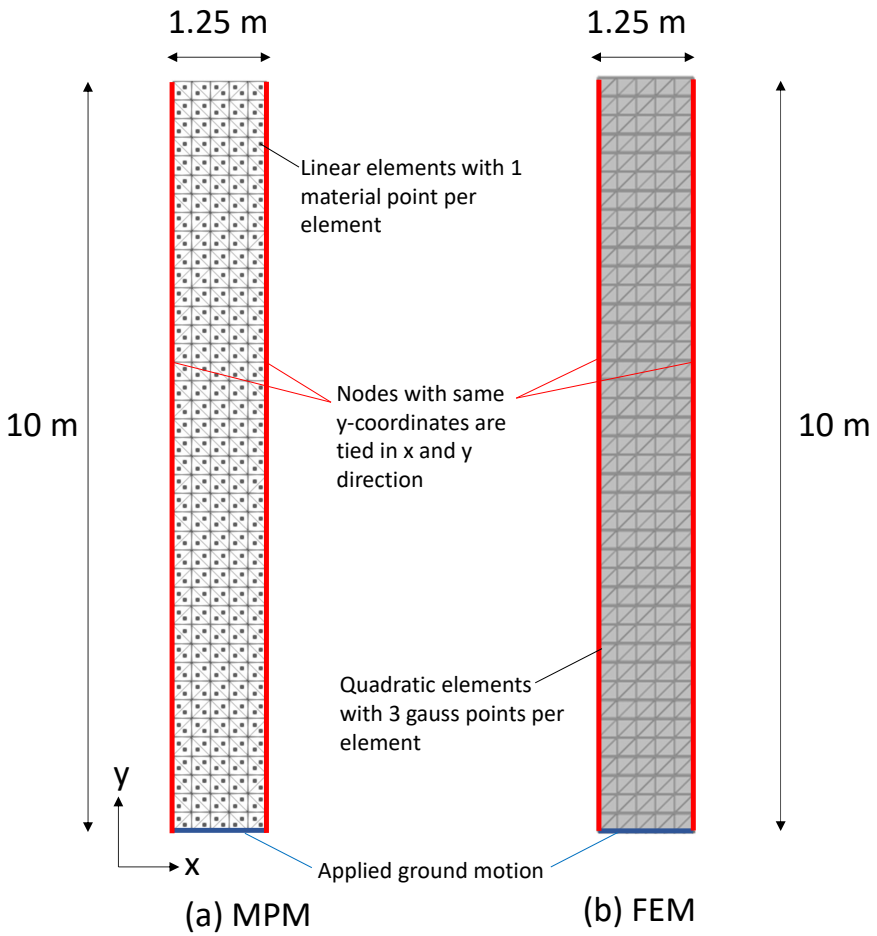

Figure 3.7: Numerical models used to simulate one-dimensional site response in 10 m soil column using (a) MPM. (b) FEM.

3.5.2 Verifying MPM against FEM and linear analytical solution

The goal here is to verify the implementation of the periodic boundary conditions and the MP relocation algorithm, and evaluate the effectiveness of the generalized-α (MPM-GA)

Table 3.2: Summary of cases simulated in MPM and FEM using soil column model.

Case	SC-1	SC-2	SC-3	SC-4
Young's Modulus, E (kPa)	10^4	1.85x10^5	10x10^5	1.85x10^5
Poisson ratio	0.33	0.33	0.33	0.33
Ground motion	Wavelet ($\beta_w = 1$ $\alpha_w = 1$ $\gamma_w = 1$ $f_0 = 1.116\ sec^{-1}$)	I	I	I
Ground motion scaling factor	1	1	1	128
Time step, Δt (sec)	2 x 10^{-3}	4 x 10^{-4}	2 x 10^{-4}	4 x 10^{-4}
MPM-GA parameters	$\rho_b = 0.4$	$\rho_b = 0.4$	$\rho_b = 0.2$	$\rho_b = 0.4$
FEM-N parameters	$\alpha_N = 0.3025$ $\beta_N = 0.6$	$\alpha_N = 0.3025$ $\beta_N = 0.6$	$\alpha_N = 0.3025$ $\beta_N = 0.6$	$\alpha_N = 0.3025$ $\beta_N = 0.6$

time integration scheme versus the forward Euler-Cromer (MPM-EC). Towards this end, MPM results are compared against FEM and the analytically derived natural frequency harmonics. Firstly, the time and frequency domain analysis is conducted in relatively small deformation cases where cell-crossing is avoided (cases SC-1, SC-2, and SC-3 in Table 3.2). Secondly, the ground motion I is scaled up (case SC-4 in Table 3.2) in order to induce large deformations and evaluate the effect of particle relocation and cell-crossing in the results.

MPM verification for small deformations (no cell-crossing)

This section presents the results obtained for cases SC-1, SC-2, and SC-3 (Table 3.2). Case SC-1 considers the Gabor wavelet load at the fundamental natural frequency of the soil column as input motion and $E = 10^4$ kPa; case SC-2 and SC-3 considers ground motion I using $E = 1.85\text{x}10^5$ kPa and $E = 10\text{x}10^5$ kPa, respectively. In all cases, the strain recorded is small and all MPs remain within their original elements. Hence, the MP relocation algorithm

is not employed.

In case SC-1, the combination of Δt and the calibrated value of ρ_b damps out frequencies higher than 35 sec^{-1}. Note that a low value of Young's modulus, E, is used in this case, which leads to a relatively large critical time step (Table 3.2). The results from case SC-1 at the top of the soil column are presented in Figure 3.8. It is seen that the horizontal acceleration, horizontal velocity, and horizontal displacement response of the MPM-EC, MPM-GA, and the FEM using the implicit Newmark (FEM-N) time scheme are at an acceptable match as shown in the time-domain in Figure 3.8a, 3.8c, and 3.8e, respectively. However, when plotting vertical displacement, it is observed that the MPM-EC results are contaminated with spurious oscillations (Figure 3.8b). These oscillations are significantly reduced when employing the MPM-GA time scheme and are more consistent with the results of the FEM-N time scheme results. Note that this noise is not generated by cell-crossing (i.e., all MPs remain in their original elements throughout the calculation). Instead, this noise might be inherited from numerical instabilities generated as a result of spurious high frequency oscillations in the nodal solution due to performing numerical integration and stress recovery at non-ideal MP locations; this is stabilized when using numerical damping from the generalized-α time scheme [72, 74].

Figure 3.9 compares the acceleration Fourier amplitude of the top and bottom MPs in the soil column for MPM-EC and MPM-GA for case SC-1. The bottom MP response is consistent with the applied wavelet ground motion. The acceleration Fourier amplitude of the bottom MP shows a single frequency component at the fundamental natural frequency of the soil column (1.116 sec^{-1}). The top MP response shows resonant behavior whereby the natural frequency component in the ground motion is amplified by an order of magnitude. In this manner, it is verified that the MPM-GA and MPM-EC schemes capture the fundamental natural frequency mode of the soil column. Although when using the MPM-EC scheme, the

top MP also experiences different spurious frequency modes different from those triggered by the input wavelet ground motion.

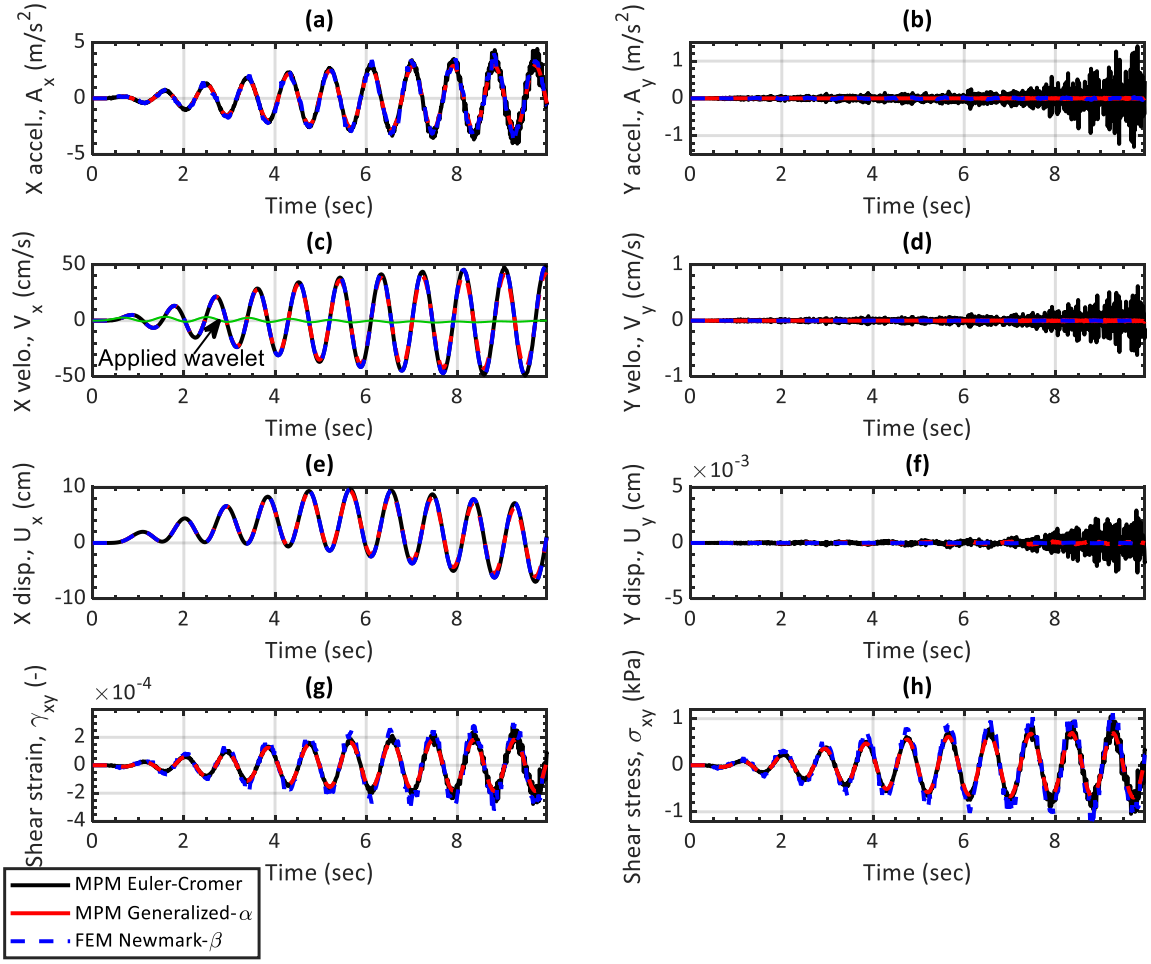

Figure 3.8: Comparison of MPM and FEM when applying wavelet at resonant frequency (Case SC-1 with MP location at (x, y) = (0.667m, 9.833m))

To investigate this further, case SC-2 (Table 3.2), uses the irregular ground motion I (Table 3.1). In case SC-2, considering the chosen Δt and ρ_b values, frequencies above 190 sec^{-1} are damped and the bifurcation frequency is 670 sec^{-1}. Similar to case SC-1, cell-crossing error is not generated in SC-2 (i.e., MPs do not move across different elements). This is because the

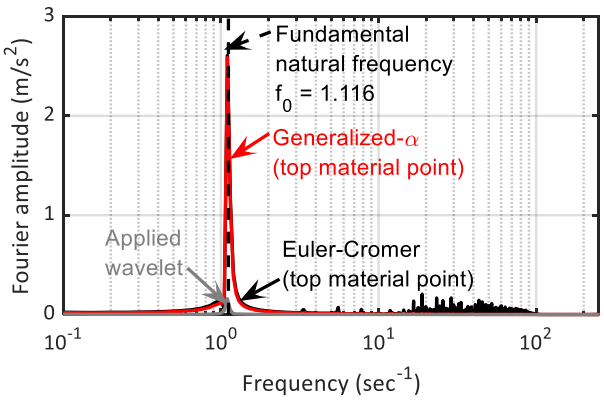

Figure 3.9: Fourier amplitude comparison of MPM and FEM when applying wavelet at resonant frequency (Case SC-1 with top MP location at (x, y) = (0.667m, 9.833m)).

low arias intensity from ground motion I results in small deformations. Reasonable match is seen between MPM-GA, MPM-EC, and FEM-N when considering horizontal acceleration, horizontal velocity, and horizontal displacement, as depicted in Figure 3.10a, 3.10c, and 3.10e, respectively. However, the results using the MPM-EC scheme show progressive deviation from the FEM-N, particularly when observing the shear strain and stress in Figure 3.10g and 3.10h, respectively. Also, the vertical spurious oscillations were exacerbated further when using MPM-EC as shown in Figure 3.8b, 3.8d, and 3.8f. It is observed that the MPM-GA time scheme reduces this spurious vertical noise when using an irregular cyclic input ground motion to be more consistent with the results of the FEM-N approach. To this end, the MPM-GA is seen to perform better than the MPM-EC in reducing the spurious numerical oscillations.

Using an irregular cyclic motion also offers the opportunity to plot a transfer function which enables the user to check for spurious frequency modes that may be inconsistent with the analytical solution. A transfer function, defined as the ratio of the Fourier amplitude of the 'output' to the 'input' ground motion, is commonly used to investigate time scheme performance in amplifying the natural frequency harmonics of a soil column [72, 150, 160]. As such, the task of numerically computing a transfer function and comparing it against the

analytical natural frequency is important for verifying the MPM framework. The 'input' motion is the one applied at the base of the model and the 'output' motion is the one obtained at the top of the soil column. This is often a required step to be conducted in linear-elasticity for verification before using more advanced constitutive models. In Figures 3.11a and 3.11b, the results of case SC-2 in the frequency domain using MPM-EC and MPM-GA are compared with the linear transfer function (TF) solution (Equation 3.19) assuming rigid bedrock and no material damping.

$$TF = \frac{1}{\left| cos\left(\frac{2\pi f}{\sqrt{\frac{E}{2\frac{\gamma}{g}(1+\nu)}}} \cdot H \right) \right|} \tag{3.19}$$

It is seen that the MPM-GA captures the fundamental, first and second frequency modes (consistent with the frequency content of the applied motion ranging from 0 - 30 sec^{-1}) with relatively low amplification for high frequency noise. The MPM-EC scheme generates results that approximately capture the first few modes but it is overall highly contaminated with low and high frequencies that are not consistent with the analytical solution. From these results, it can be seen that the MPM-EC can generate numerical results that resemble reasonable results in the time domain, but does not compare reasonably with the transfer function analytical solution in the frequency domain.

For the sake of comparison, the results from case SC-3 using MPM-GA and MPM-EC in the frequency domain are also plotted in Figures 3.11c and 3.11d. Note that the Young's modulus of case SC-3 is higher compared to SC-2, frequencies above 265 sec^{-1} are damped, and the bifurication frequency of 1430 sec^{-1} is not reached. Similarly, the MPM-GA results show that the input motion frequencies (<30 sec^{-1}) are amplified at their respective frequency modes, whereas the MPM-EC scheme shows the spurious generation of high frequency modes. Case SC-3 presents similar match with the FEM-N in the time domain to what was observed in

case SC-2. Hence, this is not presented in the paper.

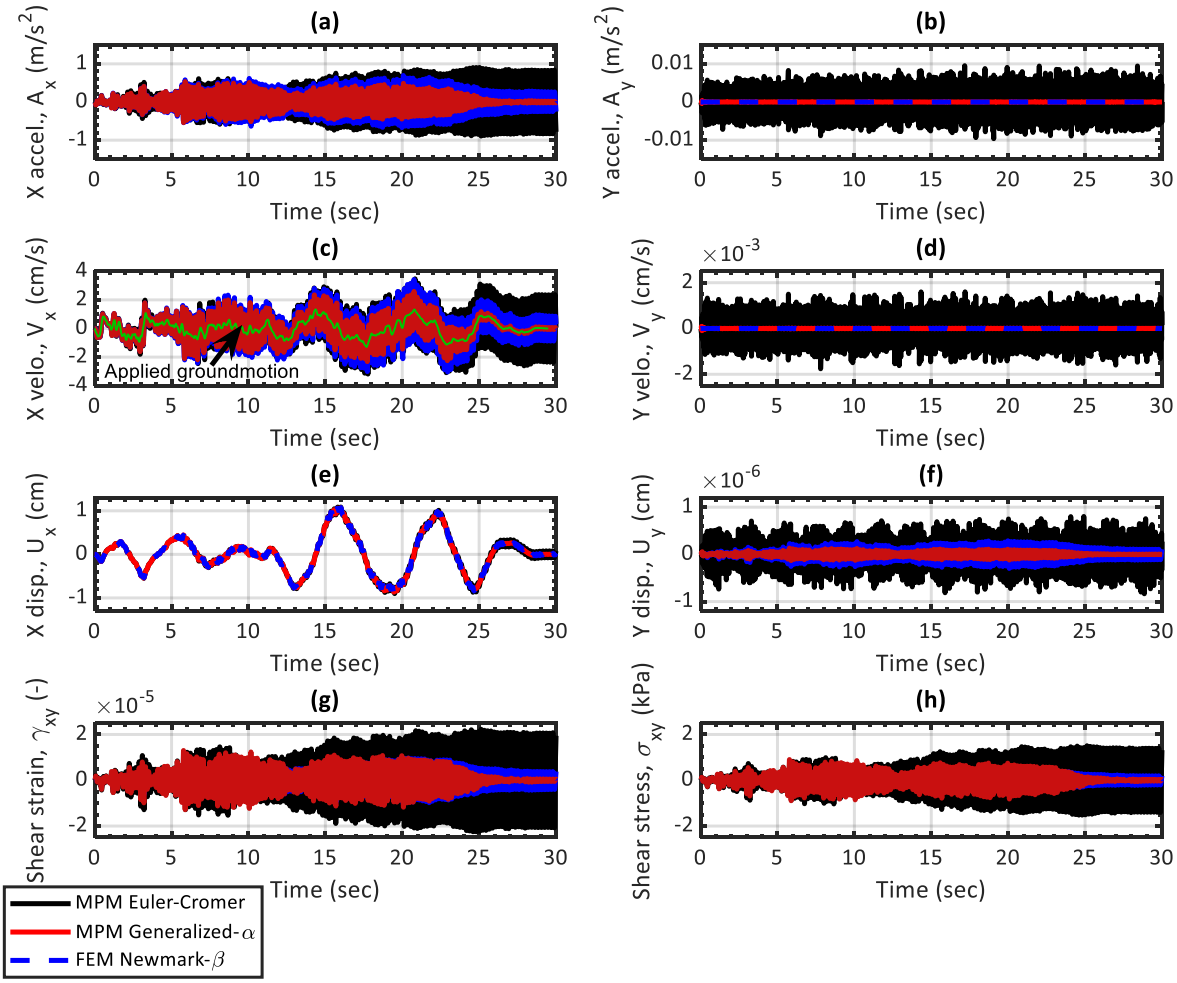

Figure 3.10: Comparison of MPM and FEM when applying irregular cyclic ground motion I (Case SC-2 with MP location at (x, y) = (0.667m, 9.833m)).

MPM verification for large deformations (with cell crossing)

This section presents the results of case SC-4 (Table 3.2), which is conducted using E = 1.85x10^5 kPa and ground motion I with a scaling factor equal to 128. This combination ensures large deformations of the model, which is essential to verify the implementation of the particle relocation technique and investigate the effect of particle cell-crossing on the

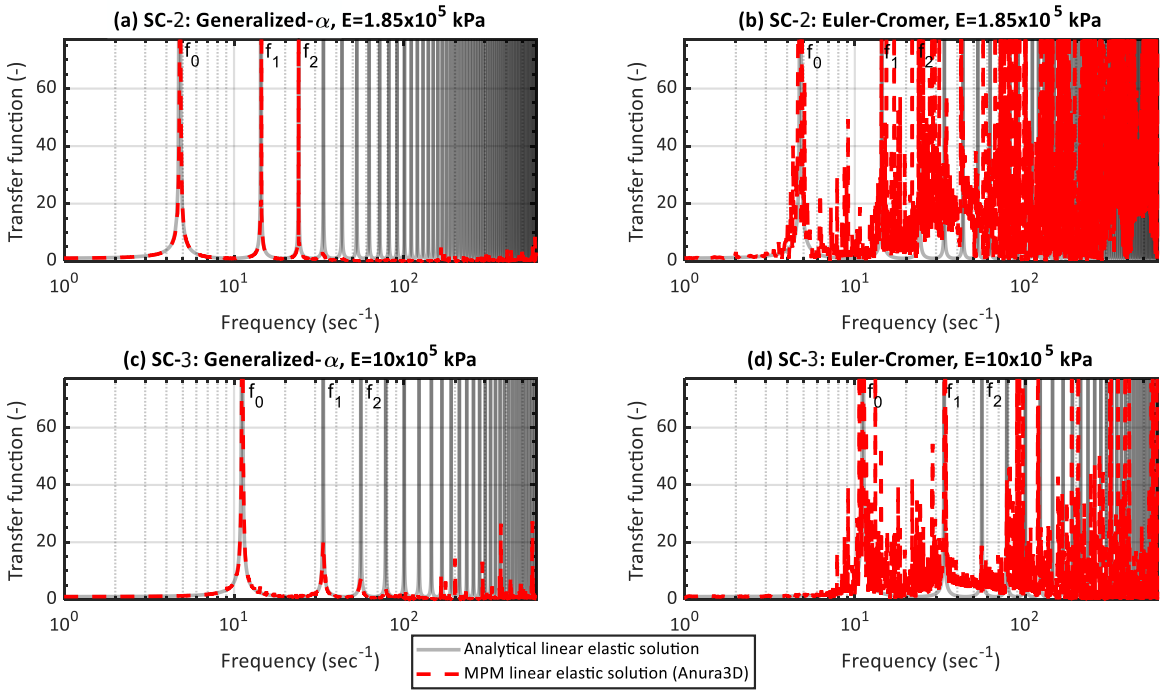

Figure 3.11: Transfer function obtained using MPM and comparing with the natural frequency harmonics of the soil column (Cases SC-2 and SC-3).

stability of the MPM time schemes. In addition, two MPM spatial integration schemes are compared, (a) the original material point integration that is performed at the mobile MPs (MP-integration) ([58]), and (b) the mixed MPM-Gauss-Point integration ([148]) that is often used to reduce cell-crossing noise. In this paper, the mixed MPM-Gauss-Point integration scheme is adopted to compute the nodal internal forces, the constitutive equation is evaluated at each individual MP to retain the history of the MP state variables.

Figure 3.12 shows the comparison between FEM-N, MPM-EC using MP integration, and MPM-EC using mixed MPM-Gauss-Point integration. The zones highlighted in gray correspond to the instants when cell-crossing occurs. Note that there is a significant deviation of the results using MPM-EC (whether MP or mixed MPM-Gauss-Point integration) from the FEM-N when cell-crossing occurs. This is particularly observed in the acceleration response in Figure 3.12a and 3.12b. The cumulative error results in spikes in the acceleration solution

of MPM-EC ultimately leading to a results that is almost one order of magnitude larger than FEM-N. Additionally, the MPM-EC shows a base drift in the vertical displacement solution which manifests as an unrealistic settlement of the linear-elastic free-field column. The mixed MPM-Gauss-Point integration scheme does not show significant improvements to the spurious oscillation or the base drift seen in this case. However, the horizontal displacement solution of MPM-EC remains acceptable when comparing it to FEM-N. This highlights the significant errors that may be generated when using MPM-EC scheme for site response analysis which might be overlooked by the user of the numerical method if attention is solely given to the horizontal displacement response of the free-field column.

Second, the same example is repeated using the MPM-GA time integration scheme and the results are plotted in Figure 3.13, using the same aforementioned values of Δt, ρ_b, and damping ranges of case SC-2. It is observed that the acceleration response in Figure 3.13a using MPM-GA (either MP or mixed MPM-Gauss-Point integration) compares reasonably well with FEM-N. This ultimately generates shear strain and shear stress profiles in MPM-GA that match the results of FEM-N, as shown in Figure 3.13g and 3.13h, respectively. Additionally, the vertical base drift is eliminated when using MPM-GA as shown in 3.13f. Although significantly reduced, it is seen that the some spurious oscillations still exist in MPM-GA particularly when observing the vertical accelerations in Figure 3.13b. Also, the mixed MPM-Gauss-Point integration is consistent with the MP-integration, and does not offer significant improvement.

Finally, case SC-4 is analyzed in the frequency domain by calculating the transfer function and comparing it to the analytical solution. It is seen that both MPM-GA and MPM-EC accurately capture the fundamental, first and second frequency modes as shown in Figure 3.14. However, the most important difference is that while the MPM-GA effectively damps the high frequencies noise partially due to cell crossing (only a few frequencies remain near

the bifurcation limit), the high frequency content in the MPM-EC results is very significant. Consistently with the time domain results, no noticeable improvement is seen when comparing MPM-EC using MP and mixed MPM-Gauss-Point spatial integration schemes. It is important to emphasize that for the previously presented cases SC-1, SC-2, and SC-3, both spatial integration schemes (MP and mixed MPM-Gauss-Point integration) give the same results; this is expected since no cell-crossing is observed.

The results presented in this section demonstrate the viability of the proposed MPM scheme to better deal with site response in small and large deformations. Consistently, all simulations presented hereafter are performed with the MPM-GA time integration scheme with the mixed MPM-Gauss-Point spatial integration.

3.6 Coseismic response of embankment slopes with MPM

Periodic boundary conditions have been often used in symmetric real-scale mesh-based numerical simulations. This is attributed to the simplicity in the boundary condition implementation and efficacy of the corresponding results when compared to more advanced site response treatments [142]. Example problems in the geotechnical literature that use periodic boundary conditions include foundation structures [72, 161], tunnels [162], retaining walls [163], and slopes [164]. The purpose of this section is to show the capabilities of the proposed MPM framework to simulate real-scale coseismic failures involving large deformations. In particular, a theoretical example of a symmetric embankment slope is used. A parametric analysis is presented to explore the effect of different size embankment geometries, and highlight the implications of using different constitutive models on the runout.

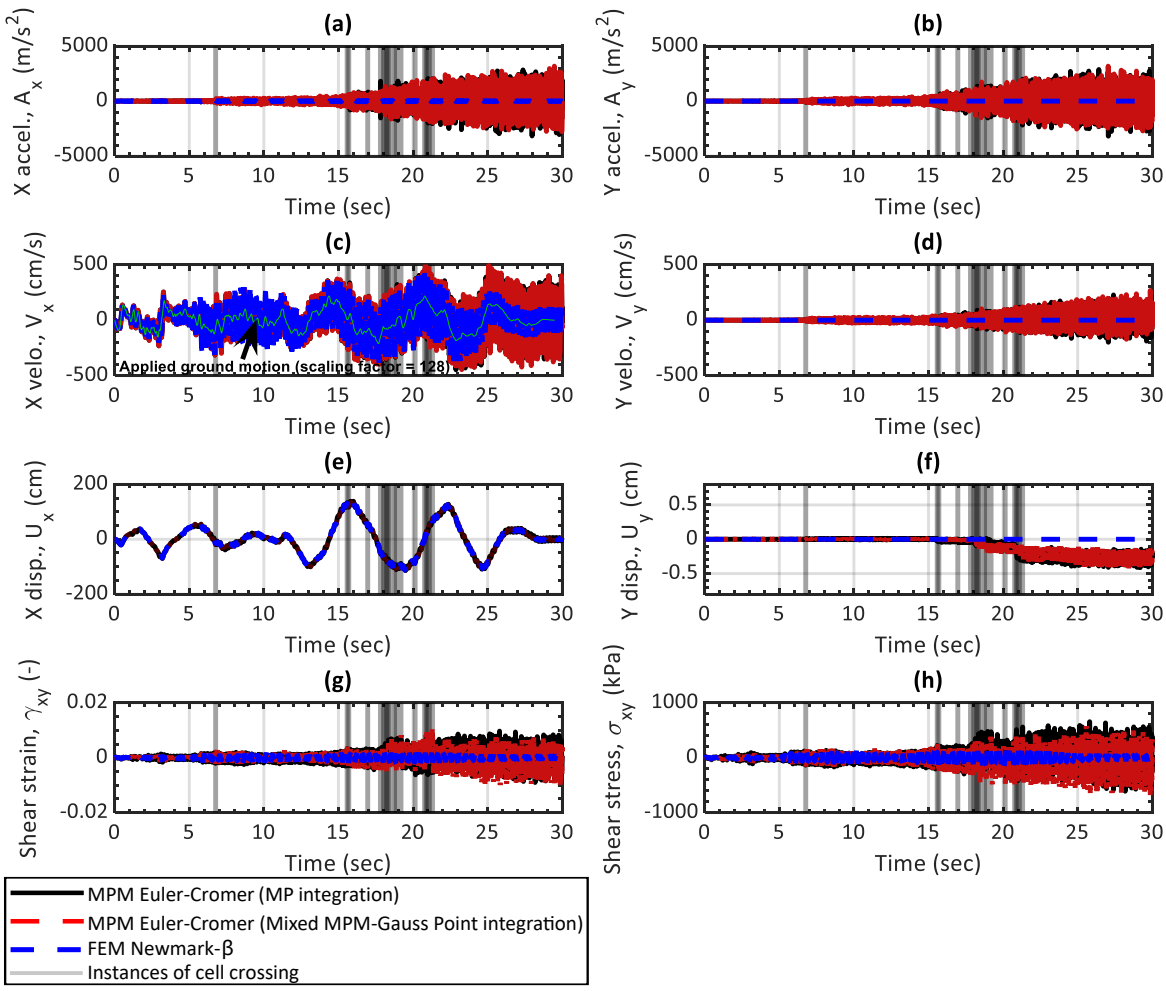

Figure 3.12: MP versus mixed MPM-Gauss-Point integration scheme on time domain results using Euler-Cromer scheme (Case SC-4 with MP location at (x, y) = (0.667m, 9.833m)).

3.6.1 MPM Numerical model.

A plane-strain 35^o embankment geometry overlying a 10 m soil foundation is considered for reference at small-size (Model 'S', 5 m high embankment) and large-size (Model 'L', 10 m high embankment). The initial spatial discretization and dimensions of both S and L models are presented in Figure 3.15a and 3.15b, respectively. The soil foundation at the base of the embankment is assumed linear-elastic with material parameters provided in Table 3.3. The MPM-GA time scheme parameters are consistent with case SC-3 in Table 3.2 since it has the

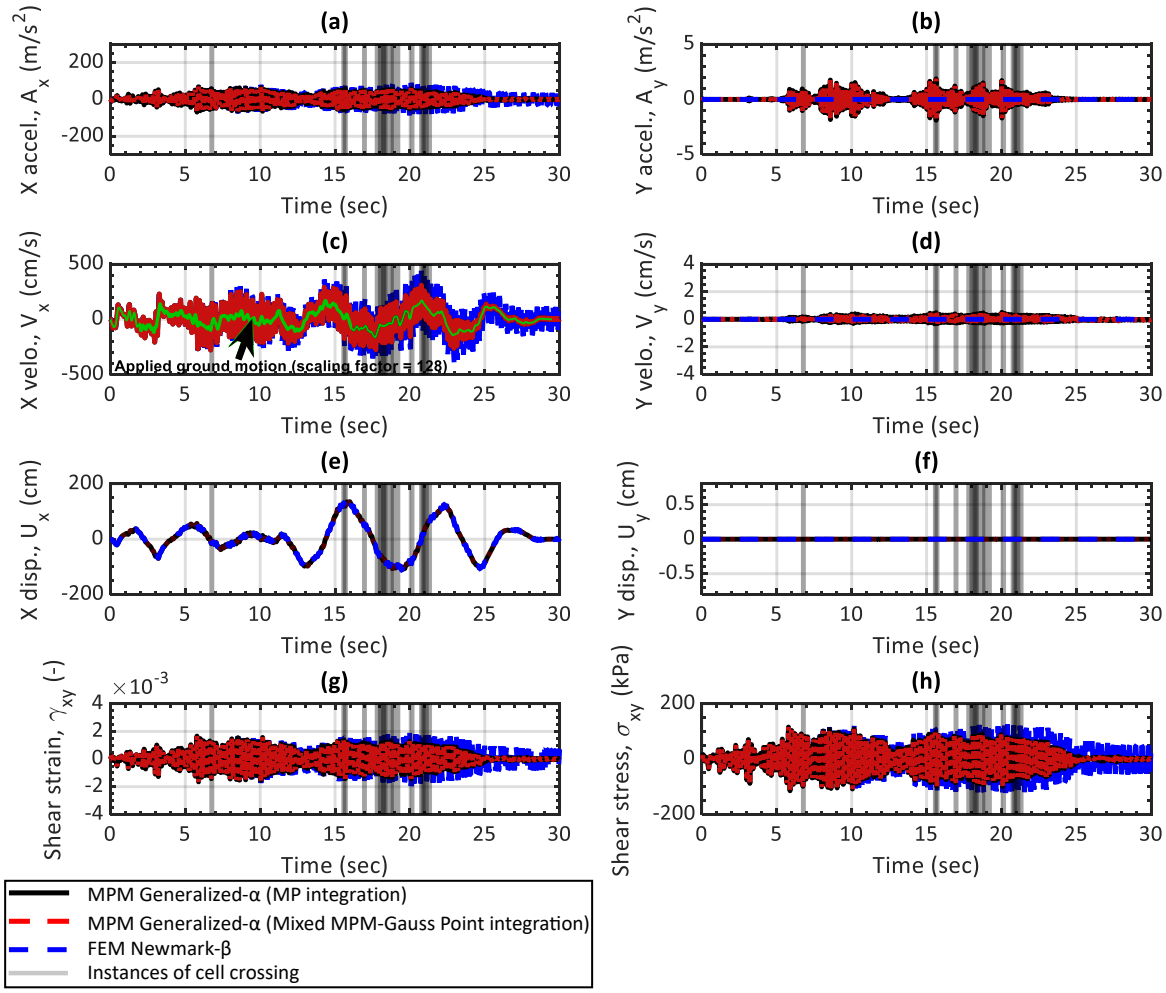

Figure 3.13: MP versus mixed MPM-Gauss-Point integration scheme on time domain results using generalized-α scheme (Case SC-4 with MP location at (x, y) = (0.667m, 9.833m)).

same linear elastic parameters value. Two different constitutive soil models are adopted for the embankment. One set of simulations is performed using the elastic perfectly plastic Mohr-Coulomb (MC) model. The second set of calculations is performed with a Mohr-Coulomb that incorporates strain-softening behavior (MCSS). The second model, qualitatively captures in a very simple way the soil strength loss suffered during cyclic loading events. The MCSS, also used by others (e.g., [57, 165, 166]), simulates material brittleness according to the exponential strain-softening laws presented in Equations 3.20 and 3.21, which shrink the MC yield surface through the reduction of the peak friction angle and cohesion (ϕ'_p, c'_p) to

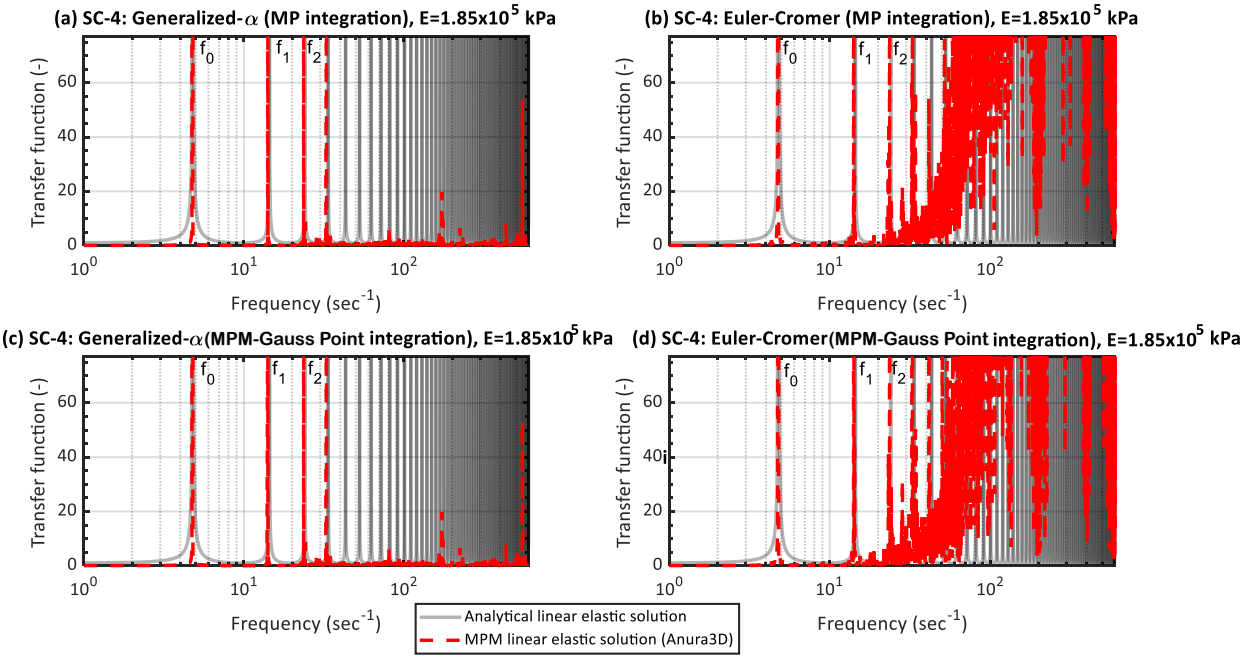

Figure 3.14: MP versus mixed MPM-Gauss-Point integration scheme on transfer function using generalized-α scheme (Case SC-4).

their residual values (ϕ'_r, c'_r) at a rate controlled by the exponential fitting factor, η, and deviatoric plastic strain, ε^p_{eq}. The peak strength parameters are consistent with silty sand material and are chosen to trigger failure for the considered ground motions so the capabilities of the MPM to capture large deformations can be demonstrated. The value of η is chosen to simulate a sharp drop from peak to residual conditions, consistent with brittle behavior. Note that the results of strain-softening constitutive models are mesh dependent and the value of η should be calibrated with laboratory data (e.g., [56, 57, 167]). This example is theoretical and a calibration is not required. All selected material parameters for the embankment are presented in Table 3.3.

$$\phi' = \phi'_r + (\phi'_p - \phi'_r)e^{-\eta\varepsilon^p_{eq}} \tag{3.20}$$

$$c' = c'_r + (c'_p - c'_r)e^{-\eta\varepsilon^p_{eq}} \tag{3.21}$$

The calculation stages include, first, a quasi-static gravity stress initialization whereby the bottom boundary is fully fixed and the lateral sides are normally fixed. Subsequently, these boundary conditions are removed in the dynamic stage, and the ground motion is prescribed as a time-dependent Dirichlet condition (as described by Alsardi et al. [57]) at the base of the model. Periodic boundary conditions are specified at the lateral sides in the dynamic stage. The moving mesh technique is also used.

The parametric analysis accounts for 18 simulations summarized in Table 3.4. Note that to improve the comprehension of this section, the cases are labelled with the employed embankment size (S/L), constitutive model (MC/MCSS), ground motion (I/II/III), and corresponding ground motion scale factor.

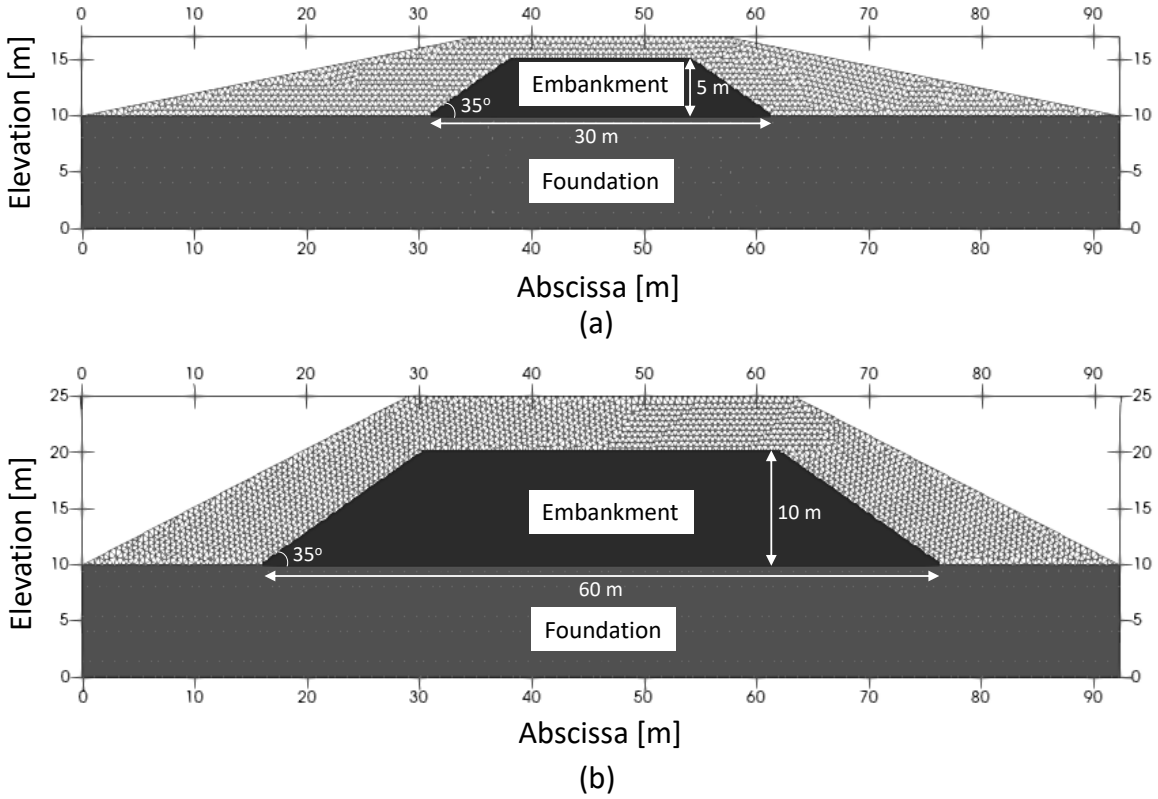

Figure 3.15: MPM model of the embankment overlying soil foundation. Two different size geometries adopted in this study: (a) Model S (small size), (b) Model L (large size).

3.6.2 Investigating the effect of ground motion arias intensity, embankment size, and constitutive model on slope runout

From the authors' experience, the horizontal movement of the MP at the crest of the embankment serves as a good approximation of the slope runout. Note that the MP initially located at the toe of the slope usually presents a more restrained movement since material located above the slope toe can override such point. To evaluate the permanent displacement from the slopes, the input ground motion at the base of the model is subtracted from the horizontal displacement time-history at the MP located at the two crests (left and right).

Table 3.3: Summary of embankment (brittle and non-brittle) and foundation material parameters used in the parametric analysis.

Material	Parameter	Value
Embankment (brittle)	Constitutive model	Mohr-Coulomb with strain-softening (MCSS)
	Peak friction angle, ϕ'_p (degrees)	37
	Residual friction angle, ϕ'_r (degrees)	20
	Peak cohesion, c'_p (kPa)	1
	Residual cohesion, c'_r (kPa)	0.5
	Exponential shape factor, η (-)	100
	Young's modulus, E (kPa)	10^6
	Poisson ratio, ν (-)	0.33
	Tension cutoff (kPa)	0
Embankment	Constitutive model	Mohr-Columb (MC)
	Friction angle, ϕ' (degrees)	37
	Cohesion, c' (kPa)	1
	Young's modulus, E (kPa)	10^6
	Poisson ratio, ν (-)	0.33
	Tension cutoff (kPa)	0
Foundation	Constitutive model	Linear-elastic
	Young's modulus, E (kPa)	10^6
	Poisson ratio, ν (-)	0.33

Table 3.4: Summary of the 18 cases simulated in the example parametric analysis with details on the embankment size, constitutive model, ground motion used and ground motion scaling factor.

Embankment scale	Embankment constitutive model	Ground motion	Ground motion scale	Case label
Small	MC	I	8	S-MC-I-8
	MC	I	16	S-MC-I-16
	MC	I	32	S-MC-I-32
	MC	II	1	S-MC-II-1
	MC	III	1	S-MC-III-1
	MCSS	I	8	S-MCSS-I-8
	MCSS	I	16	S-MCSS-I-16
	MCSS	I	32	S-MCSS-I-32
	MCSS	II	1	S-MCSS-II-1
	MCSS	III	1	S-MCSS-III-1
Large	MC	I	8	L-MC-I-8
	MC	I	32	L-MC-I-32
	MC	III	1	L-MC-III-1
	MCSS	I	8	L-MCSS-I-8
	MCSS	I	16	L-MCSS-I-16
	MCSS	I	32	L-MCSS-I-32
	MCSS	II	1	L-MCSS-II-1
	MCSS	III	1	L-MCSS-III-1

Figure 3.16 presents a comprehensive overview of the parametric analysis in terms of the horizontal runout results versus arias intensity, I_A, for the left and right crests (Figure 3.16a and 3.16b, respectively). It is seen that, the I_A versus runout trend is very similar for both small and large-sized embankments. However, for the same ground motion, the large-scale models always generates higher runout than the small-scale counterparts; for these particular results the scaling factor ranges between 2.1 and 3.4. Besides this, the permanent displacements of the embankments that behave elastic-perfectly-plastic (i.e., using the MC constitutive model) are more sensitive to the input ground motion than the brittle slopes (i.e., with MCSS constitutive model). An increase by an order of magnitude of I_A results in an increase by an order of magnitude of the runout when using the MC model. The MCSS model is seen to generate runouts that are almost independent of I_A. Additionally, the runout computed by simulations using MCSS model is always larger, ranging from one (for $I_A > 2$) to two (for $I_A < 2$) orders of magnitude than the MC counterparts. These observations are consistent with the common belief that if failure is triggered in a brittle brittle embankments and the residual strength is very low, the runout is highly controlled by the residual strength of the mobilized material, and is less dependent on than the ground motion characteristics. Additionally, despite the ground motions are not symmetric, for the set of ground motions selected, it is quantitatively inferred that the permanent displacements are almost symmetric as the left and right crest runouts are similar for all simulations (Figure 3.16a and 3.16b, respectively).

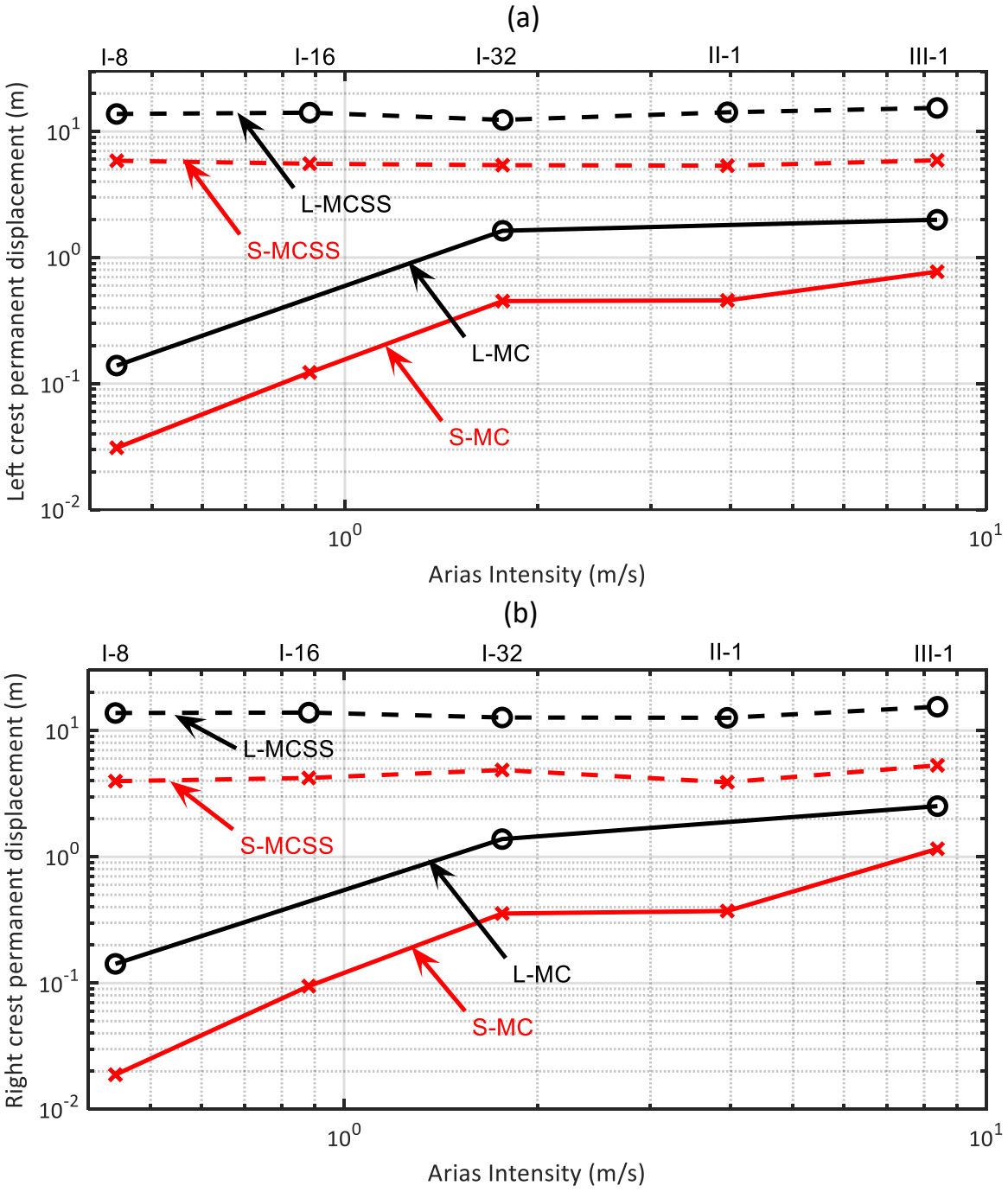

Figure 3.16: Horizontal permanent displacements of the crest obtained from 18 ground motions using the MPM model plotted against the arias intensity, I_A, of the used ground motion. (a) Left crest, (b) right crest.

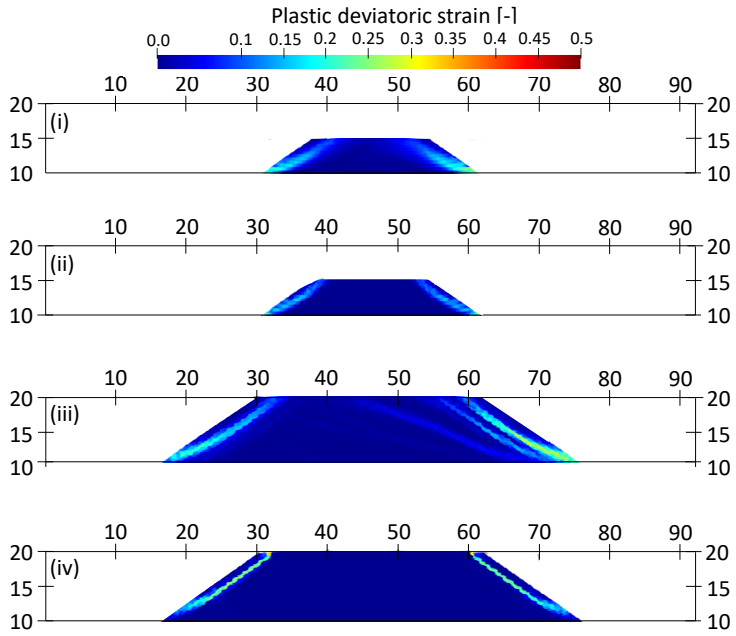

Figure 3.17: (a) Plastic deviatoric strain profile at failure initiation using ground motion III which caused the largest deformations. (i) S-MC-III-1. (ii) S-MCSS-III-1 (iii) L-MC-III-1 (iv) L-MCSS-III-1.

Figures 3.17(a), 3.18(b) and 3.19(c) present the initial failure mechanism, final plastic deviatoric strain, and final horizontal displacement contour plots, respectively, for the models with the highest intensity ground motion III (for reference). The initial failure mechanisms, presented in terms of localization of deviatoric strain, show that the deviatoric strain profile is similar in magnitude and shape in all cases. This similarity can be explained because the peak strength parameters used by the MCSS model at initiation are identical to the strength parameters of the MC model. Despite the similar initial failure mechanisms in all the models, larger proportion of mass is mobilized and larger final runout is observed when comparing the MCSS simulations (Figure 3.19(c-ii) and 3.19(c-iv)) with their MC counterparts (Figure 3.19(c-i) and 3.19(c-iii)). This is consistent with the results presented in Figure 3.16. Also, the initial failure mechanisms and final deformed geometries are approximately symmetric.

In order to analyze the performance of the slope in the time domain, (a) horizontal displace-

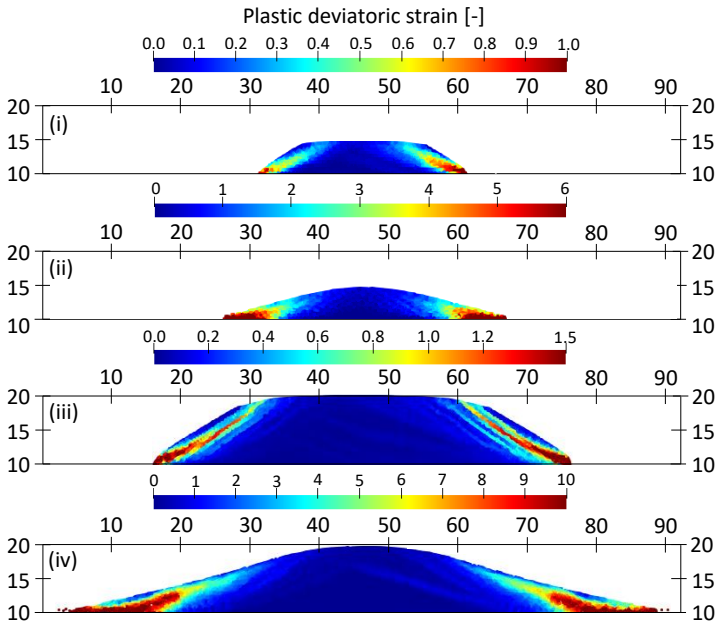

Figure 3.18: (b) Final plastic deviatoric strain profile using ground motion III which caused the largest deformations. (i) S-MC-III-1. (ii) S-MCSS-III-1 (iii) L-MC-III-1 (iv) L-MCSS-III-1.

ment and (b) settlement time-histories of the right crest are presented in Figures 3.20 and 3.21 for the simulations using MC and MCSS models, respectively. Note that the right side of the embankment is arbitrarily selected for discussion herein. The magnitude of runout is consistently larger than the corresponding settlement, but all time-histories, either runout or settlement, present an S-shape curve. At the beginning of the shaking, the slopes remains stable and no permanent displacement is observed. Then, a sudden increase indicates the initiation of the failure. Finally, a stable geometry is achieved and the permanent displacement becomes constant until the end of the shaking. From observing Figures 3.20 and 3.21, for a particular ground motion and constitutive model (i.e., MC or MCSS), the failure initiates at the same time independent of the model being large or small; hence, the time of failure initiation is not highly influenced by the scale of the problem. Instead, the failure initiation is much controlled by the ground motion. From these results, the constitutive model has a minor effect in the time of failure initiation. This is probably because the time

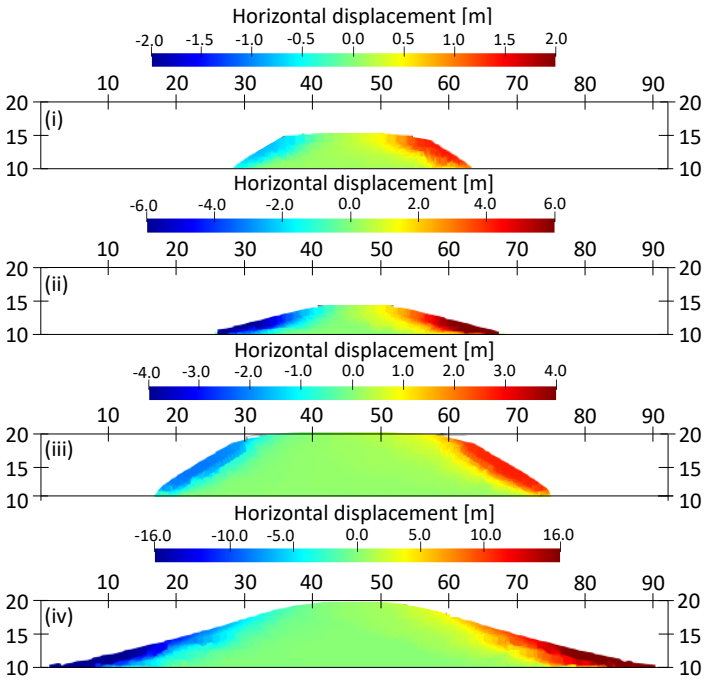

Figure 3.19: (c) Final horizontal displacement contours using ground motion III which caused the largest deformations. (i) S-MC-III-1. (ii) S-MCSS-III-1 (iii) L-MC-III-1 (iv) L-MCSS-III-1.

of failure initiation is highly controlled by the initial strength parameters in the slope, and as discussed before, the peak strength parameters considered in the MCSS model coincide with the strength parameters of the MC model.

For the simulations with MC model (Figure 3.20), it is observed that when using the same ground motion scaled with different factors (e.g., I-8, I-32), the runout and settlement time-histories are scaled. However, the runout and settlement time-history are not consistently scaled according to the scaling factor of the ground motion. To this end, the use of totally different ground motions (e.g., III-1) completely changes the evolution of permanent displacements. Also, consistently with previous observations (Figures 3.16, 3.17(a), 3.18(b), 3.19(c)) when considering the MCSS model for the same scale, Figure 3.21 shows that the crest final runouts and settlements are roughly constant for all the simulations.

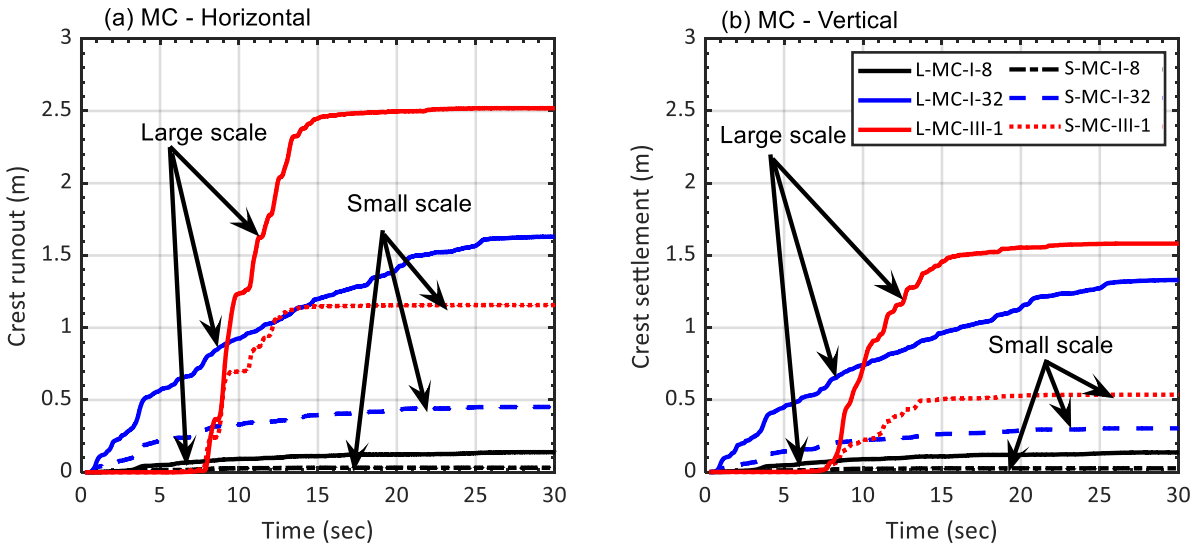

Figure 3.20: Horizontal permanent displacement time-histories of the right crest obtained using the Mohr-Coulomb (MC) constitutive model.

This parametric analysis shows the importance of geometry and material behavior characterization. The selection of an adequate constitutive model capable of reproducing the key features of the material is essential to capture the runout and settlement trends. These

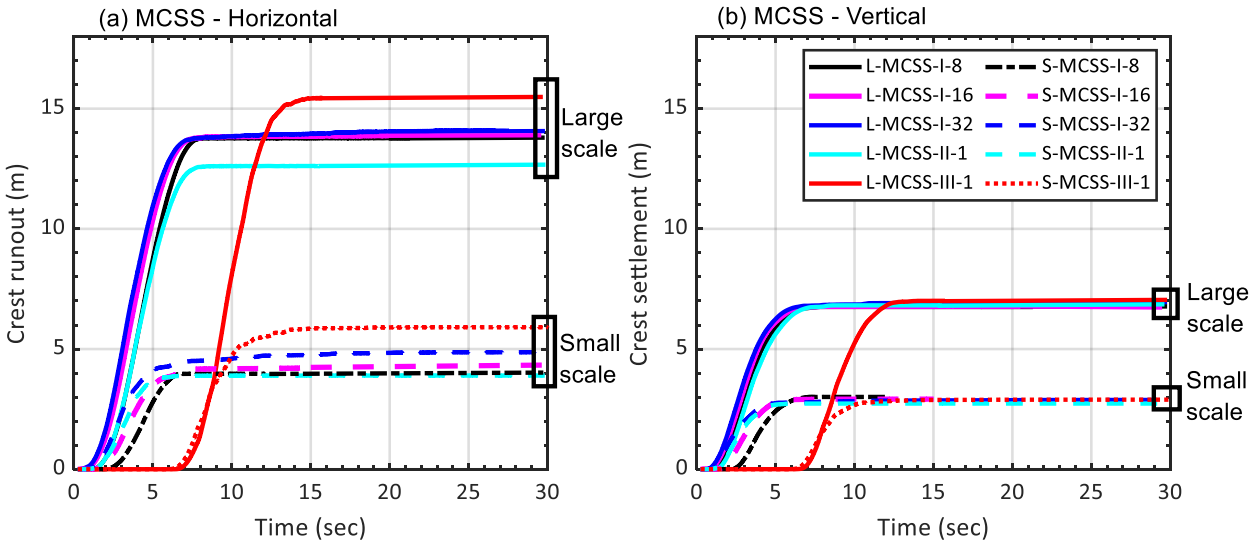

Figure 3.21: Horizontal permanent displacement time-histories of the right crest obtained using the Mohr-Coulomb with Strain-Softening (MCSS) constitutive model.

modeling decisions can greatly determine the displacement trends observed at large deformations.

3.6.3 Comparing MPM numerical results with the Newmark (1965) method

The purpose of this subsection is to compare the performance of the MPM model with the well-known Newmark sliding block solution [34]. The value of fundamental natural period of the MPM embankments, $T_0 = \frac{1}{f_0}$, is calculated as an approximation to guide whether the models can be characterised as 'rigid' or 'flexible'. The value of f_0 is calculated using Equation 3.18, assuming H equals to the height of the embankment and $n = 0$. This approximation is pragmatically adopted for slopes in geotechnical earthquake engineering (e.g., [168]). It is seen that T_0 is equal to 0.04 and 0.09 sec for small and large-sized embankments, respectively. For this study, a threshold value of T_0=0.2 sec is adopted as the limit of rigid behaviour, consistent with Fotopoulou and Pitilakis [136]. Thus, both slope geometries analyzed herein

can be characterised as rigid, which is reasonably consistent with Newmark's assumptions. As such, the numerical solution of the MPM is compared to the Newmark rigid sliding block solution, obtained using SLAMMER software [169].

To determine yield pseudostatic coefficient, k_y, for use in Newmark rigid sliding block solution, pseudostatic analyses using the Spencer [138] limit equilibrium method is performed to identify the failure surface with yield pseudostatic coefficient k_y that provides a factor of safety equal to one. The limit equilibrium software package by GeoStudio [170] was used whereby a pseudostatic analysis was conducted and k_y was varied incrementally by 0.01 until a factor of safety of one was reached for each geometry. The resulting value of k_y is 0.21 and 0.11 for model S (small-sized) and L (large-sized), respectively. Even though base-corrected, the ground motions time-histories are not symmetric in the left and right directions. Due to this, the choice of using Newmark-forward (positive k_y) and Newmark-invervse (negative k_y) methods would generate different results. It is postulated to compare Newmark-forward method with the left-to-right deformation of the right crest in the MPM model, and Newmark-inverse method with the right-to-left deformation of the left crest in the MPM model. Ground motion III that has the highest arias intensity is considered for comparison. The evolution of the horizontal permanent displacements using the MPM models and Newmark method are presented in Figure 3.22a and 3.22b for the left and right crest points, respectively. The order of magnitude of Newmark permanent displacements is consistent with the results from cases that employ the MC model (i.e., S-MC-III-1 and L-MC-III-1). The Newmark results are slightly lower than the MPM results. This can be explained because the ground motion is amplified in the numerical model when it passes through the linear-elastic soil foundation, while the Newmark approach does not account for such amplification (equivalent to a fully rigid foundation). The Newmark-forward generated results that are higher than the Newmark-inverse. This is consistently captured in the MPM

with the right crest having larger runout than the left crest. It is noted that, if a brittle material behavior is assumed, e.g., using the MCSS model, the numerical results are larger by a factor ranging from 6 to 10 times (i.e, approximately one order of magnitude) than the Newmark results. Additionally, in this case, the MCSS model predicts a slightly earlier point of failure initiation than Newmark method. This further highlights the importance of the constitutive model selection when simulating coseismic landslides and the limitations of the Newmark rigid sliding block solution to predict permanent displacements in relatively complex sites.

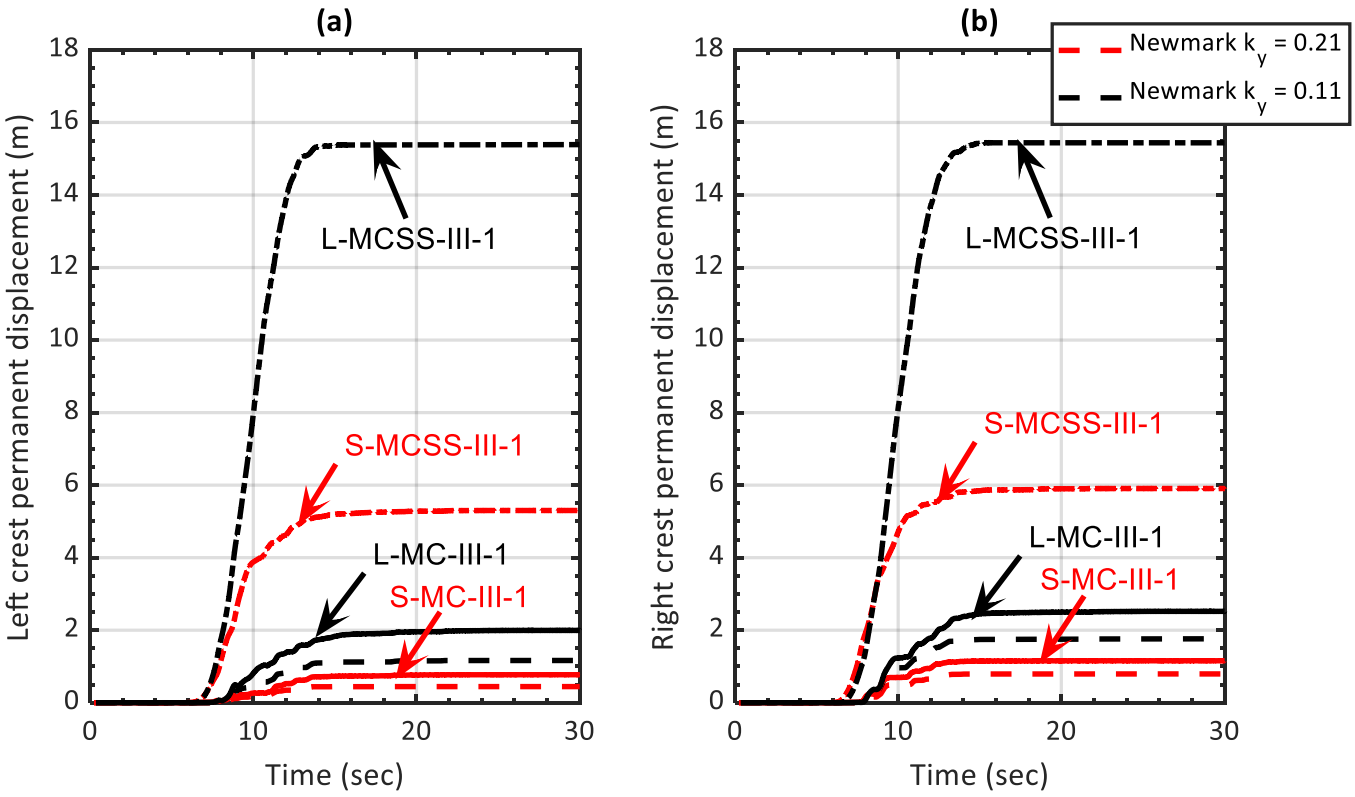

Figure 3.22: Horizontal permanent displacements of the crests compared with Newmark solutions. (a) left crest compared with Newmark-inverse (negative k_y). (b) right crest compared with Newmark-forward (positive k_y).

3.7 Conclusion

This paper presents the MPM as a capable tool to simulate coseismic site response and embankment instabilities using periodic boundary conditions. A particle relocation technique at the periodic boundaries is proposed to ensure that the material points always remain within the computational mesh. Additionally, for the first time, the explicit generalized-α time scheme is used for earthquake engineering applications in MPM. The developed MPM framework is verified at element-level against corresponding FEM simulations and the linear analytical site response approach in the time domain. Additionally, analysis of the transfer function in the frequency domain highlights the ability of the MPM framework in capturing the natural frequency harmonics of a soil column. The high frequency oscillations are appropriately damped to filter out the noise, and this effect is observed in the time-domain and frequency-domain.

A parametric analysis is provided to demonstrate the new MPM framework to simulate real-scale coseismic failures and the performance of a theoretical embankment is investigated. The effects of ground motion arias intensity, I_A, embankment size (doubling the size), and constitutive models (i.e., Mohr-Coulomb (MC) and Mohr-Coulomb with strain softening (MCSS)) are considered. The larger the model size, the higher the crest runout and settlement for the same ground motion. Brittle embankments (using MCSS) result in larger slope mobility compared to the models that use MC model. When considering MC model, the crest runout and settlement increases with I_A. Contrarily, when brittle embankment material is considered, the runout and settlement is relatively constant for the different ground motions considered, indicating that the runout of brittle embankments is highly controlled by the residual strength of the mobilized material, and is less dependent on than the ground motion characteristics. Similar failure mechanisms are observed in all cases.

Finally, the Newmark (1965) rigid sliding block solution is compared to the MPM embankment simulations. The Newmark-forward (positive k_y) and Newmark-inverse (negative k_y) are seen to be consistent with the right and left crest, respectively, when using MC model. This is consistent with the fact that the considered embankments have a low natural period (< 0.2 sec). However, the assumption of brittle embankment behavior using MCSS model leads to runout results that one order of magnitude larger. This paper highlights the importance of the geometry and the selection of appropriate constitutive models when simulating coseismic site response, failure, and post-failure behavior of slopes. Future work includes the use of advanced constitutive models especially developed for geotechnical earthquake engineering applications for a more accurate estimation of soil behavior under cyclic loading.

Chapter 4

Enhanced MPM framework with Multipatch Isogeometric Analysis for Geotechnical Applications

Published in Computers and Geotechnics, with the following reference: Alsardi, A., Yerro, A. and Long, C.C., 2026. Enhanced MPM framework with multipatch isogeometric analysis for geotechnical applications. Computers and Geotechnics, 190, p.107743.

The following authors contributed to this manuscript, as follows:

- Abdelrahman Alsardi
  - Developed and implemented the multipatch isogeometric numerical framework.
  - Performed all numerical simulations from pre-processing to post-processing and analysis.
  - Prepared all figures and wrote the original draft of the manuscript.
- Dr. Alba Yerro
  - Provided invaluable feedback throughout the implementation of the framework.
  - Discussed results and troubleshooting strategies to perform successful numerical simulations.
  - Obtained research funds to enable the development of the framework.
  - Edited and revised the manuscript.
- Dr. Christopher Curtis Long
  - Introduced the idea of incorporating multipatch isogeometric analysis in MPM.
  - Provided invaluable feedback throughout the implementation of the framework.
  - Obtained research funds to enable the development of the framework.
  - Edited and revised the manuscript.

4.1 Abstract

Achieving stable stress solutions at large strains using the Material Point Method (MPM) is challenging due to the accumulation of errors associated with geometry discretization, cell-crossing noise, and volumetric locking. Several simplified attempts exist in the literature to mitigate these errors, including higher-order frameworks. However, the stability of the MPM solution in such frameworks has been limited to simple geometries and the single-phase formulation (i.e., neglecting pore fluid). Although never explored, multipatch isogeometric analysis presents desirable qualities to simulate complex geometries while mitigating errors in the MPM. The degree of required high-order spatial integration has also never been investigated to infer a minimum limit for the stability of the stress solution in MPM. This paper presents a general-purpose numerical framework that can simulate stable stresses in porous media, capturing both near incompressibility and multiphase interactions. First, the numerical framework is presented considering Non-Uniform Rational B-splines (NURBS) to perform isogeometric analysis (IGA) in MPM. Additionally, a volumetric strain smoothing algorithm is used to alleviate errors associated with volumetric locking. Second, the manifestation of cell-crossing errors is assessed via a series of problems with orders ranging from linear to cubic interpolation functions. Third, the use of NURBS is investigated and verified for problems with circular geometries. Finally, multipatch analysis is deployed to simulate plane strain and 3D penetration in soils, considering nearly incompressible elastoplastic (total stress) analysis and fully-coupled hydro-mechanical (effective stress) analysis. The stability of the solution is also analyzed for different constitutive models. From the results, it can be concluded that the framework using cubic interpolation functions with strain smoothing is the most convenient, presenting stable stress solutions for a broad range of multiphase geotechnical applications.

4.2 Introduction

The Material Point Method (MPM) is of particular interest in engineering due to its close proximity to the Finite Element Method (FEM) in its use of the background grid, although considering deformation-dependent integration points each so-called a 'material point' (MP) or a 'particle' [58]. In this manner, the MPM is capable of simulating large deformations in history-dependent materials without exhibiting mesh entanglement, whereby ill-defined geometries occur in the background grid. Additionally, the use of material constitutive models in MPM is similar to those of the FEM. More recently, critical state and bounding surface plasticity models have been used in MPM for the simulation of penetration problems [171, 172] and landslides [81, 173].

Despite its prolific use, MPM has various well-known limitations that generate spurious noise in the solution, hindering it from achieving its full potential. This includes cell-crossing error [60], volumetric locking [174], null-space problem [74], and dynamic ringing instabilities due to Gaussian integration errors [66], among others. Most of the numerical errors, besides the cell-crossing error, can be considered pathological to FEM, and potential remedies can be extracted from existing work on mesh-based approaches (e.g., [72, 175]). In traditional mesh-based techniques (e.g., FEM), Lagrange polynomials are generated across each element, where the nodal basis functions are unitary at each node. This inevitably creates a discontinuity in the derivative of the nodal basis functions across each element. In FEM, this discontinuity affects the smoothness of the stress solution but does not affect the internal force integration, as the integration points are fixed in their local positions at the Gauss points. However, in MPM, the integration points are MPs that move within a fixed mesh. Each time MPs cross an element, the discontinuity in the derivative manifests in an error in the internal force, which introduces shock-like artifacts that deteriorate the stress solution. This, in turn, affects the velocity solution and produces inaccurate displace-

ments. The dynamic movement of the integration points also causes additional spurious ringing, which can result in diverging solutions. This phenomenon observed in MPM was coined as the 'cell-crossing error' [60]. It is well known that quadrature integration errors are inevitable in MPM due to enabling the large deformations of the Lagrangian integration points [66]. This noise highly reduces the accuracy of the solution, especially when advanced history-dependent constitutive models are used. Introducing higher-order frameworks results in continuous interpolation function derivatives between the elements and can theoretically eliminate cell-crossing error. In this manner, the overall error in MPM is reduced in higher-order frameworks. This also enables the isolation of quadrature errors, helping us innovate new approaches to ultimately alleviate them. Higher-order Lagrange polynomials can help in providing smoother solutions within the element. However, they are unable to fully eliminate cell-crossing errors because the discontinuity still exists across elements.

There are variants of MPM that have been developed to tackle these challenges with particular emphasis on solving the cell-crossing error. First, the Generalized Interpolation Material Point Method (GIMP) was introduced to numerically give the MPs a larger tributary volume than the traditional Dirac-delta function [60]. It is considered a general framework, where an arbitrary characteristic function is convolved in the weak form to enlarge the integration volume and spread the corresponding MP mass across that volume. It draws novelty from kernel functions commonly used in Smoothed Particle Hydrodynamics (SPH) techniques. The uniform 'top-hat' function is commonly adopted as the characteristic function. The tributary area of the MPs is updated according to the volumetric deformations. Specifically, the contiguous-particle GIMP (cpGIMP) is used, whereby the piecewise linear 'tent' basis functions are effectively smoothed and overlapped across neighboring elements. The basis functions are no longer equal to unity at the nodes. This approach often stabilizes the MPM stress solutions (e.g., [176]). However, it is tied to simple geometries in

a structured mesh, nodal search algorithms, and challenges with implementing boundary conditions. It also presents severe cases of MP separation under large deformations, which results in non-physical continuum behavior [63]. It also exhibits further instability under non-linear constitutive models [64]. The Convected Particle Domain Interpolation method (CPDI) was introduced as a variant of GIMP that simulates the tributary area as a parallelogram, instead of a rectangle. The deformation gradient of each MP is tracked, and the coordinates of the parallelogram are updated according to volumetric and shear deformations. The CPDI aims to maintain the integrity of the MPs and avoid the separation commonly seen in GIMP. However, the CPDI pathologically carries forward challenges associated with simple geometries and weakly enforced boundary conditions. Additionally, GIMP and CPDI are very computationally expensive and require the storage of additional numerical parameters to store the deformed tributary volume of the MPs. The Dual Domain Material Point Method (DDMP) was developed to alleviate cell-crossing error by modifying the gradient of the interpolation functions [64]. This directly affects the internal force and strain calculation, but keeps the linear 'tent' interpolation for mass and velocity field interpolation. The DDMP approach often presents superior accuracy, ensures strong boundary condition enforcement, and can be used in unstructured meshes [64, 65, 74]. However, its implementation can be complex with specific difficulties associated with the incorporation of stabilizing algorithms for dealing with volumetric locking [74]. Plus, DDMP retains lower-order stress distributions, which require extensive grid size refinement to achieve intricate simulation details.

The use of B-spline functions as MPM interpolation functions has been emerging further within the past five years as an alternative to mitigate cell-crossing error and obtain stable higher-order stress solutions [177]. The mathematical framework of B-splines introduces overlap between the elements while keeping the particles under the Dirac-delta volume dis-

tribution (i.e., infinitesimal points). The use of B-splines also offers greater flexibility in choosing the order of interpolation for MPM convergence investigations under p-refinement. Additionally, the more general isogeometric analysis (IGA) concept using Non-Uniform Rational B-Splines (NURBS) can be incorporated to streamline the process of design-to-analysis without the need for grid generation. The IGA framework enables accurate geometry representations. In this manner, the pre-processing tool is used to generate the geometry (i.e., control points and knot vectors), which seamlessly provides the numerical discretization for analysis. This discretization often consists of multiple patches to analyze complex geometries, with each node carrying a geometrical weight.

Despite the success of MPM in simulating geotechnical problems with simple elastoplastic models, sophisticated applications often require non-linear constitutive models with multiple surfaces and softening or hardening laws. Simulations can also include multiphase interactions incorporating nearly incompressible fluids in a solid skeleton (e.g., porous water in soils). Volumetric locking artifacts can occur when the material deforms at a constant volume. Sources of this error include material incompressibility (i.e., a Poisson ratio nearing the value of 0.5), non-dilative plastic deformation (e.g., large deformation of soils at critical state), and undrained behavior of porous media. Table 4.1 presents a summary of research contributions with frameworks that use recursive B-splines in MPM in a similar fashion to the ones commonly used in IGA. The maximum order of the used B-spline, the constitutive model, and multiphase formulation (or lack thereof) are outlined with additional details associated with the B-spline type and weak incompressibility enforcement (i.e., using Poisson ratio ν=0.499). Note that there is only one study [68] that uses NURBS prior to the present study, which only uses single patch domains.

The goal of this paper is to develop a stable MPM approach that can handle complex geometries, large deformations, multiphase materials, and sophisticated constitutive relationships

within reasonable accuracy. This work examines the suitability of B-splines and the IGA framework using NURBS to improve the stability of MPM for geotechnical applications. The examples presented encompass a broad range of applications, aiming to develop a stable, multi-purpose MPM code that can be deployed to simulate porous media and hydromechanical problems. The novelty in the proposed framework stems from its simplicity and comprehensiveness, to tackle a wide range of geotechnical engineering problems in effective stress with minimal modification to the MPM computational cycle. Supporting examples range from dynamic wave propagation to real-scale footing penetration problems. Specifically, the study adopts simple benchmark problems and gradually increases the complexity to understand the stability of the solution under (i) accurate geometry representations with IGA to simulate cylindrical problems, and (ii) soil-structure interactions in a multipatch IGA framework for shallow foundation penetration. The IGA-MPM framework is often verified in its B-spline form, but rarely verified using circular geometries. Only one example exists in the literature where IGA-MPM is used to simulate a circular geometry [68]. The multipatch framework has never been used in MPM prior to the present study. The multipatch framework is necessary in IGA-MPM to offer more accurate geometry discretization and spatial integration. It also offers flexibility in defining empty spaces for materials that deform much farther from the initial domain. As such, the stability of the framework is analyzed herein with particular emphasis on the MPs that cross from one patch to another, enduring the line of discontinuity between the patches. The IGA-MPM framework is also extended to the 2-phase formulation for the very first time. First, 1D simulations of pressure waves and column settlement under gravity are investigated to understand the effect of cell crossing and assess the suitability of quadratic and cubic shape functions. Convergence is assessed by comparing MPM results with analytical solutions. Second, the IGA framework is deployed to simulate the compression of complex circular geometries in 3D under the influence of gravity and internal pressurization. Next, the multipatch IGA framework is used to analyze

the soil-structure interaction of a footing penetrating through a soil stratum, considering weak incompressible behavior. The Tresca constitutive model with strain softening is also used to incorporate a level of complexity in material nonlinearity and to simulate the localization commonly observed through progressive failure in brittle soils. Finally, the 2-phase hydromechanical formulation is used to simulate the solid-liquid phase interaction in the plane-strain footing penetration problem, assuming saturated conditions.

Table 4.1: Summary of contributions that use generalized recursive B-spline generation with volumetric locking treatment to stabilize MPM.

Authors	**B-spline type**	**Constitutive model**	**Max Order**	**Highest dimensions considered**	**Volumetric locking mitigation method**	**Weakly incompressible?**	**Multiphase?**	**Multipatch?**
Tielen et al. [67]	B-spline	Linear-elastic	Cubic	1D	-	-	-	-
Gan et al. [178]	B-spline	Linear-elastic	Cubic	1D	-	-	-	-
Wobbes et al. [179]	B-spline with Taylor least square reconstruction	Linear-elastic	Cubic	1D	-	-	-	-
Tran and Solowski [74]	B-spline	Linear-elastic	Cubic	2D	-	-	Double point, $v_S - v_L$	-
Moutsanidis et al.[68]	Single patch NURBS	J_2-plasticity with isotropic hardening	Cubic	3D	$\bar{F}$	-	-	-
Yamaguchi et al. [180]	Extended B-spline	Hyperelastic	Cubic	2D	-	-	-	-
Zhang et al. [181]	Truncated B-spline	Mohr-Coulomb	Cubic	2D	-	-	-	-
Sun et al. [182]	B-spline	Drucker-Prager	Cubic	3D	-	-	Single point, $v_S - v_L$	-
Sugai et al. [183]	Extended B-splines	(a) J_2-plasticity with isotropic hardening (b) Drucker-Prager	Cubic	2D	$\bar{F}$	Yes	-	-
Xie et al.[184]	B-spline	Mohr-Coulomb	Quadratic	2D	$\bar{F}$ with stress and strain smoothing	Yes		-
Zhao et al. [174]	B-spline	J_2 plasticity with strain softening	Quadratic	3D	$\bar{F}$	Yes	-	-
Yamaguchi et al.[185]	Extended B-spline	Mohr-Coulomb	Quadratic	2D	Variational multiscale	-	Double point, $v_S - v_L$	-
Telikicherla and Moutsanidis [186], Telikicherla and Moutsanidis [187], Telikicherla and Moutsanidis [188]	B-spline	J_2-plasticity	Quadratic	3D	Stress and strain smoothing	Yes		-
Madadi and Dortdivanlioglu[189]	B-spline	Linear-Elastic	Cubic	3D	Mixed two-field	Yes	-	-
Hidano et al. [190]	B-spline	Mohr-Coulomb	Quadratic	3D	-	-	-	-
Present study	Multipatch NURBS	Tresca with strain softening	Cubic	3D	Strain smoothing	Yes	Single point, $v_S - v_L$	Yes

4.3 Numerical framework of the stabilized multipatch IGA-MPM

Geometry discretization using NURBS is often performed by adopting 'macro-elements' known as patches, whereby each patch is discretized into knot span elements. As such, the IGA framework gains its flexibility in accurately defining geometries from its multifold discretization capability, which involves creating a series of patches that interconnect to form the desired physical representation. Naturally, most computer-aided design (CAD) tools used for pre-processing utilize NURBS to enable users to specify the desired geometry. The IGA framework leverages this to perform the analysis without further simplification of the problem geometry. The hybrid IGA-MPM framework is a suitable approach for controlling the smoothness of the stress solution, eliminating cell-crossing errors, and simulating large deformations of complex geometries [68]. Unfortunately, the efficacy of the IGA-MPM has rarely been compared against analytical solutions and has never been investigated for the 2-phase formulation. First, the IGA framework is described in detail, including the multipatch implementation. Unique computational aspects associated with the interpolation function spaces and computational grid are outlined. Second, the 2-phase MPM computational cycle is briefly described, and the interconnection with the multipatch IGA framework is outlined. Third, the volumetric strain smoothing implementation, which is used to overcome volumetric locking, is also described.

4.3.1 Isogeometric analysis

The IGA framework provides structured interpolation spaces that accurately capture the discretized geometry, facilitate the generation of higher-order B-spline functions, and enable

simple spatial integration. Figure 4.1 shows a schematic that presents the three separate spaces that are considered in the IGA framework, as follows:

- **Physical space** captures the actual geometrical representation of the simulated material. Curved geometries are plotted and analyzed using NURBS. Nodal coordinates exist in this space and coincide in the same locations as the control points, consistent with the CAD design as defined by the pre-processor. The nodal coordinate locations are a consequence of the defined geometry and the minimum order to define the chosen geometry, p. The user can choose to increase p to obtain the required smoothness in the NURBS functions. The nodal coordinates are generated by the pre-processor and are imported into the subsequent analysis technique (i.e., FEM or MPM) to simulate the boundary value problem. The NURBS allow accurate material representation by assigning a geometric weight to each node, w_i, as shown in Figure 4.1(a). This can warp the material in the physical domain with the control points acting as scaffolding around the material (i.e., not conforming with the physical material). In simple geometries, conventional B-splines (equivalent to assigning geometric weights equal to one) are used instead, where the Gaussian locations conform to the rectangular background grid. This space is often referred to in the coordinates of $\vec{x} = [x, y, z]$.

- **Parameter space** is a regular, structured grid that spans from 0 to 1 in each direction (square or cube in 2D or 3D, respectively). The element discretization is performed in this normalized space, which reflects the discretization in the physical space as color-coded in Figures 4.1(a) and 4.1(b). The B-spline interpolation functions and their derivatives are generated in this space using the Cox de-Boor equation. Note that this space is geometrically warped in the physical space according to nodal coordinates and weights, which represent the material's complex geometry. Additionally, for complex geometries, NURBS require an extra normalization step to account for

the corresponding geometric weights. The interpolation function derivatives are also scaled accordingly using a Jacobian that connects the parameter space to the physical space. This space is unique to IGA and is referred to in the coordinates of $\vec{\xi} = [\xi, \eta, \zeta]$ as shown in Figure 4.1(b).

- **Parent space** spans from -1 to 1 in each direction (square or cube in 2D or 3D, respectively), where a Gauss-Legendre integration is performed in each element. This space also exists in traditional isoparametric analysis commonly adopted in FEM and MPM. This space is referred to in the coordinates of $\vec{\xi} = [\xi, \eta, \zeta]$ as shown in Figure 4.1(c).

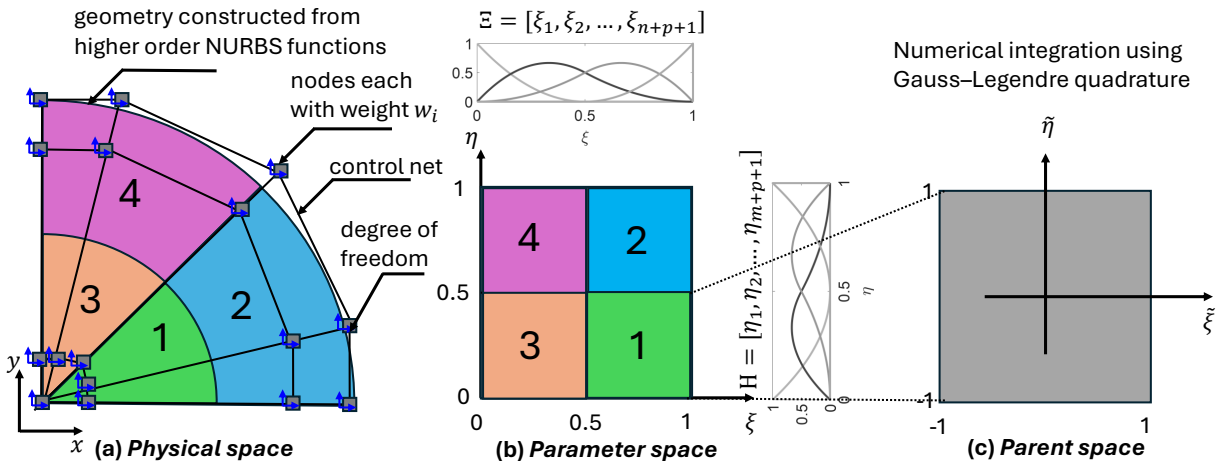

Figure 4.1: Schematic showing a single patch isogeometric discretization in the three spaces of a simulation. (a) Physical space captures the problem geometry where the nodes coincide with the control point locations for each patch as provided by the pre-processor. (b) Parameter space captures a structured (square or cube) grid where the interpolation functions are generated. n and m represent the number of interpolation functions in each direction for each patch. Knot vectors are shown for each direction of the parametric domain. (c) Parent space captures the standard Gaussian integration for each element in a patch.

B-splines and NURBS are used as spatial interpolation functions, $N_{i,p}$, in the IGA framework. B-splines use a background grid that has a box-like regular geometry. First, the interpolation functions are generated as piecewise constants of order $p = 0$ using Equation 4.1.

$$N_{i,p=0}(\xi) = \begin{cases} 1 & \text{if } \xi_i \leq \xi \leq \xi_{i+1} \\ 0 & \text{otherwise} \end{cases} \tag{4.1}$$

The knot vector, $\Xi = [\xi_1, \xi_2, ..., \xi_{n+p+1}]$, discretizes the domain into knot spans (i.e., elements), and the components of the vector are referred to as knots, where n represents the number of univariate interpolation functions. Ξ is usually normalized with knot values $0 \leq \xi \leq 1$. For 3D simulations, three knot vectors are required (Ξ, $\mathcal{H}$, and $\mathcal{Z}$) to represent each Cartesian direction in each patch. For orders higher than piecewise constant (i.e., $p \geq 1$), the 1D Cox de-Boor recursive equation [191] is used to define the NURBS, as defined by Equation 5.3.

$$N_{i,p}(\xi) = \frac{\xi - \xi_i}{\xi_{i+p} - \xi_i} N_{i,p-1}(\xi) + \frac{\xi_{i+p+1} - \xi}{\xi_{i+p+1} - \xi_{i+1}} N_{i+1,p-1}(\xi) \tag{4.2}$$

The value of $N_{i,p}$ is equal to 1 at repeated knots. This is usually enforced at the boundaries of the domain by repeating the knot p+1 times to start and end each knot vector (i.e., mathematically known as an open knot vector). The advantage of this is that boundary conditions are strongly enforced at the boundaries of the domain. However, a caveat is that discontinuities naturally arise when considering a multipatch framework. Arbitrary discontinuities can also be introduced further by including repeated knots through the vector. Interpolation function derivatives, $N'_{i,p}$, are calculated recursively using Equation 5.4.

$$N'_{i,p} = \frac{d}{d\xi} N_{i,p}(\xi) = \frac{p}{\xi_{i+p} - \xi_i} N_{i,p-1}(\xi) - \frac{p}{\xi_{i+p+1} - \xi_{i+1}} N_{i+1,p-1}(\xi) \tag{4.3}$$

When considering NURBS as an extension of B-splines, it is necessary to normalize the 1D interpolation functions so that their sum is always equal to one. The normalized functions are

$R_i^p(\xi)$. For solids (3D), the normalization equation is presented in Equation 4.4 to calculate $R_{i,j,k}^{p,q,r}$ respectively, where N, M, and L correspond to the univariate interpolation functions in the ξ, η, and ζ parametric directions.

$$R_{i,j,k}^{p,q,r}(\xi,\eta,\zeta) = \frac{N_{i,p}(\xi)M_{j,q}(\eta)L_{k,r}(\eta)w_{i,j,k}}{\sum_{\hat{i}}^{n}\sum_{\hat{j}}^{m}\sum_{\hat{k}}^{l} N_{\hat{i},p}(\xi)M_{\hat{j},q}(\eta)L_{\hat{k},r}(\zeta)w_{\hat{i},\hat{j},\hat{k}}} \tag{4.4}$$

The subscripts p, q, and r represent the orders of the interpolation functions, and n, m, and l represent the number of nodes in an element in the parametric direction. Increasing the order p for a particular geometry introduces more control points. As such, n increases to introduce interpolation functions at these control points. This enforces the length of the open knot vector to always be $n+p+1$. The derivatives of the NURBS functions are evaluated as shown in Equations 4.5-4.7.

$$\frac{d}{d\xi}R_i^p(\xi) = w_i\frac{W_i(\xi)N'_{i,p} - W'(\xi)N_{i,p}(\xi)}{(W(\xi))^2} \tag{4.5}$$

$$W(\xi) = \sum_{\hat{i}=1}^{n} N_{\hat{i},p}(\xi)w_{\hat{i}} \tag{4.6}$$

$$W'(\xi) = \sum_{\hat{i}=1}^{n} N'_{\hat{i},p}(\xi)w_{\hat{i}} \tag{4.7}$$

The nodal weight for each node, w_i, is used to obtain the univariate derivatives, $\frac{d}{d\xi}R_i^p(\xi)$, in each direction. The process of evaluating B-spline interpolation functions and their derivatives is summarized in Algorithm 1 in the supplementary document [192]. The normalization process accompanying the use of NURBS interpolation functions is also presented in Algorithm 2 in the supplementary document [192], ensuring that the interpolation functions and

derivatives add up to one and zero, respectively, at a given node. The in-house implementation of MPM used in this paper enables the analysis of 2D plane-strain and 3D problems. However, only 3D equations are presented for brevity. The global position is updated for solid simulations using Equation 4.8.

$$\mathbf{Solid}(\xi,\eta,\zeta) = \sum_{i=1}^{n}\sum_{j=1}^{m}\sum_{k=1}^{k} R_{i,j,k}^{p,q,r}(\xi,\eta,\zeta)\mathrm{Co}_{i,j,k} \tag{4.8}$$

The derivatives of the interpolation functions are ultimately obtained with respect to the physical domain through the Jacobian calculation as shown in Equation 4.9 and Algorithm 3 in the supplementary document [192] for this paper. Additionally, Further details regarding the local positions of the MP in the parent domain are presented in Section 3 of the supplementary document [192].

$$\vec{J} = \frac{\partial R}{\partial x_i} = \frac{\partial R}{\partial \xi_j}\frac{\partial \xi_j}{\partial x_i} \tag{4.9}$$

Complex geometry discretization requires multiple configurations that can be represented by different knot vector combinations. This means that different zones in the geometry need to be analyzed using different knot vectors (i.e., Ξ, $\mathcal{H}$, and $\mathcal{Z}$), as provided by the pre-processor for each patch. The IGA-MPM implementation presented herein reads the nodal coordinates for each patch and subsequently connects the nodes that exist at the same coordinates. As such, a global node numbering is given to each unique nodal coordinate upon which the degrees of freedom exist. Philosophically speaking, the multipatch implementation introduces a 'for' loop across the patches to generate the NURBS spaces for each patch. Interpolation functions are generated across each patch using their corresponding open knot vectors. It is acknowledged that a discontinuity exists between patches. This might reintroduce some

cell-crossing error along that boundary. However, the discontinuity between patches also gives the advantage of enabling the strong enforcement of boundary conditions at the patch interface, as previously discussed. Additionally, the integration can be handled in a straightforward manner along the patch boundary, allowing for the computation of nodal internal reaction forces, which are important in engineering applications. Note that only conforming multipatch simulations are considered in this paper; however, this can be easily extended to non-conforming patches using Nitsche's method for further flexibility in geometry definition [193, 194].

4.3.2 MPM computational cycle

The MPs store all the information (e.g., mass, velocity, strain, stress, constitutive state variables), which is mapped to the background mesh using nodal interpolation functions to solve the governing equations. The mass of each MP, m_{MP}, is determined using the density, ρ_{MP}. The interpolation is performed in each time step in a similar manner to the traditional FEM approach. The IGA framework enables the mitigation of cell-crossing error commonly encountered in the linear MPM, as it enables the generation of higher-order interpolation functions with minimal modification to the computational cycle. The NURBS control points act as the nodes of the background mesh with a structured connectivity matrix. MPM can be extended to IGA-MPM by replacing the interpolation function subroutines to include the information in subsection 4.3.1. The GiD pre-processor [195] is used herein to generate the NURBS control point net, which is exported into MPM as the background mesh. The MPs are often initialized at the Gaussian locations with the corresponding Gaussian weight, ω_q, which is used to obtain the volume, V_{MP}, scaled by the physical-to-parent domain Jacobian determinant, $|\vec{J}|$, evaluated in the parent space at $\vec{\xi}_q$. Despite the ability to locate MPs arbitrarily, locating them at the initial Gaussian locations reduces the initial quadrature

errors, which helps stabilize the initial geostatic stresses. The mass, m_{MP}, is calculated using the density, ρ_{MP}. The governing momentum balance equations are solved at the nodes (i.e., NURBS control points), and the nodal velocity solution is mapped to the MPs. The velocity field is used to evaluate the strain at each MP. Subsequently, the constitutive model is provided with the strain and state variables to solve for the stress at each MP. The MP global positions are updated in the physical space, and the nodal variables are reset. Theoretically, the background grid can be destroyed and regenerated in a different orientation after each time step. The moving mesh technique is particularly used to simulate the interaction between rigid and deformable bodies (e.g., penetration problem [172, 196], fully-reflective shaking table tests [197]). In this technique, a portion of the mesh is made to move in response to the velocity of the rigid material, whereby all nodal coordinates are incrementally updated. The specification of a 'compressing' mesh is often used in penetration problems, whereby the volume of the element shrinks to maintain contact with the moving mesh. In this multipatch IGA-MPM framework, the moving and compressing mesh portions correspond to different patches.

In many geotechnical applications, simulating saturated porous media requires the use of hydro-mechanical formulations that capture the interactions between the soil skeleton (i.e., the solid phase) and pore fluids (i.e., the liquid phase). In this paper, the 2-phase single-point MPM momentum formulation by [198] is implemented within the IGA-MPM framework. This formulation has been widely adopted by the MPM community to simulate saturated porous media, where a single set of MPs is used to capture the response of the two phases. This formulation is based on macro-scale continuum theory, where the behavior of the liquid is described in an Eulerian manner based on the kinematics of the solid skeleton. The global positions of the MPs are updated according to the movement of the solid phase, giving a Lagrangian description of the solid deformation. The explicit Euler-Cromer time integration

scheme is employed due to its simplicity as a solver and its convergence, eliminating the need for iterative deployment of the constitutive model to obtain the internal force. However, it is acknowledged that this time scheme can be accompanied by spurious high-frequency noise that can contaminate the solution. Further details regarding the MPM computational cycle are provided in Section 1 of the supplementary document [192].

4.3.3 Volumetric locking mitigation using strain smoothing

The simulation of nearly incompressible porous media is prevalent in geotechnical applications due to the nature of the soil mixture, which consists of a solid phase with a nearly incompressible liquid phase filling the pores. The simulation of pore water pressure is particularly challenging in MPM. This is mainly because of volumetric locking, which results in a 'checkerboarding' instability in the pressure field at large strains. Volumetric locking can also occur when simulating materials with a Poisson ratio, ν nearing 0.5, and when simulating elastoplastic materials, which deform at constant volume under a flow rule. In such circumstances, a smoothing algorithm within a higher-order framework is necessary to smooth strains and eliminate spurious oscillations, thereby achieving a convergent and stable solution.

The most prominent techniques to mitigate volumetric locking in dynamic numerical frameworks for porous media broadly include: (i) smooth volumetric deformations by means of deformation gradient (i.e., strain) smoothing (e.g., $\bar{F}$), and (ii) treating pressure and velocity fields, both, as main unknowns to alleviate the inf-sup condition. The first approach is compatible with fully dynamic higher-order formulations, e.g., the 2-phase coupled velocity formulation [199], and is often accompanied by the smoothing of volumetric stresses and pore pressures [188]. Despite requiring reconfiguration of the MPM cycle, the second approach

has been applied to simulate incompressible fluid flow in linear MPM in a predictor-corrector fractional time stepping scheme [77], and more recently in a monolithic scheme [200]. [201] employed the Hu–Washizu multi-field variational principle in linear MPM to separate volumetric and the deviatoric portions of the strain and stress fields. The fractional time stepping technique [75, 77] and multi-field strain and stress decomposition [201], among other techniques, have presented significant success in linear MPM. However, they require significant reformulation of the MPM computational cycle and have not been extended for higher order IGA-MPM frameworks. The $\bar{F}$ volumetric smoothing algorithm has been recently considered for use with B-splines and IGA [174], however, its effectiveness has not been fully assessed for large boundary value problems. Note that reduced integration is not a viable option as it accumulates significant integration errors in higher-order frameworks, rendering the simulation unstable. Although $\bar{F}$ is gaining popularity in MPM, a large degree of volumetric locking instabilities still exists in the solution, and more research is needed in this regard. [184] discussed the need for further stress and strain smoothing in addition to the $\bar{F}$ smoothing, which can exponentially increase the computational cost of MPM. Based on the authors' experience, $\bar{F}$ is seen to be unstable when used with the 2-phase formulation, resulting in smeared pore water pressure distributions extending beyond the phreatic surface. As such, in this paper, we adopt a simple strain smoothing algorithm on a higher-order grid to average the volumetric strains while keeping the deviatoric strain unchanged. The algorithm requires minimal modification of the MPM computational cycle, with no additional user inputs required. [188] adopted a strain and stress smoothing algorithm on a lower-order mesh when simulating free-surface flows to simulate history-independent materials. In this work, we avoid smoothing stresses and state variables to ensure the accurate simulation of nonlinear history-dependent materials.

The algorithm employed herein is based on decomposing the infinitesimal strains into a

volumetric and a deviatoric portion, whereby only the volumetric strains are smoothed [198]. First, the MP volumetric strains, $\Delta\varepsilon^{k+1}_{Vol,MP}$, are mapped to the background grid to obtain an averaged strain field at the nodes, $\Delta\varepsilon^{k+1}_{Vol,i}$ (Equation 5.5).

$$\Delta\varepsilon^{k+1}_{Vol,i} = \frac{\sum_{MP=1}^{n_{MP}} N_i V_{MP}(\Delta\varepsilon^{k+1}_{Vol,MP})}{\sum_{MP=1}^{n_{MP}} N_i V_{MP}} \tag{4.10}$$

Second, a smoothed MP volumetric strain, $\Delta\hat{\varepsilon}^{k+1}_{Vol,MP}$, is obtained as the averaged nodal strain field is remapped back to the MPs (Equation 5.6). Third, the updated infinitesimal MP strain, $\Delta\hat{\vec{\varepsilon}}^{k+1}_{MP}$, is calculated (Equation 4.12), where smoothed $\Delta\hat{\varepsilon}^{k+1}_{Vol,MP}$ is added to the trace of the unchanged deviatoric infinitesimal strain, $\vec{\varepsilon}^{k+1}_{Dev,MP}$.

$$\Delta\hat{\varepsilon}^{k+1}_{Vol,MP} = \sum_{i=1}^{n_{el}} N_i \Delta\varepsilon^{k+1}_{Vol,i} \tag{4.11}$$

$$\Delta\hat{\vec{\varepsilon}}^{k+1}_{MP} = \Delta\vec{\varepsilon}^{k+1}_{Dev,MP} + \Delta\hat{\varepsilon}^{k+1}_{Vol,MP}\vec{I} \tag{4.12}$$

The updated $\Delta\hat{\vec{\varepsilon}}^{k+1}_{MP}$ value is used in the subsequent constitutive model calculation to obtain the updated stress. The remaining MPM computational cycle remains unchanged. This process can be extended to an arbitrary number of velocity fields to calculate the strain of each phase in the porous media. In the case of the 2-phase formulation used in this paper, the strain smoothing algorithm is also used to stabilize the water strain field.

4.4 Comparative assessment on the effect of cell crossing in higher order B-spline MPM

In this section, we present a series of verification problems used to investigate numerical convergence with respect to mesh size (h) and B-spline order (p) refinement. The benchmark problems presented herein are common examples of dynamic problems that capture aspects that are important to geotechnics. This includes pressure wave propagation and gravity stress initialization. The aim is to investigate the stability of the B-spline framework for simple problems with large deformations. Volumetric locking is not considered in this section as the material behavior is restricted to compressible linear-elastic behavior. As such, the strain smoothing algorithm is not activated in this section.

4.4.1 Pressure wave propagation

Wave propagation is a dynamic problem that is necessary to simulate the deformation of a solid with time while capturing details such as the wave arrival time, stress amplitude, and resulting large-strain displacement. This has been investigated using lower-order interpolation functions at small-strain [120, 202]. In this section, the aim is to comparatively assess the effect of the interpolation function order (i.e., p-refinement) on the solid response due to a pressure wave induced by a traction boundary condition. The normal traction is applied on top of a 1D 1 m column with a fixed end. Note that this is a 2D MPM simulation, which is made 1D through the assignment of boundary conditions to be consistent with the analytical solution. The column is one element wide with a fixed base and rollers on the lateral edges. Specifically, the response is observed at three locations, namely, top, middle, and bottom MPs. The column has a density, ρ=2000 kPa, and is characterized by

linear-elastic behavior with Young's modulus, E=1000 kPa, and Poisson ratio, ν=0. The column is finely discretized with 50 elements, corresponding to a mesh size of 2 cm, with each element having 3 MPs in each direction. A vertical traction is applied at the top of the column. This boundary condition is carried by the row of MPs closest to the top edge, and their stresses are mapped to the nodes within the element, not just the upper column boundary.

Two values of traction are considered, with the goal of assessing the effect of cell-crossing error on the results. First, the traction is set to 1 kPa to induce small deformations and ensure no cell crossing. Subsequently, the simulation is rerun with an increased traction of 500 kPa to induce larger deformations.

The results from the first model, i.e., with no cell crossing, are shown in Figure 4.2. The stress and displacement numerical results are consistent with the small-strain analytical solution across the different interpolation function orders. The arrival time is correctly captured, as well as the reflection and the superimposition of the pressure wave over time. At small strains, the linear, quadratic, and cubic interpolation functions provide similar results. Note that in all cases, the numerical solution experiences numerical oscillations. These oscillations are not related to cell-crossing noise but to the limitations of the time integration scheme and the application of the traction boundary condition. The explicit Euler-Cromer time integration amplifies spurious high-frequency noise and hinders its capability to simulate wave propagation [202, 203]. In addition, the application of traction (Neumann) boundary condition on the MPs can introduce errors in the surface stress distribution and subsequent propagation [204].

The results of the models with larger traction values (i.e., 500 kPa in Figure 4.3), show that when using the linear interpolation (equivalent to conventional MPM), the stress response is highly unstable (Figure 4.3(a)) as a result of the cell-crossing noise. The displacement

deviates from the analytical solution as the time evolves and traction increases, resulting in a displacement drift (Figure 4.3(d)). Quadratic and cubic interpolation functions exhibit significantly superior stability. In general, pressure waves are consistent with the analytical solution when traction is equal to 500 kPa (Figures 4.3(b) and 4.3(c)). A small displacement phase drift starts to manifest with time at large strains (Figure 4.3(e) and 4.3(f)). This is a limitation of the small-strain analytical solution, which does not reflect dynamic changes in the column height over time. Overall, this example illustrates that higher-order interpolation functions are necessary for large deformation dynamic problems due to the cell-crossing instabilities seen when using linear interpolation functions, which destroy the stress solution.

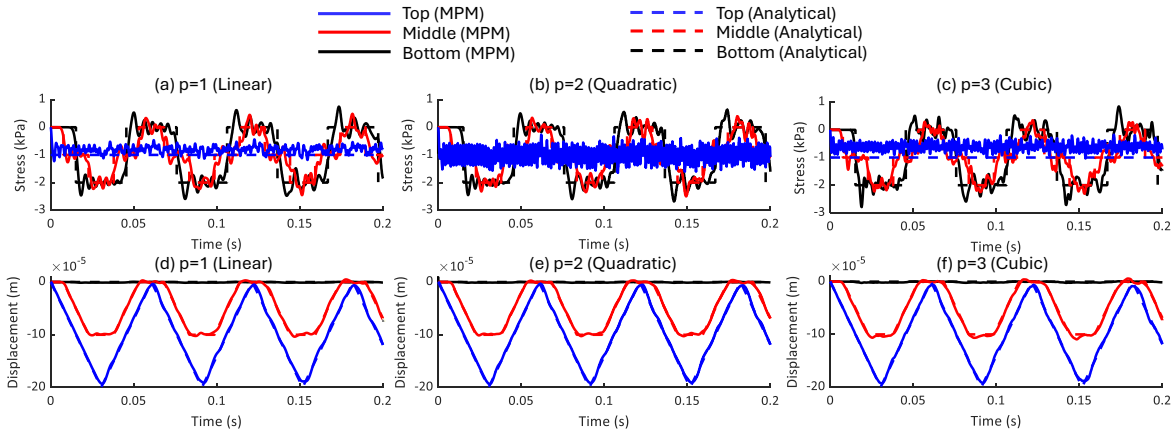

Figure 4.2: Small-strain response due to a pressure wave propagation under a traction of 1 kPa. (a)-(c) Stress response using linear, quadratic, and cubic interpolation functions, respectively. (d)-(f) Displacement response using linear, quadratic, and cubic interpolation functions, respectively.

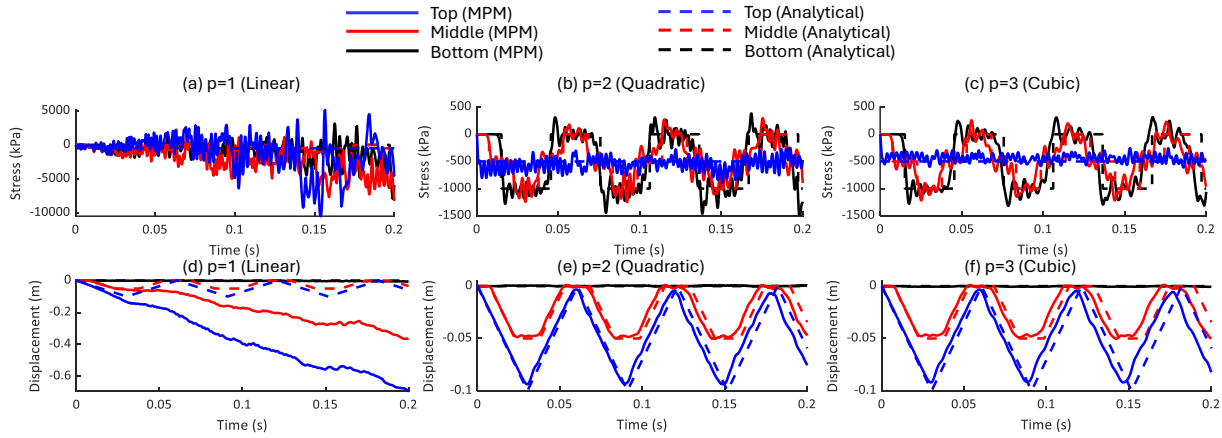

Figure 4.3: Large-strain response due to a pressure wave propagation under a traction of 500 kPa. (a)-(c) Stress response using linear, quadratic, and cubic interpolation functions, respectively. (d)-(f) Displacement response using linear, quadratic, and cubic interpolation functions, respectively.

4.4.2 Gravity stress generation

Accurate stress generation under gravity is an important benchmark problem in the simulation of history-dependent materials. Specifically, in applications pertaining to geotechnics, the stabilized initial gravity stress generated plays an important role in capturing in-situ stresses, which play a significant role in the subsequent evolution of the stress invariants during large deformations. The aim of this section is to adopt a simple 1D problem to assess the accuracy of gravity stress initialization. The impact of the following is assessed: (i) mesh refinement to assess convergence with mesh size, (ii) p-refinement to assess convergence for quadratic and cubic interpolation functions, (iii) increasing number of MPs to understand the effect of quadrature integration with higher-order integration.

A visco-elastic 2D column with height H_0=0.5m and one element wide is adopted, with Young's modulus, E=100 kPa, Poisson ratio, ν=0, and density, ρ=1000 kg/m^3. The same problem was adopted by [64] and [60] to assess the convergence of DDMP and GIMP varia-

tions, respectively. The boundaries are fully fixed at the base of the column, and the lateral sides are rollers. The visco-elastic relationship is described as shown in Equation 4.13 as a function of vertical strain, ε. The analytical solution for the stress profile of the column is provided in Equation 4.14.

$$\sigma = 2E(1 - e^{-\frac{\varepsilon}{2}}) \tag{4.13}$$

$$\sigma(y) = \rho g H_0 \frac{(1 - \frac{y}{H_0}) + (\frac{\rho g H_0}{2E})(\frac{y}{H_0})}{1 - (\frac{\rho g H_0}{2E})(1 - \frac{\rho g H_0}{2E})(\frac{y}{H_0})} \tag{4.14}$$

The gravitational field, g, is assumed equal to 8 m/s^2 as consistent with the literature for this problem [60, 64]. First, the gravitational acceleration is linearly increased from 0 to $1g$ in 10 s to induce small deformations. Subsequently, the gravity acceleration is increased linearly from $1g$ to $12.5g$ in another 10 s to induce large deformations. Note that no local damping is applied, and the loading is performed slowly in a total of 20 s to ensure a quasistatic solution by the dissipative explicit time scheme.

Figure 4.4 shows the small-strain and large-strain stress profiles for columns at $1g$ and $12.5g$, respectively, for quadratic (a-e) and cubic (f-j) interpolation functions. To better understand the convergence associated with this problem, convergence plots with element size refinement and MPs are shown in Figure 4.5 and 4.6 for quadratic and cubic interpolation functions, respectively, for the large-deformation simulation at $12.5g$. The root mean square error, RMS, is calculated using Equation 4.15 for stress and displacement, where q_{MP} is the value for the MP, q_a is the analytical solution, and q_{max} is the maximum normalizing quantity from the analytical solution.

$$\text{RMS} = \frac{\sqrt{\sum_{MP=1}^{n_{MP}} \frac{(q_{MP}-q_a)^2}{n_{MP}}}}{|q_{max}|} \tag{4.15}$$

The RMS calculation is consistent with [64]. For quadratic interpolation functions, it can be seen that the simulations reduce in error initially with mesh size refinement until the number of elements is equal to 16 (Figure 4.5(a) and 4.5(c)). However, for quadratic functions at greater refinement, the simulations are not fully stable. The numerical solution begins to diverge, indicating that stress oscillations can still occur at large deformations when using quadratic functions. Figure 4.4(d-e) clearly shows an increase in scatter in the numerical solution when using the quadratic interpolation functions at large deformations. In contrast, when using cubic interpolation functions, consistent convergence is observed with superior stability and no evidence of divergence as shown (Figure 4.4 and 4.6 (f-j)). [205] consistently showed that the minimum order to ensure numerical stability is problem dependent in FEM, and is often a function of the smoothness of the interpolation function derivatives. Quadratic interpolation functions have discontinuous piecewise-constant second derivatives. By contrast, cubic interpolation functions provide smoother second derivatives (i.e., linear) which tend to stabilize the simulation further under large deformations. This significantly favors the cubic interpolation functions for simulating large deformations in a stable manner. Despite divergence with mesh refinement for quadratic interpolation functions, reduction in root mean square error is generally observed with increasing number of MPs per element (Figure 4.5(b) and 4.5(d)). This is consistent with the cubic interpolation functions (Figure 4.6(b) and 4.6(d)). This example demonstrates that cubic interpolation functions exhibit more desirable convergence criteria at large deformations, particularly when a fine mesh is required for analysis.

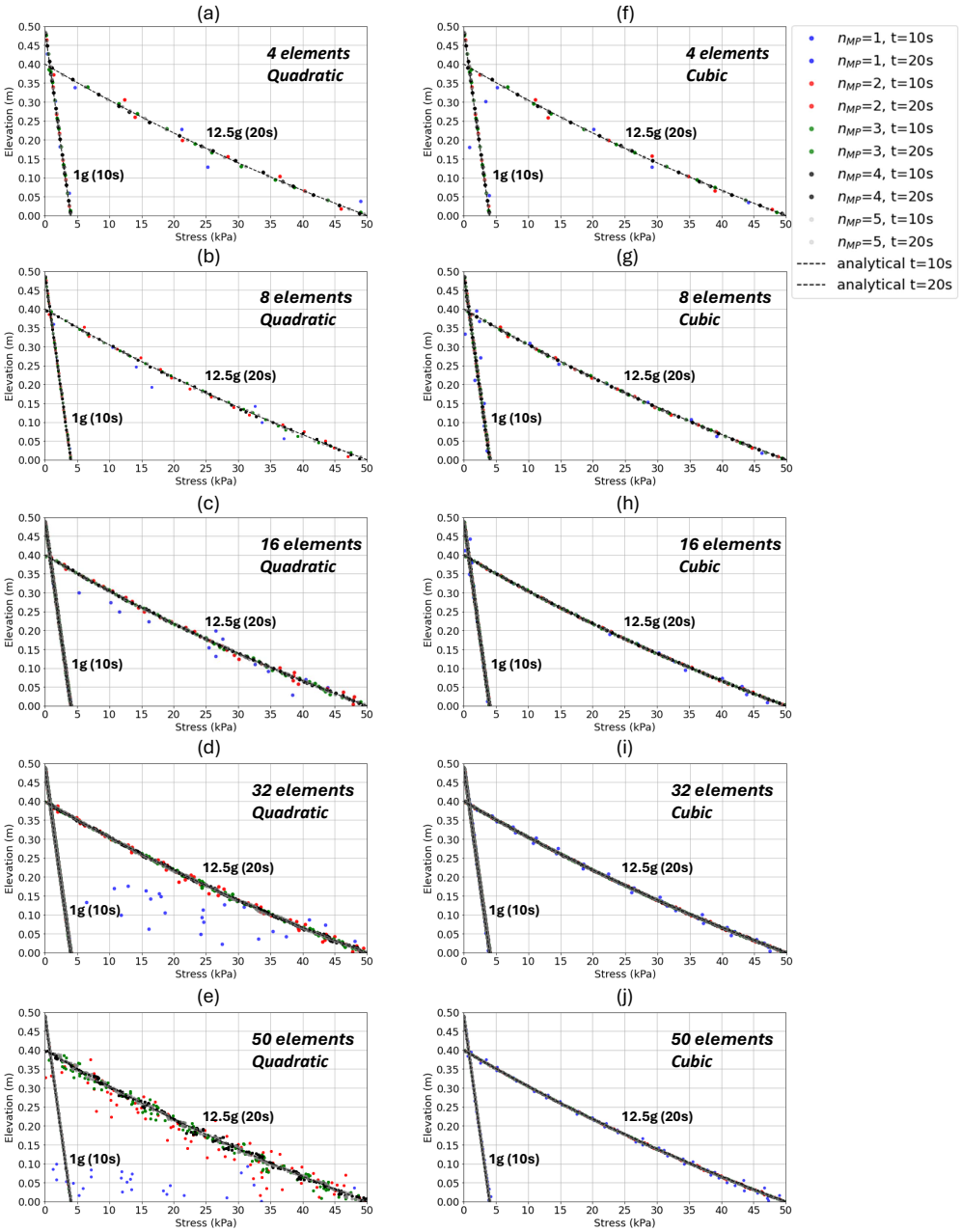

Figure 4.4: Stress versus elevation profile for 0.5 m visco-elastic column considering a quasistatic gravitational field of $1g$ and $12.5g$. Increased mesh size (a)-(e) for quadratic interpolation functions, and (f)-(j) for cubic interpolation functions.

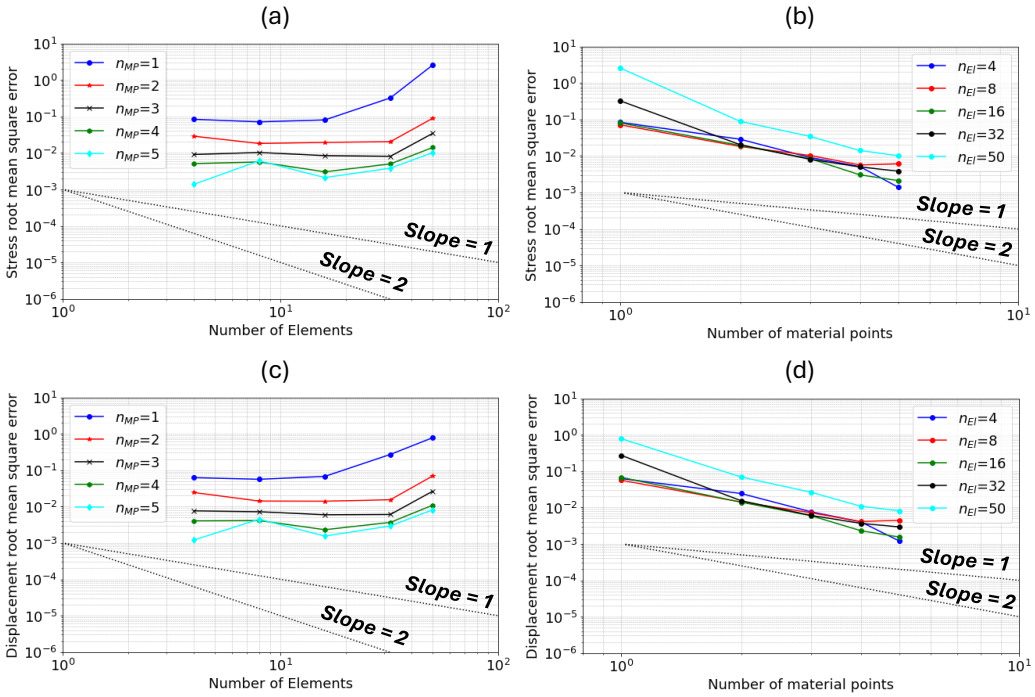

Figure 4.5: Convergence assessment for quadratic interpolation functions. (a) Stress convergence assessment with mesh refinement. (b) Stress convergence assessment with an increasing number of MPs. (c) Displacement convergence assessment with mesh refinement. (d) Displacement convergence assessment with increasing number of MPs.

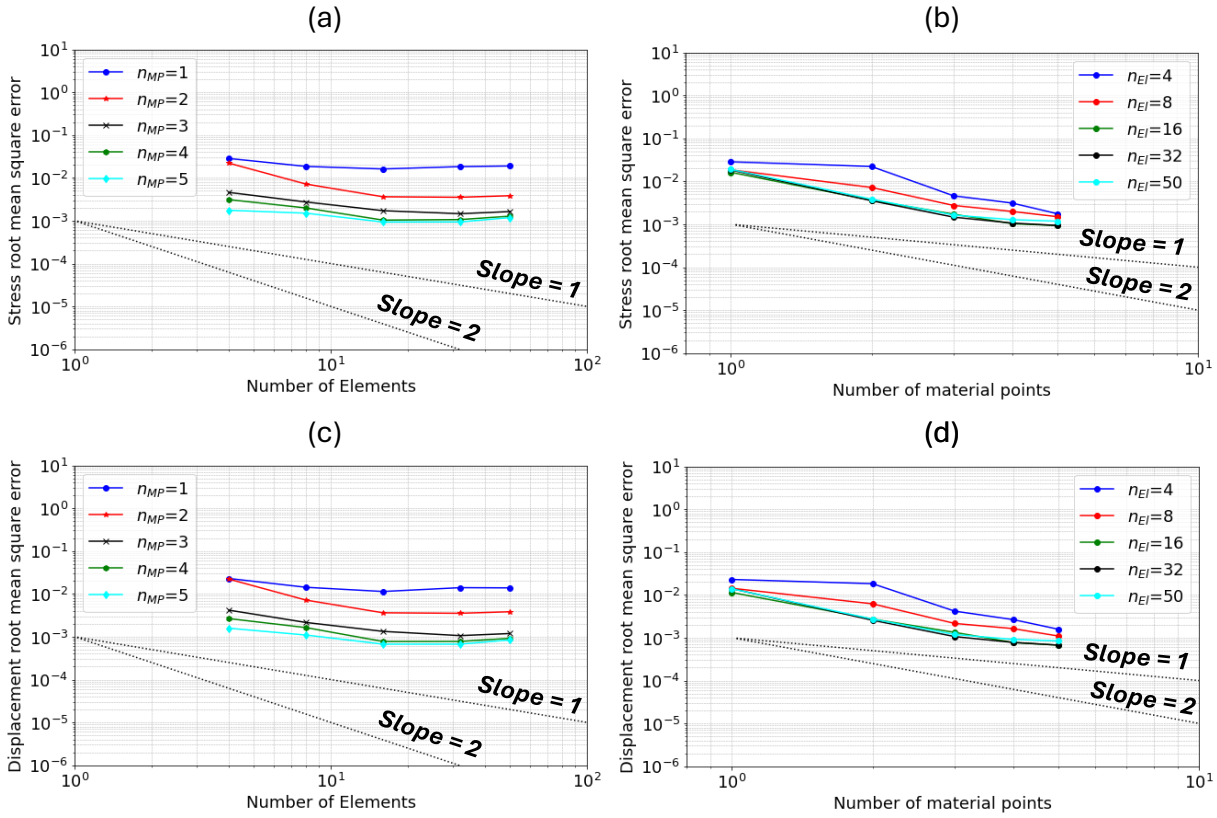

Figure 4.6: Convergence assessment for cubic interpolation functions. (a) Stress convergence assessment with mesh refinement. (b) Stress convergence assessment with an increasing number of MPs. (c) Displacement convergence assessment with mesh refinement. (d) Displacement convergence assessment with an increasing number of MPs.

4.5 Isogeometric analysis using NURBS for complex circular geometries

In this section, the capability of the IGA-MPM framework in capturing large deformations in complex circular geometries is explored. The accurate definition of circular geometries is possible in IGA using nodal non-unitary weight values. If the geometry becomes more complex, multipatches are required. Two 3D examples are provided herein. First, an axial

compression of a 10 m cylinder with a thickness of 1 m is investigated using four patches to validate the multipatch implementation. The cylinder deformation occurs in a direction that is perpendicular to the discontinuities in the multipatch discretization. As such, no inter-patch cell crossing occurs in this benchmark problem. Second, a single patch example of a 5 m internal pressurization of a cylinder with a thin wall thickness of 1 cm is investigated. This problem has an analytical solution, which is used for comparison. The behavior of the cylinder is investigated under mesh refinement in the longitudinal direction along its height, with the goal of achieving numerical stability. Note that a 2D example of a quadrant compression under gravity is presented in Section 4.2 in the supplementary document [192] to assess the plane-strain implementation of NURBS. The stress profile of the quadrant is qualitatively investigated under different mesh refinements.

4.5.1 Axial compression of a cylinder under gravity with no inter-patch MP crossing

A cylinder of outer radius of 3 m, height of 10 m, and thickness of 1 m, is discretized into 4 patches with each patch further discretized into 10 by 10 elements in the transverse, ξ and η directions, and 10 elements in the longitudinal, ζ direction. This is a simple simulation that assesses the multipatch framework. Cubic interpolation functions are used in this example. The cylinder is assumed to be linear-elastic with Young's modulus, E=1000 kPa, Poisson ratio, ν=0.2, and density, ρ=1000 kg/m^3. Each element is filled with 2 MPs per coordinate direction per element. For the very first time, the IGA-MPM framework is tested in a multipatch discretization.

The gravitational field is applied in the longitudinal direction to cause deformation along the height of the cylinder with no inter-patch cell crossing. The base is fully fixed, and the

outer sides are normally fixed (i.e., rollers). As such, lateral displacements are not allowed along the outer circular surface, and an increase of stresses across the internal circular surface is expected. The gravitational field increases linearly from 0 to $1g$, and then to $5.625g$ to ultimately cause a vertical strain of 20%. Figures 4.7 and 4.8 show the x and z-direction stress components, respectively, for $1g$ and $5.625g$. Smooth stress profiles are visually observed in the stress field, which scales linearly with an increase in the gravitational acceleration. Z-direction stress distribution is plotted against elevation in Figure 4.9. A linear line of best fit is generated for the numerical results to facilitate observation of oscillations, with a quoted R^2 value in the legend indicating the quality of the fit. As the cylinder compresses under gravity, it is allowed to laterally increase in thickness. However, the analytical 1D solution is used for reference to compare the values of the expected stress only at the base of the cylinder. At gravitational accelerations of $1g$ and $3g$, the stress distributions are linear to ultimately match the analytical basal stress value with minor oscillations. At larger acceleration fields of $5.625g$, more stress oscillations manifest, most likely due to quadrature errors, but the match remains reasonable. Note that quadrature integration is challenging in the IGA-MPM at large strains. This is consistent with efforts in the literature to perform more accurate integration when conducting NURBS-based IGA analyses [179, 206, 207], which should be further explored to improve IGA-MPM.

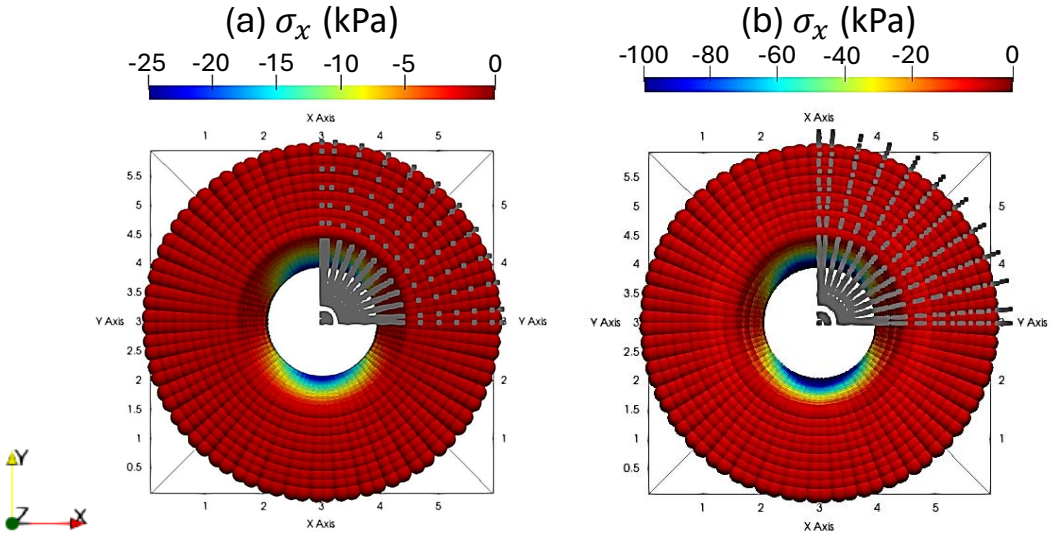

Figure 4.7: Stress component in the x-direction under (a) $1g$ and (b) $5.625g$.

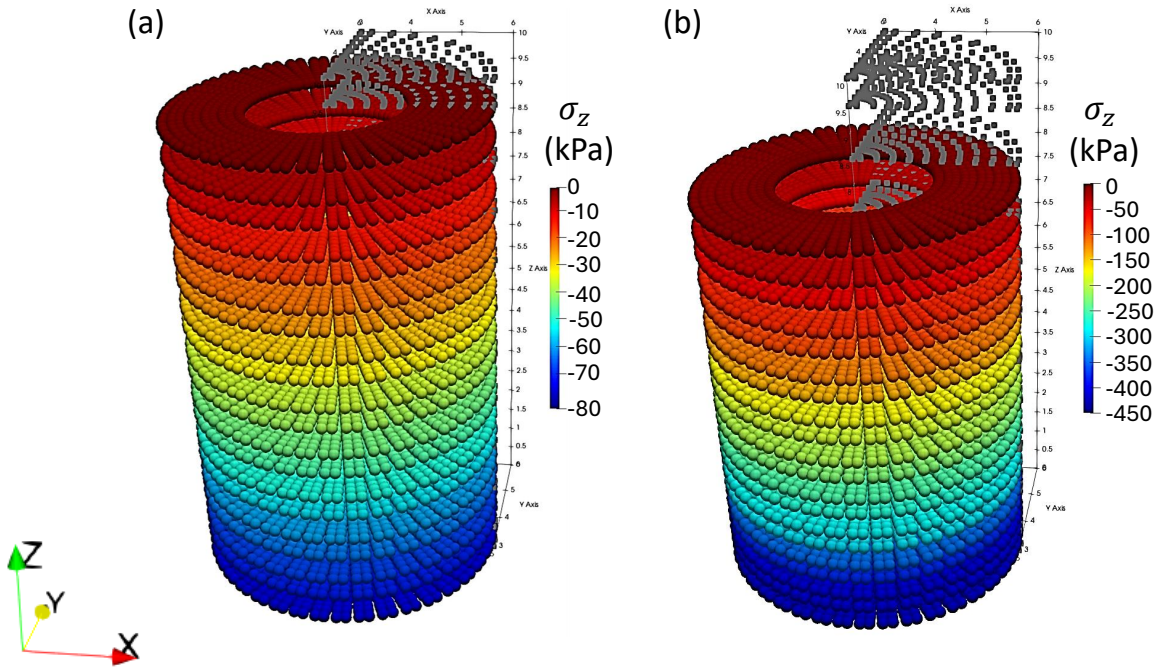

Figure 4.8: Stress component in the z-direction under (a) $1g$ and (b) $5.625g$.

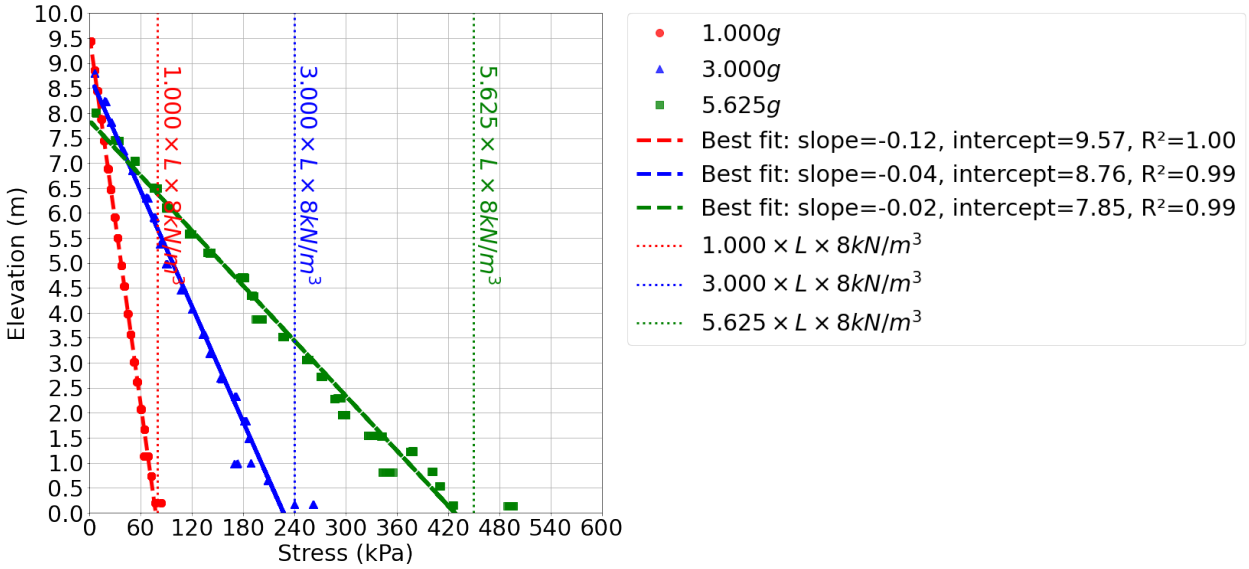

Figure 4.9: Elevation versus stress component in the z-direction.

4.5.2 Internal pressurization of a thin cylinder with fixed ends

The simulation of thin-walled structures is notoriously challenging because of their sensitivity to imperfections. Their analysis combines complex geometries and boundary condition applications that require capturing geometrical non-linearities. Applications pertinent to thin-walled structures are present in geotechnical engineering. In particular, the large-strain simulation of tunnel linings and sheet piles is very challenging in MPM due to the inability to maintain simulation stability (e.g., spurious MP separation) and the application of boundary condition on moving materials. Most MPM simulations often neglect geometrical complexities or are often performed in lower-order frameworks (e.g., [208, 209]). The analytical solution for the internal pressurization of a shell cylinder was presented by [210] under plane-stress conditions. The analytical solution was modified by [193] to capture the fixed boundary conditions at both longitudinal ends. The displacement analytical solution, u, as a function of the vertical global coordinate, z, is presented in Equation 4.16. The

displacement, u, is a function of the applied internal load, P, midplane radius, R, length, L, thickness, t, Young's modulus, E, and Poisson ratio, ν. The calculation of the internal parameters $(C_1, C_2, \beta, \alpha, \tilde{E}, \tilde{\nu}, D)$ is also presented in Equation 4.16 as per shell theory.

Single-patch 3D IGA-MPM simulations are performed using cubic interpolation functions to simulate the deformation of the thin cylinder. The goal is to understand the efficacy of the IGA-MPM framework in capturing the displacements of complex thin-walled structures. The material is assumed to be a solid linear-elastic material with no consideration of shell theory in the numerical simulation. The geometry and material adopted herein are consistent with [193], with R=1 m, t=0.01 m, L=5 m, E=1000 kPa, and ν=0.3. The density, ρ, is assumed as 1000 kg/m^3. The cylinder is discretized into 40 elements in the ξ direction and 10 elements in the η direction to define the transverse circular cross-section. The background mesh is generated for a 40 cm thick cylinder that is only partially filled with MPs to create the 1 cm thin cylinder geometry. The elements are filled with 3 MPs per direction per element. A load of up to P=10 kPa is considered. The traction is applied at the MPs on the inner surface of the cylinder to ensure continuous contact of the traction with the material. The traction direction is established at the beginning of the simulation in a direction normal to the cylinder. The traction is then mapped from the inner surface MPs to the nodes in each time step. Mesh size refinement is considered here to achieve numerical stability for the IGA-MPM model and prevent numerical fracture that occurs in the shear zones close to the ends of the cylinder. The discretization is refined in the direction corresponding to the cylinder height by reducing the knot spacing in that parametric direction. The pre-processor modifies the control net (i.e., computational mesh) according to the refined knot vector. Note that increasing the number of MPs per element is avoided as the Newton iterations to find the local position in the parent space become more computationally expensive and need refinement for faster convergence with IGA-MPM simulations (see Section 3 in the

supplementary document [192]).

Figure 4.10 presents contour plots of the stress magnitude of the cylinder simulations under various discretizations in the longitudinal ζ direction (i.e., 10, 20, and 40 elements). The nodes used for the calculation are also presented with each contour plot. The load, P, is increased from 0 to 10 kPa in 10 seconds. Approaching towards P=7 kPa, the contour plots present similar stress and displacement profiles for the various longitudinal refinements as shown in Figure 4.10(a-c). However, for P >7 kPa, it is seen that the numerical results are only stable for the fine mesh discretization of 40 elements (Figure 4.10(f, j, m)). Numerical separation of the MPs is seen at the shear zones near the fixed ends for the coarse and medium mesh discretizations (Figure 4.10(k, l)). When numerical separation occurs, the application of the traction mapping becomes erroneous as it is linked to the MP deformation.

The radial displacements for all the MPs in the simulation using the fine mesh are presented in Figure 4.11. The displacement magnitude is reasonably captured using the numerical simulations. However, discrepancies are observed near the fixed ends. This is attributed to limitations linked to the fixed traction vector in the normal radial direction. In addition, it is observed that the match with the analytical solution at the fixed ends decreases as the load increases. The traction is strongly enforced at the start of the simulation. However, the boundary conditions become weakly enforced because the traction is remapped between the MPs and the nodes in each step. It is acknowledged that MPM can have limitations when surface definition is needed. However, this field of non-conforming boundary conditions is ever growing in MPM (e.g., [211]), which can further improve the IGA-MPM simulation of cylindrical shells for future consideration.

$$
\begin{cases}
u(z) = -\dfrac{PR^2}{\tilde{E}t}\big(1 - C_1 \sin(\beta z)\sinh(\beta z) - C_2 \cos(\beta z)\cosh(\beta z)\big) \\
\quad z \in \left(-\dfrac{L}{2}, \dfrac{L}{2}\right) \\
\quad C_1 = \dfrac{\sin(\alpha)\cosh(\alpha) - \cos(\alpha)\sinh(\alpha)}{\sinh(\alpha)\cosh(\alpha) + \sin(\alpha)\cos(\alpha)} \\
\quad C_2 = \dfrac{\cos(\alpha)\sinh(\alpha) + \sin(\alpha)\cosh(\alpha)}{\sinh(\alpha)\cosh(\alpha) + \sin(\alpha)\cos(\alpha)} \\
\quad \beta = \left(\dfrac{\tilde{E}t}{4R^2 D}\right)^{\frac{1}{4}} \\
\quad \alpha = \dfrac{\beta L}{2} \\
\quad \tilde{E} = \dfrac{E}{1-\nu^2} \\
\quad \tilde{\nu} = \dfrac{\nu}{1-\nu} \\
\quad D = \dfrac{\tilde{E}t^2}{12(1-\tilde{\nu}^3)}
\end{cases}
\tag{4.16}
$$

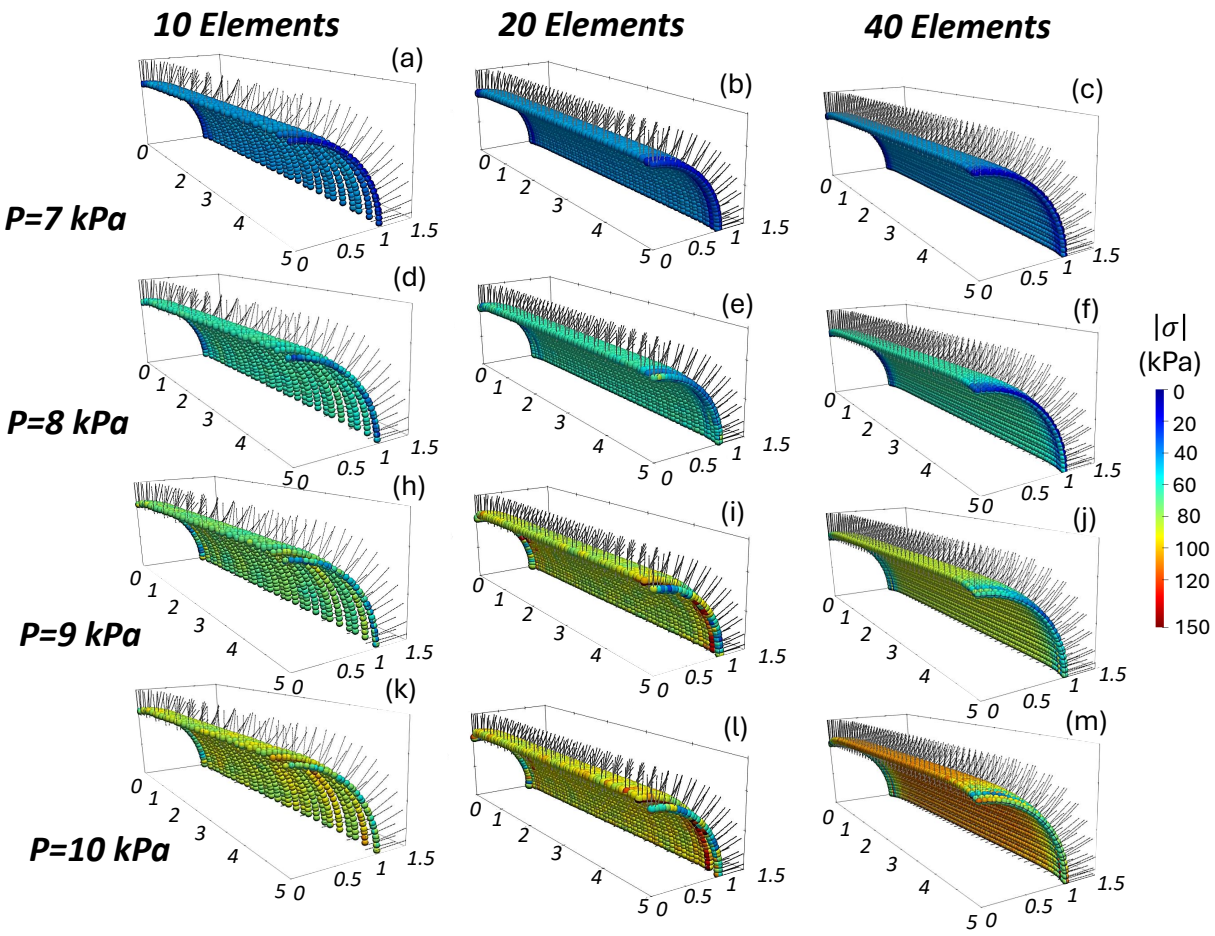

Figure 4.10: Stress magnitude profiles for increasing applied internal traction for different longitudinal refinements for loads $7 \leq P \leq 10$ kPa.

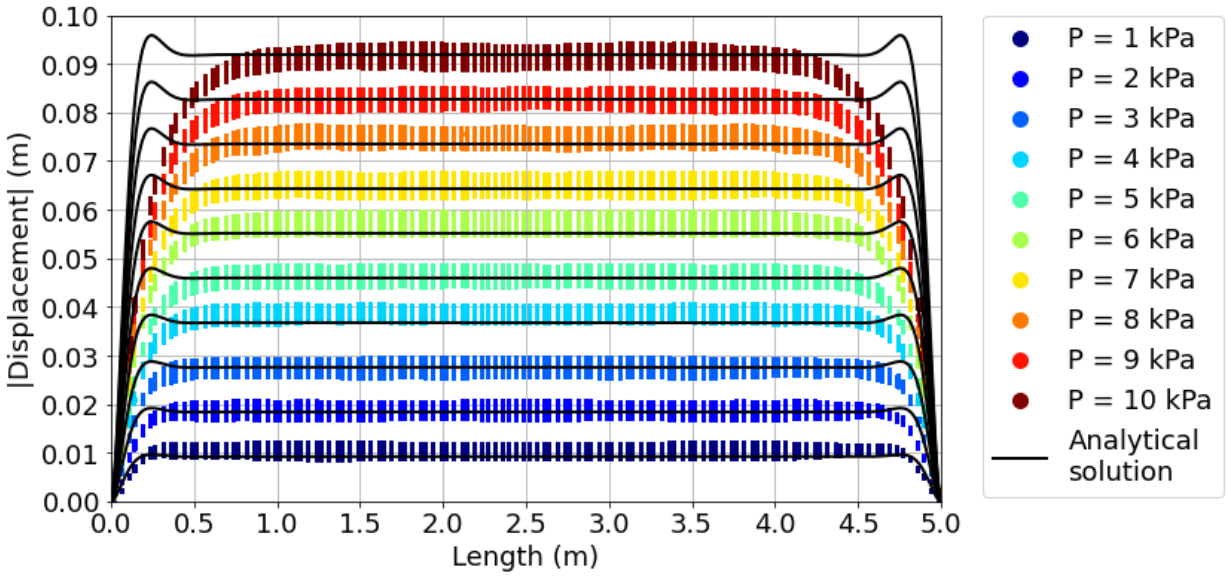

Figure 4.11: Comparison of the radial (x and y) displacement magnitude profiles using 40 elements in the longitudinal direction with the analytical solution from shell theory. Data points represent the numerical solution from the all the MPs, and solid lines represent the analytical solution at the corresponding load, P, value.

4.6 Multipatch analysis of a footing penetrating nearly incompressible elastoplastic material

A footing penetration problem is considered herein as a practical example that incorporates inter-patch cell crossing, near incompressibility, and elastoplasticity. Two patches are considered, whereby footing MPs are placed in the moving patch and the soil MPs are initially placed in the compressing patch. The moving patch follows the movement of the linear-elastic footing to compress the patch as it penetrates the elastoplastic soil layer. The MPs of the footing are given a prescribed velocity, which is maintained throughout the calculation. As such, the footing behaves as a rigid body. As the penetration occurs, soil MPs move from one patch to the other. Geostatic stresses are initialized in the soil material based on the K_0

procedure. The use of multipatches offers easy integration to obtain the reaction force for verification. This problem is often simulated without including the footing material. This eliminates soil-structure interaction considerations by means of a nodal prescribed velocity boundary condition (e.g., [184]). The multipatch framework herein opens up the opportunity to simulate penetration with minimal cell-crossing error while using non-linear constitutive models. Generally speaking, there is more flexibility in multipatch IGA-MPM in defining empty spaces for materials to deform into as the user can theoretically control the geometry of each patch. However, careful consideration of the geometry transitions and some degree of conformity is usually necessary to ensure theoretical numerical stability in IGA-MPM. Cell-crossing noise is incurred only when the MPs cross from one patch to another. The efficacy of the strain smoothing algorithm is also assessed herein.

Two examples build up in complexity as follows. First, a 2D plane-strain geometry is adopted to verify the multipatch MPM framework with inter-patch cell crossing. This problem is performed in total stress with near incompressibility enforced through a Poisson ratio approaching 0.5. The potential manifestation of errors due to the discontinuity line in the interpolation function derivatives between patches is investigated. To the authors' knowledge, this is the first time that multipatch IGA-MPM has been verified in a real-scale geotechnical example. Second, the numerical framework is deployed in a 3D parametric analysis of the footing problem. The scope of the parametric analysis covers studying the effect of near incompressibility, strain softening, and footing shape. Despite the adoption of a theoretical geometry, the examples in this section highlight the framework's behavior from a practical perspective, incorporating large deformation penetration and consolidation effects.

4.6.1 Plane-strain strip footing penetrating nearly incompressible elastoplastic soil in total stress

The 2D plane-strain problem considered herein is simulated using quadratic and cubic interpolation functions to investigate the stability of the MPs that cross from one patch to another. The cubic background mesh, MP geometry, and the stress initialization are presented in Figure 4.12, where two patches are used. The width of the footing considered is B=4 m, although only half of the problem is simulated as per the line of symmetry. The univariate interpolation functions, N, and corresponding derivatives, $\tilde{N}=\frac{dN}{d\xi}$, in the parameter domain are shown for each patch. Note that the same knot vectors are used for both patches in the global x-direction, which also coincides herein with the ξ-direction in the parameter domain. Different knot vectors are used for the y-direction, albeit the same element sizes are maintained in the physical domain (i.e., 60 elements in the x-direction for moving and compressing patches, and 12 and 40 elements are used in the y-direction). Each element is filled with 4 MPs initialized at their corresponding Gaussian locations. The simulation has 9,728 MPs in total.

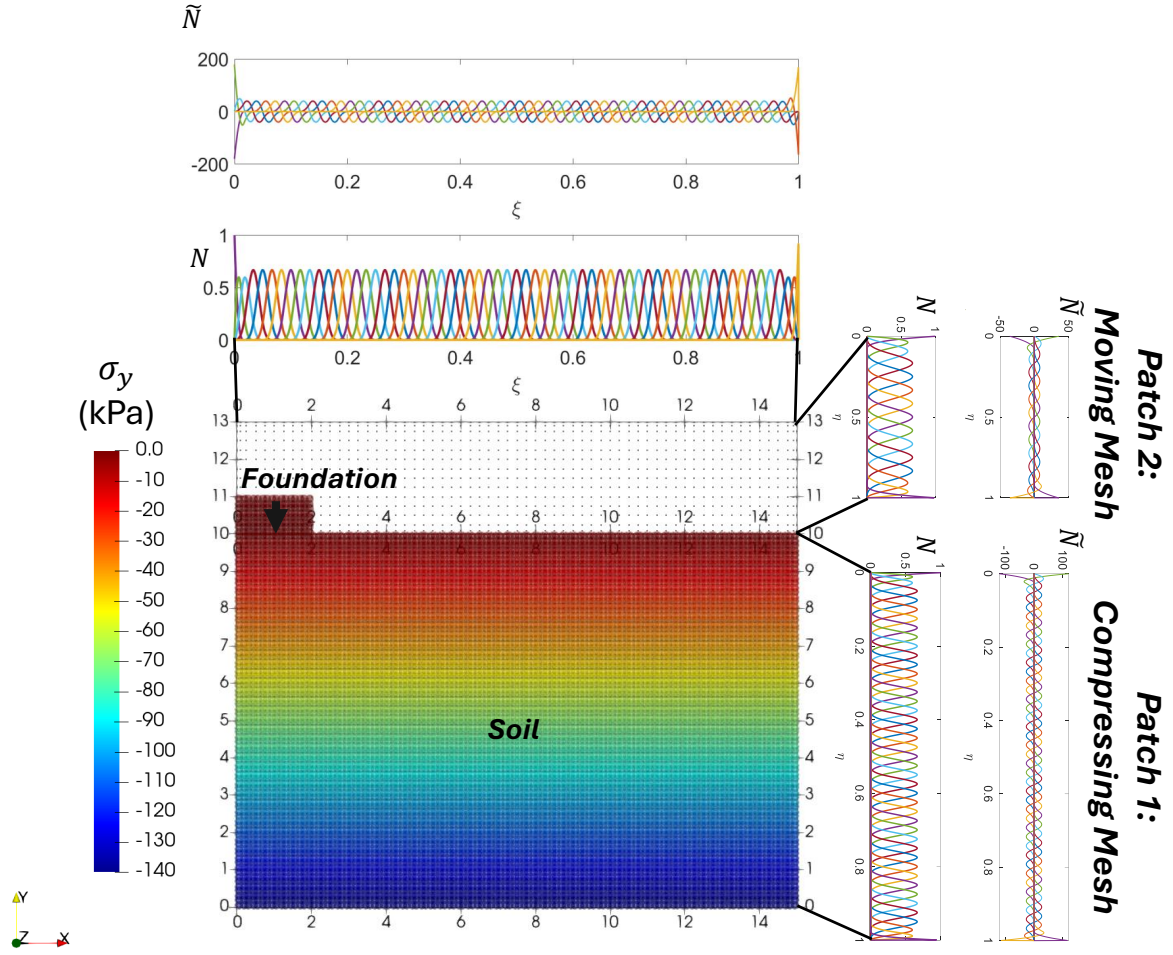

Figure 4.12: Multipatch discretization of a linear-elastic footing penetrating into undrained elastoplastic soil, considering two patches (moving and compressing patch). Quasistatic gravity initialization stresses are generated prior to footing penetration, where the vertical component is shown in the figure.

The penetration velocity of the footing is 2 cm/s. Geostatic stress initialization is assumed to correspond to a lateral pressure coefficient, K_0, of 0.5 and g=9.81 m/s^2 with zero static shear stresses. The soil material is assumed undrained through a non-associative Tresca constitutive model. No softening law is considered herein to stay consistent with the assumptions of the theoretical Prandtl limit of 2+π from plasticity theory [212]. The constitutive model is equipped with a Modified-Euler strain substepping scheme with an automatic local error

control [213]. The material parameters are density, ρ=1400 kg/m^3, elastic shear modulus, G=9 MPa, Poisson ratio, ν=0.499, dilation angle, ψ=0, and undrained shear strength, S_u=50 kPa. The footing material is linear-elastic with G=20 MPa and ν=0. However, due to the moving mesh setup, the footing is considered a rigid body as the prescribed velocity is overwritten for those MPs.

Figures 4.13 present the results of the 2D footing penetration problem for penetration distance, d, of 0.5 m, respectively, in terms of contour plots of mean stresses, $\bar{\sigma}$, plastic deviatoric strain, γ_d , and displacement magnitude, $|u|$. Specifically, sub-figures (a,b) and (c,d) present the results without and with strain smoothing, respectively. For the non-smoothed results, it is observed that cubic interpolation functions (Figure 4.13(b-i)) present a more stable stress distribution compared to the quadratic counterpart (Figure 4.13(a-i)) for the MPs that cross from one patch to another. This specifically manifests in a spurious discontinuity in the developed shear band (Figure 4.13(a-ii)). Although improved when using cubic interpolation functions (Figure 4.13(b-ii)), the stress distribution is 'checkerboarded' with spurious zones across the failure shear band. The displacement predictions are consistent for quadratic and cubic interpolation functions. These oscillations can be attributed to volumetric locking.

When using strain smoothing with quadratic and cubic functions, the shear bands are thinner with clear separation into the triangular zones and the theoretical log-spiral curve adopted in plastic limit analyses by [212] and Terzaghi [214] (Figures 4.13(c-ii) and 4.13(d-ii) for cubic and quadratic interpolation functions, respectively). It is noted that the quadratic interpolation functions can manifest some oscillations as inter-patch cell crossing occurs (Figures 4.13(c-i)). This is significantly alleviated when using cubic interpolation functions. Cubic interpolation functions generate smoother stress profiles during the penetration process at 0.5 m (Figures 4.13(d-i), respectively) than their quadratic counterparts. The contour plots shown herein illustrate that cubic interpolation functions should be used at a minimum to

prevent stress oscillations caused by inter-patch cell crossing.

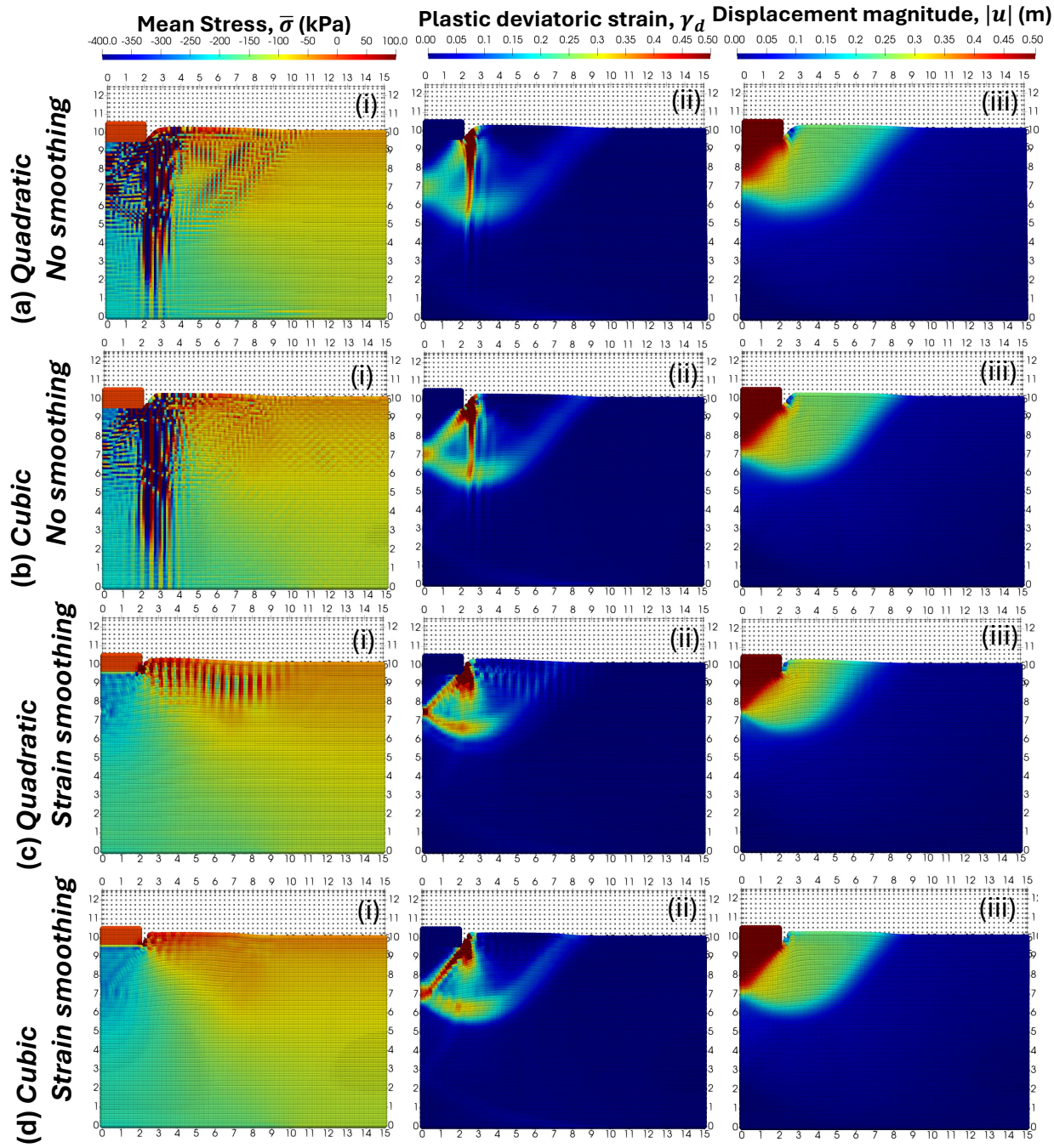

Figure 4.13: Shallow foundation penetration of 0.5 m with contour plots of mean stress, plastic deviatoric strain, and displacement magnitude for various interpolation function orders and smoothing, as follows: (a) Quadratic (without strain smoothing), (b) Cubic (without strain smoothing), (c) Quadratic (with strain smoothing), (d) Cubic (with strain smoothing).

For quantitative verification, the reaction of the soil in contact with the footing is calculated at the inter-patch boundary. This reaction force is equal to the integration of the stresses of the soil MPs at that boundary. Figure 4.14 shows the evolution of the normalized reaction force with penetration distance for the cubic and quadratic interpolation functions, considering strain smoothing. The [212] undrained shear strength theoretical lower limit (also known as the N_c factor in geotechnical engineering) is plotted in the Figure 4.14 for verifying the numerical results. Upon integration to obtain the force, it is observed that the results at the nodal level average out to provide reasonable normalized vertical reaction forces for both cases with and without smoothing as per the [212] theoretical limit. Note that some discrepancy is expected with the theoretical lower limit as the simulations are performed at large strain, which presents a reaction force that is expected to increase with depth, contrary to the analytical solution assumptions [174, 196]. When using quadratic interpolation functions, more spurious spikes are observed in the force solution. This supports the observations seen in the stress contour plots in Figure 4.13.

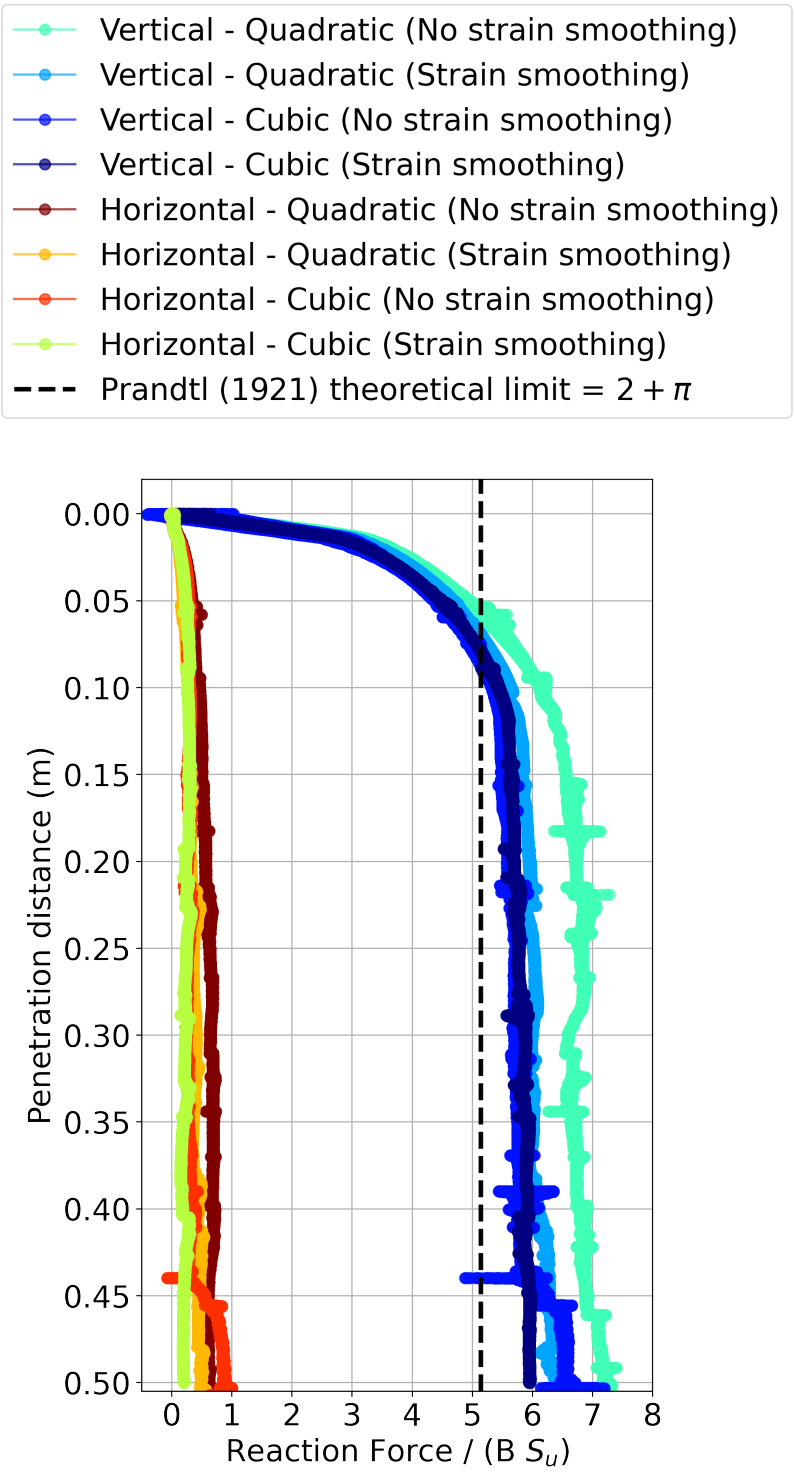

Figure 4.14: Normalized soil reaction force (Tresca model) versus footing penetration distance for different interpolation function orders with and without strain smoothing.

4.6.2 Parametric analysis of 3D footing penetration with emphasis on material behavior and geometry

A 3D analysis is performed to investigate the stability of the higher-order framework with strain smoothing. A footing of width B=2 m is considered with two lines of symmetry. As such, only a quarter of the footing is simulated. The footing penetrates a 5 m by 5 m by 5 m soil cube. Each hexahedron element is filled with 16 MPs, totaling 64,128 MPs in the simulation. Three cases of material behavior are considered to progressively increase the complexity of the constitutive model, ultimately simulating the behavior of brittle soils. Linear-elastic (LE), Tresca, and Tresca with strain-softening (TSS) are considered. An exponential softening law is considered to simulate brittleness through the reduction of the undrained shear strength, S_u, as presented in Equation 4.17.

$$S_u = S_{u,resd} + (S_{u,peak} - S_{u,resd})e^{-\eta\varepsilon^p_{eq}} \tag{4.17}$$

The softening law is a function of peak undrained shear strength, $S_{u,peak}$, residual undrained shear strength, $S_{u,resd}$, softening parameter, η, and the MP cumulative equivalent plastic strain, ε^p_{eq}. A circular footing of the same width is then simulated for the qualitative comparison of the stress profile. Cubic interpolation functions are used throughout the 3D analyses due to their more stable behavior as observed in the 2D version of this example. Material parameters considered are density, ρ=1400 kg/m^3, elastic shear modulus, G=100 kPa, Poisson ratio, ν=0.3 (i.e., compressible), softening parameter, η=100, peak and residual undrained shear strengths, $S_{u,peak}$=50 kPa and $S_{u,resd}$=25 kPa, respectively. The value of G is reduced herein compared to the 2D case to enable an increase in the critical time step, thereby improving computational efficiency and alleviating the additional cost associated with 3D analyses. Cases of incompressibility are considered in the elastic regime by

specifying a Poisson ratio of ν=0.499. Sources of volumetric locking due to elastoplasticity are also explored through the Tresca and TSS models.

First, a base case simulation is considered with a compressible linear-elastic soil behavior being penetrated, with a rectangular footing without strain smoothing. The footing is assumed to be linear-elastic, consistent with the previous 2D footing simulations penetrating at a velocity of 20 cm/s in the z-direction. Geostatic stresses are generated assuming zero lateral deformations using the K_0 procedure with K_0=0.5. Figures 4.15(a(i-v)) and 4.15(b(i-v)) present the stress and displacement results in the z-direction, respectively. The geometry of the soil block during penetration is illustrated, inducing large strains with inter-patch cell crossing. The simulation presents a stable numerical solution, with an increase in stress beneath the footing. The increase in stress tapers gradually to maintain a geostatic profile away from the penetrating footing (Figure 4.15). Consistent with the previous example, the moving mesh technique is successful in enforcing the prescribed velocity boundary conditions at the footing MPs. Additionally, no significant inter-patch cell-crossing oscillations are observed, consistent with the findings in the 2D example.

Second, parametric simulations are performed to analyze the effects of incompressibility, elastoplasticity, and strain softening on the results. The base simulation is repeated with the assignment of ν=0.499 to force near incompressibility. It is observed that the same stress pattern manifests, albeit with larger maximum vertical stress, as shown in Figures 4.16(a)(i-iii), compared to the compressible counterparts in Figures 4.15(a)(i-iii). The stress profile is shown using the Tresca elastoplastic model considering the compressible Poisson ratio without smoothing in Figure 4.16(b) and with strain smoothing in 4.16(c). The strain smoothing algorithm remedies some erroneous stress oscillations across the free surface near the footing. However, the solutions are generally stable without strain smoothing when considering the compressible elastoplastic material, with minor differences in stress distribution

compared to the smoothed solution. When considering the incompressible Poisson ratio with the Tresca model, a bulb-shaped stress concentration is observed under the footing that tapers smoothly away from the free surface. The concentration does not generate a localized slip surface with significant spread across the depth of the soil profile as shown in Figure 4.16(d-iii).

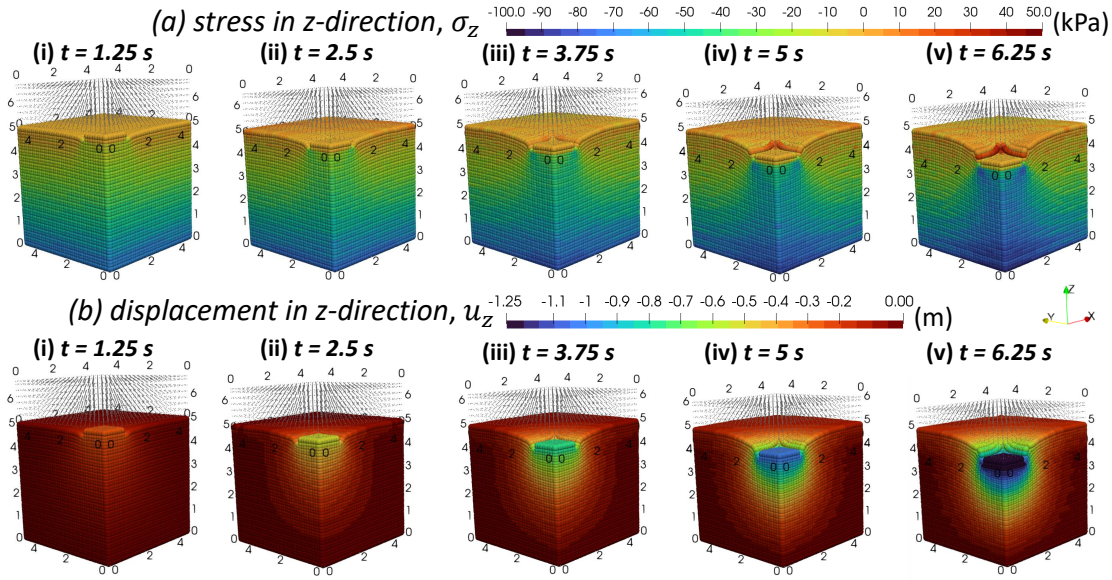

Figure 4.15: Contour plots of (a) stress and (b) displacement in the z-direction parallel to the prescribed velocity vector with magnitude 20 cm/s assuming linear-elastic behavior. The presented evolution corresponds to penetration distances of (i) 0.25 m, (ii) 0.5 m, (iii) 0.75 m, (iv) 1 m, and (v) 1.25 m.

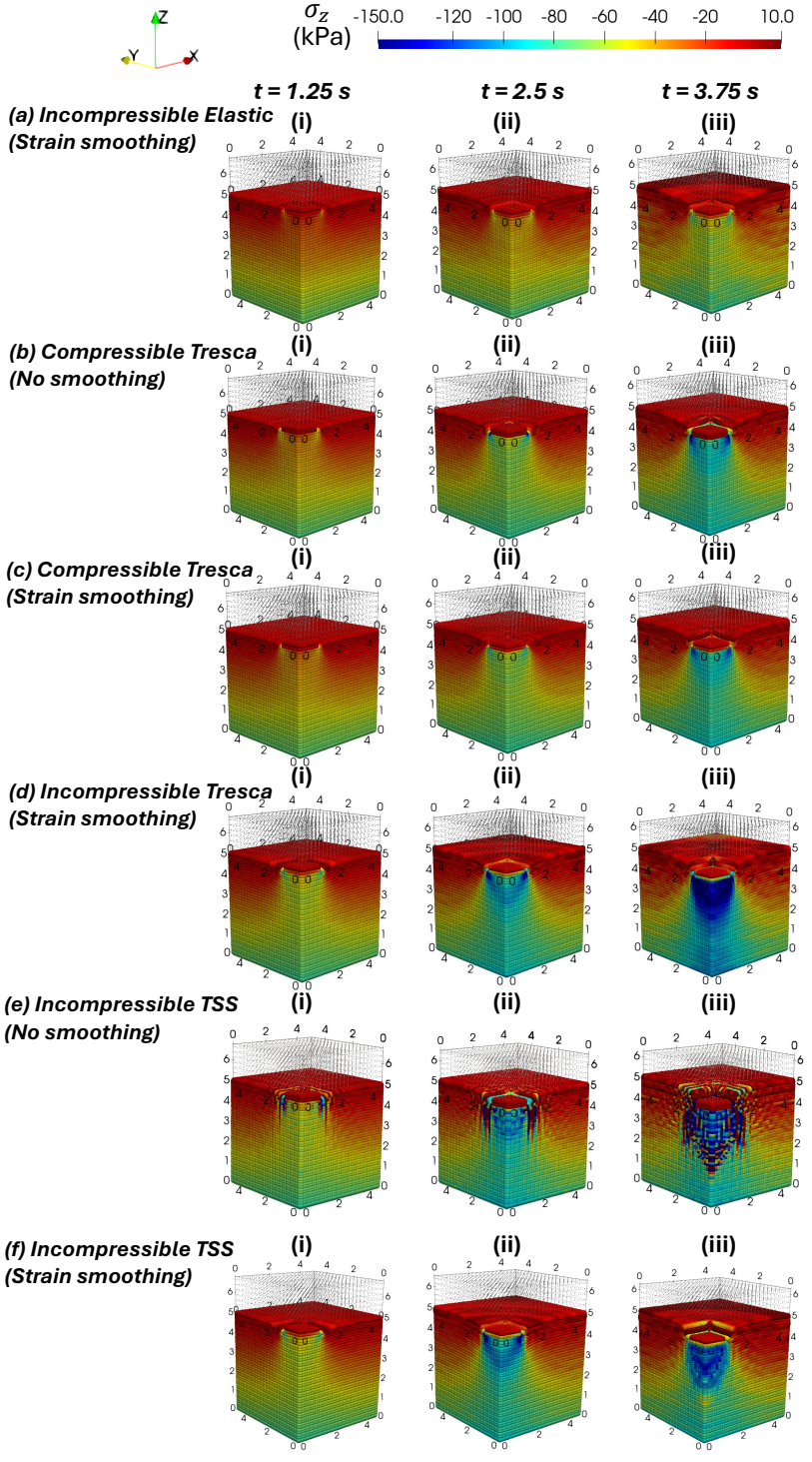

Figure 4.16: Stress contour plots associated with investigating the effect of incompressibility and elastoplasticity on the stability of the numerical solution at penetration depths of (i) 0.25 m, (ii) 0.5 m, and (iii) 0.75 m.

Third, stress oscillations are known to increase when softening constitutive laws are used with a significant increase in the error due to volumetric locking [174]. The aim is to simulate failure that captures the behavior of brittle soils with a localized slip surface using the higher-order framework. The TSS constitutive model is used, which activates the softening law to present progressive failure as the footing penetrates the soil. The mobilized undrained shear strength, S_u, is presented in Figure 4.17, where subfigures (a) and (b) show the failure mechanism without and with strain smoothing, respectively. The failure starts near the footing at the free surface, which propagates progressively to form a well-defined slip surface as shown in Figure 4.17. When using strain smoothing, the thickness of the slip surface is approximately constant across the homogeneous soil profile (Figure 4.17(b-iii)). Irregularities in the failure surface thickness manifest when smoothing is not used (Figure 4.17(a-iii)). The stress profiles for the simulations using TSS are presented without smoothing in Figure 4.16(e) and with strain smoothing in Figure 4.16(f). The irregularities observed in the slip surface when smoothing is not used are due to volumetric locking artifacts, which surround the failed elastoplastic material and the footing edge. The 'checkerboard' stress instability is observed in Figure 4.16(e-iii) when strain smoothing is not used. Stress oscillations associated with volumetric locking are significantly suppressed when the smoothing is activated (Figure 4.16(f-iii)). The stresses of MPs below the footing are plotted to perform a more quantitative comparison (Figure 4.18). In this example, the accumulated cell crossing occurrence (i.e., percentage of MPs moving from compressing patch to moving patch) linearly increases from 0 to 20% at penetration distance of 0.95 m. Specifically, the stresses are seen to exhibit severe drift and oscillation at large strain when no smoothing is performed (Figure 4.18(a)). This specifically occurs as the S_u value of the MP reduces due to softening, which reflects the erroneous stress distribution seen in Figure 4.16(e-iii). If strain smoothing is used, the MPs exhibit a decrease in the stresses associated with activating the softening law beyond failure, which decreases the strength. This confirms that strain smoothing is a viable technique to

generate stable stress distributions when simulating incompressible media using advanced constitutive models. However, other successful volumetric locking techniques should also be considered for use within the IGA-MPM to assess the robustness of the higher-order framework (e.g., [75, 200, 201]).

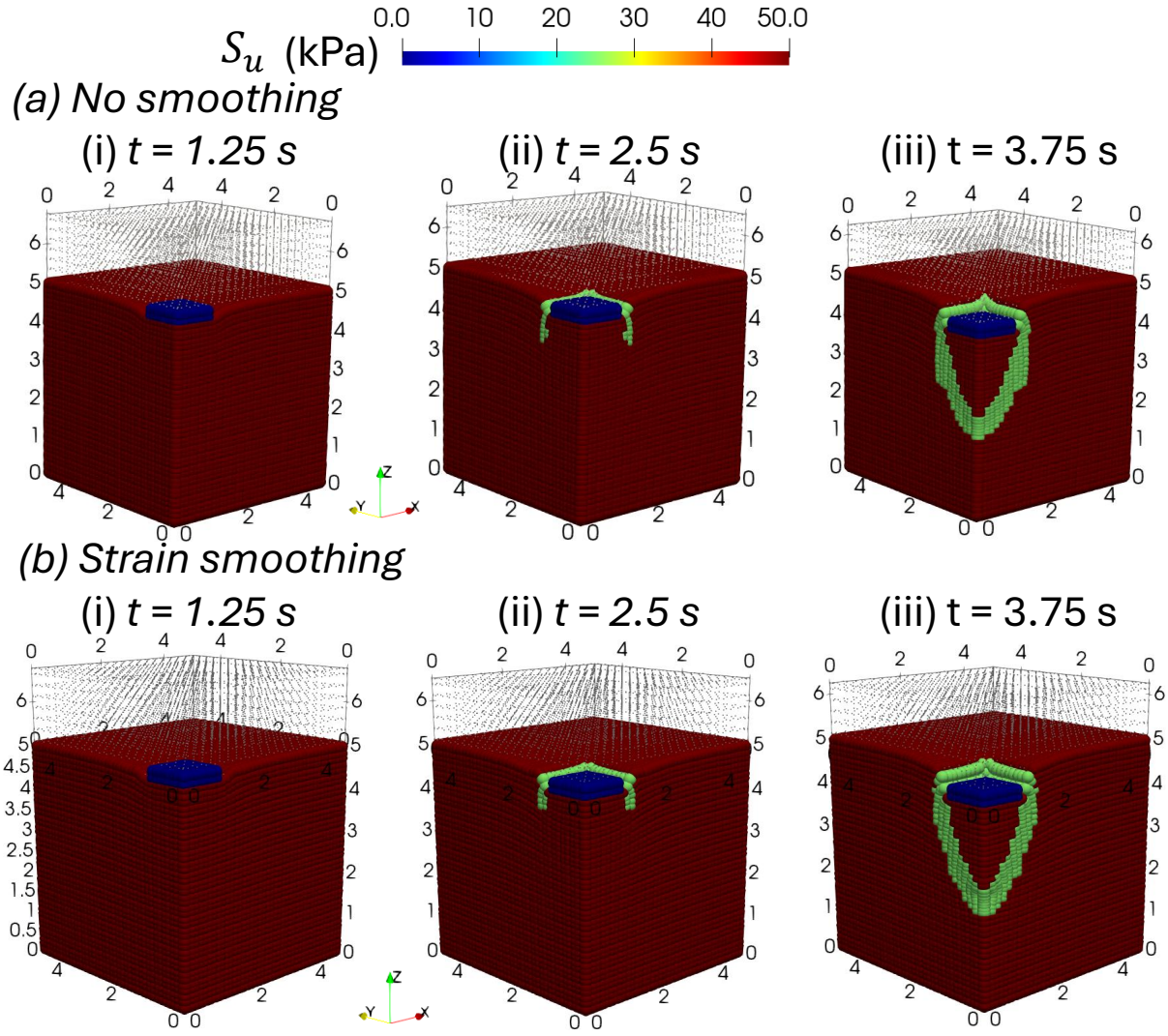

Figure 4.17: Mobilized undrained shear strength, S_u, considering brittle Tresca soil behavior: (a) with no strain smoothing, (b) with strain smoothing.

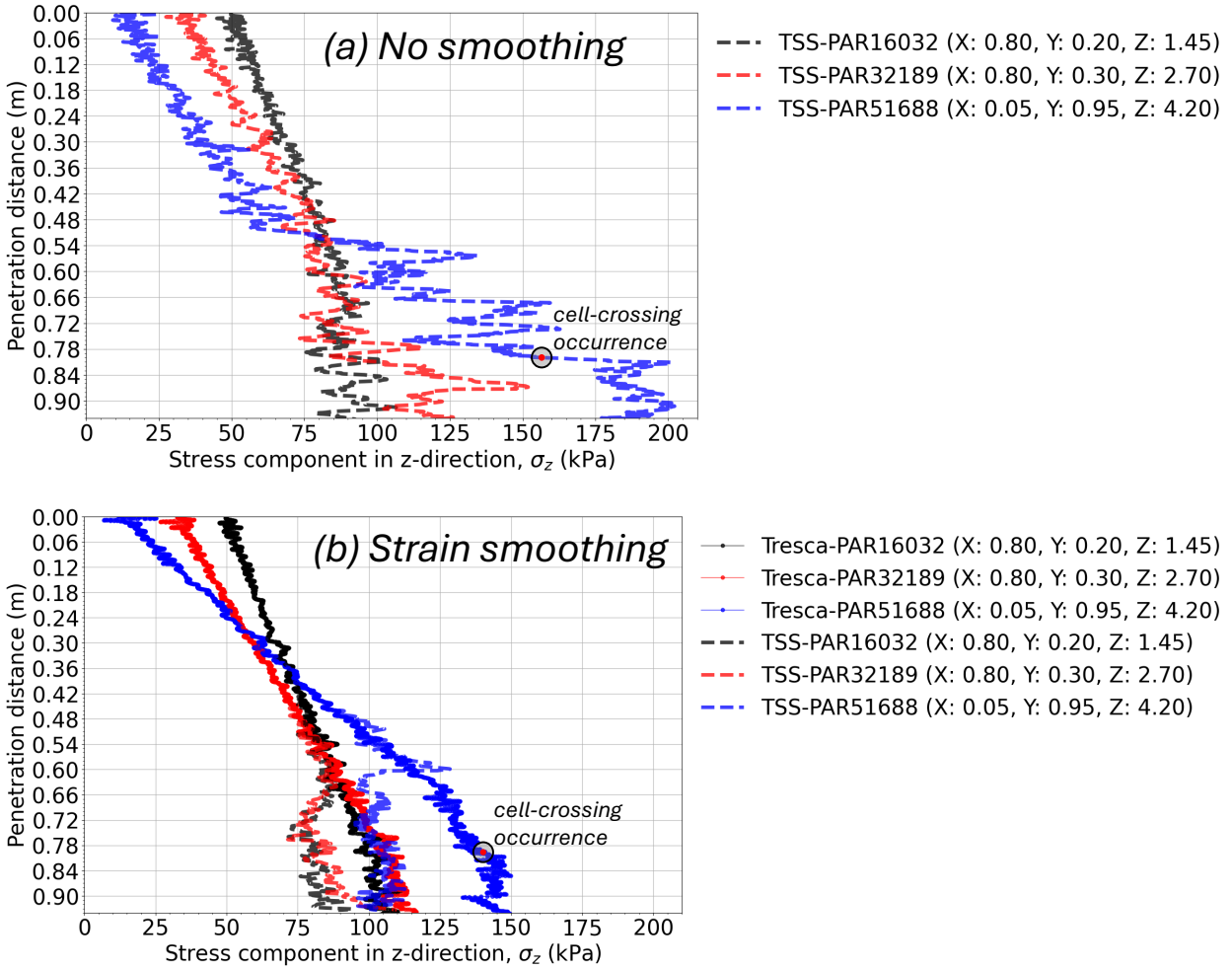

Figure 4.18: Comparison of MP stresses as the footing penetrates the elastoplastic Tresca and Tresca with strain softening (TSS) soil materials, where 20% of MPs exhibit cell crossing by 0.95 m penetration with (a) no strain smoothing, and (b) strain smoothing. The x, y, and z coordinates, and index are specified in the legend for each MP.

Finally, a circular footing is simulated using the IGA-MPM framework, considering identical footing width and material parameters as in the previous example. The incompressible LE material behavior is assumed for simplicity. Contour plots of the stress distribution are shown in Figure 4.19. At plan view, the geometry of the stress localization at the surface is highly dependent on the footing geometry as captured in Figure 4.19(a) and 4.19(b) for square and circular footings, respectively. However, the stress propagation with depth is

nearly identical, as shown in the 3D perspectives in Figures 4.19(c) and 4.19(d), respectively. For a quantitative comparison, a few MPs are selected underneath the footing to track the stress evolution as the footing penetrates the elastoplastic soil (Figure 4.20). It is seen that the stress trends are almost identical. It is acknowledged that the iterative process to find the local position of the MPs in the parent space is more expensive when simulating the circular footing relative to the square geometry. In summary, the proposed 3D multipatch IGA-MPM framework provides a stable overall numerical solution for the simulation of penetration problems, considering complex geometries and material behaviors.

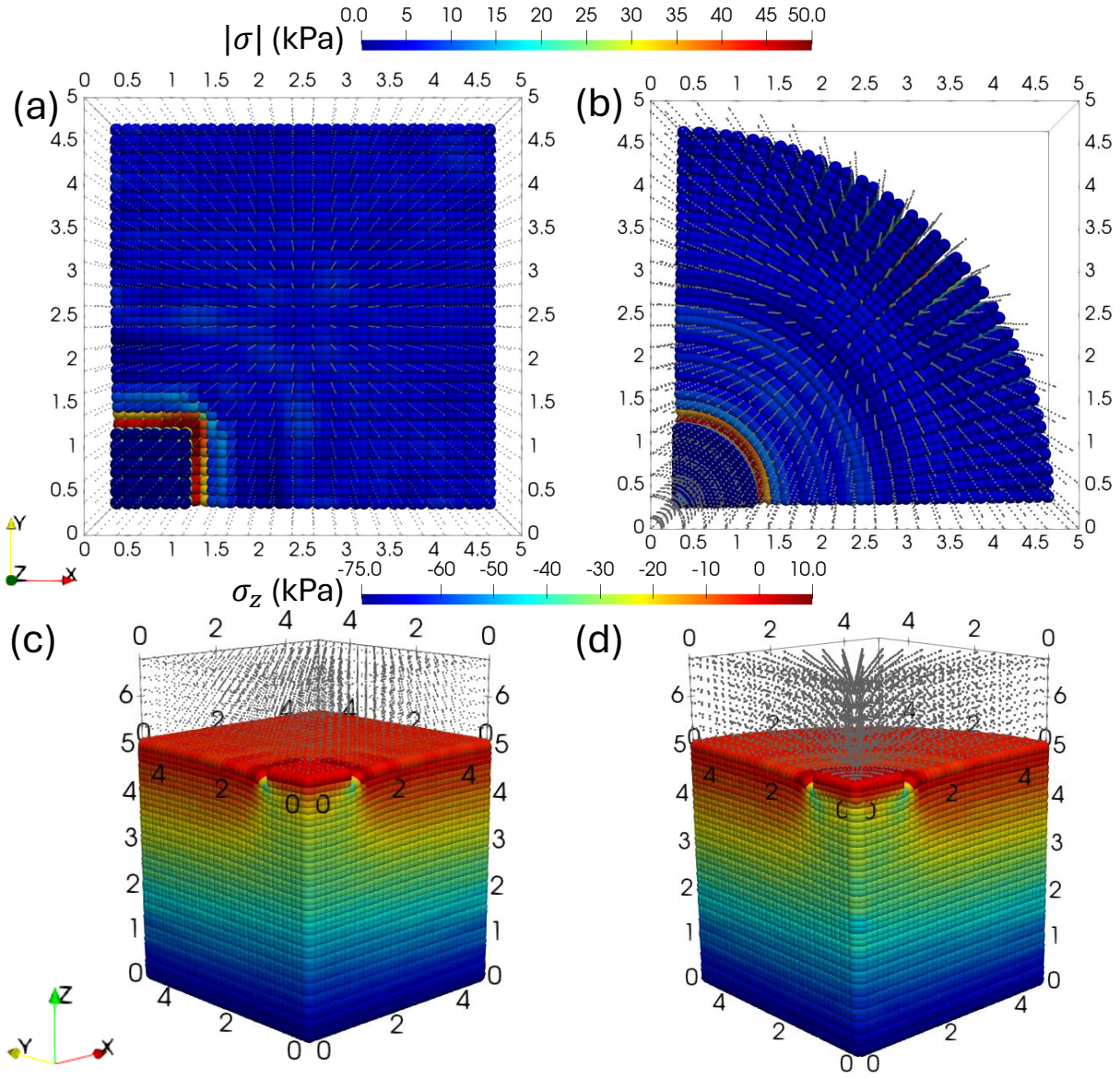

Figure 4.19: Using the multipatch IGA-MPM framework to compare stress distributions of square versus circular footing penetrating incompressible linear-elastic media at penetration distance of 0.25m at t=1.25 s. (a-b) Plan view. (c-d) 3D view.

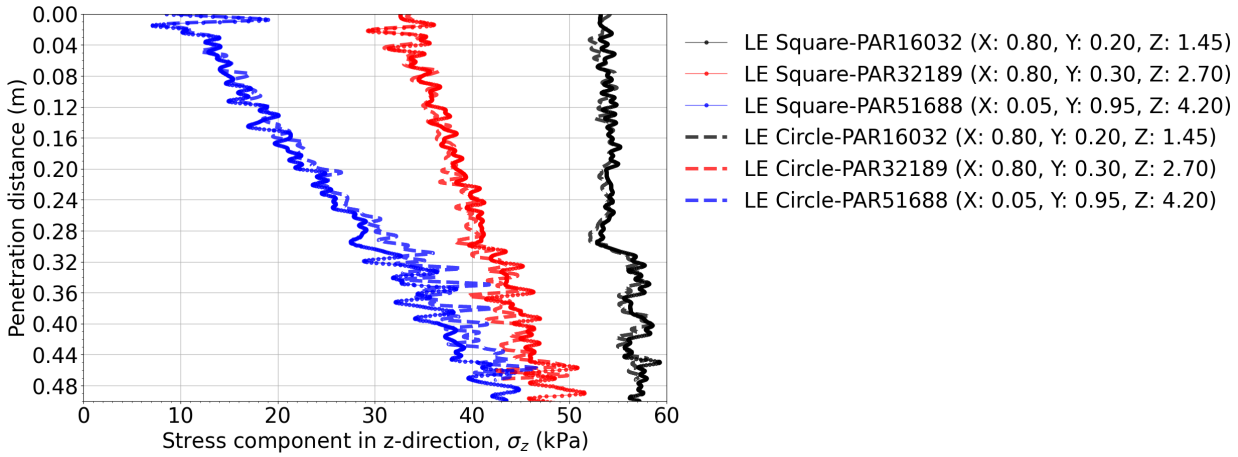

Figure 4.20: Evolution of MP stresses considering square and circular geometries. The x, y, and z coordinates of each MP are specified in the legend. Particle indices are quoted for reference.

4.7 Multipatch footing penetration considering hydromechanical interactions

The fully-coupled 2-phase formulation is necessary to accurately capture pore water pressure and subsequent drainage exhibited during consolidation [198]. First, the implementation of the hydromechanically 2-phase MPM formulation using the higher-order framework is verified herein by means of a simple 1D oedometer benchmark. Despite its simplicity, this verification is necessary to ensure the right consolidation trends according to effective stress theory, which is fundamental to geotechnical engineering [215]. Second, the plane-strain footing geometry in section 4.6.1 is simulated again using an effective stress framework and the fully-coupled hydromechanical formulation to investigate pore water generation and dissipation due to penetration.

4.7.1 Oedometer consolidation

A linear-elastic soil column is considered herein with height, H_0=1m, in fully saturated conditions. A traction value of q_u=10 kPa is applied at the nodes at the upper boundary. Three mesh refinements are considered herein: coarse (n_{El}=5), medium (n_{El}=20), and fine (n_{El}=50). This analysis is performed using two porosity values, namely n_L=0.3 and 0.4, to investigate stability. The material parameters are: solid density, ρ_s=2700 kg/m^3, liquid density, ρ_L=1000 kg/m^3, Young's modulus, E=1000 kPa, Poisson ratio, ν=0, Bulk liquid modulus, K_w=200 MPa, liquid dynamic viscosity, μ=10^{-6} kPa·s, and liquid intrinsic permeability, κ_L=10^{-11} m^2/s. This corresponds to a Darcy hydraulic conductivity of 10^{-4} m/s consistent with a silty sand material.

The analyses use cubic interpolation functions, and the stability of the solution in terms of pore water pressure evolution is assessed considering different spatial discretizations by comparing it to the [215] analytical solution (Equation 4.18). For the coarse mesh, it is seen that n_{MP}=3 per element per direction is needed to achieve a convergent solution (Figure 4.21(a)). However, for finer meshes, e.g, n_{El}=20 and 50, it is observed that n_{MP}=2 per element per direction results in convergent results (Figure 4.21(b) and 4.21(c)). Note that no initial conditions were assigned to the pore water pressure. Hence, the pore water pressure profile is dynamically generated, resulting from the nodal traction boundary condition. As such, a mismatch is expected until the pore water pressure profile is quasi-statically generated across the entire column height. The root mean square error is plotted with time in Figure 4.22. The purpose of this plot is to show error trends with time to indicate quasi-static stability. Discrepancy with the [215] analytical solution due to dynamic pore water pressure generation is initially observed in all simulations at the first data point, where the errors are all initially the same. These are attributed to the initial dynamic pore water pressure generation until equilibrium is reached. With time, the quasi-static solution is reached to better match

the [215] analytical solution. This confirms that the higher-order framework is capable of numerically simulating pore water pressure consolidation in a stable and convergent manner.

$$\begin{cases} C_v = \dfrac{\kappa_L E}{\mu_L} \\ M = \left(m - \dfrac{1}{2}\right)\pi \\ T_v = \dfrac{C_v t}{H_0^2} \\ p_t(y) = \displaystyle\sum_{m=1}^{\infty} \frac{2}{M}(-1)^{m-1} \cos\left(\frac{My}{H_0}\right) e^{-M^2 T_v} \end{cases} \tag{4.18}$$

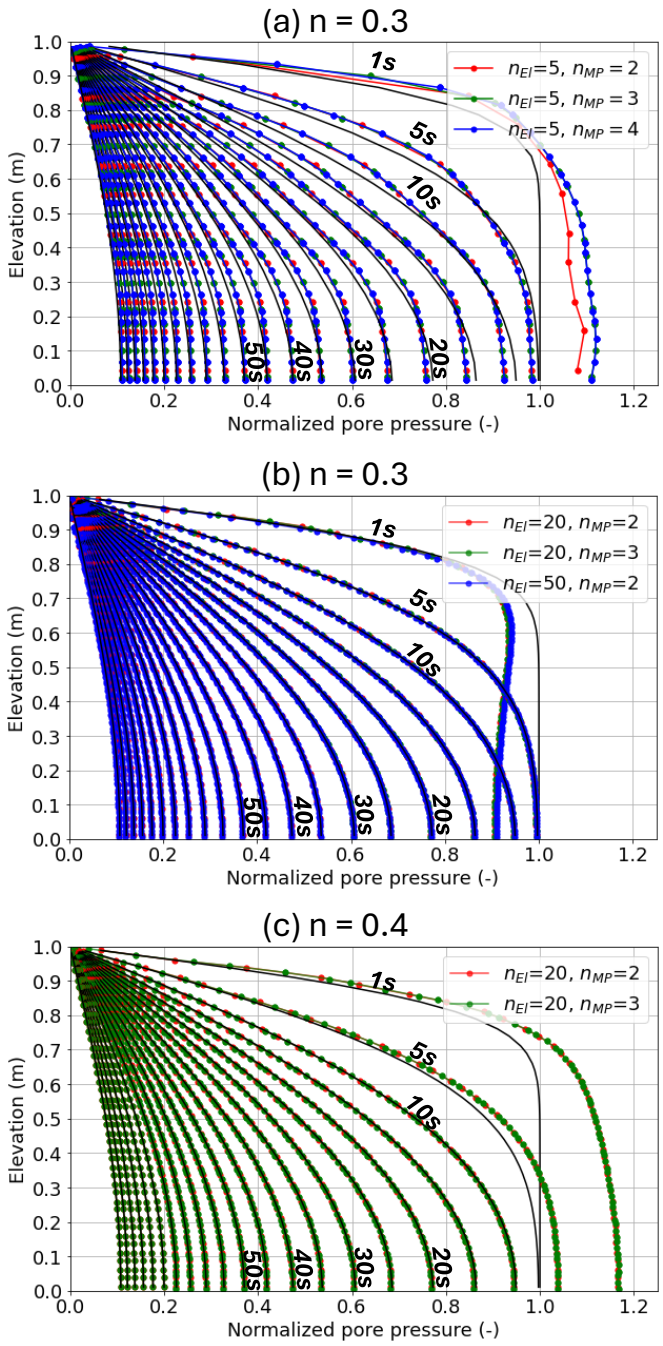

Figure 4.21: Pore pressure evolution as consolidation occurs in a saturated linear-elastic material using cubic interpolation functions. (a) Coarse mesh of n_{El}=5 elements for different number of MPs per element, n_{MP}, and porosity n=0.3. (b) Medium and fine mesh of n_{El}=20 and n_{El}=50 elements, respectively, and porosity n_L=0.3. (c) Medium mesh of n_{El}=20 elements, and porosity n_L=0.4.

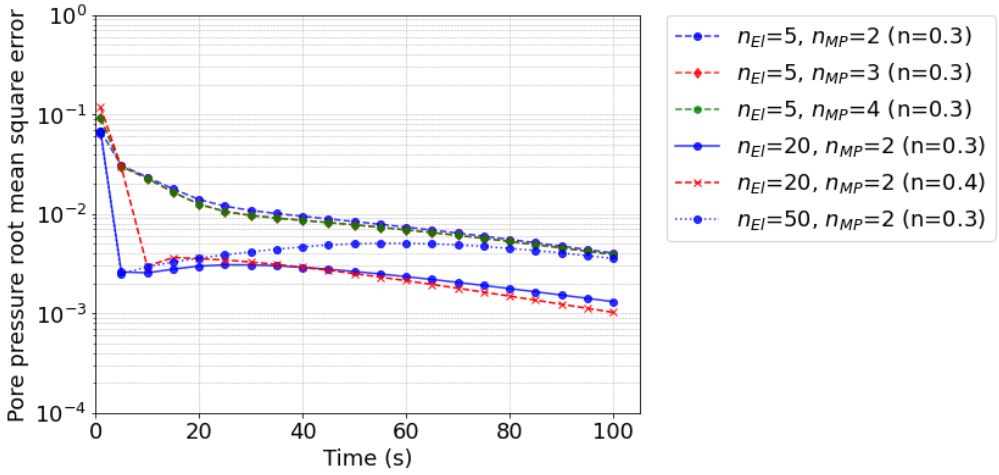

Figure 4.22: Pore pressure error evolution with time as consolidation occurs in the saturated linear-elastic soil column with different numbers of elements, n_{El}, number of MPs, n_{MP}, and porosity, n_L. Cubic interpolation functions are used.

4.7.2 Plane-strain strip footing penetrating saturated elastoplastic soil in effective stress

The 2D plane-strain footing simulation is repeated considering an identical Tresca shear strength (S_u=50 kPa) and stiffness (G=9 MPa) to those used in section 4.6.1. However, the fully-coupled 2-phase formulation is used to simulate saturated soil within an effective stress framework. Cubic interpolation functions are used herein as they presented a more stable numerical solution in previous examples. The following parameters are also assumed: porosity, n_L=0.3, solid phase density, ρ_S=2000 kg/m^3, porous water density, ρ_L=1000 kg/m^3, intrinsic permeability, κ_L=1x10^{-12} m^2, bulk water modulus, K_w=20,000 kPa, and dynamic water viscosity, μ=1x10^{-6} kPa/s. The Darcy permeability of the porous material is 1x10^{-3} m/s, consistent with clean sands. The input Poisson ratio, ν, in the 2-phase formulation must be consistent with a drained condition. A parametric analysis is performed herein for values ν=0.3 and 0.4. The geometry and the boundary conditions are applied to the water

and solid phases in an identical manner to that of the total stress simulations in subsection 4.6.1.

Figures 4.23 present the mean effective stress evolution, respectively, for the footing considering (a) ν=0.3, and (b) ν=0.4 for different penetration depths, d (0.25 m, 0.5 m, and 0.75 m). A smooth mean effective stress solution is observed with a bulb-like distribution developing beneath the footing. It is noted that a larger ν value results in a larger mean effective stress below the footing (Figures 4.23(a-iii) and 4.23(b-iii)). On the contrary, a larger ν=0.4 value results in lower pore pressures compared to the ν=0.3 counterpart. When using nu=0.4, the solid phase takes more of the footing load, which compensates for the lower pore pressures for the corresponding increase in the mean effective stress. Figure 4.24 presents the corresponding pore water pressure evolution considering the aforementioned ν value.

To quantitatively assess the numerical solution, the normal reactions for the solid and water phases are plotted in Figure 4.25 for ν=0.3 and 0.4, with their corresponding total values. As penetration occurs, the water reaction force presents a peak which decreases to reach a plateau. By contrast, the solid skeleton reaction presents a downward concave trend. A steady-state solution is reached with further footing penetration as the stress confinement increases. This is a consequence of the decrease in volumetric deformations at greater penetration depths. A higher ν=0.4 value results in a lower peak for the water reaction force than when using ν=0.3. However, the total reaction force at steady-state is consistent with the [212] solution. As expected, the ν value plays a significant role in how the load partitions between the solid and the water phase in saturated soils. In summary, the proposed framework is reasonably stable when considering coupled 2-phase problems in 2D geometries. It enables the capturing of intricate details associated with hydromechanical interactions.

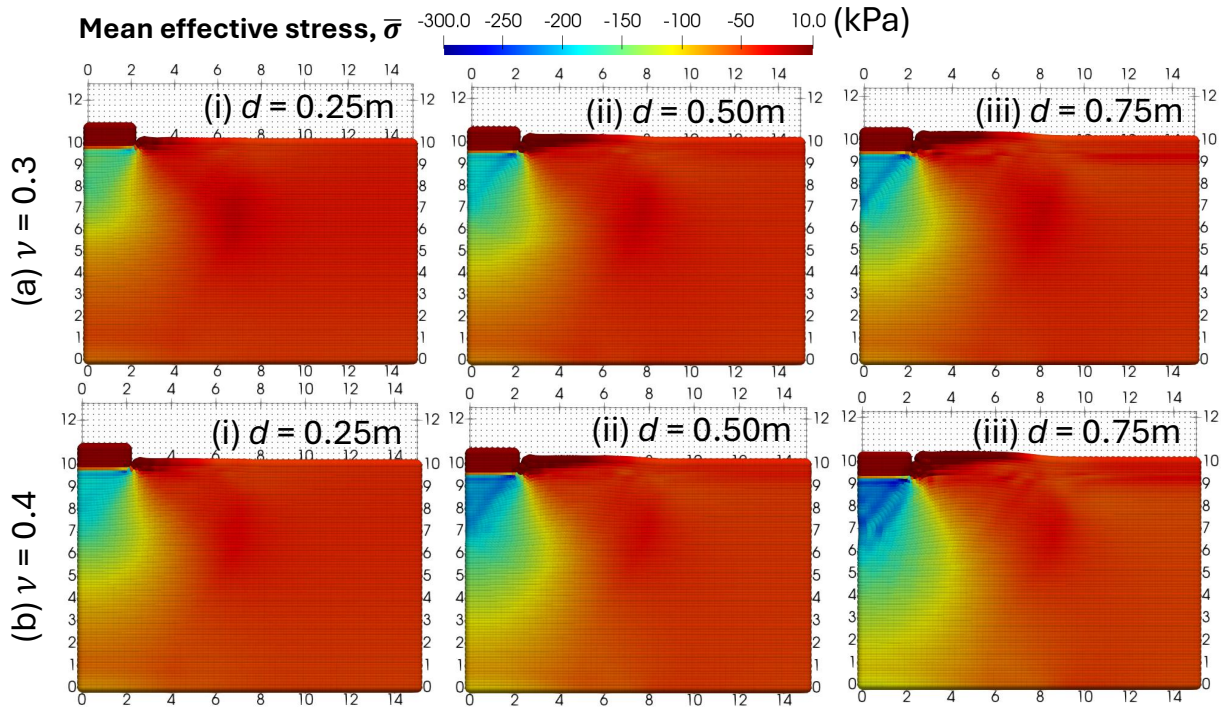

Figure 4.23: Mean effective stress evolution for MPs below the footing considering Poisson ratios, (a) ν=0.3 and (b) 0.4, at penetration depths, d, of (i) 0.25 m, (ii) 0.5 m, and (iii) 0.75 m.

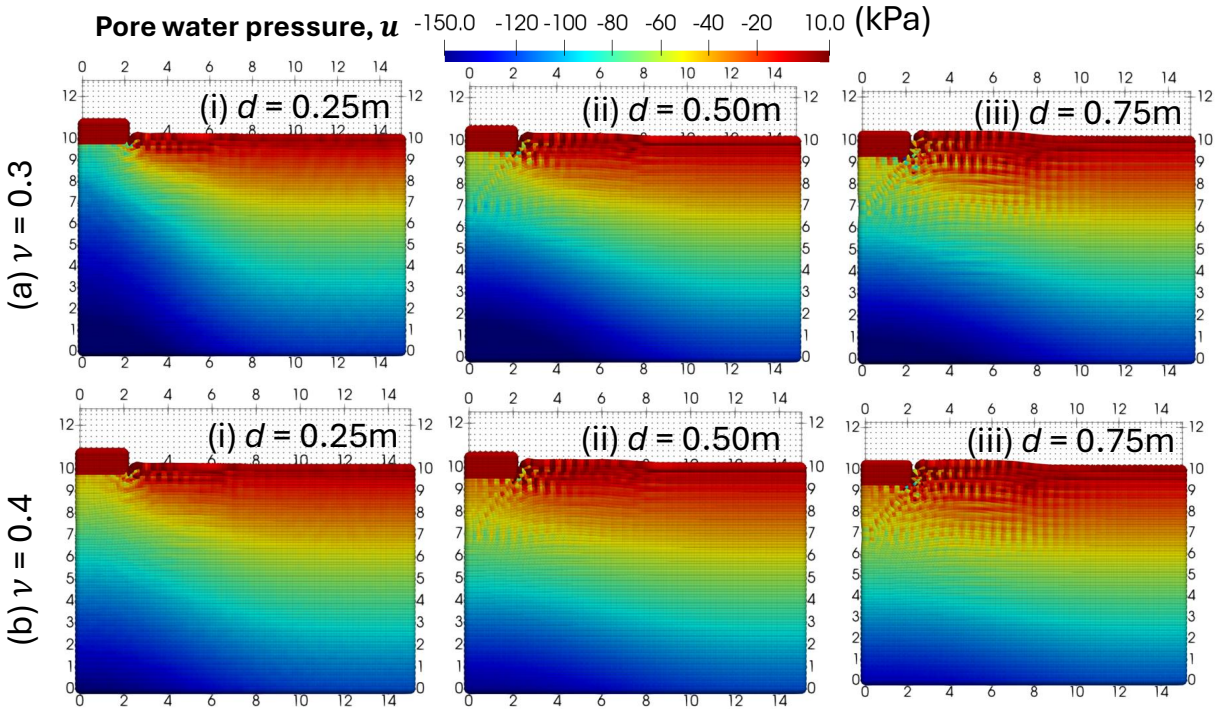

Figure 4.24: Pore pressure evolution for MPs below the footing considering Poisson ratios, (a) ν=0.3 and (b) 0.4, at penetration depths, d, of (i) 0.25 m, (ii) 0.5 m, and (iii) 0.75 m.

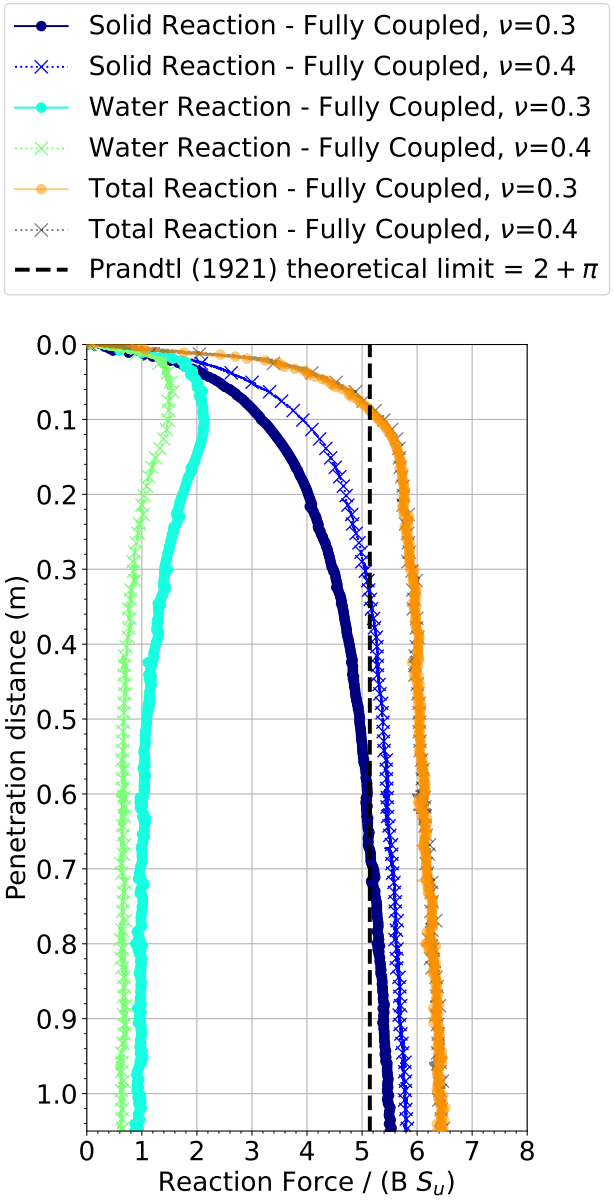

Figure 4.25: Normalized soil reaction force versus footing penetration distance for different Poisson ratios.

4.8 Conclusions

The use of MPM is growing in geotechnical engineering, albeit most contributions employ models that are contaminated with cell-crossing error. The use of B-splines in MPM is gaining popularity to eliminate cell-crossing error. For the first time, this paper presents an exploratory investigation into the use of multipatch analysis in isogeometric MPM to stabilize the stress solution in geotechnical applications. This includes the simulation of wave propagation, gravity stresses, multiphase interactions, cylindrical geometries, and nonlinear soil penetration problems. This is achieved through simple numerical benchmarks, which are supplemented by analytical solutions when available. The strain smoothing algorithm is used to alleviate volumetric locking errors. It is observed that cubic interpolation functions are often necessary to achieve a stable and convergent stress solution. This also applies to the 2-phase formulation to capture stable pore water pressure evolution in saturated soils. The framework is also seen to provide reasonable results when it comes to cylindrical geometries. Some discrepancies with analytical solutions are attributed to integration errors and challenges in tracking non-conforming boundaries in MPM. The multipatch framework is verified for the very first time against theoretical limits from plasticity theory commonly adopted in geotechnical engineering. Errors associated with inter-patch cell crossing manifest when using quadratic interpolation functions, supporting the claim that cubic functions should be used at a minimum in large-strain problems. The evolution of stresses is significantly improved in penetration problems when using strain smoothing to alleviate volumetric locking that occurs near incompressibility. This particularly eliminates drift in the stress solution caused by volumetric locking. The footing penetration problem is seen to be minimally dependent on the shape of the footing, with minor differences when comparing circular and square geometries. When considering a softening law, the shear band is seen to be more uniform in thickness when using the strain smoothing algorithm compared to the non-smoothed

counterpart. Ultimately, the framework is a promising platform to further develop geotechnical engineering problems with significant practical applications that incorporate complex geometries and multiphase interactions within a stable numerical framework.

Chapter 5

Assessment of the Hydromechanical Higher-Order MPM for the Simulation of Geotechnical Problems

Submitted for consideration in Computational Particle Mechanics (Review 1 completed), with the following reference: Alsardi, A., Yerro, A. and Long, C.C., 2026. Assessment of the Hydromechanical Higher-Order MPM for the Simulation of Geotechnical Problems. Computational Particle Mechanics (Submitted).

The following authors contributed to this manuscript, as follows:

- Abdelrahman Alsardi
  - Developed and implemented the multipatch B-spline MPM numerical framework.
  - Reviewed the literature and adopted the footing penetration and Selborne slope failure as benchmark examples.
  - Performed all numerical simulations from pre-processing to post-processing and analysis.
  - Prepared all figures and wrote the original draft of the manuscript.
  - Addressed journal peer-review comments.
- Dr. Alba Yerro
  - Provided invaluable feedback throughout the implementation of the framework.
  - Discussed results and troubleshooting strategies to perform successful numerical simulations.
  - Obtained research funds to enable the deployment of the framework for geotechnical applications.
  - Edited and revised the manuscript.
- Dr. Christopher Curtis Long
  - Provided invaluable feedback throughout the implementation of the framework.
  - Obtained research funds and computer to enable the deployment of the framework for geotechnical applications.
  - Edited and revised the manuscript.

5.1 Abstract

The Material Point Method (MPM) has been increasingly used to simulate large strain deformations. Linear interpolation functions are commonly used to perform the spatial integration. It is well-known that the discontinuities in the interpolation function derivatives induce shock-like artifacts known as 'cell-crossing' error. These errors compound with volumetric locking errors when used with hydromechanical formulations for porous media, where different velocity fields are used for each phase. The capabilities of higher-order MPM frameworks have not been explored for real-scale geotechnical problems. As such, this paper aims to assess, validate, and further discuss a higher-order B-spline MPM (BS-MPM) framework. First, the BS-MPM framework is verified against the large-strain oedometer consolidation problem. Second, the framework is validated against a real-scale slope failure experiment triggered by pore water pressure recharge. Landslide features that are captured using the higher-order framework are specifically highlighted, and results (e.g., pore water pressure and deformation) are validated with field measurements. A generally convergent numerical solution is observed when using cubic interpolation functions. Third, a footing penetration problem is simulated using the multi-patch BS-MPM. Trends are examined with respect to penetration velocity and variation in hydraulic conductivity. The BS-MPM framework ultimately presents a stabilized numerical solution that captures plausible hydromechanical interaction trends important in geotechnical engineering applications.

5.2 Introduction

The hydromechanical simulation of large deformations in granular porous media is an important endeavor in geotechnical engineering to better capture accurate soil mechanics. The

numerical prediction of the constitutive stress evolution is ever-growing with the aim of performing effective stress analyses. However, the simulation of porous granular media remains challenging due to complexities associated with capturing multi-phase interactions in a stable manner. Recently, particle-based numerical approaches have risen into prominence to enable the large strain simulation in geotechnical applications. Length-scale simulations of granular media are often performed using the Discrete Element Method (DEM), where the particles are simulated as rigid structures that interact together based on the principle of momentum conservation [216]. If fluid interactions are to be simulated, the DEM has to be combined with another numerical framework to capture pore pressures. For example, Computational Fluid Dynamics (CFD) or Lattice Boltzmann Method (LBM) can be used to capture either continuum or mesoscale fluid interactions, respectively [217, 218]. Although DEM contributions have been instrumental in understanding element-level constitutive behavior of soil, the framework's capability is limited to theoretical small-scale geometries due to its significant computational expense [219, 220]. Geotechnical Engineers often resort to continuum numerical frameworks to simulate real-scale problems based on constitutive behaviors observed at length scales from the DEM and experiments [221, 222]. In particular, the Finite Element Method (FEM) has garnered popularity due to its practicality in simulating real-scale multi-phase geotechnical problems [223, 224]. However, the FEM encounters numerical errors when large strains occur [225]. Over the past decade, significant research has been conducted to develop alternative tools, such as the Smooth Particle Hydrodynamics (SPH), the Material Point Method (MPM), or the Particle Finite Element Method (PFEM), as alternatives to enable the simulation of large strains within a single numerical framework. In case of the MPM, key advances include the development of multi-phase formulations [121, 141, 153, 226], boundary conditions[82, 204], and enhanced computational power efficiency [227, 228]. While stability remains an important topic, ongoing research continues to evaluate and refine the method's accuracy and convergence characteristics [183, 192, 229].

Over the past two decades, several numerical errors have been identified in the MPM, prompting the development of variants to combat these errors and enhance the overall accuracy of large-strain simulations. Numerical errors can be categorized into two, namely spatial and temporal errors. Numerical spatial errors can be further subcategorized into (a) integration and (b) locking errors, as follows:

(a) The most prominent spatial integration error in the MPM is the 'cell-crossing' error. This is specifically observed in the linear MPM. The abrupt change in the sign of the derivative of the interpolation functions results in a shock-like oscillation in the nodal internal force as an integration point, often referred to as a material point (MP), crosses from one element to another. This manifests in a distorted stress solution, which ultimately ends up causing a base-line drift in the displacement solution [60, 197]. A dynamic ringing error is also seen at large deformations, whereby newly introduced MPs cause temporary spurious spikes in the nodal solution as they cross from one element to another. In addition, numerical integration inaccuracies are inevitable as the MPs rarely remain in their pristine Gaussian locations.

(b) Volumetric-locking errors occur in all numerical techniques that employ a numerical mesh to perform the spatial integration. The MPM unavoidably inherits volumetric locking errors from its small-strain counterpart, FEM. This occurs when attempting to simulate materials behaving in a nearly incompressible manner. This includes materials with Poisson's ratio close to 0.5, materials deforming at constant volume under the plastic flow rule, and initially undrained porous media. Without stabilization, the error manifests in a 'checkerboard' stress solution and a restricted deformation profile.

Prominent examples of MPM variants that tackle 'cell-crossing' error include mixed Gauss-point-MP mixed integration (GP-MP) [119], Generalized Interpolation Material Point (GIMP)

[60], Convective Particle Domain Interpolation (CPDI) [63], Dual Domain Material Point (DDMP) [64], and Isogeometric Material Point Method (IGA-MPM) [68]. Additionally, B-spline MPM (BS-MPM) is simplified variant of the IGA-MPM framework that employs B-splines instead of NURBS interpolation functions. Each approach has its advantages and challenges. The GP-MP mixed integration maps the strain information from the MPs to a set of points, each located at a Gaussian point (GP), whereby the constitutive and internal force integration is performed at the GPs. The stress solution and state variables are remapped back to the MPs. This approach is simple and has been successful when simulating simple constitutive behaviors [119]. However, this integration approach can be erroneous and unstable when simulating history-dependent materials with complex constitutive models as the stress and state variables are not accurately tracked. These instabilities are exacerbated further when used with a dynamic boundary condition [197]. The GIMP and CPDI approaches draw from the SPH technique, whereby each MP is surrounded by a kernel volume. The spatial integration is performed on that MP volume. Additionally, the discontinuities in the derivative of the interpolation function are smoothed, resulting in a smoother transition of the MPs between elements of the background mesh, which addresses the ringing error instability. The DDMP approach directly smooths the derivatives of the interpolation functions while maintaining the lower-order spatial integration. Both approaches are considered effective in mitigating the cell-crossing error despite sporadic instabilities reported in the literature, which require further stabilization [65]. A lower-order stress distribution can generally result in numerical instabilities [66]. The IGA-MPM achieves a higher-order framework by using Non-uniform Rational B-splines (NURBS) as interpolation functions. The higher-order IGA-MPM intrinsically eliminates 'cell-crossing' error and mitigates the ringing error as there is more nodal overlap between the elements. The IGA-MPM framework bridges the gap between design and simulation, where the control points are used as nodes, thereby enabling the accurate simulation of complex geometries. However, an increase in the

computational cost is expected due to the Newton iterations to find the local position in the parent space from the calculated physical position in the non-conforming background mesh [192]. This search approach is commonly adopted when using non-structured meshes. When simulating simple geometries in geotechnical engineering, it is acceptable to use the B-spline (BS) instead of NURBS for this purpose. The BS-MPM employs higher-order B-spline functions to interpolate information between the background mesh and MPs. This reduces the computational cost compared to the IGA-MPM, as the local position in the parent domain can be analytically calculated within the structured background mesh [192].

To the authors' knowledge, there are no real-scale geotechnical benchmark simulations in the literature that validate the multi-phase higher-order BS-MPM framework at large strain. The goal of this paper is to validate and further analyze the behavior of the higher-order MPM (i.e., BS-MPM) framework in conjunction with a multi-phase formulation for real-world applications in geotechnical engineering. Overall, we attempt to address the following question: What is the added benefit of using a higher-order BS-MPM framework for manifestations important to geotechnical consolidation, slope stability, and penetration problems? To achieve the goal, the paper assesses the stability of the 2-phase single-point BS-MPM using real-scale geotechnical examples with orders ranging from linear to quartic. In addition to using the higher-order interpolation functions that mitigate cell-crossing error, we employ a simple strain smoothing algorithm to alleviate volumetric locking. This algorithm smooths the volumetric strains without altering the deviatoric strains. After presenting the BS-MPM framework, three distinct geotechnical problems are examined. First, the BS-MPM is verified using the Terzaghi oedometer consolidation problem. The applied load is increased to progressively increase deformations and assess the framework for numerical instabilities. Second, the Selborne slope failure experiment is simulated and compared to physical observations. The failure is triggered in the porous media by increasing the wa-

ter pressure through a traction boundary condition, which simulates water recharge into the slope. An exponential strain-softening law is used to simulate progressive failure in the slope. The effect of the B-spline order on the stresses and displacements is investigated. Third, a strip footing is simulated to penetrate a saturated homogeneous soil profile in a multi-patch BS-MPM framework. The variation in hydraulic conductivity and penetration velocity is investigated in the consolidation analysis by means of measuring the reaction force. This paper presents and validates the capabilities of the 2-phase BS-MPM in achieving accurate and stable numerical solutions for geotechnical applications.

5.3 MPM numerical framework

The simulation of large strains is possible in the MPM using Lagrangian MPs that move within an Eulerian background mesh. The background mesh is merely used as a scratch pad to solve the governing equations, whereby all the information is retained by the MPs. As such, numerical instabilities associated with mesh entanglement are prevented. The ingredients of the hydromechanical BS-MPM framework are presented in this section, including the 2-phase computational cycle, the recursive formula used to generate higher-order B-splines that prevent cell-crossing error, and the volumetric strain smoothing algorithm used to stabilize the numerical framework against volumetric locking. Finally, the multi-patch capability of the BS-MPM framework is described. The presentation of the framework is kept brief herein, and the reader is directed to Alsardi et al. [192] for the implementation details.

5.3.1 2-phase single-point MPM framework

To simulate the deformation of saturated porous media, a 2-phase formulation is needed to capture the coupled solid-liquid behavior. In particular, an explicit update-stress-last momentum formulation commonly used in geotechnical engineering applications is considered in this research [119, 177]. Each MP represents a portion of the solid material that is saturated with water that moves following the deformation of the solid phase. A set of MPs is used to represent the deformation of the solid phase in a Lagrangian manner. The liquid in the pores is simulated in an Eulerian manner by the same set of MPs. The numerical framework solves the momentum balances of the liquid phase and the solid-liquid mixture. First, the external forces corresponding to traction and gravity, $\vec{f}_{i,L}^{k,trac}$ and $\vec{f}_{i,L}^{k,grav}$, respectively, acting on the liquid phase are calculated based on the applied boundary conditions. The internal force of the liquid, $\vec{f}_{i,L}^{k,int}$, is calculated by numerically integrating the derivative of the pore pressures. The drag force is calculated using the drag matrix, $Q_{i,L}^{k}$, as a function of the porosity, Darcy permeability, and the relative difference between the solid and liquid nodal velocities, $\vec{v}_{i,L}^{k}$ and $\vec{v}_{i,S}^{k}$, respectively. The liquid momentum balance (Equation 5.1) is solved by dividing the resultant forces by the mass of the liquid assuming the entire volume is filled by the liquid, $\tilde{M}_{i,L}^{k}$, to obtain the acceleration of the liquid, $\vec{a}_{i,L}^{k}$. The mass balance of the liquid phase is solved to update the pore pressures. Similarly, the traction and gravity forces of the solid phase, $\vec{f}_{i,S}^{k,trac}$ and $\vec{f}_{i,S}^{k,grav}$, respectively, are calculated using the applied boundary conditions. The internal force of the solid, $\vec{f}_{i,S}^{k,int}$, is calculated by numerically integrating the derivative of the effective stresses. The momentum balance of the solid-liquid mixture (Equation 5.2) is used to obtain the acceleration of the solid, $\vec{a}_{i,S}^{k}$, whereby $M_{i,L}^{k}$ and $M_{i,S}^{k}$ are the nodal liquid and solid masses, respectively.

$$\vec{a}_{i,L}^{k}\tilde{M}_{i,L}^{k} = \vec{f}_{i,L}^{k,trac} + \vec{f}_{i,L}^{k,grav} + \vec{f}_{i,L}^{k,int} + Q_{i,L}^{k}(\vec{v}_{i,L}^{k} - \vec{v}_{i,S}^{k}) \tag{5.1}$$

$$\vec{a}^k_{i,S} M^k_{i,S} = \vec{f}^{k,trac}_{i,S} + \vec{f}^{k,grav}_{i,S} + \vec{f}^{k,int}_{i,S} - M^k_{i,L}\ \vec{a}^k_{i,L} \tag{5.2}$$

The acceleration fields of the solid and liquid phases, $\vec{a}^k_{i,S}$ and $\vec{a}^k_{i,L}$, respectively, are used to update the MP velocity fields. The MP momentum is then mapped to the nodes, which is then used to calculate the nodal velocity field for each phase. The strains of each phase are calculated to obtain the pore pressures and the effective solid stresses using the constitutive model. Finally, the positions of the MPs are updated according to the solid velocity field, and the mesh is regenerated to start the next step.

5.3.2 Higher order B-spline functions

The spatial integration is performed using B-spline functions. The use of these functions in numerical analysis is advantageous as they maintain positive definiteness and derivative smoothness across the entire patch domain. This is important to combat cell-crossing error. The recursive Cox de-Boor (CDB) equation is used as presented in Equations 5.3 and 5.4 for the 1D interpolation function, $N_{i,p}$, and its derivative, $N'_{i,p}$, where p is defined as the function order.

$$N_{i,p}(\xi) = \frac{\xi - \xi_i}{\xi_{i+p} - \xi_i} N_{i,p-1}(\xi) + \frac{\xi_{i+p+1} - \xi}{\xi_{i+p+1} - \xi_{i+1}} N_{i+1,p-1}(\xi) \tag{5.3}$$

$$N'_{i,p} = \frac{d}{d\xi} N_{i,p}(\xi) = \frac{p}{\xi_{i+p} - \xi_i} N_{i,p-1}(\xi) - \frac{p}{\xi_{i+p+1} - \xi_{i+1}} N_{i+1,p-1}(\xi) \tag{5.4}$$

In each time step, the computation using the CDB equation starts from piecewise constant to the required order, p. Note that the recursive equation is used herein to give greater

flexibility in inputting the required order of the interpolation functions. Each element is bound by the knots, ξ_{i+1} and ξ_i, where the integration is performed at ξ in the parent space. The 1D interpolation function is evaluated in each coordinate direction. Subsequently, the tensor product of the interpolation functions is performed to obtain the multi-dimensional interpolation functions. The chain rule is used to calculate the derivative with respect to the global domain. Implementation pseudocode algorithms are provided for reference in Alsardi et al. [192].

5.3.3 Strain smoothing algorithm

Errors associated with volumetric locking often distort strain fields due to sources of incompressibility. These manifest when loading undrained porous media and subsequent elastoplastic deformations at constant volume. As such, it is necessary to stabilize the strain field to prevent the accumulation of error in regions of localized elastoplastic deformations. In this paper, a simple strain smoothing algorithm is adopted to smooth the volumetric strains while keeping the deviatoric strain unchanged. The MP volumetric strains, $\Delta\varepsilon^{k+1}_{Vol,MP}$, are mapped to the nodes to obtain the nodal volumetric strains, $\Delta\varepsilon^{k+1}_{Vol,i}$. This is presented in Equation 5.5 where V_{MP} is the tributary volume of the MP. The values of $\Delta\varepsilon^{k+1}_{Vol,i}$ are mapped back to the MPs to recalculate $\Delta\varepsilon^{k+1}_{Vol,MP}$ (Equation 5.6). This serves as a simple yet effective method to mitigate volumetric locking, without significantly altering the MPM computational cycle.

$$\Delta\varepsilon^{k+1}_{Vol,i} = \frac{\sum_{MP=1}^{n_{MP}} N_{i,p} V_{MP} (\Delta\varepsilon^{k+1}_{Vol,MP})}{\sum_{MP=1}^{n_{MP}} N_i V_{MP}} \tag{5.5}$$

$$\Delta\hat{\varepsilon}^{k+1}_{Vol,MP} = \sum_{i=1}^{n_{el}} N_{i,p}\Delta\varepsilon^{k+1}_{Vol,i} \tag{5.6}$$

5.3.4 Multi-patch framework

Multi-patch analysis can be performed using BS-MPM by connecting the degrees of freedom of nodes that exist at the same coordinates. The interpolation functions are equal to one at the interface between the patches (i.e., $N_{i,p} = 1$). This facilitates the stress integration to measure the reaction forces between different materials (e.g., in penetration problems) and ensures the strong enforcement of boundary conditions. However, this introduces a discontinuity in the derivatives of the interpolation functions that the MPs must endure as they transition from one patch to another. Alsardi et al. [192] showed that a stable numerical solution can be achieved in multi-patch BS-MPM despite the discontinuity in the derivative of the interpolation functions. This paper further explores this topic to assess the stability of the framework under different loading and hydraulic conductivity conditions in a 2-phase hydromechanical footing penetration problem.

5.4 Verifying oedometer consolidation at large strain

When a load is applied to a saturated porous medium, the load is initially carried by the pore water pressure because water is relatively incompressible compared to the soil skeleton. Over time, the excess pore water begins to dissipate, and the load is transferred to the solid phase through seepage, leading to an increase in the effective stress. This process is well-known as consolidation, and manifests in the settlement of the soil column. In the literature, analytical solution of Terzaghi´s consolidation theory is commonly used to validate the oedometric

consolidation problem at small strains with no cell-crossing occurrence [77, 153, 182]. Two contributions also utilized the large-strain consolidation problem in the verification process. In particular, Martinelli and Galavi [196] performed this large-strain simulation using linear interpolation functions while using a mixed GP-MP spatial integration scheme. They also smoothed the volumetric portions of the effective stresses and pore water pressures to enforce a constant value for these secondary variables within the element. This provides stability by the concept of reduced integration, but ultimately overwrites the stresses and the state variables of all the MPs within the element. Although this approach is sometimes effective for simple simulations, it cannot be generalized for more complex problems that use complex history-dependent constitutive relationships. On the other hand, Zheng et al. [230] used GIMP with a selective reduced integration at the GPs for the pore water pressure integration in the large-strain consolidation problem. This involves storing the hydromechanical state variables at the GPs and the MPs. Selective reduced integration is not an option in higher-order frameworks, as a larger number of integration points is required for stable numerical integration.

This section verifies the consolidation process at small and large strains for BS-MPM at spatial integration orders, p, ranging from linear to quartic. The parametric analysis of p to investigate stability using this large-strain benchmark has never been performed using BS-MPM. Note that the traditional MP integration is adopted within the BS-MPM framework, maintaining the respective stresses and state variables. This maintains a high resolution for the pore water pressures across the spatial domain. First, the linear MPM is verified at small strains with applied loads of 1 and 10 kPa. Second, the higher-order BS-MPM is used to simulate the problem at large strains with applied loads equal to 100 and 200 kPa. The numerical results are compared with the singly-drained analytical solution from Xie and Leo [231], where the base is considered impervious and the dynamic updating of porosity and

hydraulic conductivity is accounted for.

5.4.1 Problem statement, geometry, and analytical solution

A linear-elastic saturated soil column is simulated with height, H_0=1 m. The material parameters for the soil column are presented in Table 5.1. The column is vertically discretized into 50 square elements, each one element wide. The simulation is 2D plane-strain with a fixed base and normally fixed sides to enforce one-dimensional behavior. The porosity, n, and Darcy hydraulic conductivity, k, are updated throughout the simulation as per the volumetric strains and Equation 5.7, respectively, relative to initial values (n_0 and k_0).

$$k(n) = k_0 \left(\frac{1 - n_0}{1 - n} \right)^2 \tag{5.7}$$

Each element is filled with 4 MPs per element per coordinate direction at the corresponding GP locations. The column is initialized with a uniform pore water pressure profile consistent with the traction value. The traction force, q_u, is applied at the MPs in the uppermost row of the column, and the evolution is investigated in real time, t. In each time step, the traction is mapped from those MPs to the background nodes of the containing element. The coefficient of consolidation, C_v, and dimensionless time, T_v are presented in Equations 5.8 and 5.9, respectively, as a function of the intrinsic liquid permeability, κ_L, and dynamic viscosity, μ_L.

$$C_v = \frac{\kappa_L E}{\mu_L} \tag{5.8}$$

$$T_v = \frac{C_v t}{H_0^2} \tag{5.9}$$

Table 5.1: Material parameters used to simulate oedometric consolidation assuming Darcy hydraulic conductivity consistent with silty sands (10^{-4} m/s).

Material	Linear-elastic
Porosity, n_0 (-)	0.3
Coefficient of lateral earth pressure, K_0 (-)	0..0
Intrinsic permeability, κ_L (m^2)	10^{-11}
Bulk modulus liquid, K_L (MPa)	200
Solid density, ρ_S (kg/m^3)	2700
Liquid density, ρ_L (kg/m^3)	1000
Liquid dynamic viscosity, μ_L (kPa/s)	$1x10^{-6}$
Young's modulus, E (kPa)	1000
Poisson ratio, ν (-)	0.0

The analytical large-strain pore water pressure, p_t, and settlement, z_t, profiles are calculated as shown in Equations 5.10 and 5.11, respectively. Variable M is a non-dimensional factor as per the Fourier series solution of the linear second-order partial differential equation associated with the 1D Terzaghi consolidation solution (Equation 5.12).

$$p_t(y) = \frac{E}{q_u}\, ln\left(1 + (e^{\frac{1}{E}q_u} - 1)\sum_{m=1}^{\infty}\frac{2}{M}\sin\left(\frac{My}{H_0}\right)e^{-M^2T_v}\right) \tag{5.10}$$

$$z_t = H_0(1 - e^{-\frac{1}{E}q_u})\left(1 - \sum_{m=1}^{\infty}\frac{2}{M}e^{-M^2T_v}\right) \tag{5.11}$$

$$M = \left(m - \frac{1}{2}\right)\pi \tag{5.12}$$

5.4.2 Results

The analysis presented herein begins by examining the BS-MPM framework, utilizing linear (p=1) interpolation functions for verification. The load q_u=1 kPa is chosen to induce small

strains with no cell-crossing. The simulation is then repeated with a load q_u=10 kPa, which induces no more than a single cell-crossing instance for each MP. Figure 5.1 presents the pore pressure and settlement evolution with time for an MP located at an elevation of 0.48 m from the base of the column. The analytical solution is also plotted for reference. When considering q_u=1 kPa, the evolution of pore pressure and settlement matches the analytical solution almost identically. When the load is increased to q_u=10 kPa, discrepancies arise between the numerical solution and the analytical solution. Specifically, cell crossing occurs at 21 s for this particular MP, and discrepancies with the analytical solution accumulate over time, resulting in a predicted settlement that is slightly overestimated.

Figure 5.2 presents the evolution of elevation versus pore water pressure with time. When q_u=1 kPa (Figure 5.2(a)), with no cell crossing, the numerical solution smoothly matches the analytical solution. Instead, when q_u=10 kPa (Figure 5.2(b)), the pore water pressure profile gets distorted in the upper half of the column because 28% of the MPs near the surface exhibit cell crossing. Instabilities propagate downward as deformation occurs; however, despite the pore pressure instabilities, the linear interpolation functions are effective in satisfactorily capturing the small-strain consolidation process.

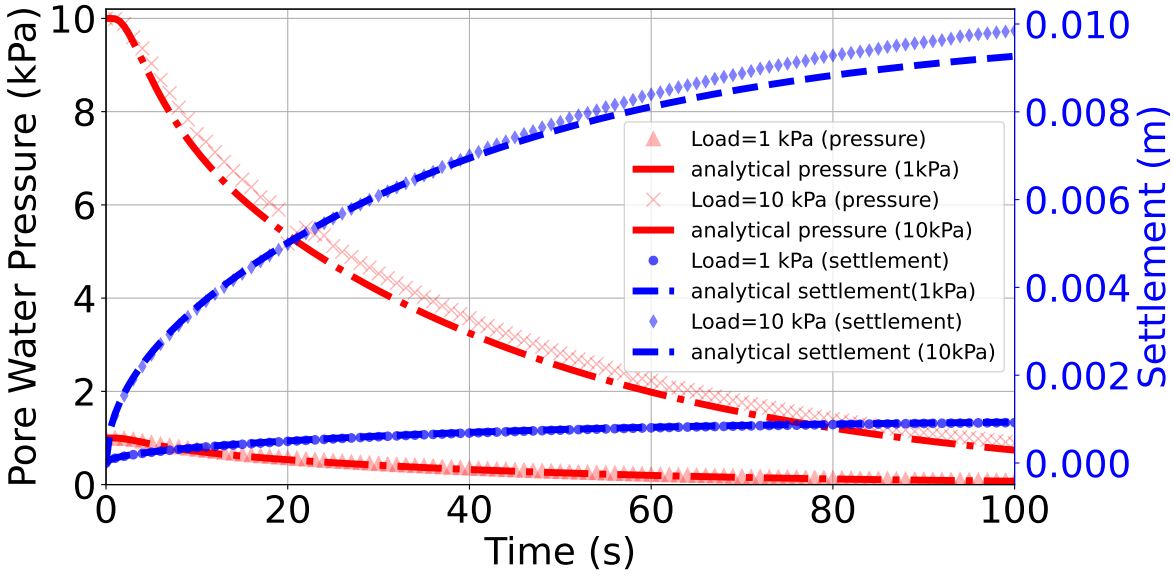

Figure 5.1: Pore water pressure and settlement evolution with time using linear (p=1) interpolation functions for applied load, q_u, equal to 1 kPa and 10 kPa for an MP at an elevation of 0.48 m. The Terzaghi analytical solution [215] is plotted for reference.

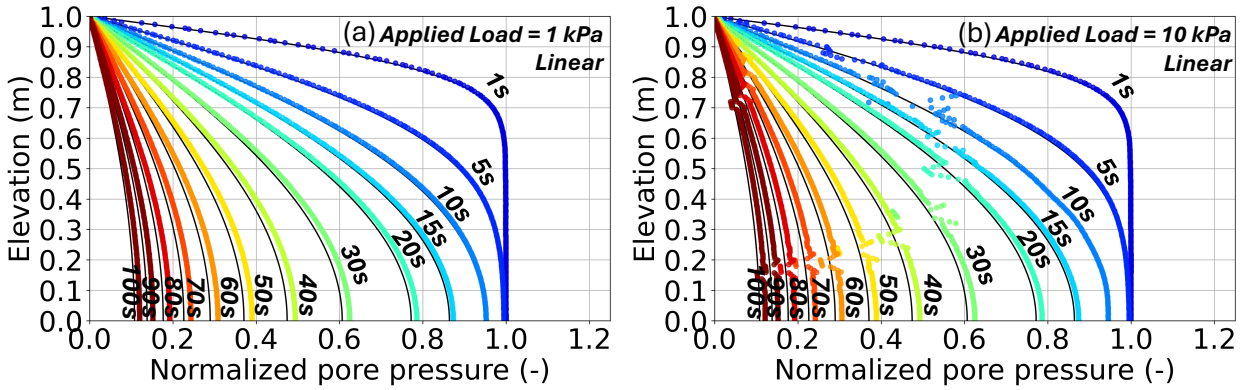

Figure 5.2: Normalized pore water pressure distribution versus elevation with time as consolidation occurs using linear (p=1) interpolation functions for applied load equal to (a) 1 kPa (no cell-crossing), and (b) 10 kPa (28% of MPs exhibit cell-crossing). The Terzaghi analytical solution [215] is plotted in background for reference.

To induce larger deformations, applied load values q_u up to 200 kPa are considered herein to assess the stability of the solution with increasing degrees of cell crossing, quantified in Table 5.2. Figure 5.3 presents the column settlement and pore water pressure evolution at

an elevation of 0.48 m with time, considering (a, b) linear, (c, d) quadratic, (e, f) cubic, and (g, h) quartic interpolation functions, respectively. As expected, when using linear (p=1) interpolation functions, the high-frequency noise in the pore water pressure results in a major low-frequency drift in displacement, rendering the solution unacceptable. The solution is extremely improved when using higher-order interpolation functions. When using quadratic (p=2) interpolation functions, the numerical stability is maintained up until q_u=100 kPa. However, some pore pressure oscillations manifest when larger deformations occur at q_u=200 kPa. This does not cause a major drift as commonly seen when using linear (p=2) elements, but these errors can worsen with real-scale simulations. When using cubic (p=3) interpolation functions, it is observed that the solution is numerically stable at large strains, as observed while using q_u=200 kPa. The solution also matches the analytical solution. Similarly, the quality of the solution is maintained when using quartic (p=4) interpolation functions for both settlement and pore pressure. No further improvement is seen at p >3 by visual inspection of the results in Figure 5.3(h).

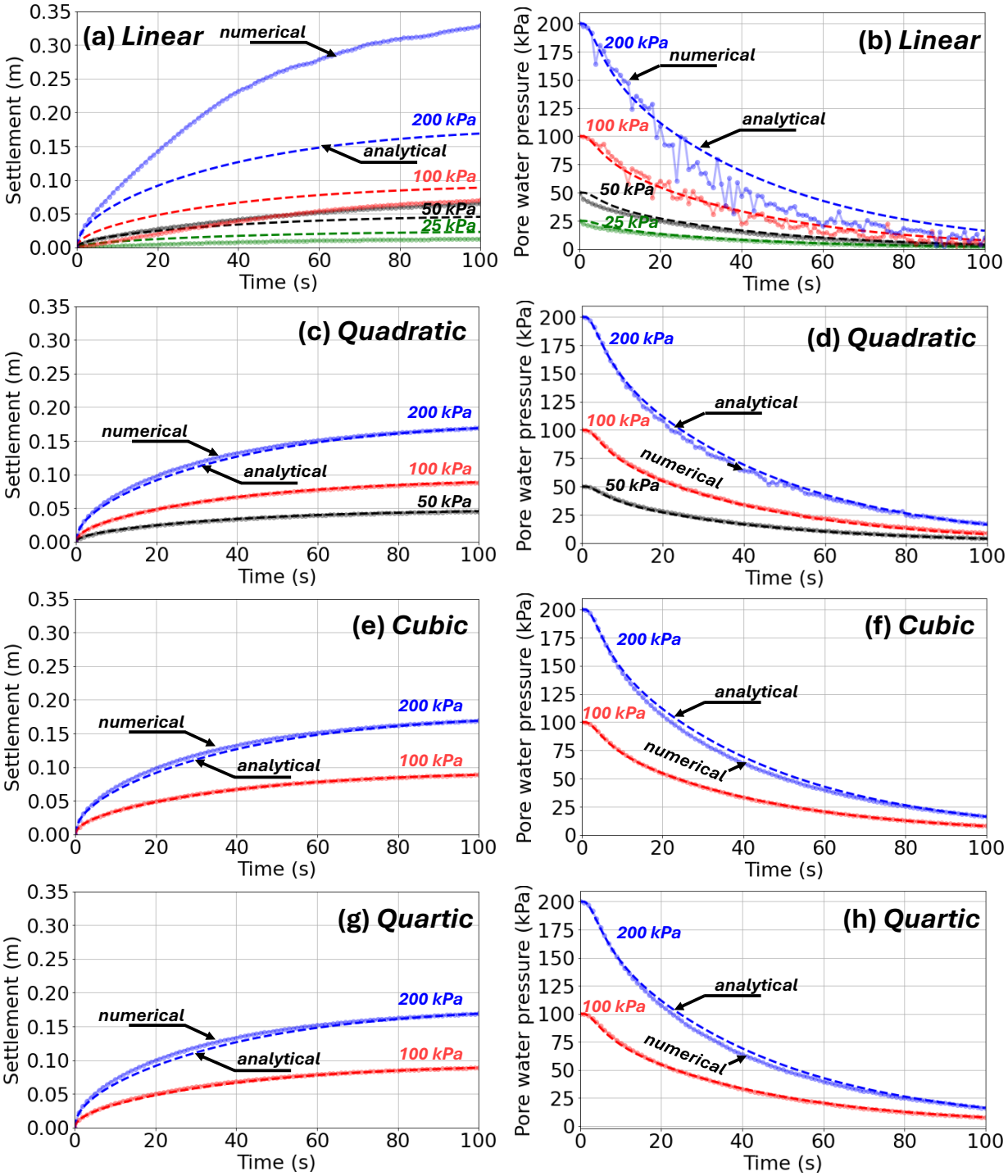

Figure 5.3: Comparing settlement and pore water pressure evolution with time for (a, b) linear (p=1), (c, d) quadratic (p=2), (e, f) cubic (p=3), and (g, h) quartic (p=4) interpolation function orders, respectively. The Terzaghi analytical solution [215] for the pore pressure and settlement is generated using Equations 5.10 and 5.11. The MP is located at an elevation of 0.48 m.

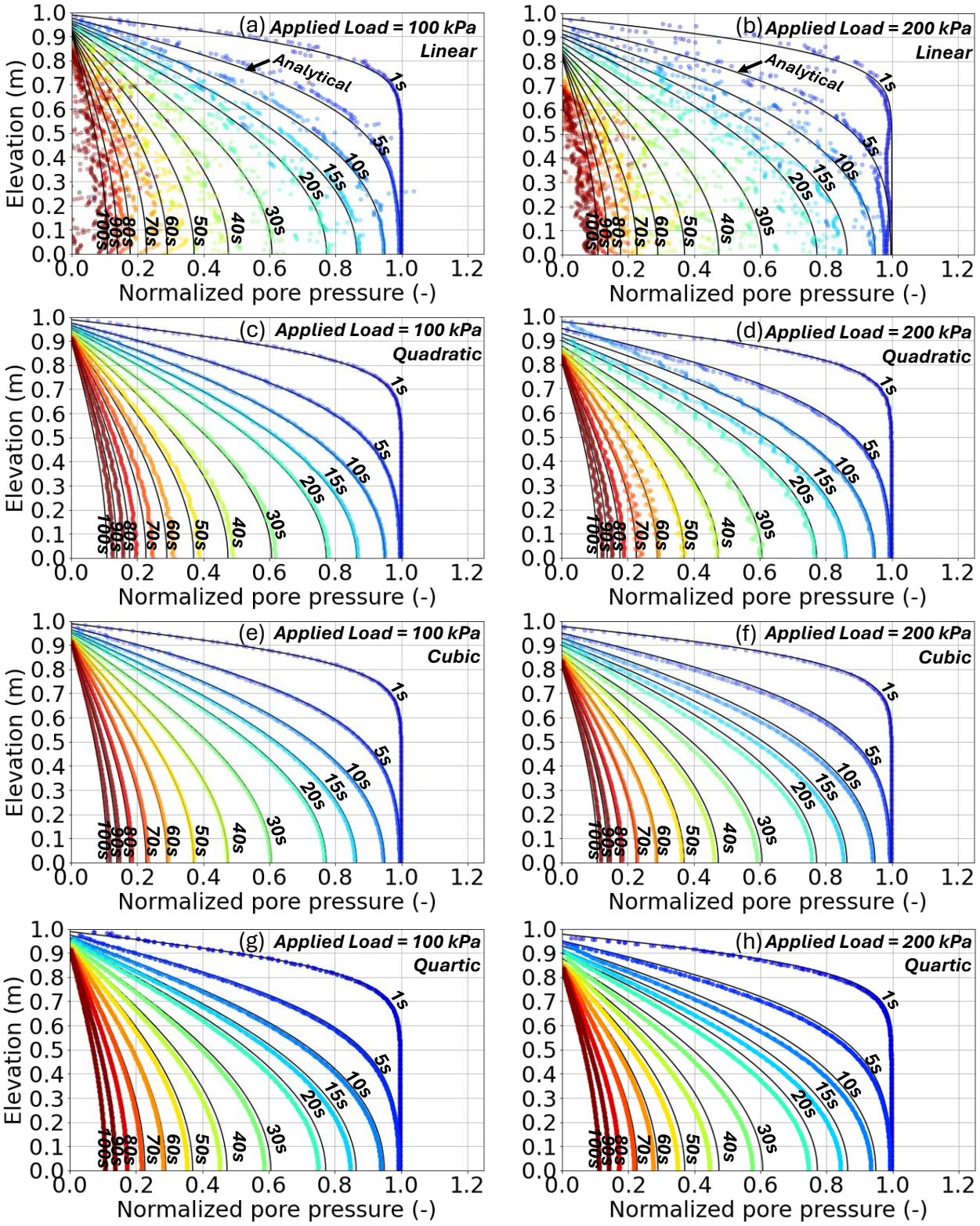

Figure 5.4: Comparing normalized pore pressure distribution as the soil column deforms with time for (a, b) linear (p=1), (c, d) quadratic (p=2), (e, f) cubic (p=3), and (g, h) quartic (p=4) interpolation function orders.

To assess the stability of the entire column, the pore pressure profile evolution with elevation is plotted in Figure 5.4 for (a, b) linear, (c, d) quadratic, (e, f) cubic, and (g, h) quartic interpolation functions. The quantitative comparison of the final predicted settlement with the analytical solution is also summarized for all models in Table 5.2. Observations are consistent with those in the previous paragraph. The use of linear interpolation functions presents an extremely distorted pore pressure profile for q_u values of 100 kPa and 200 kPa. The use of quadratic interpolation functions yields a stable solution when a load q_u of 100 kPa is applied, but when increased to q_u=200 kPa, sinusoidal oscillations manifest throughout the column. As such, this analysis confirms that quadratic (p=2) interpolation functions can be unstable for the entire column at large deformations. Using the cubic (p=3) interpolation functions (Figure 5.4(f)) generates smoother pore water pressure profiles compared to using p=2 interpolation functions (Figures 5.4(d)). Consistently, spurious cell-crossing oscillations in the pore water pressure are not observed when using p=3 interpolation functions. This improvement in the solution upon upgrading p=2 to p=3 can be attributed to the smoother derivatives, which aid in further stabilizing the solution. The use of quartic (p=4) interpolation functions presents a similar degree of consistency with the analytical solution as p=3. Upon quantitative inspection (Table 5.2), quartic interpolation functions present a settlement solution that is closest to the analytical prediction. However, the cubic (p=3) interpolation functions are sufficient for achieving a stable consolidation solution. In summary, although quadratic (p=2) interpolation functions present more stable solutions relative to the linear (p=1) counterparts at large strains, the solution is deemed stable only when using cubic (p=3) interpolation functions as per the displacement and pressure results in the oedometer consolidation problem.

Table 5.2: Percentage of MPs exhibiting cell-crossing and quantitative comparison of the consolidation displacement results for orders ranging from linear to quartic ($1 \leq p \leq 4$).

	Percentage of MPs cell-crossing (%)				Settlement at 100 s (m x 10^{-4})				Analytical settlement at 100 s (m x 10^{-4})
Load, q_u (kPa)	p=1 (Linear)	p=2 (Quadratic)	p=3 (Cubic)	p=4 (Quartic)	p=1 (Linear)	p=2 (Quadratic)	p=3 (Cubic)	p=4 (Quartic)	-
1	0	-	-	-	9.21	-	-	-	9.31
10	28	-	-	-	98.47	-	-		92.66
100	90	88	88	88	1672.61	882.12	882.14	887.52	886.21
200	95	94	94	94	3290.53	1694.10	1694.10	1689.94	1688.10

5.5 Simulating progressive failure in earthen slopes

The simulation of landslides in sloping grounds is a prime example of large-strain deformations that requires a stable numerical framework. For the first time, a real-scale slope is simulated using the higher-order BS-MPM. Numerical results are compared with field observations to validate the numerical framework. This particular experiment has become a staple for validating emerging particle-based numerical frameworks [56, 77, 120, 232, 233, 234]. Yerro [120] and Soga et al. [56] were the first to use data from the Selborne field-scale experiment to assess the linear (p=1) MPM using triangular elements with a strain-smoothing algorithm. Although the deformation profile was generally well-captured with the standard MPM, acceleration, stress, and pore water pressure solutions exhibited significant oscillation due to cell-crossing error. They used a mixed GP-MP algorithm in tandem with a Mohr-Coulomb with exponential strain-softening (MCESS) constitutive model. Jin and Yin [232] simulated the same experiment using Particle Finite Element Method (PFEM) and the same MCESS model to obtain similar results to the linear MPM. Kularathna et al. [77] also used this slope experiment to validate their linear MPM framework with quadrilateral elements combined with a Mohr-Coulomb with linear strain-softening and fractional step stabilization to alleviate volumetric locking. More recently, Morikawa and Asai [233] developed a hydromechanical SPH framework, which was validated against the Selborne experiment. Morikawa and Asai [234] assessed the effect of an arbitrary plastic deformation threshold

to numerically induce more separation between the integration points to better capture the discontinuous slope scarp in the Selborne experiment.

First, the Selborne field experiment is described as performed by Cooper et al. [235], including geometry and failure triggering mechanism. Second, the exponential strain-softening material model is described, and the calibration process is outlined, involving the BS-MPM higher-order framework for the first time. Third, the simulated slope profile is presented and compared with the observed slip surface for different orders ($1 \leq p \leq 4$). Fourth, the kinematics of the mobilized mass are studied by means of tracking MPs within the mass. Specifically, the displacement, velocity, and acceleration evolutions are studied to assess the stability of the numerical solution, considering different orders up to p=4. The final displacement profiles of the slope are also presented for the different p orders. Finally, we consider pore water pressure, stress invariant, and stress path evolution to assess the stability of the stress secondary variables commonly used in geotechnical engineering.

5.5.1 Experiment and problem setup

A field-scale experiment of an earthen slope failure was performed by Cooper et al. [235] in Selborne, Hampshire, in the United Kingdom to document a controlled benchmark of a landslide runout. The underlying geology presents an outcropping Gault Clay layer with two apparent sub-layers, where the discontinuity between the two layers is thought to be due to weathering processes. A 10 m weathered layer overlies an unweathered layer, where a 1:2 vertical-to-horizontal slope inclination was cut for the field-scale experiment. Low-friction synthetic panels were used to force a 2D plane-strain displacement profile commonly observed in large-scale case histories. The slope was equipped with inclinometers and piezometers to track failure movements and pore water pressures, respectively. The slope was brought to

failure by controlled pore pressure recharge, where water wells were raised to inject water into the slope. The landslide was seen to have a compound sub-circular deep-seated slip surface, which was confined to the weathered upper Gault Clay layer. A rotational rupture occurred with a near-horizontal emergence just above the slope toe. The slope was surveyed to determine the final deformed profile after restabilization, A laboratory testing program was performed to estimate the effective shear strength. First, the program consisted of triaxial tests (drained and undrained) and direct shear box tests to estimate peak and fully-softened strengths. Second, ring shear tests were performed to estimate the residual strength. The effective shear strength varied depending on the degree of weathering, with the upper layer having lower shear strength parameters.

The simulated geometry is presented in Figure 5.5 showing the slope profile where the Weathered Gault Clay slope overlying a level layer of Unweathered Gault Clay. Structured square elements of 0.5 m by 0.5 m are used. Each element of the upper weathered clay, where failure is expected to develop, is filled with 16 MPs. Only 4 MPs are used in the lower unweathered clay layer to reduce the computational cost. The MPs are initialized at the GP locations. The total number of MPs in the simulation is 20,927. The base of the model is fully fixed, and the sides are normally fixed. Geostatic stresses are initially generated assuming linear-elastic behavior until quasistatic convergence is achieved. The pore water pressure is generated by means of a traction boundary condition on the liquid phase, which extends for 24 m at the lower left side of the model. The liquid pressure is linearly increased from 0 to 110 kPa in 10 seconds and is then maintained. This is consistent with Soga et al. [56] in an attempt to capture the trends of pore water pressure increase observed in the field experiment. Eight MPs are used for reference (Figure 5.5), four MPs located along the shear band (i.e., A to D), to monitor pore water pressure and stress solutions, and four MPs close to the slope surface (i.e., E to H) to assess the landslide kinematics.

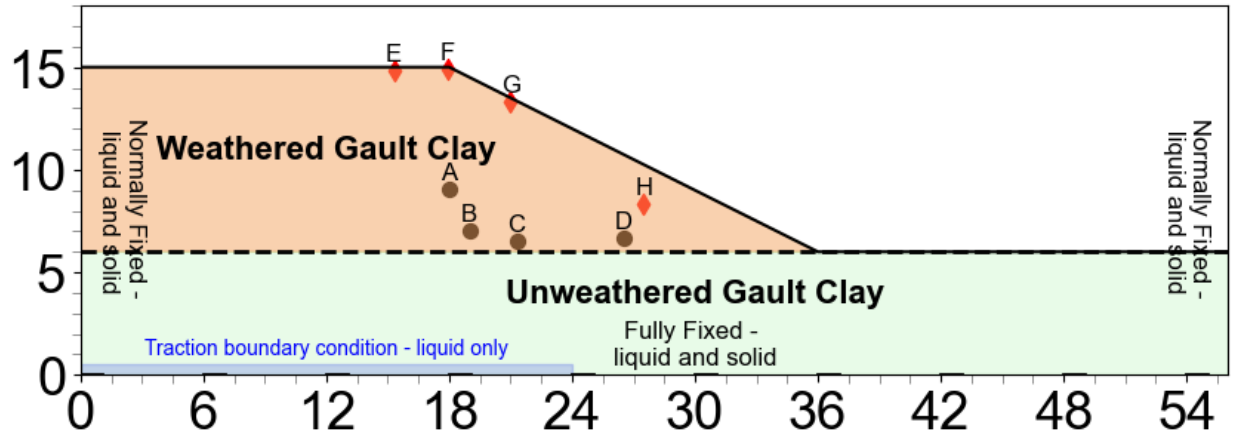

Figure 5.5: Schematic presenting real-scale slope geometry and boundary conditions with locations of tracked MPs consistent with sensor locations from the experiment by Cooper et al. [235].

5.5.2 Material calibration

Stiff, fissured clays are characterized by their brittle behavior. In this research, we adopt the MCESS model for both of the Gault Clay materials as presented in Table 5.3, consistent with Soga et al. [56] and Jin and Yin [232]. To account for the material non-linearity, an explicit modified Euler integration scheme is implemented with automatic error control by means of Pegasus substepping and final stress correction [213]. The adopted Darcy permeability for the materials is equal to $1\text{x}10^{-3}$ m/s, consistent with Soga et al. [56] to decrease the computational cost of the simulation. The adopted exponential softening laws are presented in Equations 5.13 and 5.14 for the effective friction angle, ϕ', and effective cohesion, c', respectively.

$$\phi' = \phi'_r + (\phi'_{pk} - \phi'_r)e^{-\eta\varepsilon^{pl}_{eq}} \tag{5.13}$$

$$c' = c'_r + (c'_{pk} - c'_r)e^{-\eta \varepsilon_{eq}^{pl}} \tag{5.14}$$

The subscripts 'pk' and 'r' represent the peak and residual parameters, respectively. The accumulated equivalent plastic strain, ε_{eq}^{pl}, drives the exponential softening process towards a residual value. The rate of softening is controlled by the degradation shape factor, η. A larger η value results in faster strength degradation as more ε_{eq}^{pl} is accumulated.

Strain-softening behavior is known to be mesh-dependent and requires calibration [98, 121, 130, 225]. Specifically, it depends on the active nodal span, h, for an element. In linear MPM, h is equal to the element size. However, in BS-MPM, h is affected by element size and interpolation function order (p). The nodes tend to not overlap with the boundaries of the element. Rather, when p >1, more nodes are shared with neighboring elements. It is important to calibrate the strain softening behavior for each background mesh with order p with its corresponding h value to ensure consistent results across the different meshes. More nodes are introduced in the background mesh by treating it as a B-spline 'macro-element'. However, the extra nodes crowd near the boundary leaving the nodal spacing uniform away from this boundary. Note that the value of h increases with increase in p as it consists of more nodes in each coordinate direction (i.e., not because of element size increase as per traditional linear element refinement).

Soga et al. [56] and Alonso [98] presented a method for easily calibrating linear meshes for different element sizes based on the smeared-crack approach [130]. The underlying concept proposes that the work done in the shear band should be approximately equated when using different h values to achieve a consistent solution and alleviate the mesh-dependency. An FEM true triaxial test is performed using an active node span consistent with the element size of 0.5 m by 0.5 m by 0.5 m for the different orders to ensure consistency. Figures

Table 5.3: Material parameters for the clay layers used in the Cooper et al. [235] slope experiment assuming MCESS constitutive model. This is also consistent with Soga et al. [56].

Material	Weathered Gault Clay	Unweathered Gault Clay
Porosity, n_0 (-)	0.3	0.3
Coefficient of lateral earth pressure, K_0 (-)	0.5	0.5
Intrinsic permeability, κ_L (m^2)	$1x10^{-10}$	$1x10^{-10}$
Liquid bulk modulus, K_L (kPa)	$2.15x10^5$	$2.15x10^5$
Solid density, ρ_S (kg/m^3)	2750	2750
Liquid density, ρ_L (kg/m^3)	1000	1000
Liquid dynamic viscosity, μ_L (kPa/s)	$1x10^{-6}$	$1x10^{-6}$
Shear modulus, G (kPa)	7500	7500
Poisson ratio, ν (-)	0.3	0.3
Tensile mean effective strength (kPa)	0	0
Dilatancy angle, ψ (°)	0	0
Effective peak cohesion, c'_{pk} (kPa)	12.5	25.0
Effective residual cohesion, c'_r (kPa)	4.5	0.5
Effective peak friction angle, ϕ'_p (°)	24.5	26.0
Effective residual friction angle, ϕ'_r (°)	13.5	15.0

5.6(a) and 5.6(b) show strain-stress curves for the non-calibrated and calibrated degradation factors. If the same degradation factor is used, a clear discrepancy is observed in the post-peak strain-stress curves. Instead, the strain-stress curves converge for the same element size with different nodal spacing when the degradation factor is calibrated. These calibrated factors were used in the slope runout simulations.

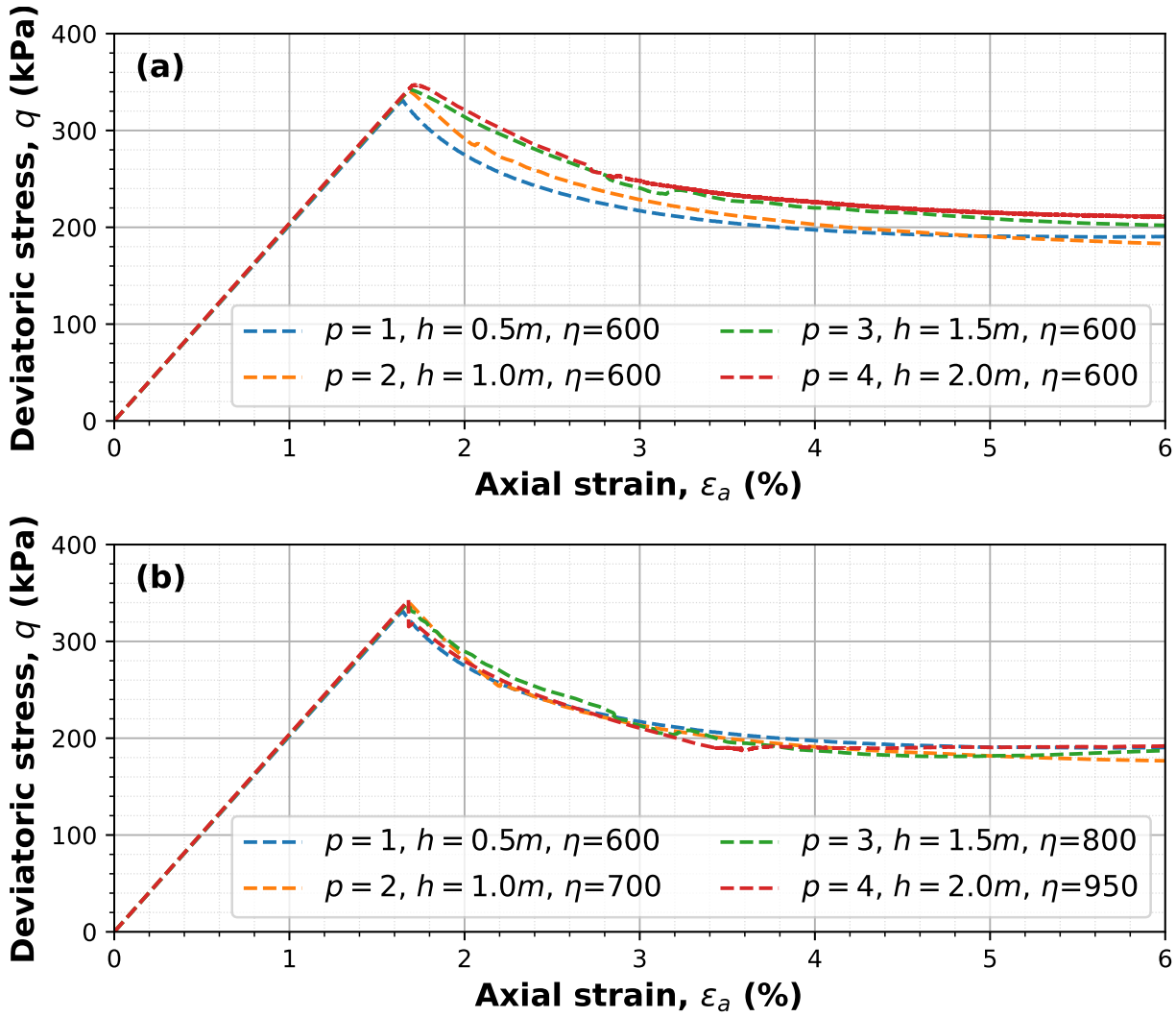

Figure 5.6: Smeared-crack approach for calibrating strain-softening factor to obtain a fit for different orders with different node spacing. (a) Non-calibrated strain-stress plots for a consolidated-drained triaxial test. (b) Corresponding strain-stress plots using calibrated degradation factors, η; p indicates interpolation function order, and h indicates node spacing for each order.

5.5.3 Assessment of slope kinematics for different orders

Figure 5.7 presents the final displacement magnitude contour plots for linear (p=1), quadratic (p=2), cubic (p=3), and quartic (p=4) interpolation functions. In a similar arrangement,

Figure E.19 presents the accumulated plastic deviatoric strain after the slope stabilization for the different p values. It is observed that all models capture a similar displacement trend, with the peak value of the displacement magnitude achieved for point H initially near the undeformed toe of the slope. However, the geometry of the mobilized mass is slightly different when using linear (p=1) or higher-order (p >1) interpolation functions. When p=1, the mobilized mass above the shear band tends to accumulate internal plastic deformations due to the numerical cell-crossing noise (Figure E.19(a)). Instead, when p >1, the mobilized mass behaves almost as a solid rigid (Figure E.19(b-d)). Additionally, the shear band width appears to increase with an increase in the p value. This is attributed to the increased overlap of nodes between neighboring elements. Unfortunately, a discontinuous scarp, as observed in the experiment, is not observed in any of the models (Figure E.19). This is common in almost all MPM numerical frameworks due to the continuum nature and the natural sticky contact between the MPs. Morikawa and Asai [234] argue that a numerical fracture algorithm (controlled by the accumulated plastic strain) can be used in continuum particle-based methods like SPH and MPM to capture the relative movement at the scarp in slope stability problems. Interestingly, their numerical results do not indicate any impact on the maximum runout, and further development of the MCESS constitutive model is outside the scope of this paper.

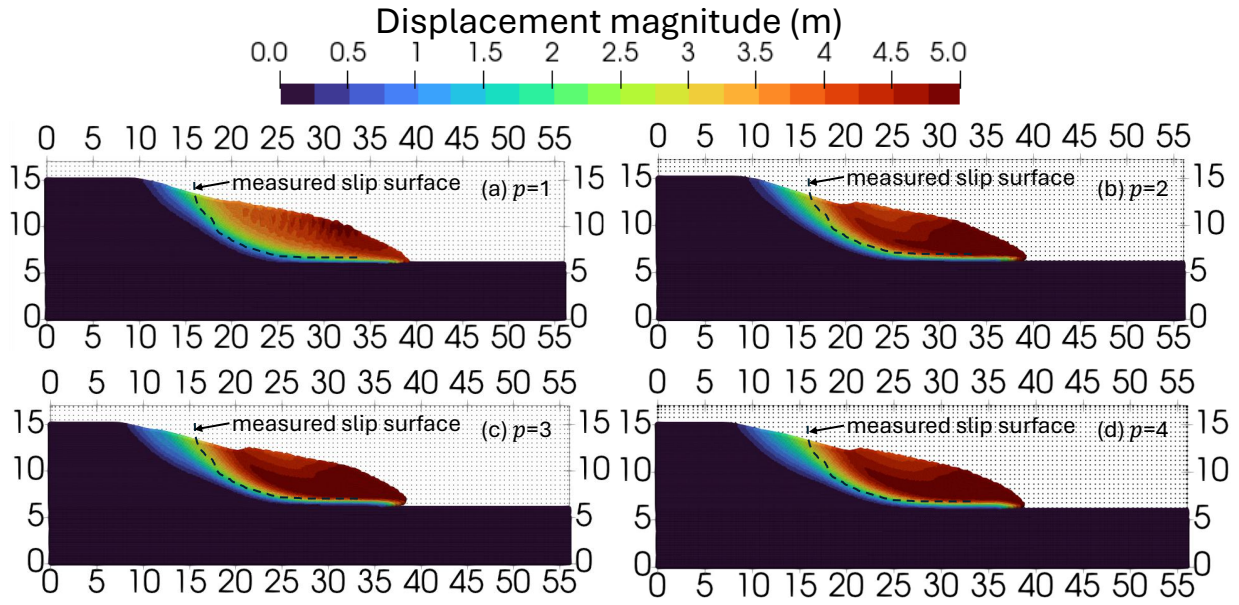

Figure 5.7: Final displacement magnitude contour plots after stabilization for (a) linear (p=1), (b) quadratic (p=2), (c) cubic (p=3), and (d) quartic (p=4) interpolation functions. The experimentally measured slip surface is outlined for reference.

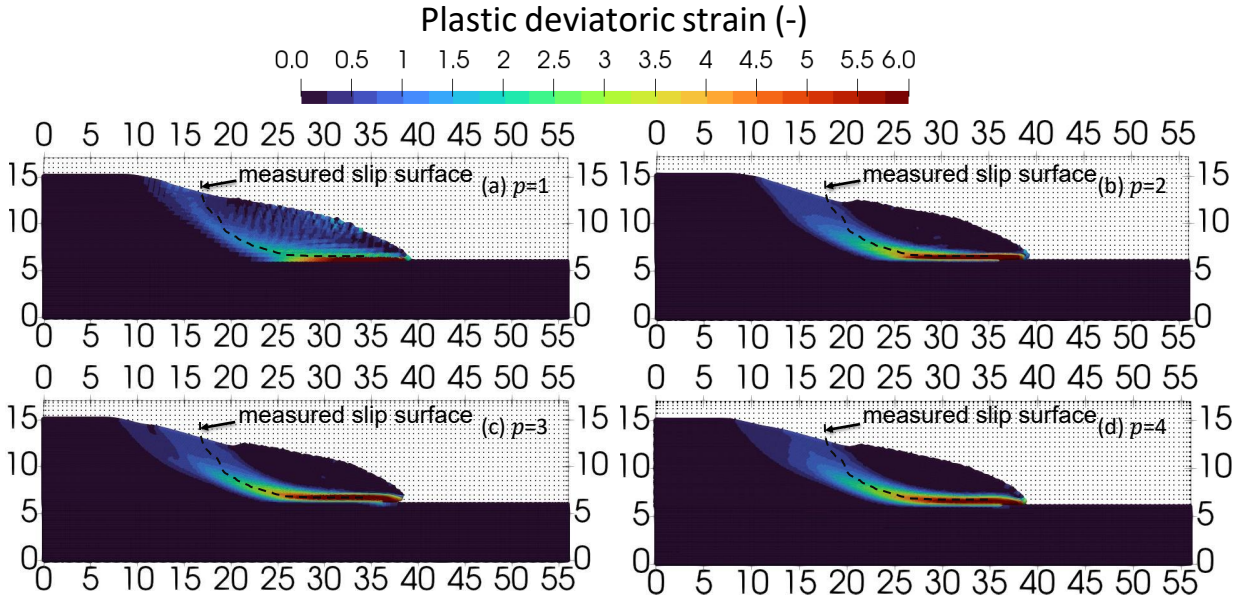

Figure 5.8: Final plastic deviatoric strain contour plots after stabilization for (a) linear (p=1), (b) quadratic (p=2), (c) cubic (p=3), and (d) quartic (p=4) interpolation functions. The experimentally measured slip surface is outlined for reference.

The final deformed profile is traversed to obtain the horizontal distance traveled by each MP at the surface. Figure 5.9 presents the horizontal surface deformation with respect to the initial slope geometry and compares it with the surveyed data from the slope experiment. It is seen that the higher-order interpolation functions present a local maximum of displacement at the crest, and a true maximum slightly before the toe. This trend is consistent with the experimental data, where the simulated results better capture the northern measurements in value. The discontinuity present in the numerical results is due to the fact that the MPs of the upper clay override the MPs of the lower clay layer. The experimental data reveal some 3D effects, where the northern and southern measurements exhibit deformations that are different in magnitude. Overall, the measured slip surface and horizontal surface movement on the northern part of the slope validate the numerical MPM results, with numerical stability discrepancies in the mobilized mass due to the smoothness of the solution, which depends on the chosen order p.

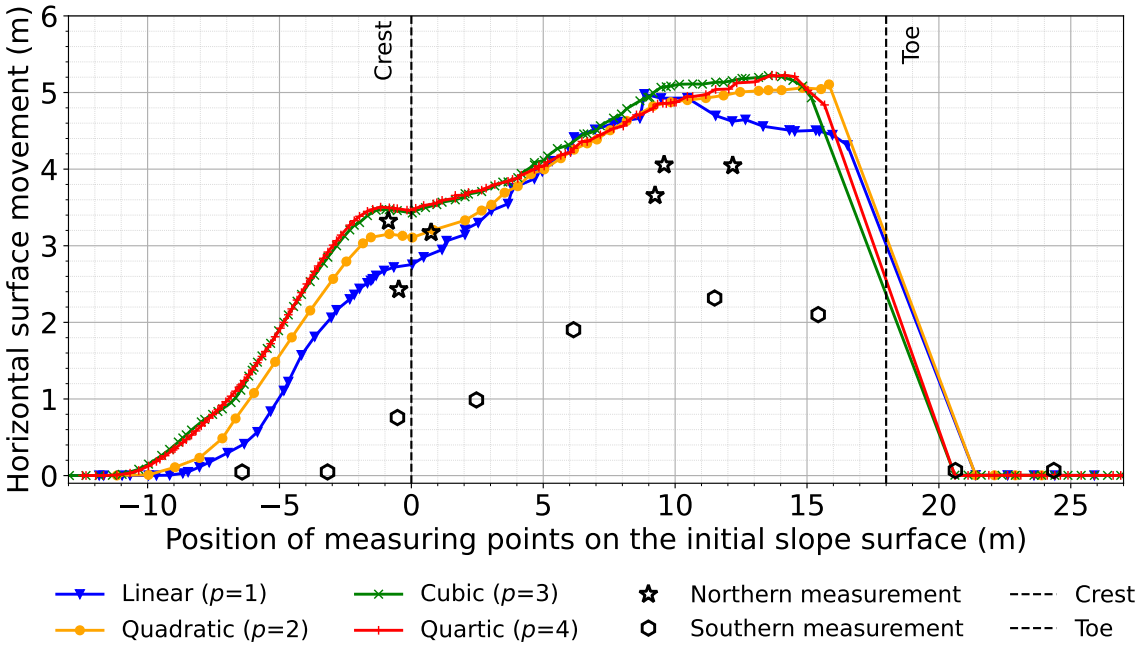

Figure 5.9: Horizontal surface movement versus position of the MP on the initial slope surface for different orders. Northern and southern experimental measurements are also plotted for comparison.

The kinematics (i.e., accumulated displacement, velocity, and acceleration) captured by the reference MPs on the slope surface (E to H) are presented in Figure 5.10 considering linear (a-c), quadratic (d-f), cubic (g-i), and quartic (j-l) interpolation functions. Points E-G and H represent points close to the crest and toe, respectively. The time is normalized by the time of failure initiation, t_f, when the full shear band manifests and major displacement accumulates. The value of t_f was approximately equal to 20 s across all p orders. Consistent with observation from Figure 5.7, the maximum displacement is seen at the toe (Point H). As expected, the smoothness of the displacement solution is maintained for all p orders. However, the smoothness of the velocity and acceleration solutions is more dependent on the p order. When examining velocities using order p =1, a high-frequency noise manifests with a spurious velocity drift. This causes the generally Gaussian velocity trend with time

to skew for points E to G near the crest (Figure 5.10(b)). At orders $p \geq 2$, the almost symmetric Gaussian trend is maintained in the velocity evolution (Figure 5.10(e, h, k)). Similarly, the acceleration at $p = 1$ is contaminated with high-frequency noise, which greatly masks the underlying trend in acceleration-time evolution. This is greatly alleviated when considering $p \geq 2$, whereby a smooth acceleration profile is observed that mimics the shape of a sinusoidal wave. Note that the spurious spikes in the acceleration results when $p = 1$ are an order of magnitude larger than when $p > 1$. From the kinematic analysis, it is evident that higher-order interpolation functions significantly reduce high-frequency noise, resulting in a more stable numerical solution for dynamic problems. The remaining numerical errors in the higher-order formulation primarily stem from the use of explicit Euler time integration and the compressibility of the fluid phase. These issues can be mitigated through stabilizing strategies such as implicit dissipative integration and fractional-step incompressibility [77], respectively.

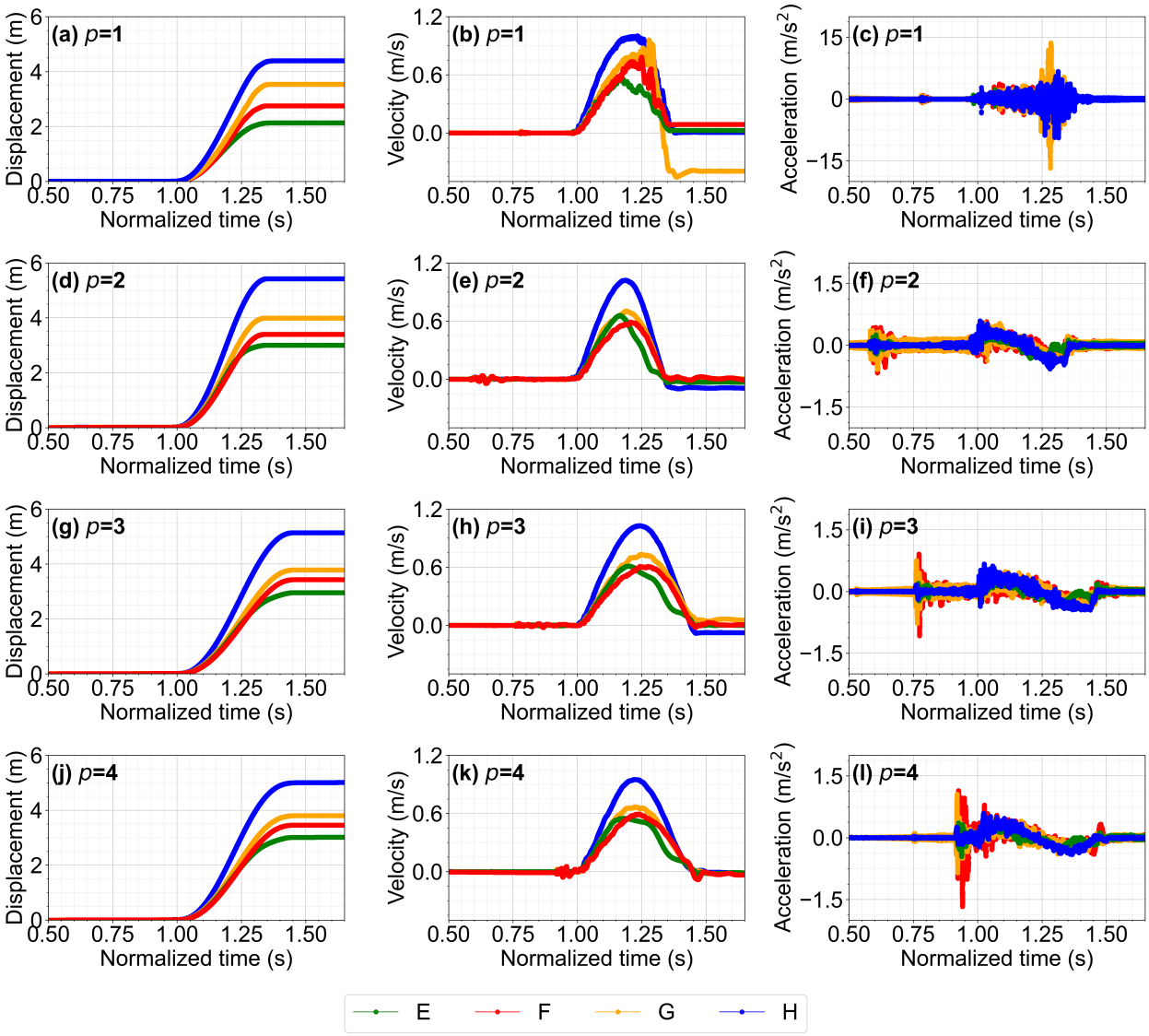

Figure 5.10: Kinematic plots of displacement, velocity, and acceleration for linear (a-c), quadratic (d-f), cubic (g-i), and quartic (j-l), respectively, for MPs located at E-H.

5.5.4 Assessment of pore pressure and stresses for different orders

Figure 5.11 shows the evolution of excess pore water pressure and vertical effective stress for different p values at three reference points located in the shear band (i.e., Points A, C, and D, which progressively get farther from the recharge area and closer to the initial slope

toe). The pore pressure numerical results are compared to field measurements. In all cases, pore pressure increases, and the magnitude is consistent with the recordings and the point location with respect to the recharge area. The evolution of excess pore water pressure for all numerical solutions is identical until failure occurs (i.e., at a normalized time of 1). After that, significantly high-frequency oscillations are exhibited when p=1, while the solutions of higher-order interpolation functions present smoother pressure variations. Finally, when the slope stabilizes (i.e., normalized time of 2), the pore pressure predicted by the models with $p > 2$ matches; however, when using p=1, the excess pore water pressure exhibits a drift. Consistent with the evolution of pore water pressure, a decrease in the vertical effective stress is observed as the soil mass mobilizes, accompanied by further stress redistribution until the final stabilization of the slope (Figure 5.11(d-f)). In a similar manner, the use of linear (p=1) interpolation functions tends to manifest in stress oscillations and a drift. In this example, the pore water pressure generally exhibits a greater degree of oscillation compared to the stresses.

A general overview of the vertical effective stresses in the slope after final stabilization are presented for different interpolation functions in Figure 5.12. When p=1, the vertical effective stress within the mobilized mass presents a highly distorted 'checkerboard' distribution (Figure 5.12(a)). This is consistent with the distorted strain profile observed in the slope (Figure E.19). When considering p=2, the stress in the mobilized mass is smooth and stable (Figure 5.12(b)). However, there is some degree of distortion above the toe near the interface between the two clay layers. When considering $p \geq 3$, the stress profile is smooth with minimal stress instabilities when p=4 (Figure 5.12(d)).

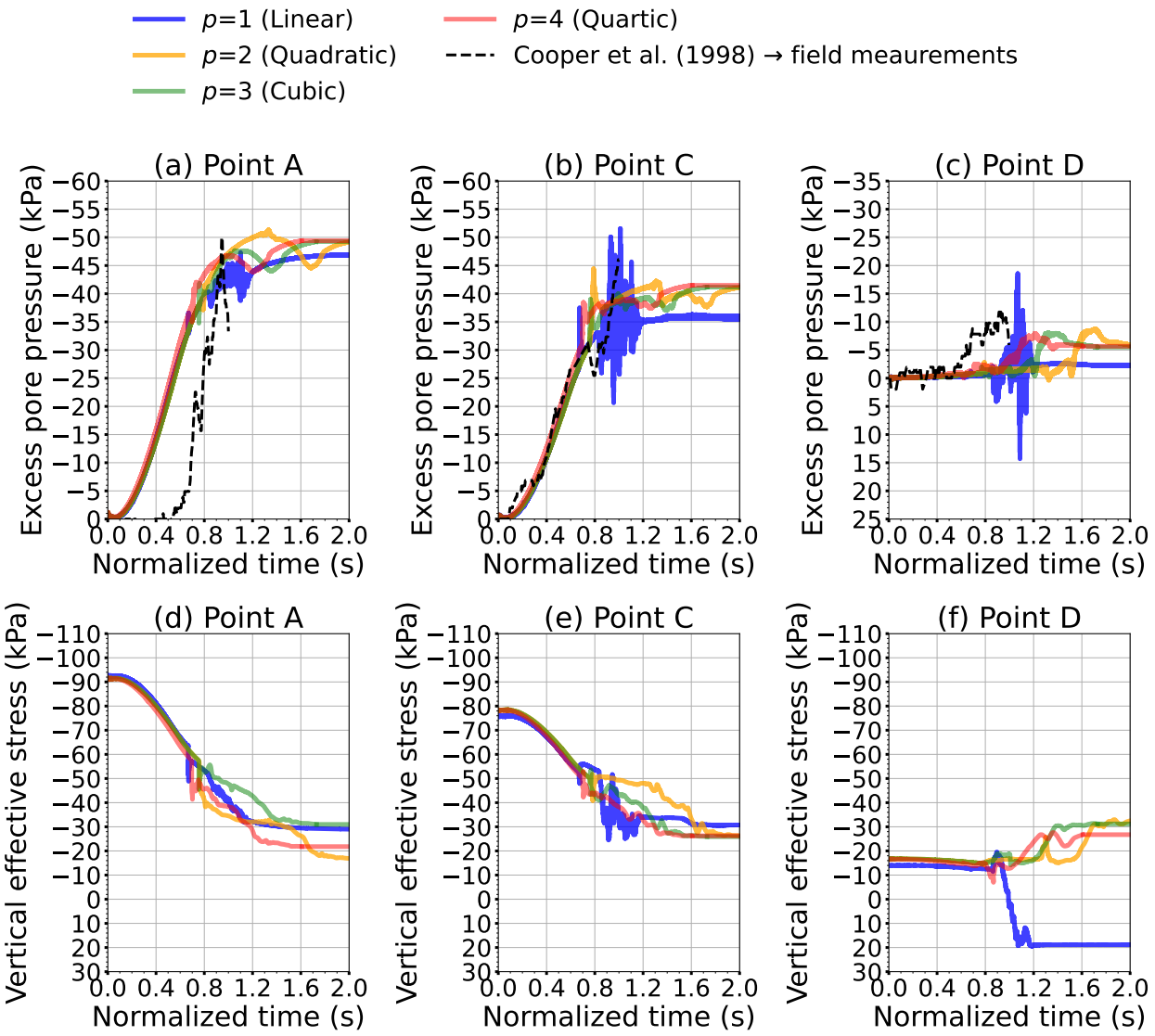

Figure 5.11: Comparing numerical results and field measurements for (a-c) Excess pore water pressure, and (d-f) vertical effective stress for MPs at locations A, C, and D, respectively, considering $1 \leq p \leq 4$.

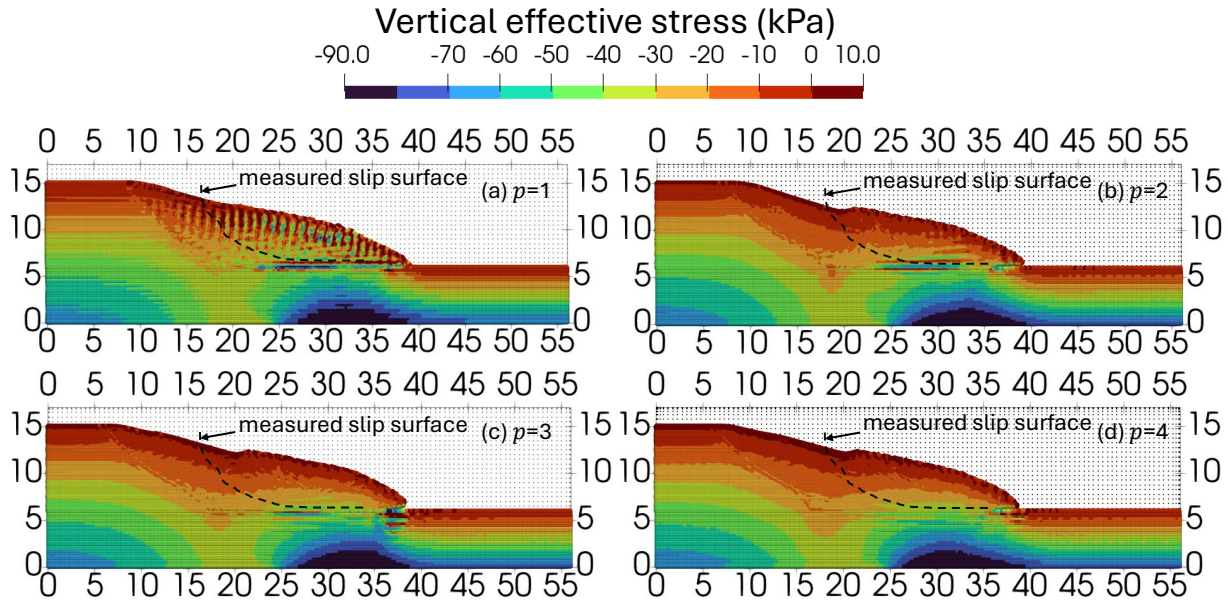

Figure 5.12: Vertical effective stress contour plots after stabilization for (a) linear (p=1), (b) quadratic (p=2), (c) cubic (p=3), and (d) quartic (p=4) interpolation functions. The experimentally measured slip surface is outlined for reference.

In geotechnical engineering, the invariants $\bar{\sigma}'$ (Equation 5.15) and J (Equation 5.16) are often plotted against each other to mechanistically understand the effective stress path with respect to the failure envelope, whereby the subscripts represent the Cartesian stress components.

$$\bar{\sigma}' = \frac{\sigma'_{xx} + \sigma'_{yy} + \sigma'_{zz}}{3} \tag{5.15}$$

$$J = \frac{1}{\sqrt{6}} \sqrt{(\sigma'_{xx} - \sigma'_{yy})^2 + (\sigma'_{yy} - \sigma'_{zz})^2 + (\sigma'_{zz} - \sigma'_{xx})^2} \tag{5.16}$$

Figure 5.13 presents the effective stress paths for reference points located in the shear band (i.e., A-D) for different interpolation function orders. Note that the normalized time is shown by the color evolution of the plot (from blue to red). The peak and residual failure envelopes are also plotted. All stress paths indicate an initial elastic volumetric unloading (i.e., stress

paths move to the left) due to the increase in the pore water pressure until plastification initiates (at slightly different instants for the different points) when the stress path meets the peak Mohr-Coulomb yield surface. Note that this happens when t_f<1, meaning that the slope has not mobilized yet. The progressive softening of MPs down to a residual state, accompanied by the progressive load transfer as the MPs soften, induces the progressive localization of a 'zipper'-like shear band. Although the general trends are reasonable when using the linear (p=1) interpolation functions, the post-failure stress paths are contaminated with high-frequency noise when the normalized time is greater than 1 (Figure 5.13(a-d)). Specifically, the noise reveals that the linear interpolation functions present lots of erroneous stress reversals as the soil softens to its residual strength value. Smoother stress paths are observed when $p \geq 2$, with significant reduction in artificial stress reversals and consistent convergence achieved when $p \geq 3$. As such, this demonstrates that higher-order interpolation functions are necessary to capture the stress path mechanism in a reasonable manner. This observation is extremely important because some advanced constitutive models are very sensitive to stress reversal (e.g., [110, 236]). In this regard, linear interpolation functions can significantly affect the performance of such models, inducing false numerical artifacts that contaminate variables associated with hardening and fabric evolution. In summary, despite the valid displacement trends in the linear MPM, the simulation of stable stress paths in history-dependent materials necessitates a smooth strain field that ensures the correct dynamic evolution within the constitutive model. Consistent with the small-scale oedoemeter, stress path convergence is successfully achieved with cubic (p=3) interpolation functions.

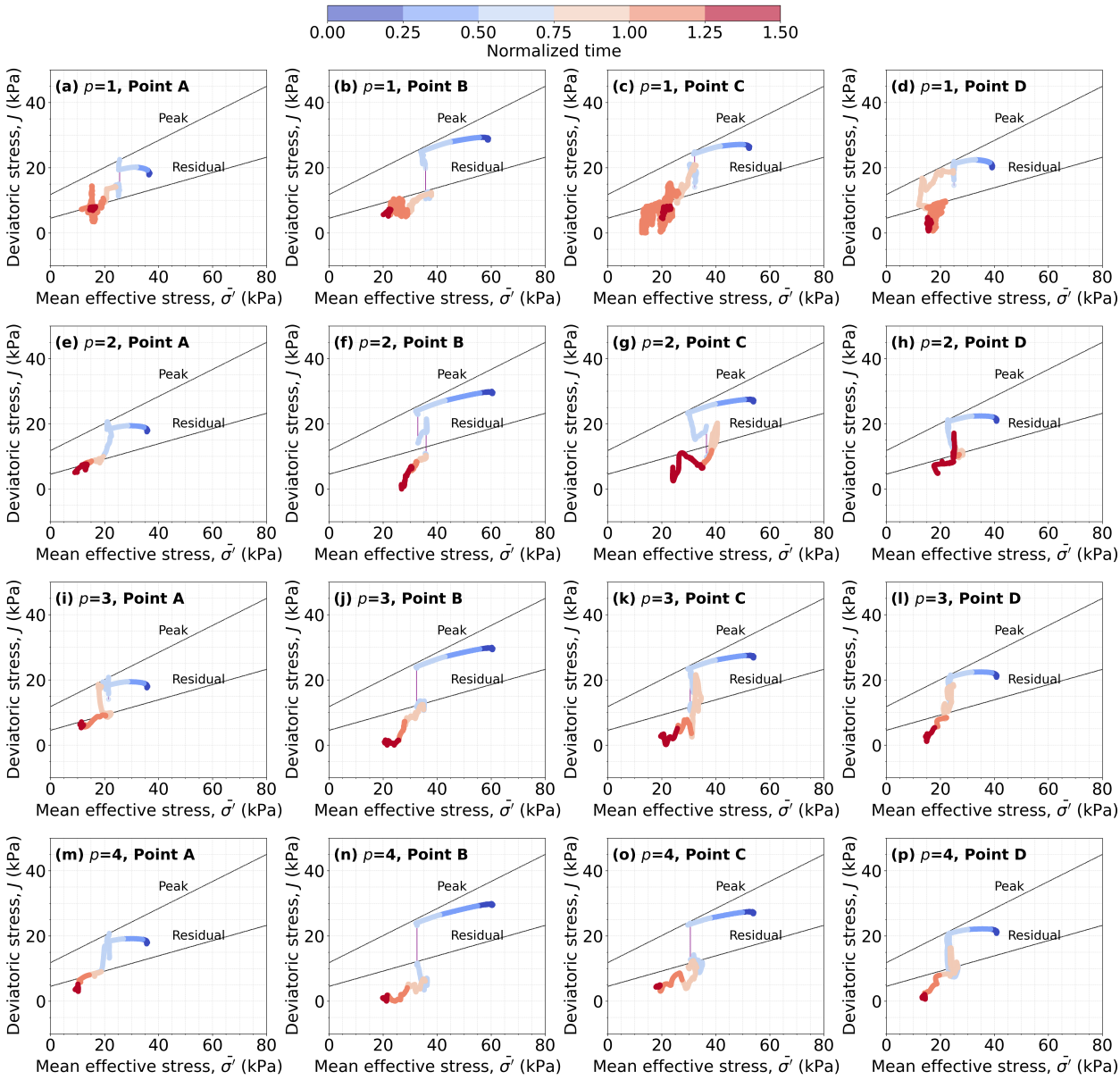

Figure 5.13: Stress path evolution with time to assess the mechanism of failure as the peak failure envelope softens to its residual for (a-d) linear (p=1), (e-h) quadratic (p=2), (i-l) cubic (p=3), and (m-p) quartic (p=4) interpolation functions for MPs at locations A-D, respectively.

5.6 Simulating shallow footing penetration in saturated soils

A strip footing penetration in saturated soil is analyzed in this section. There is an added challenge in this example: a multi-patch isogeometric framework with a moving mesh technique is employed. The multi-patch discontinuity facilitates the integration of the stresses to obtain the reaction force at the soil-foundation contact. However, the MPs that exhibit inter-patch crossing endure an abrupt discontinuity in the interpolation functions' derivatives (i.e., equivalent to a single cell-crossing occurrence in the linear MPM). As such, despite the use of a higher-order framework, inter-patch crossing error can still occur. Therefore, the aim of this section is to assess the general stability of the 2-phase multi-patch framework with respect to different interpolation orders and to investigate its behavior under various drainage conditions. First, the multi-patch geometry and material parameters are described. Second, the effective stress and excess pore water pressure contour plots are presented and discussed for quadratic (p=2) and cubic (p=3) interpolation functions. Third, the reaction forces of the soil in contact with the footing are plotted to facilitate a quantitative comparison of the simulation results. The variation in the reaction of each phase is assessed with penetration velocity and Darcy permeability.

5.6.1 Problem statement and multi-patch discretization

A 1 m thick and $\frac{B}{2}$=2 m wide footing is simulated to penetrate a 10 m thick elastoplastic soil layer. The problem is assumed to be symmetric and plane-strain. Figures 5.14 (a) and (b) present the background mesh discretization, univariate interpolation functions in each direction, and the geostatic vertical effective stress initialized using the K_0 procedure

for the quadratic and cubic interpolation functions, respectively. A prescribed velocity is applied at the MPs representing the footing, which penetrates into the soil layer. The base of the soil patch (i.e., Patch 1) is fully fixed, and the sides are normally fixed. The footing patch (i.e., patch 2) moves with the linear elastic footing while compressing the soil patch (i.e., patch 1) by means of a moving mesh technique. As a result, MPs from the soil layer cross from patch 1 to patch 2 as the footing penetrates. Note that moving mesh techniques have been employed in other MPM frameworks for simulating soil-structure interaction (e.g., penetration problem [196, 237], fully-reflective shaking table tests [225]).

The domain is discretized into 0.25 m by 0.25 m square elements, whereby each element is filled with 4 MPs. The total number of MPs in each simulation is equal to 9,728. The multi-patch framework is necessary in this example to ensure the strong enforcement of the prescribed velocity condition on the footing. The material parameters used herein are summarized in Table 5.4. Two values of intrinsic permeability are considered to simulate soils with Darcy permeability, k, ranging from 10^{-3} (fine sands) to 10^{-4} m/s (silty sands). An undrained effective stress MPM formulation is also explored herein as a critical case where no internal drainage is allowed. Under fully undrained conditions, the incremental pore water pressure, Δu, is calculated using Equation 5.17 as a function of the liquid bulk modulus, K_w, initial porosity, n_0, and the incremental volumetric strain, $\Delta\varepsilon_{Vol,MP}$.

$$\Delta u = \frac{K_L}{n_0}\Delta\varepsilon_{Vol,MP} \tag{5.17}$$

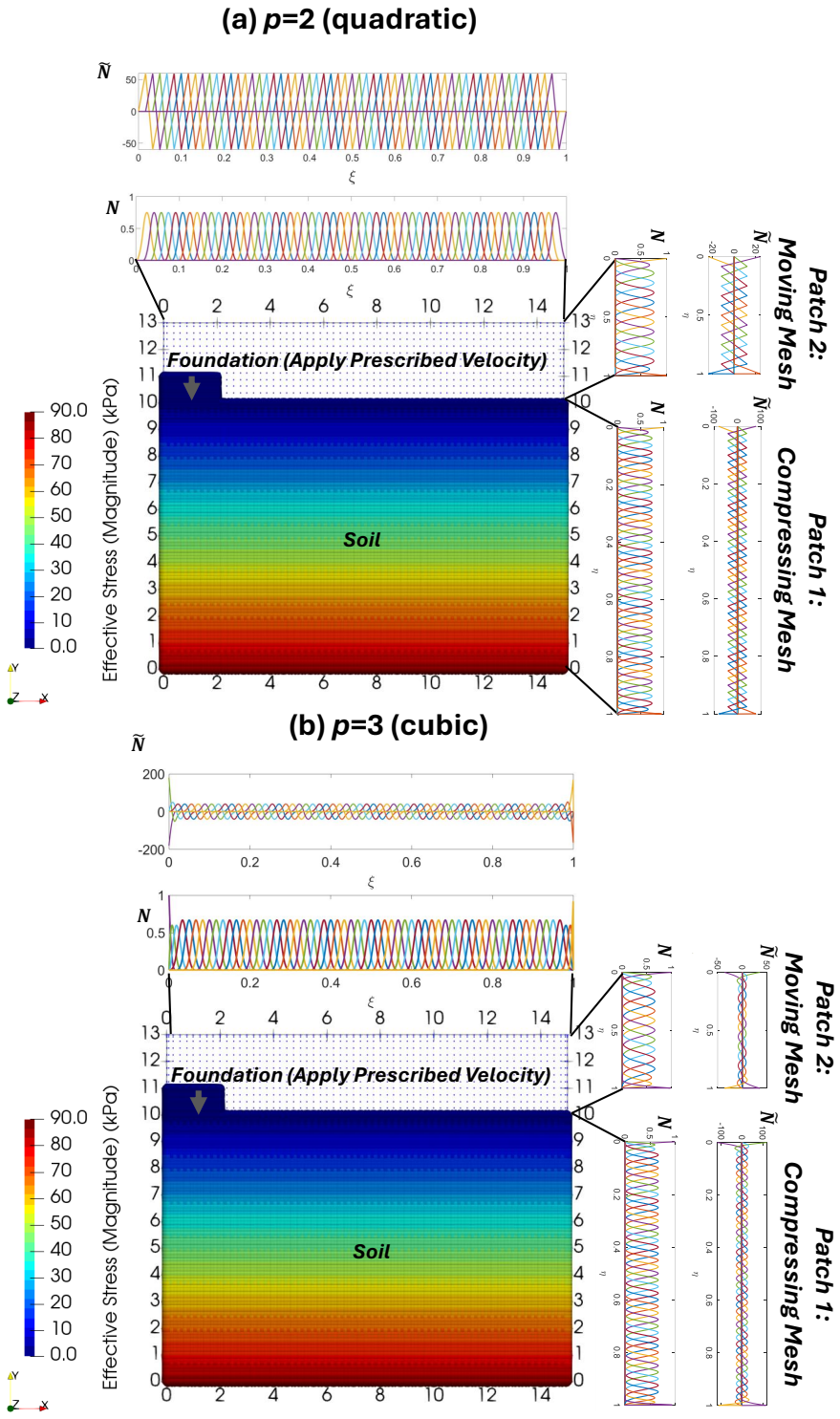

Figure 5.14: Schematic showing multi-patch geometry and geostatic effective stress distribution for (a) quadratic (p=2) and (b) cubic (p=3) interpolation functions. Prescribed velocity is applied on the foundation material, which is followed by the moving mesh (patch 2).

Table 5.4: Material parameters for the shallow footing penetration problem.

Material	Soil	Footing
Constitutive model	Tresca	Linear-Elastic
Porosity, n_0 (-)	0.3	0.3
Coefficient of lateral earth pressure, K_0 (-)	0.5	-
Intrinsic liquid permeability, κ (m^2)	10^{-10}-10^{-11}	-
Bulk modulus liquid, K_w (MPa)	2.15x10^4	-
Solid density, ρ_S (kg/m^3)	2000	2000
Liquid density, ρ_L (kg/m^3)	1000	-
Liquid dynamic viscosity, μ (kPa/s)	1x10^{-6}	-
Shear modulus, G (kPa)	9000	10,000
Poisson ratio, ν (-)	0.3	0.0
Undrained shear strength, S_u (kPa)	50	-

5.6.2 Parametric analyses with respect to interpolation function order, penetration velocity, and hydraulic conductivity

First, the effect of inter-patch cell crossing is investigated to assess stability with respect to order. Figures 5.15(a-c) and 5.15(d-f) present displacement, effective stress, and excess pore water pressure considering quadratic (p=2) and cubic (p=3) interpolation functions, respectively. The lower Darcy permeability, $k = 10^{-4}$ m/s, is used in Figures 5.15 with a penetration velocity of v=10 m/s. The displacement profile is almost identical when considering the quadratic and cubic interpolation functions. The effective stress contour plots are seen to be similar, although there is more spurious distortion when using the quadratic interpolation functions. The excess pore water pressure presents a bulb-shaped distribution with a maximum value right underneath the footing, which dissipates away from the footing. Quadratic interpolation functions yield a significantly distorted pore water pressure in those MPs that exhibit cell crossing. Similar to observations from the Selborne experiment in section 5.5, the pore pressure solution is more sensitive to p than the effective stress solution. As such, further parametric analyses herein will be performed using p =3

due to the superior stability.

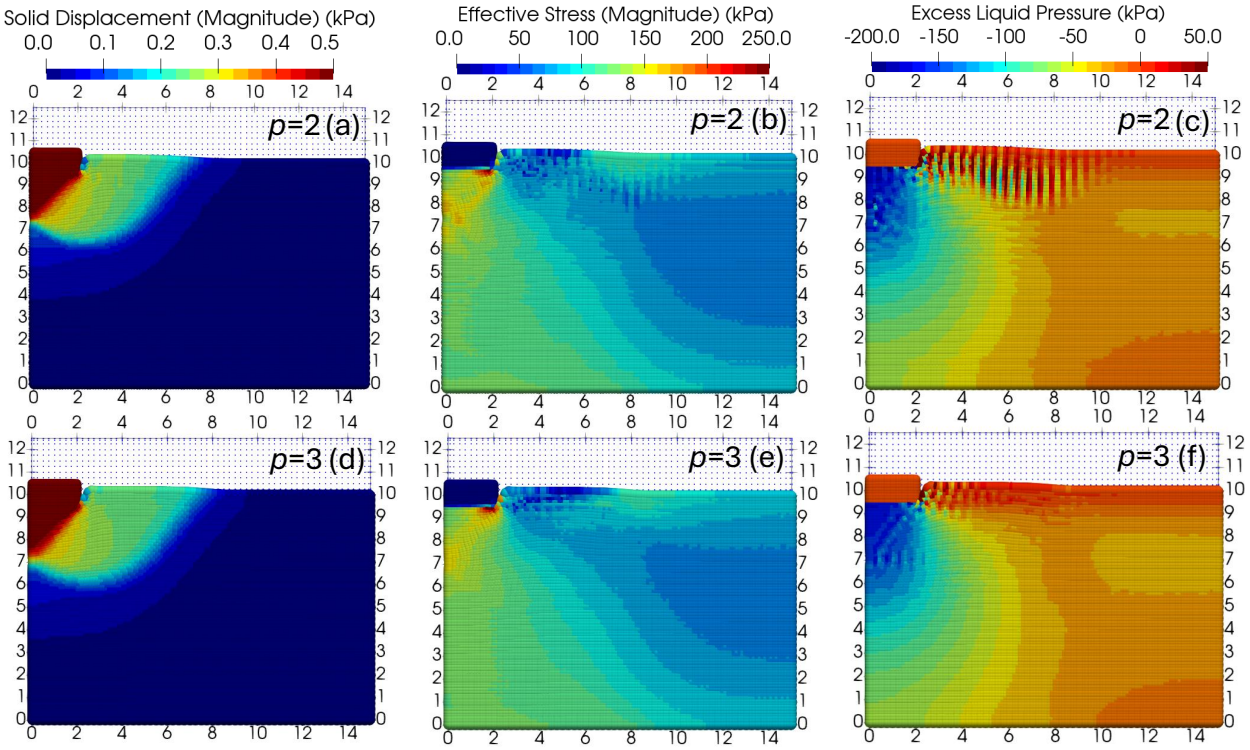

Figure 5.15: Contour plots to show solid skeleton displacement, effective stress, and excess pore pressure for 0.5 m footing penetration into silty sand (Darcy permeability, k=1x10^{-4}) with velocity, v=10 cm/s, considering (a-c) quadratic (p=2), and (d-f) cubic (p=3) interpolation functions.

The footing response and bearing capacity of the soil are assessed quantitatively by calculating the reaction force through the integration of the vertical stresses corresponding to each phase. Figure 5.16 presents the normalized reaction force evolution versus footing penetration considering different penetration velocities ranging from 1-20 cm/s for (a) $k = 10^{-3}$ m/s, and (b) $k = 10^{-4}$ m/s. Consistent with saturated soil mechanics, the liquid reaction exhibits a sudden increase as the footing begins to penetrate, which is larger as the penetration velocity increases. With further penetration, it decreases due to the dissipation of pore pressure. The solid reaction, on the other hand, increases asymptotically towards a threshold as penetration increases, as effective stresses carry a greater load. The combination of solid

and water forces represents the total reaction, which at deeper locations is consistent with the Prandtl theoretical limit [212]. For velocities higher than 10 cm/s, the reaction force of the liquid phase suffers from numerical oscillations during the first instants of penetration and tends to stabilize at higher confining stresses. This distortion in the reaction force has been observed by others in similar 2-phase formulations [196]. This is attributed to the weakly compressible nature of the liquid phase, especially at low confining pressure [77]. In addition, the Euler-Cromer time integration scheme tends to amplify high-frequency noise [202].

Figure 5.16(b) shows that decreasing the Darcy permeability reduces the rate of pore water pressure dissipation. The fully undrained velocity-independent solution in Figure 5.16(b) presents a critical case that is most consistent with the 2-phase fully-coupled solution with the lower Darcy permeability and the highest penetration velocity. Overall, the trends shown in this example present a plausible stabilized BS-MPM framework using cubic interpolation functions that can be extended to simulate geotechnical applications associated with complex penetration problems such as pile driving, in-situ testing, and ground reinforcement columns.

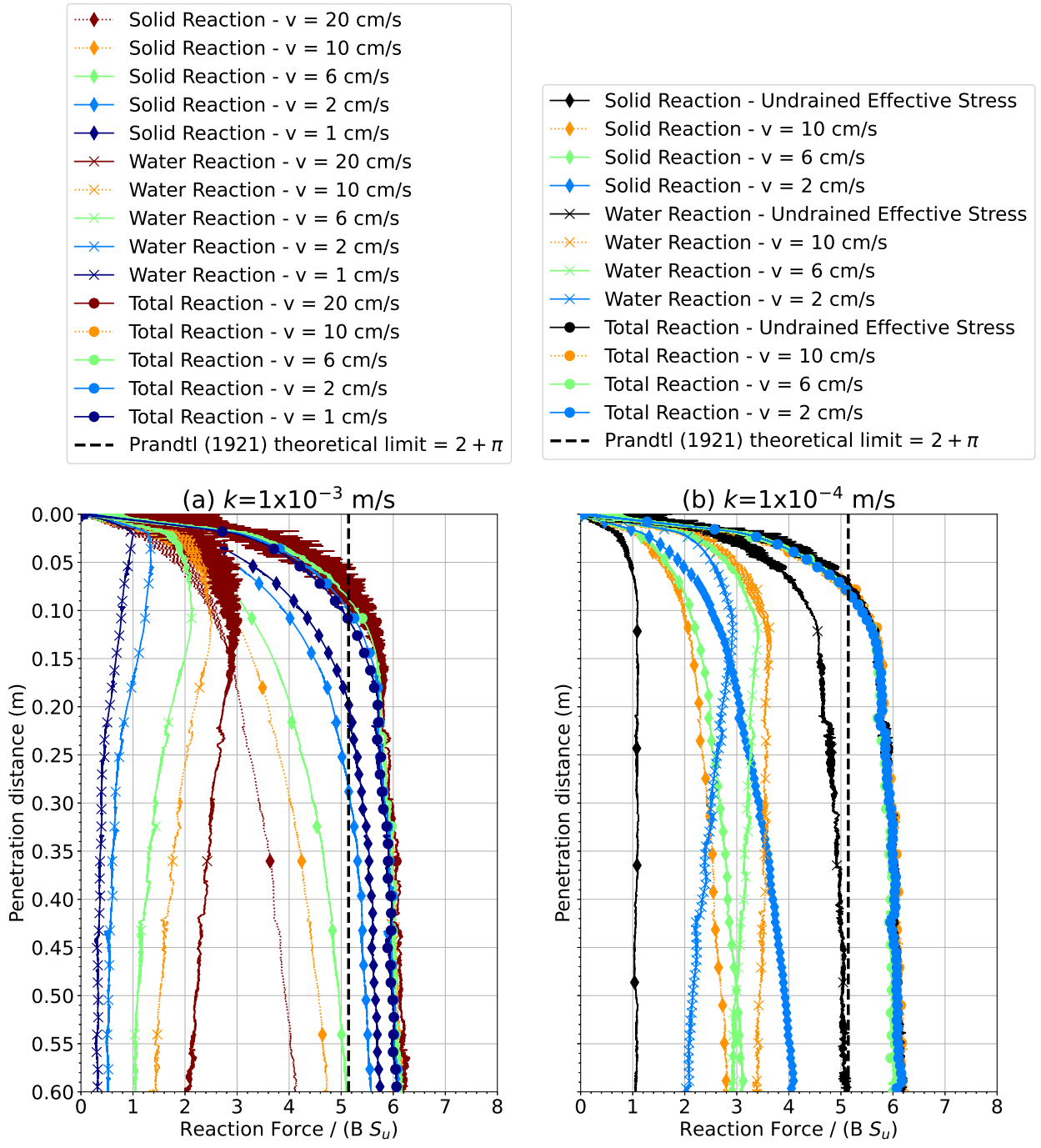

Figure 5.16: Normalized reaction force for using cubic (p =3) interpolation orders considering different penetration velocities, v. Darcy permeability is (a) k=1x10^{-3} m/s, and (b) k=1x10^{-4} m/s, as consistent with fine sands and silty sands, respectively. Prandtl [212] theoretical limit is plotted for reference.

5.7 Conclusions

The MPM has been increasingly used to simulate the deformation of saturated porous media through 2-phase formulations. Most MPM contributions involving porous media use linear interpolation functions. These are well-known to cause numerical instabilities in the large-strain solution due to the discontinuous derivatives of the interpolation function. This paper incorporates a fully-coupled 2-phase formulation within a stabilized higher-order MPM framework. Specifically, B-splines are used as interpolation functions, which enable the MPM framework to have continuous shape function derivatives across the entire patch domain. The advantages of using a higher-order B-spline MPM (BS-MPM) framework remain unclear in real-scale simulations. As such, this paper presented a series of simulations with increasing complexity to assess the advantages and limitations of employing a higher-order framework. First, the BS-MPM framework is verified using the 1D large-strain oedometer consolidation problem by comparing it to the analytical large-strain solution. It is seen that superior pore water pressure stability is achieved when orders beyond quadratic are used. Second, the real-scale Selborne slope failure experiment is simulated to further validate the 2-phase BS-MPM framework and explore the benefits of the higher-order frameworks for slope stability problems. A Mohr-Coulomb with an exponential softening law is used to simulate the progressive failure naturally observed in stiff fissured clays on sloping grounds. The manifestation of the slip surface, pore pressure generation in the slope, and deformed profile are validated with experimental data. The results obtained using the linear interpolation functions reveal internal deformation within the mobilized mass, which is attributed to excessive numerical noise. Higher-order interpolation functions present a more stable solution, with a rigid-like mobilized mass with a slightly wider shear band. The main advantage of BS-MPM is the stability in the effective stress and pore water pressure distribution, with stress path convergence achieved through the use of cubic interpolation functions. Finally,

a footing penetration into saturated soil is simulated using multi-patch BS-MPM. When using higher-order interpolation functions. Cubic interpolation functions present a favorable contribution in mitigating cell-crossing and volumetric locking in the liquid phase, despite MPs crossing from one patch to another. Trends of the normalized force reaction build-up are compared for different penetration velocities and hydraulic permeability values with reference to a fully undrained penetration problem. In summary, the higher-order BS-MPM framework is a robust framework that offers flexibility in the choice of interpolation function order and geometry with favorable stability when used in tandem with 2-phase coupled problems in geotechnical engineering.

Chapter 6

Simulating earthquake-triggered liquefaction using higher-order MPM and PM4Sand

Contents of this chapter will be submitted for consideration in Computers and Geotechnics, with the following preliminary reference: Alsardi, A., Yerro, A. and Long, C.C., 2026. Simulating earthquake-triggered liquefaction and runout using higher-order MPM and PM4Sand. Computers and Geotechnics (to be submitted).

The following authors contributed to this chapter, as follows:

- Abdelrahman Alsardi
  - Implemented the PM4Sand in the multipatch B-spline MPM numerical framework.
  - Reviewed the literature and adopted the VELACS centrifuge test by Adalier et al. [238].
  - Performed all numerical simulations from pre-processing to post-processing and analysis.
  - Prepared all figures and wrote the original draft of the manuscript.
- Dr. Alba Yerro
  - Provided invaluable feedback throughout the implementation of the framework.
  - Discussed results and troubleshooting strategies to perform successful numerical simulations.
  - Obtained research funds to enable the implementation and deployment of the PM4Sand in MPM.
  - Edited and revised the chapter.
- Dr. Christopher Curtis Long
  - Provided invaluable feedback throughout the implementation of the MPM framework.
  - Obtained research funds and computer to enable the deployment of the framework for geotechnical applications.

6.1 Abstract

Earthquake-triggered liquefaction manifestations are often associated with large-strain deformations that can pose significant risks to downstream communities and infrastructure. Recently, particle-based approaches, such as the Material Point Method (MPM) have been developed to simulate large strain runouts. However, most contributions have been limited to simple linear elastic or elastic-perfectly-plastic stress-strain behavior. State-of-the-practice constitutive models have been developed to accurately capture cyclic stress-strain behavior of soils; more prominently, PM4Sand has been developed to capture the cyclic constitutive behavior of sand with primary parameters that can be calibrated from in-situ field data. The PM4Sand model has never been incorporated in a particle-based method. In this research, the PM4Sand model is implemented in the MPM for the first time to capture the liquefaction-triggering and subsequent cyclic mobility. Two centrifuge test experiments were simulated to validate the MPM and PM4Sand framework. First, a submerged slope is simulated from the LEAP centrifuge program [239]. Second, a centrifuge experiment from the VELACS program [240] of a clay embankment overlying a saturated sand layer is simulated. Shakes of different amplitudes are applied and compared to the experimental data. For both centrifuge experiments, kinematic deformation and excess pore water generation trends generally match the experiment. In summary, this framework presents a promising tool that can capture nonlinear soil behavior and the entire deformation evolution from liquefaction-triggering to post-failure cyclic mobility.

6.2 Introduction

Earthquake-triggered landslides pose a significant risk to infrastructure due to their potential adverse effects when large deformation occurs. Small magnitude earthquakes often result in ground motions that are described with low values of intensity measures. Despite complexities in assessing the site response, soil behavior can be assumed to resemble linear constitutive behavior. The equivalent-linear approach is often used to approximate nonlinear elastic behavior to assess the site's response to dynamic shaking. This provides a practical and simplified approach to capture the corresponding combination of elastic stiffness degradation and material damping effects. The development of the Newmark method [34] benefited from advances in the equivalent-linear method to capture coupled site-response and landslide runout. However, the assumed soil behavior still corresponds to a single-phase material with no consideration of the behavior of the porous media under cyclic loading. In addition, level-ground stratification is assumed. The equivalent-linear and Newmark techniques can be adequate in practice, especially for low-risk infrastructure and small magnitude earthquakes, where there is leeway to neglect the effects of multiphase interactions and soil elastoplasticity. Alternatively, mesh-based Lagrangian numerical tools, such as the finite element method (FEM), are often used to simulate nonlinearity using elastoplastic constitutive models. These mesh-based numerical tools represent a paradigm shift from simplified techniques in geotechnical engineering practice, where only failure triggering is captured at small strains. Additionally, surface tracking is simple in mesh-based techniques, which enables the easy implementation of boundary conditions to represent field conditions under earthquake loading. However, the caveat of using these numerical approaches is that mesh-based techniques are incapable of simulating large deformations. Progress in understanding large-strain manifestations has been hindered by the lack of suitable tools to model such manifestations and the limited assessment of constitutive models at large strains.

Particle-based tools have emerged over the past two decades for geotechnical applications, enabling the simulation of the entire process of landslide instabilities. Particle-based numerical tools such as the Material Point Method (MPM) and the Smoothed Particle Hydrodynamics (SPH) method have been employed in the literature to simulate geotechnical engineering problems. This includes slope failures, installation and penetration problems, and tunnel deformations [98, 121, 196, 208]. More recently, there is interest in extending particle-based approaches to simulate earthquake-triggered landslides using MPM [57, 78, 81, 82, 197] and SPH [241, 242]. The MPM is specifically of interest because of its similarity with FEM. This also includes its capability to inherit dynamic boundary conditions developments from FEM to capture site response. However, the MPM has never been validated against centrifuge tests that simulate the deformation of liquefiable grounds under earthquake loading. The MPM has significantly progressed in incorporating multiphase formulations, including the two-phase formulation, which is important to simulate pore pressure generation and consolidation in saturated soils [119]. In addition, the geotechnical state-of-the-practice PM4Sand [110] constitutive model has never been incorporated into the MPM. The PM4Sand model is appealing due to its practicality, whereby only a primary set of parameters needs to be calibrated. In this manner, key sand parameters for liquefaction-triggering and subsequent cyclic mobility can be approximated accurately. The primary parameters include relative density and elastic stiffness, which can be calibrated using in-situ field testing data. The cyclic resistance curves also need to be calibrated to capture the number of cycles to reach liquefaction given a shear stress amplitude. A secondary set of parameters is present that can be calibrated to better capture intricate sand-specific details. This includes minimum and maximum void ratios, as well as fabric accumulation parameters.

The goal of this paper is to assess the use of the high-order MPM with advanced history-dependent constitutive models such as PM4Sand in capturing liquefaction-triggering and

subsequent deformations relative to experimental data. First, the MPM computational framework is described. Second, the PM4Sand framework is outlined, along with element-level comparison of the implementation with the open-access Opensees implementation [113, 114]. Third, the PM4Sand constitutive model is employed for the first time in the MPM framework, specifically simulating two centrifuge laboratory tests. This includes a submerged homogeneous sandy slope from the LEAP centrifuge program [239], and a clay embankment resting on a liquefiable layer of saturated sand from the VELACS centrifuge program [240].

6.3 MPM framework

The MPM is a Lagrangian-Eulerian numerical tool in which the deformation of a continuum can be simulated by a set of points, each referred to as a material point (MP). A background computational mesh is used to solve the governing equations in each time step. Nodal interpolation functions are used to map information back-and-forth between the MPs and the background mesh. An update-stress-last (USL) computational cycle is adopted herein. The momentum balance equations are solved to ultimately compute the nodal acceleration field for each phase based on the internal and applied external forces. The explicit Euler-Cromer time scheme is used to integrate the nodal acceleration to velocity. The velocity field and the interpolation function derivatives are used to calculate the strain tensor for each MP. The strain and the state variables are used as constitutive model inputs, which compute the stress for each MP. The global positions and MP displacements are updated using the velocity field. In this paper, a hydromechanical 2-phase B-spline higher-order MPM framework, as described in Alsardi et al. [243, 244] and Chapter 5 in this dissertation, is used to combat cell-crossing error. The volumetric strain and pore pressure increment

smoothing are implemented to mitigate volumetric locking.

6.4 PM4Sand constitutive model

This section aims to summarize the most pertinent features of the PM4Sand constitutive model based on the formulation by Boulanger and Ziotoupolou [110, 111], as implemented in the MPM framework. Further details and formulation equations are provided in Appendix E of this dissertation. The critical state framework of PM4Sand uses the relative state parameter as formulated by Bolton [21]. It is noteworthy that PM4Sand is effectively a simplification and empirical calibration of the Sanisand bounding surface plasticity model by Dafalias and Manzari [32]. As such, PM4Sand employs a simplified 2D formulation of the bounding, dilatancy, and critical state surfaces with a kinematic hardening yield surface. Stress reversal considerations are also taken to more accurately capture the hardening evolution of the plastic modulus throughout dynamic loading and prevent the drift commonly seen in Sanisand. Stress reversal is detected by means of the back-stress ratio tensor and the yield surface normal under plastic loading [111]. Nonlinear elastic modulus calculation in PM4Sand is also a function of the mean effective stress. Plastic strain components are calculated using the loading index with an associative hardening rule to update the back-stress ratio. The calculation of the plastic modulus in PM4Sand is also separated into dilation and contraction, contrary to Sanisand. This prevents the one-directional plastic strain locking in PM4Sand. Fabric effects are incorporated in the entire framework, including plastic modulus, elastic modulus, and dilatancy. The dilatancy calculation split also enables different expressions for fabric accumulation in contraction versus dilation. Finally, PM4Sand is equipped with a simple post-consolidation switch. This switch is activated after the application of the ground motion to force a reduced elastic modulus of the soil material, thereby

better capturing post-liquefaction reconsolidation predictions.

It is important to note that the integration scheme can slightly alter the response of PM4Sand [113]. The original implementation by Boulanger and Ziotopoulou [111] was performed using the Forward Euler integration scheme. Based on a study of four different integration schemes in Opensees [114], Chen [113] proposed the use of the Modified Euler integration scheme for bounding surface plasticity models like Sanisand and PM4Sand. As such, the explicit iterative Modified Euler integration scheme is adopted herein with automatic error control [213]. This research presents the first time the PM4Sand is used in a large-strain particle-based framework. The strain increment input to the constitutive model is limited to 10^{-7} as a maximum for each tensor component. This is because large strain increments, allowed in the MPM framework, can render the model unstable due to the high nonlinearity exhibited in the stress evolution [113]. Stress drift check and corresponding correction for consistency are also included to ensure model stability.

6.4.1 Verification of PM4Sand

The PM4Sand model was developed to capture the empirical trends seen during liquefaction (cyclic mobility) case studies pertinent to geotechnical engineering practice [111, 113]. This includes capturing the cyclic resistance ratio (CRR) against liquefaction-triggering, the response to irregular cyclic loading produced during earthquakes, and the effect of confining stress and sustained static shear stresses, among other relationships. To verify our UMAT implementation of PM4Sand, the work from Boulanger and Ziotopoulou [111] and Chen [113] is reproduced and compared using the Incremental Driver platform [245]. Table 6.1 presents the primary set of parameters used here, identical to those used by Boulanger and Ziotopoulou [111] and Chen [113]. The in-situ, D_R, value is calibrated based on the Stan-

Table 6.1: PM4Sand primary parameters based on calibration by Boulanger and Ziotopoulou [111].

Sand description	Relative Density, D_R (%)	Small-strain shear modulus coefficient, G_0 (-)	Contraction rate parameter, h_{po} (-)
Loose	35	476	0.53
Medium	55	677	0.40
Dense	75	890	0.63

dard Penetration Test (SPT) $N_{1,60,cs}$ blow count value. The shear modulus coefficient, G_0, is based on the in-situ shear wave velocity, V_S, which can be used to calculate the shear stiffness of the material. The contraction rate parameter, h_{po}, is the only parameter that needs experimental cyclic simple shear data to calibrate the number of cycles to reach liquefaction. The reader should refer to the Boulanger and Ziotopoulou [111] for details regarding the secondary parameters.

Parametric analysis of the stress-strain response of this model involves varying the relative density, D_R, along the corresponding primary parameter set for loose, medium, and dense sands as shown in Table 6.1. Since the current PM4Sand implementation follows the same Modified Euler integration scheme of Chen [113], the stress-strain plots are verified against their results. The implementation of PM4Sand by Chen [113] is also the only open-source implementation in the literature (in C++), which offers greater transparency in ensuring the identical formulation of our Fortran UMAT. In particular, stress-strain plots for monotonic and cyclic undrained stress-controlled plane-strain direct simple shear (DSS) test are analyzed relative to those by Chen [113]. Figure 6.1 presents the undrained monotonic DSS stress-strain and stress path results for loose, medium, and dense sands for an initial vertical effective stress, σ'_{vc}= 0.25, 1, 4, and 16 atm as compared to Chen [113]. Overall, the results from the UMAT PM4Sand implementation are consistent with Chen [113]. At high σ'_{vc}, strain-softening is observed for the loose sand material (Figure 6.1(a)), and strain-hardening

is observed for the dense sand material (Figure 6.1(c)). Figure 6.2 shows the comparison between the cyclic undrained DSS UMAT implementation (reported for 20 cycles) and the results from Chen [113] (reported for a total of 4 cycles). There is a good fit for the medium sand material when considering the cyclic undrained DSS test (Figures 6.2(c) and 6.2(d)). However, small discrepancies are observed primarily for the loose (Figures 6.2(a) and 6.2(b)), and dense (Figures 6.2(e) and 6.2(f)) sand materials.

Despite several attempts to ensure that the Fortran UMAT implementation is identical to the C++ implementation in Opensees, Figures 6.1 and 6.2 still show small discrepancies. This can raise concerns about the reproducibility of PM4Sand's element-level results across programming languages. Ultimately, to improve the transparency of this work, it was decided to show the discrepancies and avoid any type of model reformulation or tweaking input parameters.

To further ensure the consistency of the Fortran implementation relative to that of Chen [128], Figure 6.3 presents the cyclic stress ratio (CSR) versus the number of cycles to achieve a 3% shear strain for different relative densities and confining pressures. This is achieved by simulating cyclic direct simple shear tests, and the number of cycles until liquefaction is reported as an output. The value of CSR is equal to the single amplitude shear stress (τ) normalized by the initial vertical confining stress values (σ'_{vc}). Three values of σ'_{vc} are adopted, ranging from 1 atm to 8 atm. Despite minor discrepancies [113], the results are very similar and follow the trend of decreasing number of cycles until 3% strain as CSR increases for the different vertical confining stresses. Given the significant nonlinearity and sensitivity of PM4Sand to implementation details, the new implementation is considered valid.

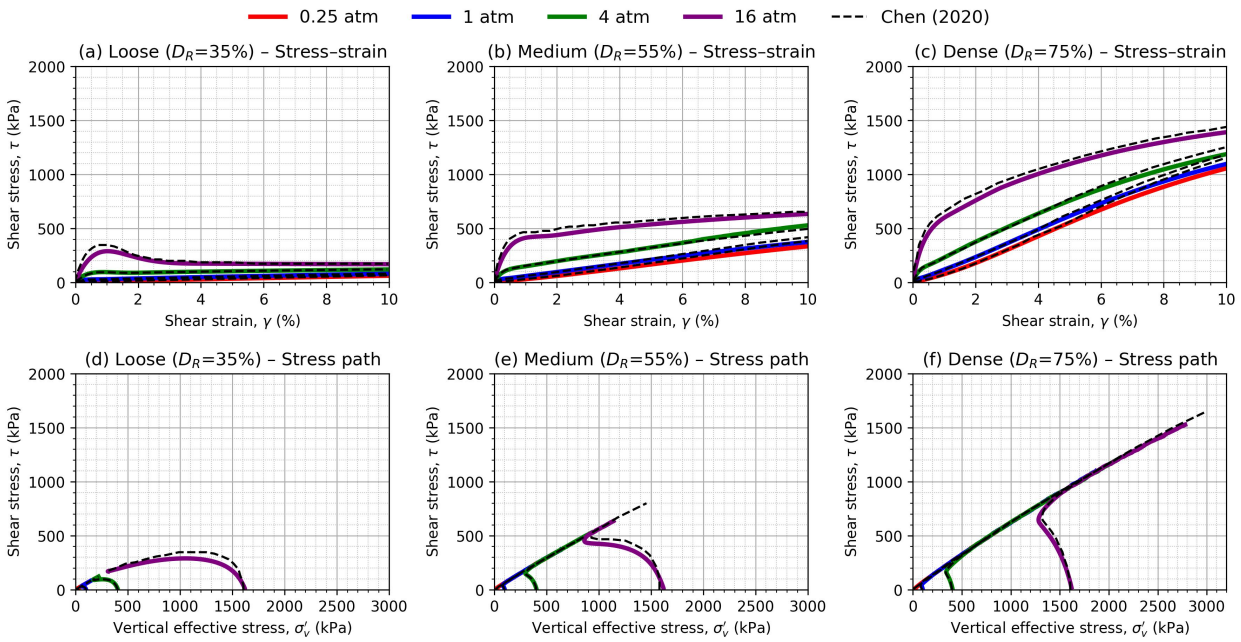

Figure 6.1: Comparison of monotonic undrained stress-strain and stress paths with the implementation in Opensees [114] by Chen [113]. The results are presented for different initial vertical effective stresses, σ'_{vc}=0.25, 1, 4, and 16 atm with K_0=0.5.

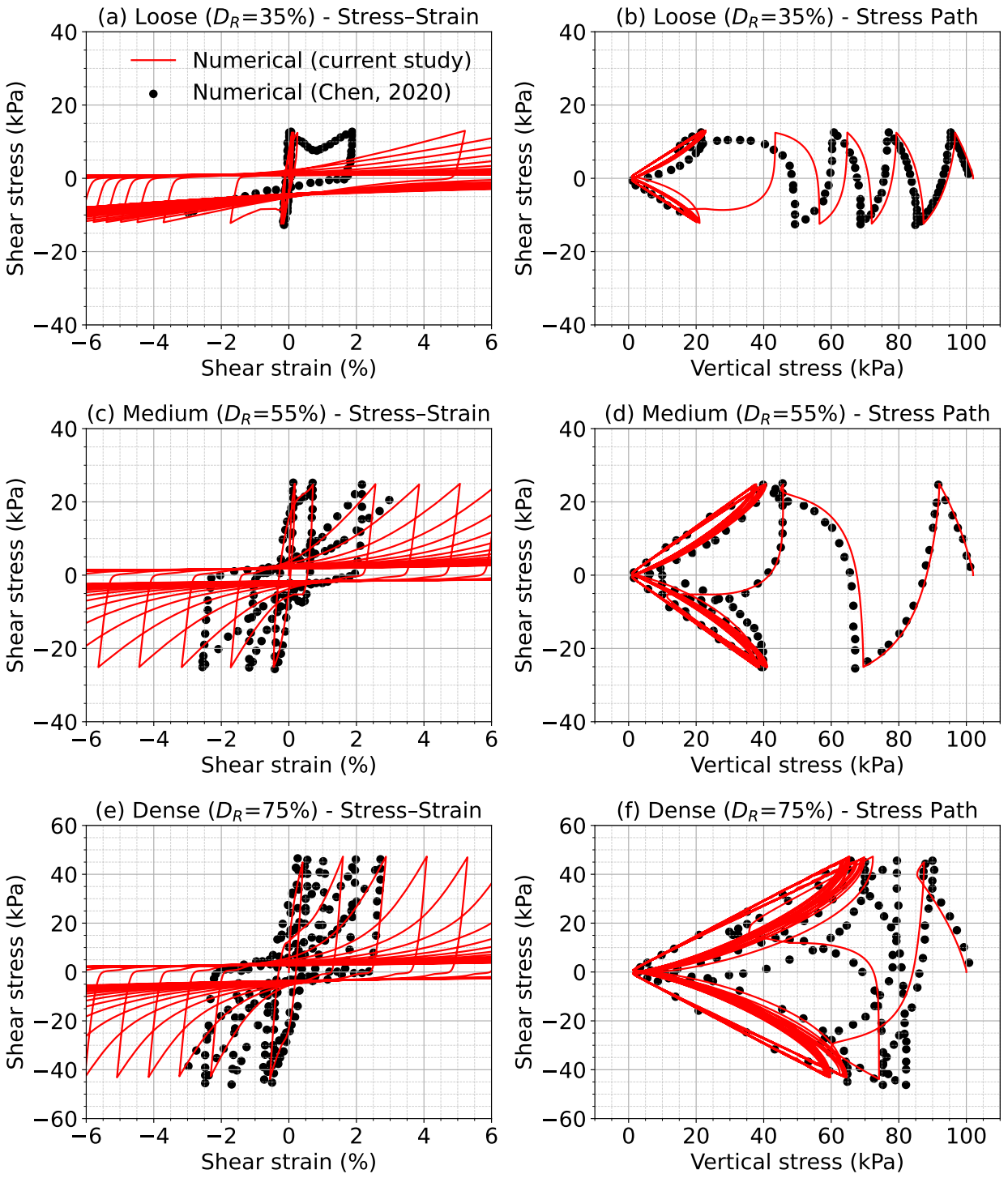

Figure 6.2: Comparison of the cyclic undrained direct simple shear stress-strain and stress paths with the implementation in Opensees [114] by Chen [113]. The initial vertical stress is σ'_{vc}=1 atm (i.e., 101.3 kPa) under K_0=0.5 conditions.

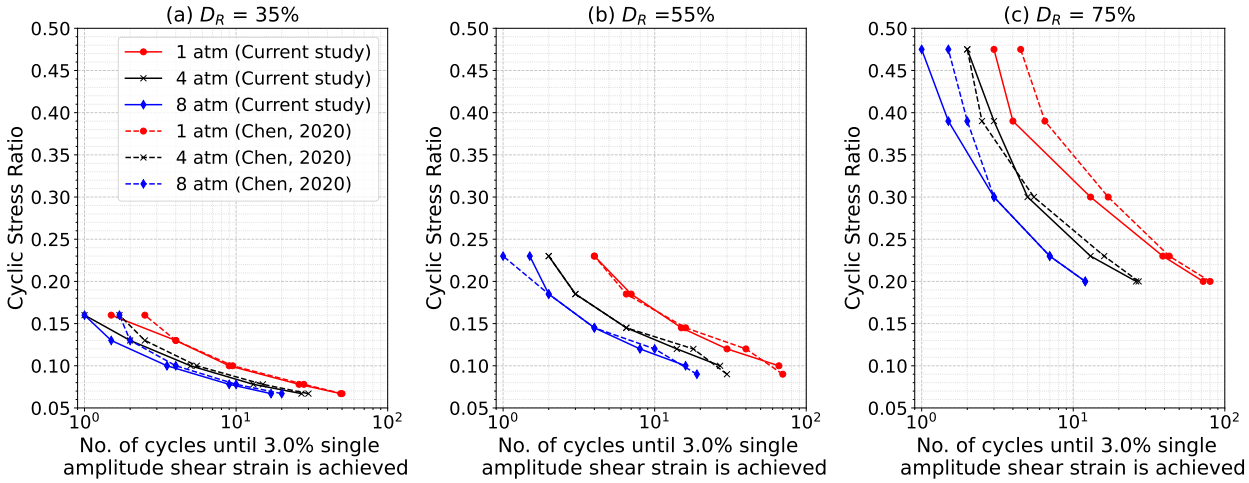

Figure 6.3: Cyclic stress ratio (CSR is the ratio of shear stress to confining vertical stress, i.e., $\frac{\tau}{\sigma'_{vc}}$) versus number of cycles to achieve a 3% shear strain for (a) loose, (b) medium, and (c) dense sand. Results are presented for normal vertical stresses, σ'_{vc}, equal to 1, 4, and 8 atm.

6.5 Simulating earthquake-triggered liquefaction in a homogeneous sandy slope from the LEAP centrifuge experiment.

The LEAP (Liquefaction Experiments and Analysis Projects) centrifuge experiments were performed to create high-quality data for validating numerical models used in Geotechnical Earthquake Engineering. The experiments are a major international contribution to assessing reproducibility using global centrifuge facilities. In this work, we adopt the LEAP-UCD3 centrifuge experiment of a submerged slope of Ottawa F-65 sand performed at the University of California, Davis (UCD) [239]. First, the MPM is described, including geometry, discretization, and input ground motion. Second, the numerical results are compared to the experimental data by Kutter et al. [239].

6.5.1 MPM model of the centrifuge experiment

The geometry of the trapezoidal slope and the corresponding sensor locations are shown in Figure 6.4 as per the MPM model discretization ("P" for pressure transducers, "AH" for the accelerometers, and a potentiometer in the middle of the slope to measure runout). This simulation is performed at prototype scale. The rectangular background mesh is discretized into 100 by 27 elements in the horizontal and vertical directions, respectively, with 8,000 MPs. Single-patch cubic interpolation functions are used to eliminate cell-crossing error [243]. The slope is assumed to be saturated and is simulated using the 2-phase single-point formulation. The PM4Sand calibration parameters used are presented in Table 6.2 as per Montgomery and Ziotoupolou [246]. The dry density, ρ_d, and hydraulic conductivity, k, of the sand is equal to 1600 kg/m^3 and 1.1x10^{-4} m/s. The Gravity stresses are initiated assuming linear-elastic behavior with a fixed base and normally fixed lateral sides. The constitutive model is then changed to PM4Sand, and quasistatic convergence is achieved. Fully reflective dynamic boundary conditions are then applied to induce the horizontal shaking performed in the centrifuge experiment, and the background mesh is moved to follow the input motion. The base of the model remains normally fixed. Details of the boundary condition implementation are described in Alsardi et al. [57]. The input applied ground motion is shown in Figure 6.5, which comprises a wavelet functional form.

Table 6.2: Parameters of the F-65 Ottawa sand used in the LEAP UCD3 centrifuge experiment.

Material	Relative Density, D_R (%)	Small-strain shear modulus coefficient, G_0 (-)	Contraction rate parameter, h_{po}
PM4Sand	65	670	0.1

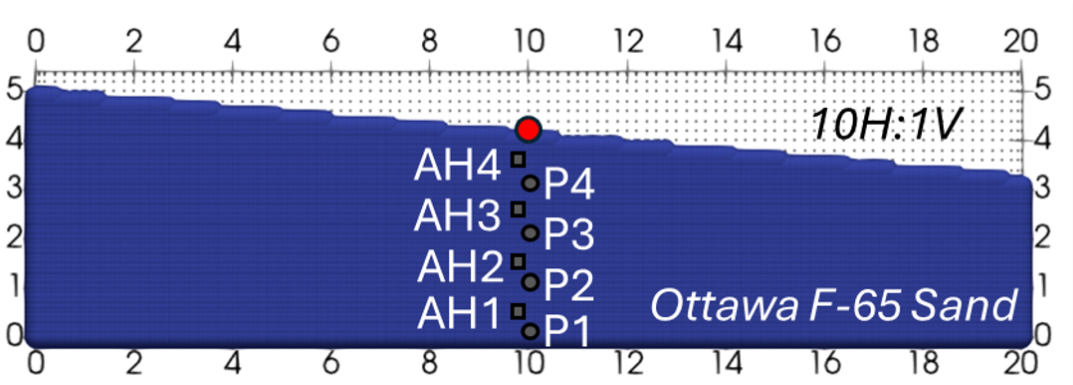

Figure 6.4: MPM Slope cross-section and sensor configurations of the UC3 LEAP centrifuge experiment.

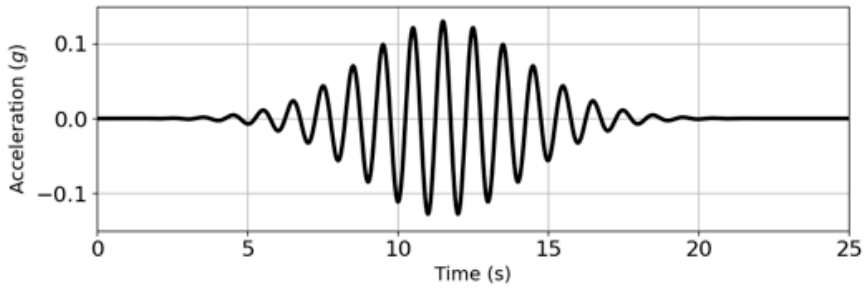

Figure 6.5: Input acceleration-time in the simulation as used in the LEAP UCD3 centrifuge test.

6.5.2 Results of the numerical model compared with centrifuge experiment.

The numerical and experimental acceleration response of the slope are compared at different depths in Figure 6.6. The numerical acceleration-time plots are consistent with the experiment. Larger peak accelerations are observed at shallower depths (Figure 6.6(c) and 6.6(d)). As such, the MPM and PM4Sand models present a satisfactory match when comparing the site response results with the experiment. The excess pore pressure, Δu, and vertical effective stress, σ', results are presented in Figure 6.7. Despite discrepancies in numerically

capturing the point of initiation, the general Δu trends and values match the experiment. Larger Δu is generated in deeper transducer P1 (Figure 6.7(a)) as compared to shallower transducers. The σ' evolution is also presented in Figure 6.7. Liquefaction triggering occurs when the pore water pressure ratio ($R_u = \Delta u/\sigma'$) reaches one, which indicates the complete transfer of the effective stresses in the solid skeleton to pore water pressure. Subsequently, cyclic mobility deformations are accumulated after $R_u = 1$ is reached. Contour plots of Δu and σ' are presented in Figure 6.8. Maximum Δu is generated at the base of the model (6.8(f)). The runout is plotted for the surface midpoint of the slope as shown in Figure 6.9. Contour plots of the displacement magnitude at the end of shaking are shown in Figure 6.10. This validation example using MPM and PM4Sand demonstrates a stable numerical framework consistent with centrifuge experimental observations.

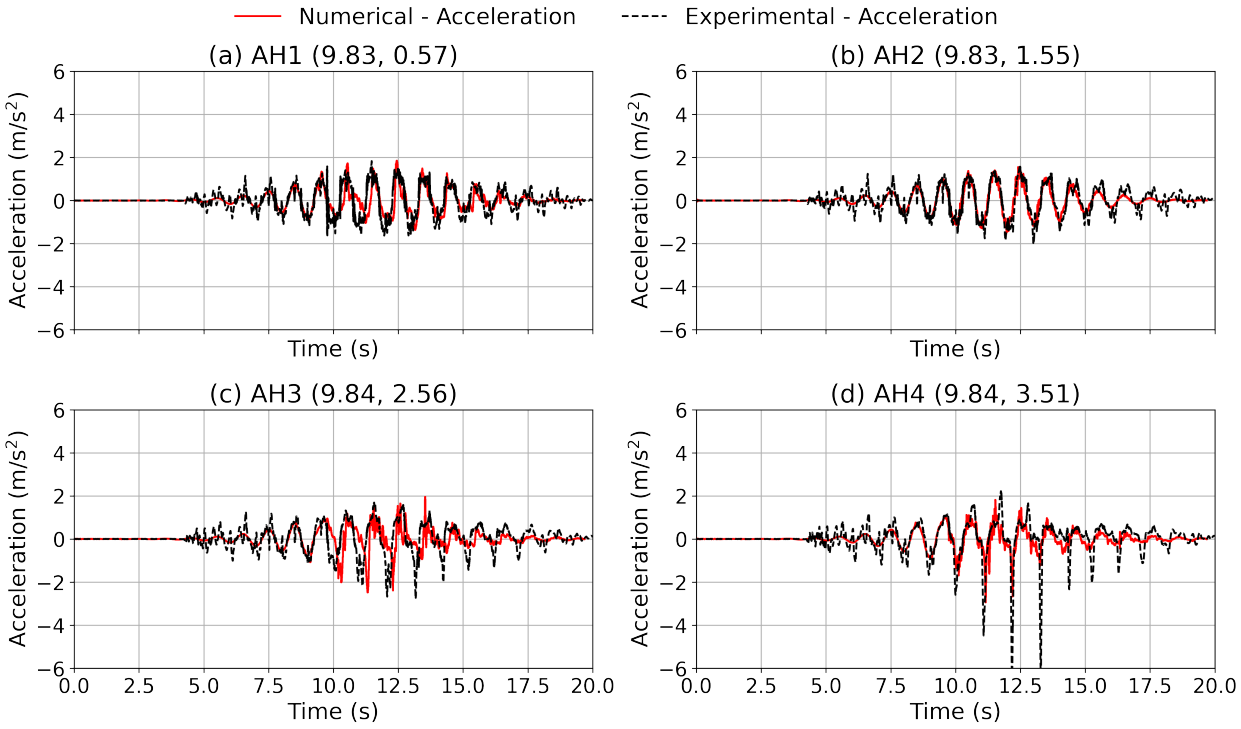

Figure 6.6: Acceleration response of accelerometers located in (a) AH1 (deepest), (b) AH2, (c) AH3, and (d) AH4 (shallowest) in the middle of the LEAP UC3 centrifuge configuration.

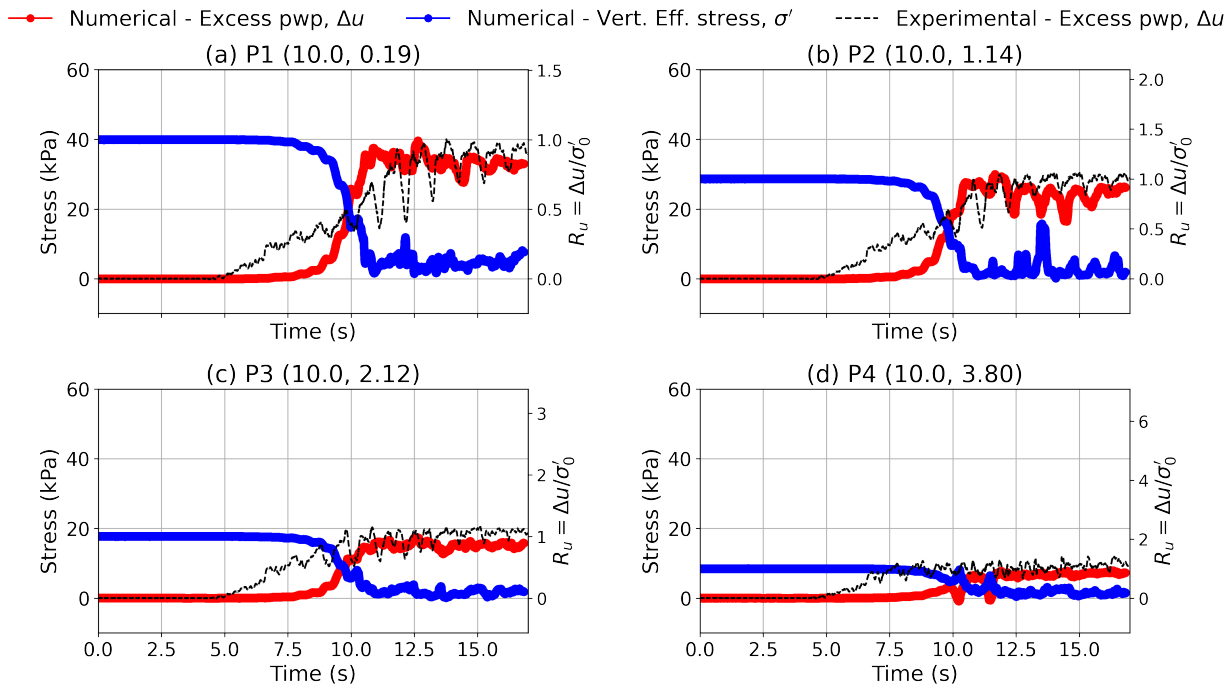

Figure 6.7: Excess pore water pressure evaluated at pore pressure transducers located at (a) P1 (deepest), (b) P2, (c) P3, and (d) P4 (shallowest) in the middle of the LEAP UCD3 centrifuge configuration.

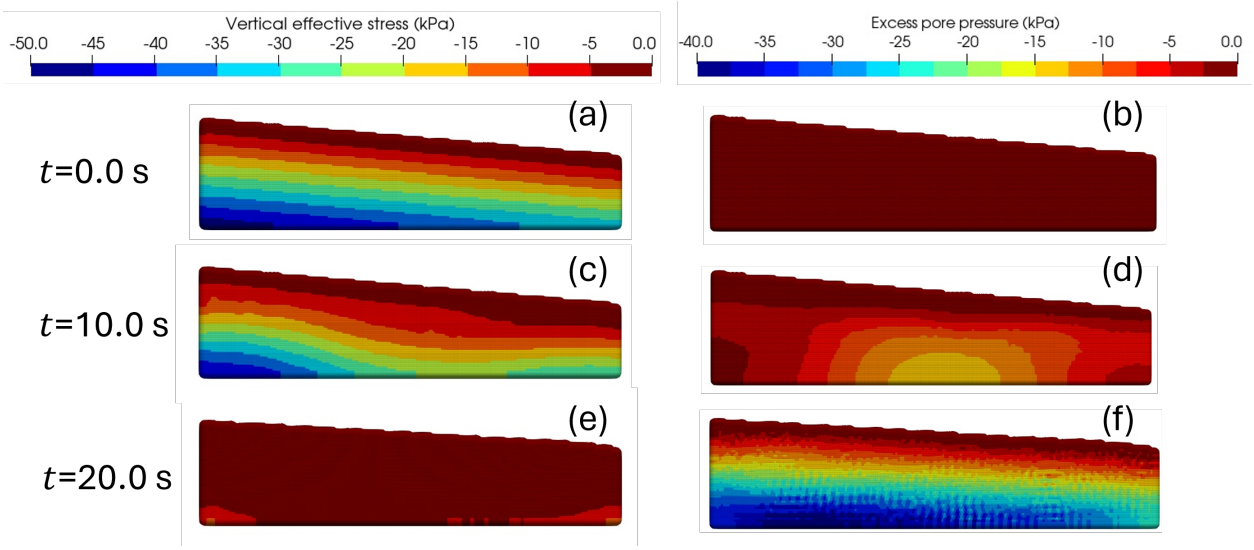

Figure 6.8: Vertical effective stress and pore pressure evolution within the LEAP UCD3 slope.

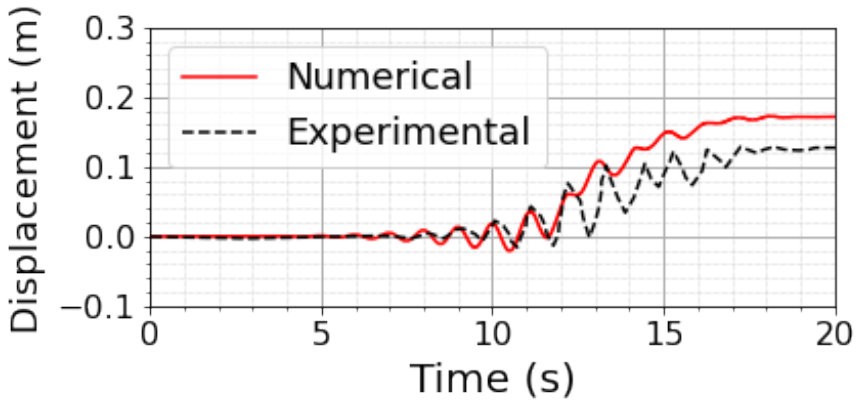

Figure 6.9: Runout of the middle MP (x=10 m, y=4 m) on the slope's surface as compared with the experimental runout at the same location.

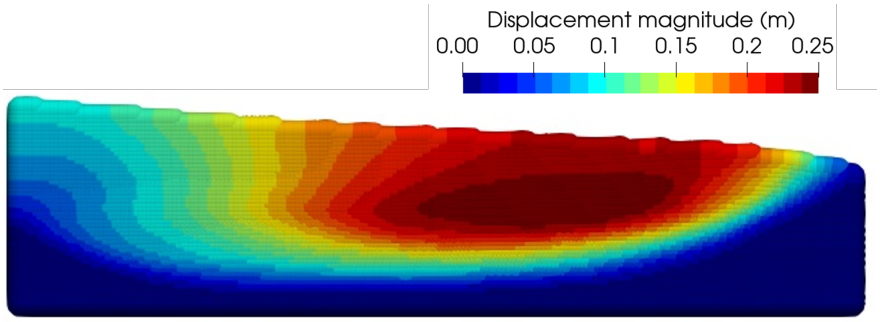

Figure 6.10: Contour plot of displacement magnitude within the LEAP UCD3 slope at the end of shaking.

6.6 Simulating earthquake-triggered liquefaction of sand underlying a clay embankment in a centrifuge test

A multilayered centrifuge test is used to further validate the PM4Sand implementation in the higher-order MPM. A large-deformation centrifuge test from the NSF-funded VErification of Liquefaction Analyses by Centrifuge Studies (VELACS) testing program [1, 238, 240] is adopted for reference. Specifically, the centrifuge model by Adalier et al. [238] is considered, in which a clay embankment with a trapezoidal geometry (4.5 m high and 5.75 m wide, with

a 1:1 slope on both sides) is built on a 6 m deep, saturated, loose Nevada sand foundation layer. In the following subsections, the MPM model description is provided first. This includes geometry, material parameters, and a sinusoidal ground shaking record. Second, the MPM numerical results are described and compared to experimental data from Adalier et al. [238].

6.6.1 MPM model of the centrifuge experiment

Figure 6.11 presents the simulation geometry and sensor locations ("P" for pressure transducers and "AH" for the accelerometers). This simulation is performed at prototype scale. The clay embankment is described by an elastic-perfectly-plastic Mohr-Coulomb model with the following material parameters based on Dinesh et al. [247], and Hoang et al. [241] as shown in Table 6.3. The dry density of the clay is ρ_d=1630 kg/m^3. The sand layer is described using the PM4Sand model as per the parameters shown in Table 6.4. The PM4Sand parameters are consistent with Dinesh et al. [247] except h_{p0}, which was increased to match the number of cycles in the experimental cyclic simple shear test. Hydraulic conductivity, k, of Nevada sand is 6.6x10^{-5} m/s, consistent with Hoang et al. [241]. In the centrifuge test by Adalier et al. [238], three sinusoidal shakes are adopted. Shake 1, shake 2, and shake 3 have the same frequency of 1.6 Hz, with ten load cycles, although scaled with acceleration amplitudes of 0.09g, 0.18g, and 0.3g as shown in Figure 6.12. Appropriate time gaps were allowed in between the shakes to allow the pore water pressure to dissipate and effective stresses to re-stabilize into a geostatic configuration.

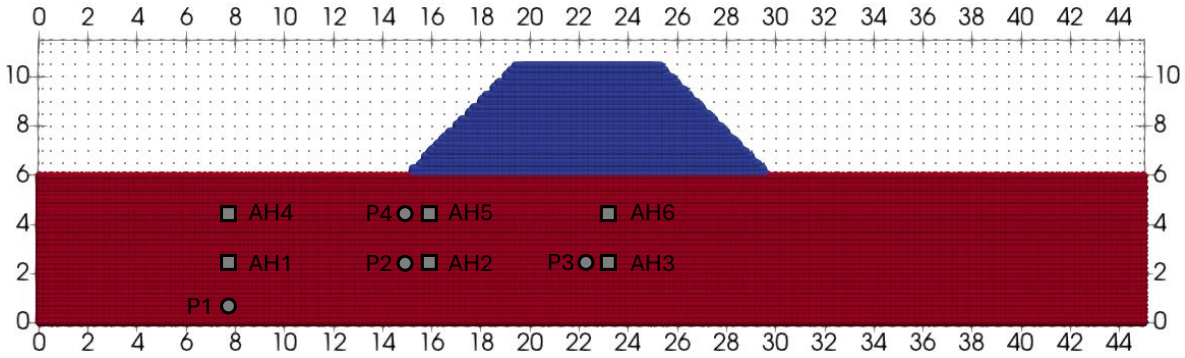

Figure 6.11: Centrifuge test geometry consistent with Adalier et al. [238] where a clay embankment is built on top of a layer of saturated Nevada sand. Acceleration transducers are labeled AH1-AH6. Pore pressure transducers are labeled P1-P4.

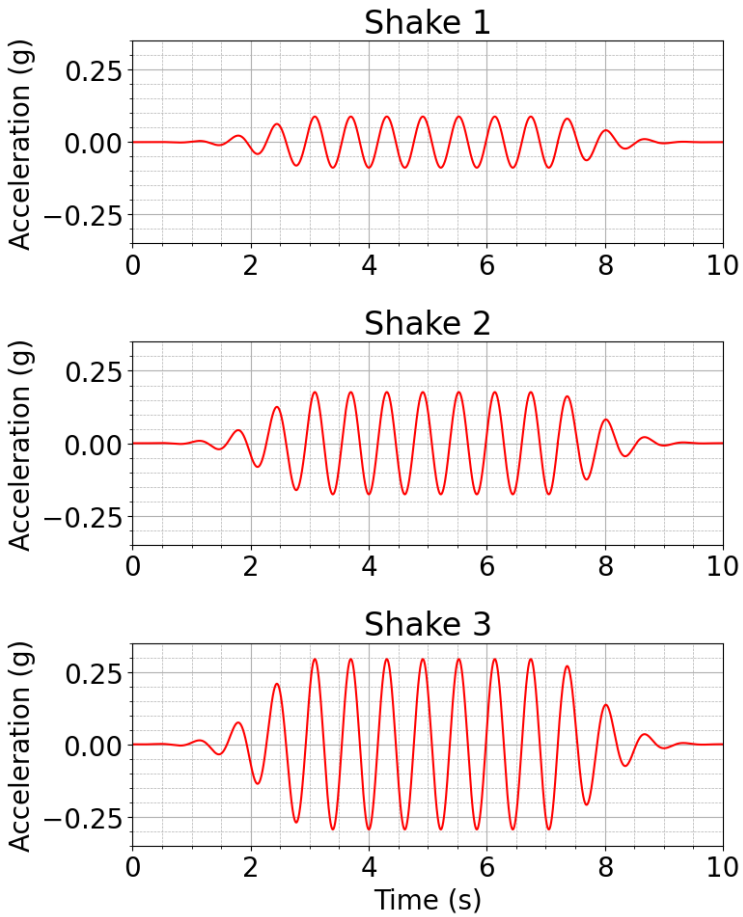

Figure 6.12: Input acceleration-time in the simulation as used in the VELACS centrifuge test.

Table 6.3: Parameters of the clay used in the VELACS centrifuge experiment.

Material	Small-strain shear modulus coefficient, G_0 (-)	Poisson ratio, ν (-)	Cohesion, c' (kPa)	Friction angle, ϕ (degrees)
Clay	197	0.3	22	31

Table 6.4: Parameters of the Nevada sand used in the VELACS centrifuge experiment.

Material	Relative Density, D_R (%)	Small-strain shear modulus coefficient, G_0 (-)	Contraction rate parameter, h_{po} (-)
PM4Sand	40	726	0.05

A single patch with cubic interpolation functions is adopted with a rectangular background mesh of 45 m by 11 m, discretized into 90 by 23 elements. Each element is approximately filled with 4 MPs initially located at their Gauss point locations, with a total number of 11,386 MPs. The sand material is simulated using the 2-phase single-point formulation, while the clay is simulated using the 1-phase formulation. Gravity stresses are initiatized using the K_0 procedure, assuming a K_0 value of 0.5. The base of the model is fully fixed, and the lateral sides are normally fixed. A quasistatic convergence step is performed with a 75% homogeneous local damping to achieve a stable geostatic stress field. After the initiation of gravity stresses, the boundaries of the centrifuge box are simulated using a non-zero kinematic boundary condition that applies fully reflective prescribed kinematics, mimicking the conditions of the centrifuge. As such, acceleration, velocity, and displacement solutions are enforced as per the applied ground motion. Similar to the previous example, the non-zero kinematic condition is applied to generate the horizontal shaking, while the base of the model remains normally fixed. The background mesh is moved to follow the applied ground motion.

In the centrifuge experiment, the three shakes were applied consecutively, allowing sufficient

time between shakes for pore pressure dissipation and restabilization [238]. The time allowed between the shakes was undisclosed by the authors of the experiment [238]. In this manner, there is cumulative deformation that is incurred with each shake. It is essential to note that experimental data are available only for shake 3, which is the one used for comparison in this study. In the current numerical study, the shakes are applied separately. There are several reasons for this decision. First, this reduces the computational cost as the analysis is restricted to the coseismic deformation (i.e., deformation during the ground motion). Also, the three separate simulations are run concurrently, which reduces the overall analysis time for an initial check of the boundary value problem.

6.6.2 Results of the numerical model compared with centrifuge experiment.

Figure 6.13 presents the numerical results of the acceleration response with time at points AH1-AH6. The accelerometer data from the sensor are plotted with the MPM results for shake 3. The acceleration response exhibits a trend that matches the experimental data. Additionally, the increase in shaking amplitude from shake 1 to shake 3 leads to a higher peak ground acceleration (PGA) response.

Figure 6.14 presents the excess pore pressure for each of the shakes. Pore pressure generation occurs fastest during shake 3, as it has the highest shaking amplitude. However, the trends are very similar, as liquefaction is reached in all three shakes. Greater hydrodynamic excess pore water pressures are present during shake 3, which manifests in a high-frequency pore water oscillation. However, this oscillation is present only during shaking and is not observed during the initial dissipation.

Contour plots of the pore water pressure evolution are presented in Figure 6.15. Pore pressure

accumulation occurs at the base of the model under the clay layer (Figure 6.15(o)). This location initially has the greatest vertical effective stress, which is directly transferred to the pore fluid as liquefaction manifests. The pore pressure ratio, r_u, distribution at the end of shake 3 is shown in Figure 6.13(t). Liquefaction begins at shallow depths at both sides near the embankment, with the eventual liquefaction of the sand at the base of the model under the embankment. As such, the sand layer almost entirely liquefies except at the interface between the embankment and saturated sand. The region below the embankment with the largest vertical effective stress exhibits the largest pore-water pressure generation.

Figure 6.16 presents a comparison of the numerical deformed profile with the experimental data after shake 3. Although the numerical model overestimates the deformation, the deformed profile is reasonable when compared with the experiment. Hoang et al. [241] reported an even greater overestimation in the captured displacements when using SPH and Sanisand. Accordingly, the deformed profile is considered satisfactory, given the simulation's qualitative nature and the use of independent ground-motion shakes.

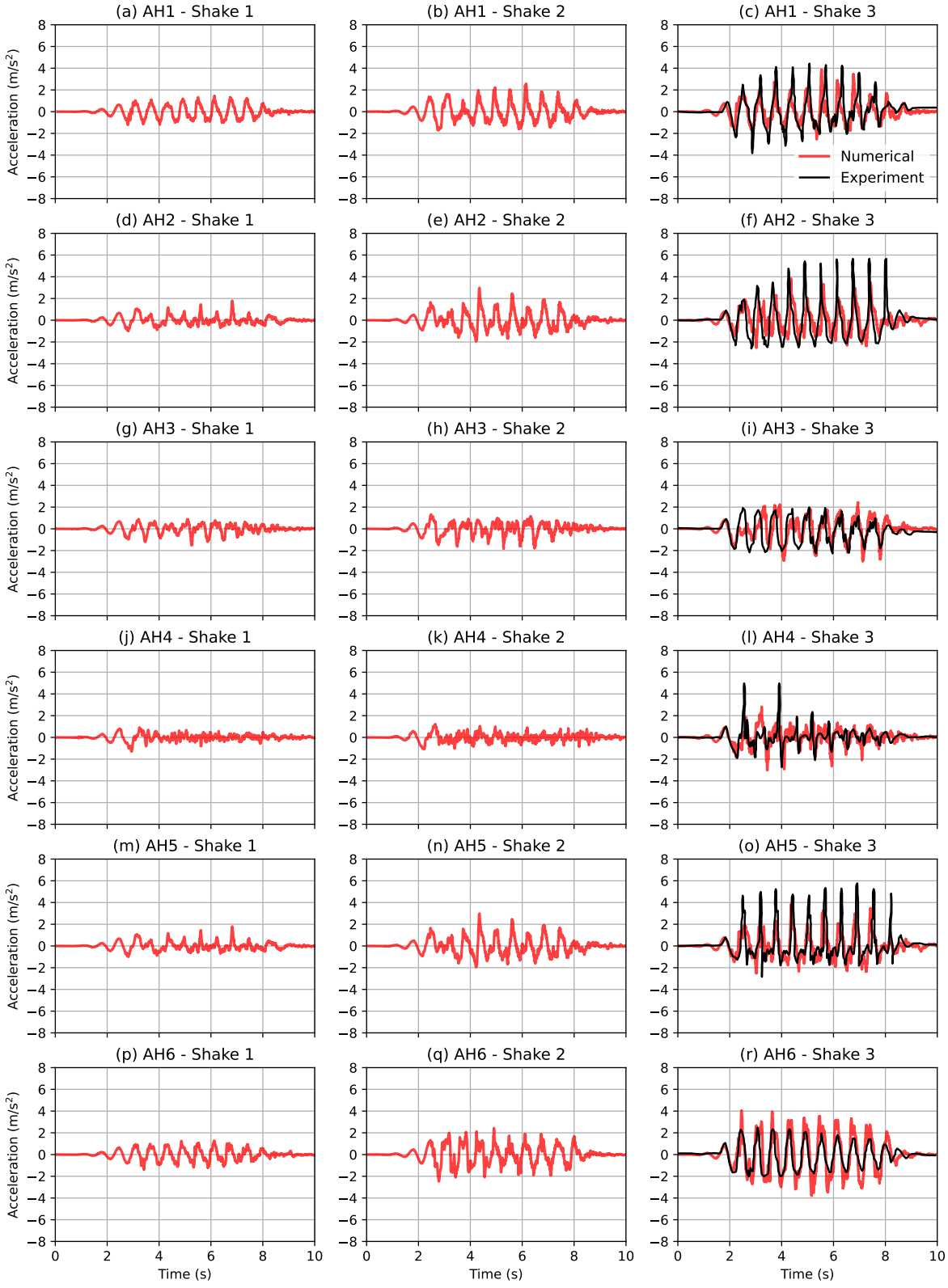

Figure 6.13: Acceleration response for MPs in locations AH1-AH6 for shake 1 (a,d,g,j,m,p), shake 2 (b,e,h,k,n,q), and shake 3 (c,f,i,l,o,r). Experimental data is plotted with MP data for shake 3.

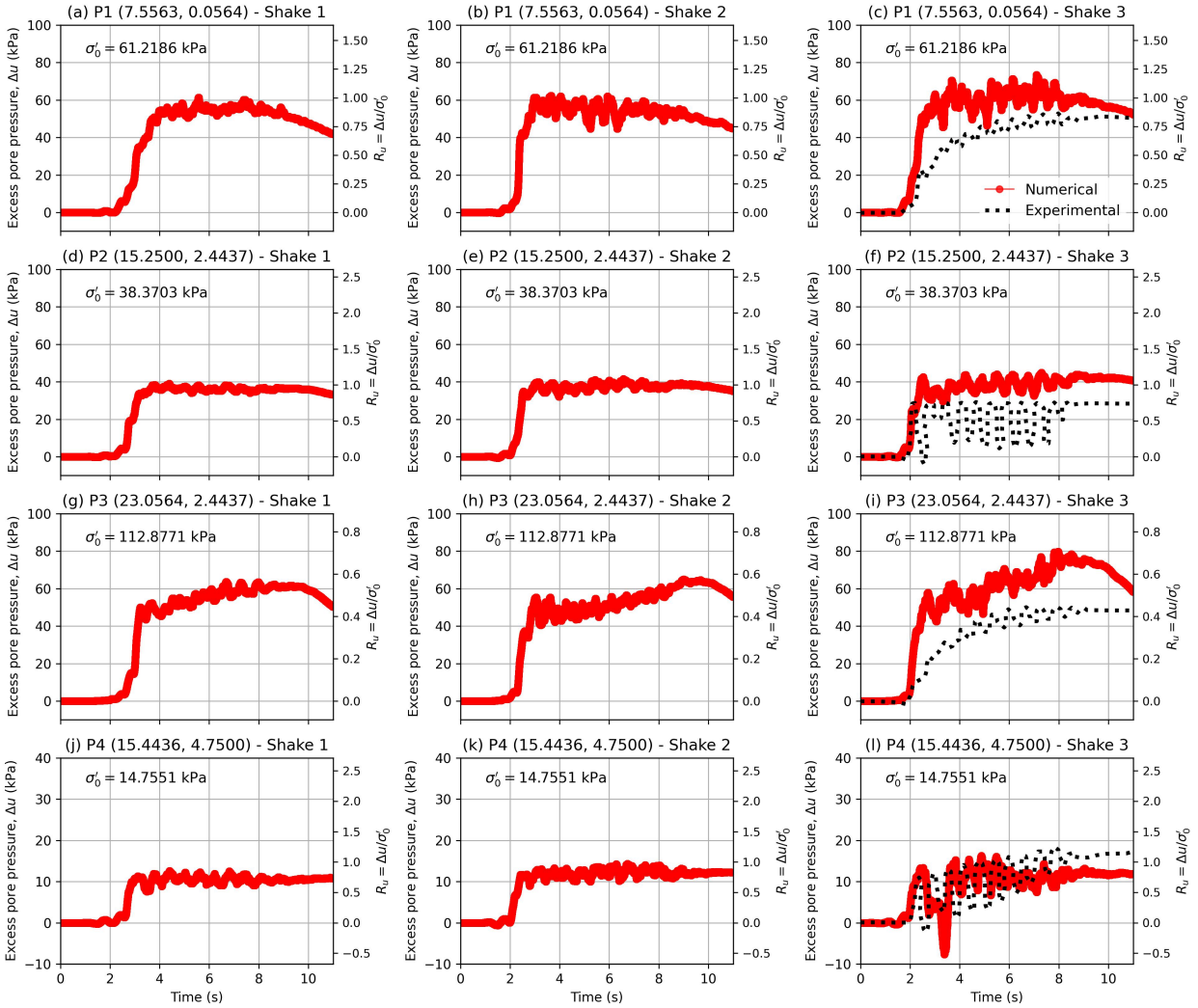

Figure 6.14: Excess pore water pressure results for shake 1, shake 2, and shake 3.

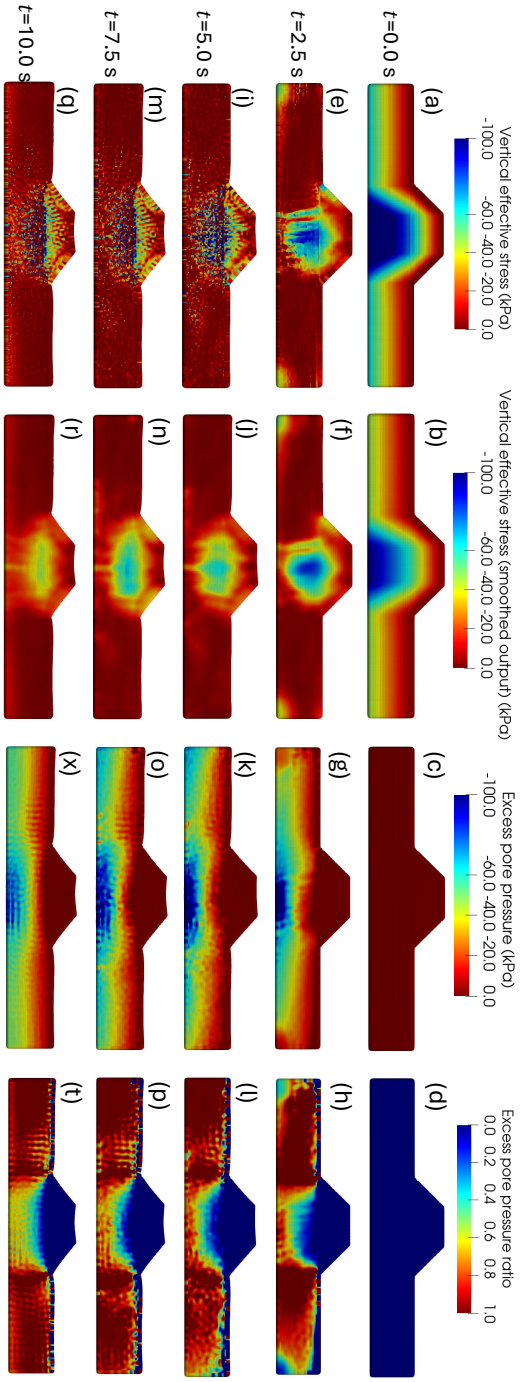

Figure 6.15: Contour plots of effective stress and pore pressure evolution during shake 3: (a,e,i,m,q) vertical effective stress, (b,f,j,n,r) vertical effective stress smoothed for output purposes, (c,g,k,o,x) excess pore pressure, (d,h,l,p,t) excess pore pressure ratio.

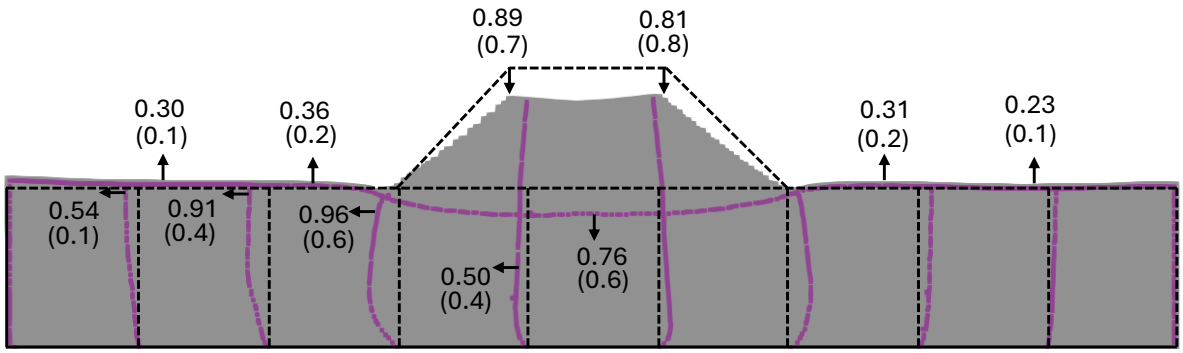

Figure 6.16: Comparison of the experimental deformation after shake 3 with the numerical results. Values in brackets represent the experimental deformation as compared to the values of the numerical model presented without brackets.

6.6.3 Conclusions

This paper presents the deployment of the PM4Sand model in the higher-order MPM. The PM4Sand framework was described and implemented as a UMAT with an explicit Modified Euler integration scheme. Monotonic and cyclic simple shear element-level examples were presented to show the trends of stress-strain and stress paths. The implementation is verified against the numerical implementation in Opensees [113, 114]. The numerical cyclic simple shear test is repeated using an array of values for the cyclic stress ratio (CSR), and the number of cycles to achieve a 3% strain is calculated. These trends are compared to those in Opensees, whereby a satisfactory match was observed for vertical normal stresses ranging from 1 to 8 atm. The MPM framework with PM4Sand is then deployed to simulate two centrifuge tests. First, the LEAP-UCD3 test was simulated, which comprises a homogeneous sand slope. The sand was simulated using PM4Sand. A wavelet-input ground motion was used, consistent with the experiment. The site response was captured as consistent with the experiment. Discrepancies were observed in the generation of excess pore-water pressure. However, the trends and final pore-water pressure values were consistent with the experimental results. Also, the runout trend was satisfactorily captured. Second, VELACS

test of a clay embankment resting on a layer of saturated Nevada sand. The clay is modeled as a Mohr-Coulomb material resting on a PM4Sand material calibrated to reproduce Nevada sand parameters. Three shakes were performed independently, and the results of shake 3 are validated against the experimental data. The acceleration response is satisfactorily captured using the PM4Sand model when compared with the accelerometer data. Liquefaction-triggering occurs faster in shake 3 as compared to shakes 1 and 2 due to the higher shaking amplitude. The pore pressure trends are consistent with the experiment. Liquefaction-triggering occurs at the sides of the model at shallow depths as excess pore pressure gets generated. The largest value of excess pore pressure is generated at the base of the model, close to the centrifuge box under the embankment. The location of the highest initial vertical effective stress exhibited the highest excess pore pressure. Liquefaction initially started at shallow depths and eventually occurred below the embankment at the base of the model. These exploratory validation simulations using MPM in conjunction with the PM4Sand model present, for the first time, a robust framework for geotechnical practice to reasonably predict pore pressures and deformation runouts.

Chapter 7

Conclusions

The simulation of earthquake-triggered liquefaction and landslides is challenging due to the scarcity of reliable numerical tools that accurately capture cyclic soil behavior. Despite its practicality, the Material Point Method (MPM), among other particle-based techniques, has suffered from numerical errors that prevented it from achieving its full potential in geotechnical earthquake engineering. This dissertation advances the simulation capabilities of coseismic landslides using the MPM as a tool for analysis. This includes the development of boundary conditions, explicit time integration schemes, spatial integration schemes, and the implementation of advanced constitutive models for simulating coseismic landslides.

First, dynamic earthquake-loading necessitates time-dependent boundary conditions to capture the shaking. A non-zero kinematic boundary condition was developed to simulate the bedrock or shaking table acceleration. The boundary condition is enforced at the velocity field within the computation cycle of the MPM. Periodic boundary conditions were also extended for large deformations to enforce identical velocities and displacements for the nodes at the same spatial level. The small-strain modal site response was successfully verified against mesh-based techniques. This presents a robust set of boundary conditions that do not presume a material constitutive behavior.

The Euler-Cromer time scheme of the MPM has tendencies to amplify high-frequency noise leading to unstable dynamic results. As such, the explicit generalized-α time scheme was incorporated in the MPM for the simulation of earthquake-triggered runout. The results were

also compared to the Newmark method [34]. Runout results are consistent with the Newmark method when considering an elasto-plastic soil material. However, if strain-softening was introduced, the runout increases by an order of magnitude.

Despite the development of boundary conditions and time schemes, the use of advanced constitutive models is necessary to capture earthquake-triggering and cyclic mobility. The standard linear MPM is incapable of reflecting a stable element-level response due to the discontinuity of the interpolation functions. This is commonly known as 'cell-crossing error'. As such, a higher order isogeometric MPM framework was developed to eliminate cell-crossing error and enable the simulation of history-dependent materials using advanced constitutive models. A series of verification examples were used to assess the stability of the framework. Cubic interpolation functions were required at minimum to achieve a stable solution. A multipatch isogeometric framework was also developed to offer greater flexibility in the geometry definition. The simplified B-spline framework was then deployed to simulate real-scale multiphase problems such as the Selborne slope experiment [235].

The PM4Sand bounding surface model UMAT was implemented in the higher-order MPM framework to capture state-of-the-practice liquefaction trends in sands. Monotonic and cyclic undrained element-level trends were verified against the C++ open-access implementation in Opensees [113]. Subsequently, two centrifuge experiment configurations were simulated to validate the framework. First, a trapezoidal homogeneous saturated Ottawa sand slope is simulated. Second, the runout of a clay embankment overlying a saturated Nevada sand layer. Comparisons of pore water pressure, acceleration, and displacement results were performed, whereby the trends were successfully captured.

Finally, the research and conclusions achieved in each chapter are outlined in more detail for reference, as follows:

- Chapter 2 develops a non-zero kinematic boundary condition to enable the simulation of centrifuge and shaking table tests. The moving mesh approach is used to follow the ground motion, which strongly enforces the boundary condition at the nodes. The moving mesh also reduces cell-crossing error to the MPs that exhibit a relative deformation response to the applied ground motion. Validation efforts are performed by simulating a large deformation shaking table test by Wartman et al. [26]. The framework is also compared to Newmark [34], simplified Newmark-type techniques, and mesh-based numerical techniques for verification. Results show that traditional mesh-based approaches are incapable of simulating large-strain runouts (i.e., Arias intensity greater than 3 m/s for the considered geometry). On the other hand, MPM is capable of numerically capturing the runout of an experimental large-strain shaking table experiment in a non-liquefiable material. The slip surface localization is accurately captured at the interface between the soft and stiff clay layers. A satisfactory match is observed between the MPM and Newmark behaviors when assuming simple elastoplastic slope behavior.

- Chapter 3 proposes periodic boundary conditions in the MPM framework equipped with a particle relocation technique to capture site response in unbounded domains more accurately. The explicit generalized-α time scheme is implemented to suppress high-frequency noise beyond a reasonable frequency threshold. The results of the implementation using irregular cyclic loading are compared with those from FEM. The runout of an elastoplastic embankment resting on a linear-elastic foundation is simulated. Parametric analysis is performed to investigate the effects of strain-softening, geometry, and ground motion Arias intensity. The results are also compared with the Newmark [34] sliding block solution. The results show that in the lower-order framework, high-frequency oscillations originate from cell crossing noise. This noise

is successfully mitigated using the explicit generalized-α time scheme, demonstrating the capability of the MPM in capturing large-strain site response. When considering embankment geometries, the results show that embankment runouts in brittle soils are less sensitive to the ground motion Arias intensity than ductile or strain-hardening soils.

- Chapter 4 develops a higher-order isogeometric MPM using NURBS or B-splines to combat the notorious cell-crossing error. General benchmark examples are presented in 2D and 3D geometries to demonstrate the superior stability of the framework compared to lower-order frameworks. Volumetric strain smoothing is used to mitigate volumetric locking in materials that deform at a constant volume. Circular geometries are also adopted to benchmark the isogeometric framework. A multipatch framework is also proposed for penetration problems. Simulations of shallow footing penetration, assuming elastoplastic and incompressible materials. The two-phase formulation is used to capture the fully coupled evolution of effective stress and pore pressure in simple benchmarks. The results highlight the superior stability and convergence characteristics of cubic interpolation functions compared to quadratic interpolation functions. The isogeometric framework also reasonably captures the analytical solution when simulating complex circular geometries. The strain smoothing algorithm is also successful in reducing volumetric locking without requiring modifications to the time integration scheme of the MPM. This includes capturing smoother strain localization when using the nonlinear exponential strain-softening law. The superior stability of the new framework is also demonstrated when using the hydromechanical formulation.

- Chapter 5 validates the use of the hydromechanical formulation in the higher-order B-spline MPM in large-scale geomechanical applications. The stability of B-spline orders ranging from linear to quartic is explored. The aim is to bridge the gap between

B-spline theoretical considerations and practical geotechnical applications. Assessed simulations include large-strain consolidation, Selborne slope failure case study, and footing penetration in saturated soils. The results demonstrate the superior stability of the cubic and quartic B-splines through the Selborne slope failure experiment, whereby the sliding mass behaves as a rigid body without oscillation within the mass. The stress paths also converge when using the cubic interpolation function, with no significant variation when using the quartic interpolation function.

- Chapter 6 implements the PM4Sand constitutive model in MPM for the first time, to capture the cyclic behavior of sand, including liquefaction. The implementation is performed in UMAT format. Verification efforts, including the assessment of the Cyclic Stress Ratio (CSR) versus number of cycles to trigger large deformations relative to an independent implementation in OpenSees [113, 114]. The PM4Sand model is deployed within the higher-order MPM computational cycle to simulate a VELACS and LEAP centrifuge test [238, 239, 240, 246]. The kinematic response and pore water pressure trends are satisfactorily captured in accordance with the experimental data, and the numerical framework is considered fully validated. The capability of the higher-order MPM when incorporating PM4Sand for liquefaction assessment is validated. This includes stable pore pressure solutions that capture liquefaction-triggering and post-failure deformations. This work presents progress in incorporating material and geometrical complexities within a promising and stable multiphase higher-order MPM framework.

The following is proposed as future work to extend this research:

- The implementation of free-field boundary conditions will enable the simulation on non-symmetric geometries while capturing radiation damping. Note that the under-

lying formulation of the free-field boundary conditions in FEM is usually performed assuming a viscoelastic soil material. This can introduce instabilities when free-field columns are attached to highly nonlinear plastic models such as PM4Sand.

- Dynamic time schemes play an essential role in ensuring the stable evolution of the kinematics in numerical techniques. It is well-known that explicit time schemes introduce errors with time. Additionally, in hydromechanical formulations, the critical time step reduces to an extremely small value when simulating fine-grained soils. As such, an implicit user-controlled dissipative time scheme is needed to stabilize dynamic simulations and alleviate the restriction on the critical time step. The use of Rayleigh damping can also be explored to investigate its effect on large deformations.

- The development of new features in the MPM framework increases the computational cost. Additionally, there is a need to deploy the MPM framework to simulate kilometer-length real-scale model geometries. As such, parallel computing should be incorporated in the MPM framework to reduce the overall computational cost. This includes exploring CPU and GPU parallelization features.

- The higher-order isogeometric multipatch framework has the potential to simulate accurate and smooth stress fields. The multiphase framework in this thesis can be extended to capture accurate soil stratification in tailing dam geometries. Theoretical consideration can be revisited to smooth discontinuities between patches. Additionally, non-conforming patches can be explored to enable a more practical combination of different geometries, facilitating isogeometric analysis.

- Volumetric locking mitigation strategies should be explored in linear and higher-order MPM frameworks to understand the manifestation of locking. Advanced volumetric locking mitigation strategies should be considered to assess their efficacy and suitability

in real-scale multiphase geotechnical engineering problems.

Through this dissertation, the MPM was enhanced to solve earthquake-triggered landslide problems, focusing on both theoretical computational advancements and practical geotechnical considerations, to reduce their risk and mitigate their overall consequences.

Appendices

Appendix A

Runout modeling of earthquake-triggered landslides with the Material Point Method

Published in International Foundations Congress & Equipment Expo (IFCEE) proceedings, with the following reference: Alsardi, A. and Yerro, A., 2021. Runout modeling of earthquake-triggered landslides with the material point method. In IFCEE 2021 (pp. 21-31).

The following authors contributed to this manuscript, as follows:

- Abdelrahman Alsardi
  - Developed and implemented kinematic prescribed velocity on the nodes and the MPs.
  - Performed all numerical simulations from pre-processing to post-processing and analysis.
  - Prepared all figures and wrote the original draft of the manuscript.
  - Addressed journal peer-review comments.
- Dr. Alba Yerro
  - Provided invaluable feedback throughout the implementation of the framework.
  - Discussed results and troubleshooting strategies to perform successful numerical simulations.
  - Obtained research funds to enable the deployment of the framework for geotechnical applications.
  - Edited and revised the manuscript.

A.1 Introduction

Earthquake-induced landslides and slope instabilities are considered as one of the most relevant secondary effects of earthquakes, being responsible for a significant part of the damage and loss of human life. For example, the 2008 Wenchuan earthquake in China triggered more than 15,000 landslides, claiming the lives of 20,000 people, which was about a third of the victims associated with the earthquake [248]. In particular, landslides triggered by earthquakes mobilize a large amount of mass, risking the communities downstream. A prominent example of such a large landslide runout occurred in the 1964 Alaska earthquake, destroying communities across an area of more than 40,000 m^2 [249]. Despite these catastrophic socioeconomic impacts of such earthquake events, the relationship between failure triggering and the post-failure mechanics of the sliding mass associated with these phenomena is not clear. Also, the mechanics behind the pore pressure generation and post-shaking void redistribution in saturated and partially saturated landslides are not fully understood.

Fully controlled experimental models have been conducted to simulate these complex phenomena at a prototype scale and in centrifuge [3, 26]. However, conducting centrifuge or shaking table tests in the laboratory requires experimental facilities that are not widely available and can be extremely expensive. Due to this, numerical models play an irreplaceable role in simulating these phenomena using mathematical formulations. The most widely used seismic slope stability methods are the pseudo-static and the sliding block analyses, respectively established by Terzaghi [33] and Newmark [34]. These analytical methods can provide preliminary estimations of stability and permanent displacements of slopes. However, they are highly idealized, enforcing crude assumptions to simulate the dynamic loading and the geology of these complex scenarios. Although numerical models are more computationally expensive than these analytical methods, recent developments in multiphase numerical for-

mulations and constitutive modeling present promising opportunities to develop an accurate understanding of the dynamic behavior of slopes during realistic earthquake events.

This paper aims to assess the applicability of various state-of-the-art nonlinear dynamic numerical tools to model earthquake-induced large-strain deformation of slopes, with emphasis on the capabilities of the Material Point Method. In particular, the explicit one-phase Material Point Method framework in the Anura3D software (http://www.anura3D.com) [149] is extended to simulate earthquake shaking effects using a non-zero kinematic velocity boundary condition. The shaking table laboratory experiment by Hiraoka et al. [115] is simulated using the Material Point Method, the Finite Element Method, and the Finite Difference Method. The outputs are compared to the results available in the literature obtained with the Smoothed Particle Hydrodynamics method. Finally, a parametric analysis is performed to discuss the effect of partially saturated conditions.

A.2 Nonlinear Dynamic Numerical Approaches

The most common nonlinear dynamic analysis methods are the Finite Element Method (FEM) and the Finite Difference Method (FDM) (e.g., [223]). These mesh-based methods are conceptually simple and are capable of modeling history-dependent materials. In both cases, a nodal computational mesh discretizes the continuum and represents its deformation. As a result, these mesh-based methods exhibit severe element distortion when large deformations appear, leading to significant errors and an unstable numerical solution. An effort has been made to improve these techniques to extend their applicability to large strain problems with rezoning, remeshing, and remapping algorithms. However, these techniques are computationally expensive and interpolate the history variables at the nodes which ultimately cause numerical instabilities in the stress calculation [55].

To overcome these limitations, particle-based mesh-free methods, such as the Smoothed Particle Hydrodynamics (SPH) method [250] are developed. In SPH, the continuum domain is discretized into a set of Lagrangian particles, whereby an influence domain is defined spatially for each particle using kernel functions to detect neighboring particles. SPH has been successfully applied to solve large deformation problems in geomechanics (e.g., [128]). However, the application and development of boundary conditions in SPH can be challenging for various engineering applications, requiring the introduction of an additional set of particles known as 'ghost' particles (e.g., [115]). Additionally, the neighboring particle search particularly makes the SPH an expensive computational technique.

This research is mostly focused on the Material Point Method (MPM) [58], which is also a particle-based method, but in this case, it also uses a background computational mesh. While the continuum body is discretized into a finite number of mobile Lagrangian points so-called material points (MPs) that move together with the material carrying the updated variables (e.g., velocity, density, strain, stress, state parameters), the main governing equations (i.e., dynamic momentum balances) are solved at the nodes of the mesh that usually remain fixed and do not store permanent information. With this dual description, the MPM prevents mesh distortion that is seen in fully Lagrangian methods at large strain (i.e., FEM, FDM), and also overcomes the difficulty of tracking history-dependent materials in fully Eulerian methods. Moreover, the application of boundary conditions in MPM is facilitated for many different engineering applications, with the ability to apply these boundary conditions directly on the nodes (i.e., similar to mesh-based methods) or on the material points [59]. Some of the limitations of the MPM include the potential generation of numerical noise due to the particles crossing the elements of the background mesh when using lower-order elements [251]. Several techniques, such as the mixed MPM integration scheme, were introduced to mitigate the cell-crossing noise [119, 121]. Over the past decade, the MPM successfully incorporated

multi-phase hydro-mechanical formulations [119, 121, 139] and thermal interactions [252]. This research focuses on the MPM numerical tool to advance the understanding of the kinematics of landslides triggered by earthquakes.

A.3 Developments in the MPM for Earthquake Induced Shaking

The MPM computational cycle can be summarized with the following steps: (1) map information from the MPs to the background mesh by using linear shape functions; (2) assemble the dynamic linear momentum balance equation at the nodes of the mesh and solve for the nodal acceleration; (3) update velocity and momentum balance at the MPs from nodal accelerations; (4) update nodal velocity from MP velocity and evaluate strain increments at the MPs; (5) update state variables at the MPs by using constitutive equations and mass balance equations (if required); and (6) update the position of the MPs and discard nodal values.

The simulation of seismic motions requires the application of time-dependent kinematic boundary conditions. In general, the input ground motion is applied in terms of velocity as v_{input}(t). The duration of each timestep, t, in explicit integration schemes is limited by the critical timestep to maintain the stability of the solution, which is usually much smaller than the sampling timestep of ground motions velocity-time histories. In this analysis, linear interpolation is adopted to approximate the value of v_{input} at the beginning of each computational cycle. It is also assumed that v_{input} remains constant throughout the time step duration.

To the authors' knowledge, only three attempts to simulate earthquake-induced landslides

(either shaking table or natural scale models) with MPM exist in the literature [78, 124, 125]. All of them impose the non-zero kinematic boundary condition by prescribing velocity at the corresponding MPs (MPs-PV) representing the shaking table box or the bedrock from a natural site, depending on the problem (Figure A.1(a)). In this paper, the kinematic boundary condition is applied at the boundary nodes (Ns-PV) instead (Figure A.1(b)). In both approaches, v_{input} can be applied between steps (4) and (5) of the computational cycle. In the first approach, the velocity of the MPs-PV is overwritten with v_{input} and the momentum balance is recalculated with Equation A.1. In order to ensure that in step (5) the strains at the MPs-PV are consistent with the v_{input}, elements containing MPs-PV are determined at each timestep and the nodal velocity is updated according to Equation A.2. Note that p_{MP} is the MP linear momentum, m_{MP} is the MP mass, v_i is the velocity of the i-th node, m_i is the mass of the i-th node, and N_i is the nodal shape function evaluated at the MP.

$$p_{MP} = m_{MP} v_{input} \tag{A.1}$$

$$v_i = \frac{1}{m_i} \Sigma_{MP} N_i p_{MP} \tag{A.2}$$

In the second approach, the velocity of the Ns-PV is rewritten with the v_{input}. Also, the velocity of those MPs located in the elements containing the Ns-PV is recalculated considering the updated nodal velocities according to Equation A.3 to properly update their position in Step (6). Note that v_{MP} is the MP velocity. While both approaches have essentially the same applications, applying the boundary conditions at the nodes can give more flexibility and the definition of a 'basal' material is not mandatory, resulting in a reduction of the computational time.

$$v_{MP} = \Sigma_i N_i v_i \tag{A.3}$$

The original MPM framework considers the background mesh fixed during the calculation. This can lead to MPs leaving the computational domain as a result of the back-and-forth motion. To solve this issue, previous authors [78] included additional boundary elements on the sides of the model. Also, the nature of the shaking can substantially increase the cell-crossing instabilities [60] because MPs keep alternating the direction of the velocity. In this paper, the moving mesh feature proposed by Al-Kafaji [119] is considered; hence in Step 6, the position of the mesh nodes is updated with v_{input} according to Equation A.4, where u is the incremental displacement. In this manner, the cell-crossing is minimized and MPs remain in the computational domain.

$$\Delta u = v_{input} \Delta t \tag{A.4}$$

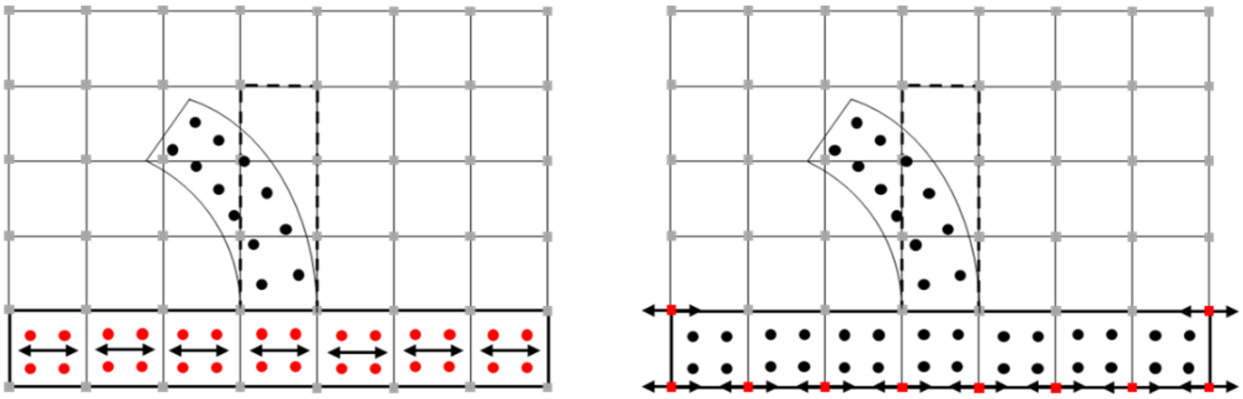

Figure A.1: Schematic comparison of non-zero kinematic boundary conditions applied at (a) the MPs and (b) nodes; indicated in red color.

A.4 Modeling a Shaking Table Experiment

A shaking table experiment was conducted by Hiraoka et al. [115] to understand the effect of seismic shaking on the deformation of a 0.5 m-high slope of sand. It was reported that the sand was partially saturated with a moisture content of 10%. The soil parameters provided are effective friction angle, $' = 23^o$, apparent cohesion, c'= 0.78 kPa, Young's modulus, E=2.57 MPa, Poisson ratio, =0.33, and moist unit weight, =16.5 kN/m^3. According to Hiraoka et al. [115], the dilatancy angle, , of the soil was considered to have a value that ranges from 0^o to $'$. The shaking table box used in the experiment had a steel horizontal base and smooth glass vertical sidewalls. The displacement of the toe and the crest were monitored by means of laser sensors. The velocity-time history used in the experiment is shown in Figure A.2. In the literature, attempts to model this experiment were made by Bhandari et al. [78] and Hiraoka et al. [115], using MPM and SPH models, respectively. Hence, the selection of this benchmark provides an opportunity to compare the proposed MPM implementation of the boundary condition and the moving mesh with previous MPM results and other particle-based and mesh-based approaches.

A plane-strain MPM model is developed as shown in Figure A.3a. A non-associated Mohr-Coulomb constitutive model is adopted for the sand using the material parameters presented above. A dilatancy angle of 0^o is considered, which is consistent with the assumptions presented by Hiraoka et al. [115] and Bhandari et al. [78]. The shaking table is modeled as a rigid body considering the algorithm developed by Zambrano-Cruzatty and Yerro [237]. The interaction between the slope and the shaking table is simulated with a frictional contact algorithm that allows free separation [251]. While the horizontal base is considered fully rough, the vertical contact is fully smooth, consistent with Bhandari et al. [78]. The stress initialization is performed with a quasi-static gravity loading, the vertical boundaries are

rollers, and the base is fully fixed. After gravity initiation, the horizontal fixities on the vertical boundaries and the base are removed and replaced by the Ns-PV boundary condition in the horizontal direction (Figure A.2). The MPM system has 5% of local damping during the shaking. Two MPs, located at the toe and at the crest of the slope (indicated in Figure A.3(a)), are tracked to compare the runout and crest settlement from numerical results with the experimental data.

Similarly, FEM and FDM models were developed with PLAXIS 2D and FLAC 2D software, respectively. Figures A.3(b) and A.3(c) present the corresponding initial mesh configurations. The slope geometry and soil parameters are identical to the MPM model, whereby the gravity stresses were similarly initiated. The dynamic shaking (Figure A.2) is then prescribed directly at the boundary nodes of the slope mesh using rigid velocity boundary conditions. The FEM and the FDM systems are considered to have 5% of damping during the dynamic shaking. The reader is referred to software manuals for details regarding the damping scheme and time integration scheme used in the FEM [145] and the FDM [253] models.

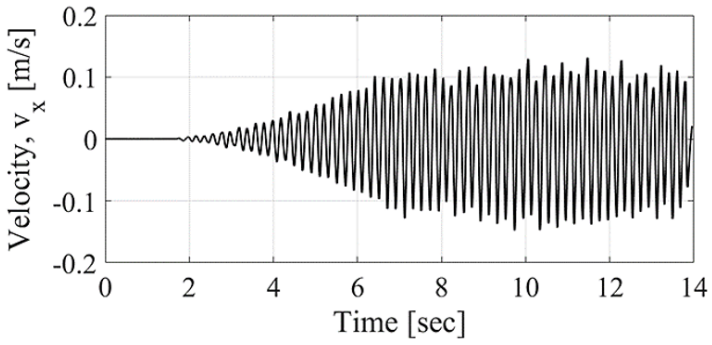

Figure A.2: Velocity-time history used in Hiraoka et al. (2013).

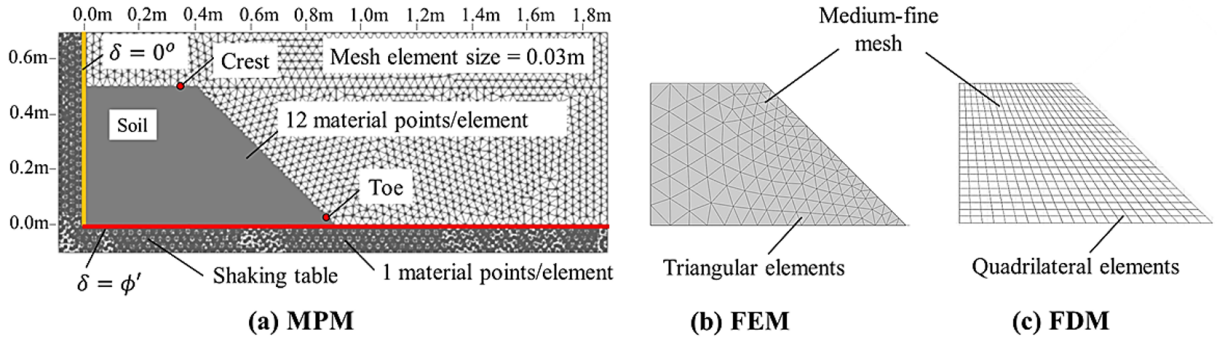

Figure A.3: Plane-strain numerical models of the shaking table experiment.

A.5 Results and Discussion

The scope of the discussion can be organized into two parts: First, the MPM results obtained herein are compared with the MPM simulation from Bhandari et al [78], and other particle-based methods (i.e., SPH) and mesh-based methods (i.e., FDM and FEM). Second, a parametric analysis is conducted to analyze the effects of varying the dilation angle and the cohesion of the slope. Comparison of MPM results with other particle-based and mesh-based methods. Figures A.4(a) and A.4(b) respectively present the toe runout and crest settlement obtained in the laboratory and with mesh-based methods (i.e., FEM and FDM) and particle-based methods (i.e., MPM and SPH). It is noted that MPM results obtained using the Ns-PV approach and moving mesh technique are consistent with those presented by Bhandari et al. [78] using the MPs-PV condition. Also, it was seen that the Ns-PV approach reduced the computational time by 21% with an Intel Core i7 at 3.30 GHz CPU. Both analyses predict a similar runout and underpredict the crest settlement. The final deformed MPM configuration is presented in Figure A.5(a). The SPH results presented by Hiraoka et al. [115] obtained with the mesh-based methods (FEM and FDM) are inconsistent with the laboratory data. The FEM model experiences extremely large deformation as a result

of mesh entanglement (Figure A.5(b)). The FDM mesh also suffered from severe distortion at the toe of the slope (Figure A.5(c)) and the calculation crashed after approximately 7 seconds of shaking. All numerical models predict the failure initiation approximately 2 seconds sooner than the experiment. These results confirm that the mesh-based methods are not suitable to simulate large deformations. Therefore, this highlights the importance of the development of particle-based methods for the study of landslide risk assessment practice.

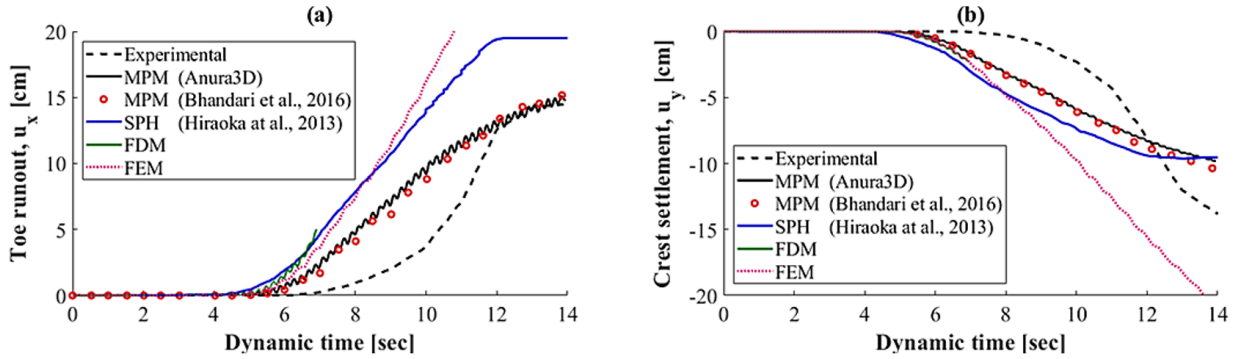

Figure A.4: Comparison between laboratory tests and numerical results obtained with different mesh-based and particle-based methods. (a) toe runout and (b) crest settlement.

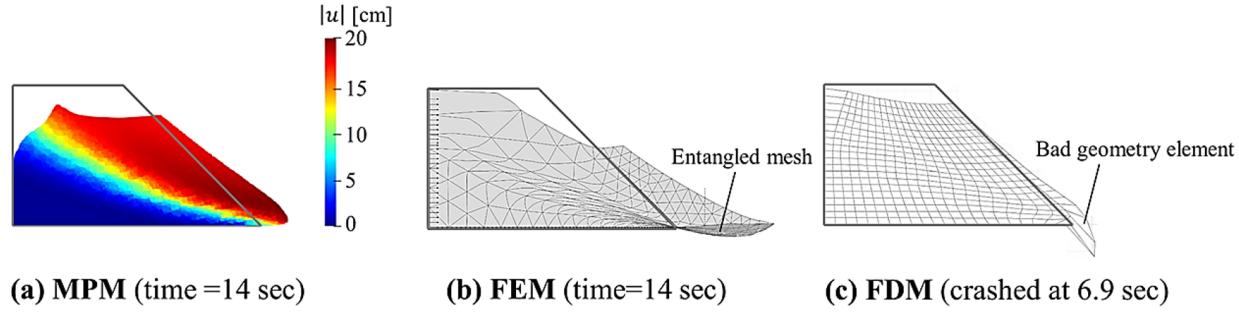

Figure A.5: Deformed slope profile.

Parametric analysis: The discrepancies observed between MPM results and laboratory data can be explained because the soil in the experiment was in partially saturated conditions. The coexistence of the solid grains with the porous liquid and gas phases makes the scenario much more complex and difficult to accurately predict with a one-phase formulation and a

simple Mohr-Coulomb failure criterion without suction effects. Additionally, Hiraoka et al. [115] observed the formation of multiple shear failure surfaces, which indicates that the sand is potentially dilatant. To have a preliminary understanding of the deformation mechanism in this partially saturated condition, a parametric analysis is conducted by varying the and c'.

Figure A.6 shows the toe runout and crest settlement for ranging between 0^o and 2^o. It is seen that larger results in larger runouts. Additionally, greater dilatancy results in a more brittle deformation at the triggering onset. The trend of deformation at greater dilatancy fits better the experimental results. Figures A.7(a) and A.7(b) show the deviatoric strain for of 0^o and 1^o, respectively. When no dilatancy is considered (i.e., $= 0^o$), a single distinct shear band develops. However, the larger the dilatancy (i.e., > 0), the failure surface becomes more dispersed and multiple shear bands can be observed. During the experiment, as the seismic loading was applied, Hiraoka et al. [115] reported that the deformation of the slope was triggered by several shear surfaces. This can be explained by the light dilatancy effect.

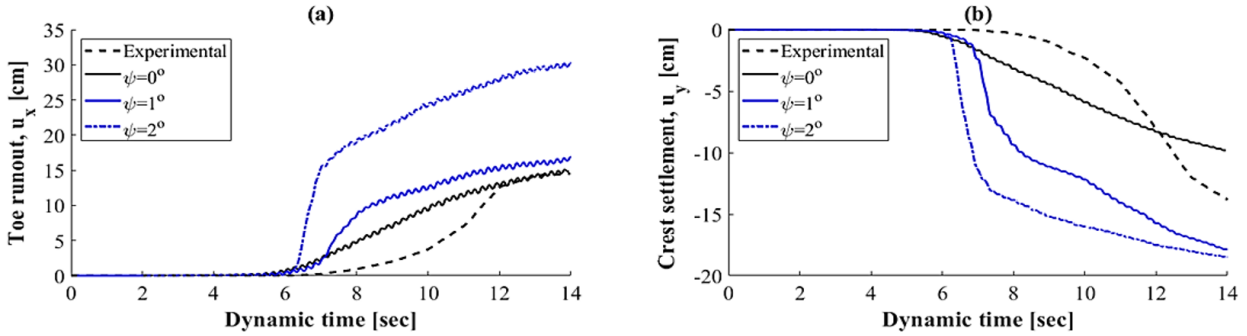

Figure A.6: Parametric analysis for different dilatancy angles. (a) toe runout and (b) crest settlement.

In partially saturated conditions, an increase in and volume leads to an increase in suction and apparent cohesion [254]. It is important to note that the apparent cohesion adopted by Hiraoka et al. [115] does not capture the dynamically varying suction magnitude during

the experiment. This motivated the parametric analysis of $c^{'}$ (considering 0.78, 1, and 1.2 kPa) with $=1^{o}$ presented in Figure A.8. As the c' increases, a larger duration of shaking is required to trigger the deformation of the slope. It is shown in Figure A.8 that the triggering onset of the toe runout and crest settlement occur at a later time when considering a larger value of c'. The toe runout and the crest settlement in Figure A.8(a) and Figure A.8(b), respectively, have a better fit to the experimental results when using the parameters $c'=$ 1 kPa and $=1^{o}$. The deviatoric strain profile of the slope considering these c' and values is shown in Figure A.7(c).

The trends observed in the parametric analysis of c' and depict the coupled nature of the dilatancy and suction in partially saturated soils. In the real scenario, the values of c' and evolve with time in a different manner at different points of the slope. To fully capture this behavior, a multi-phase formulation is required with a suction dependent constitutive model.

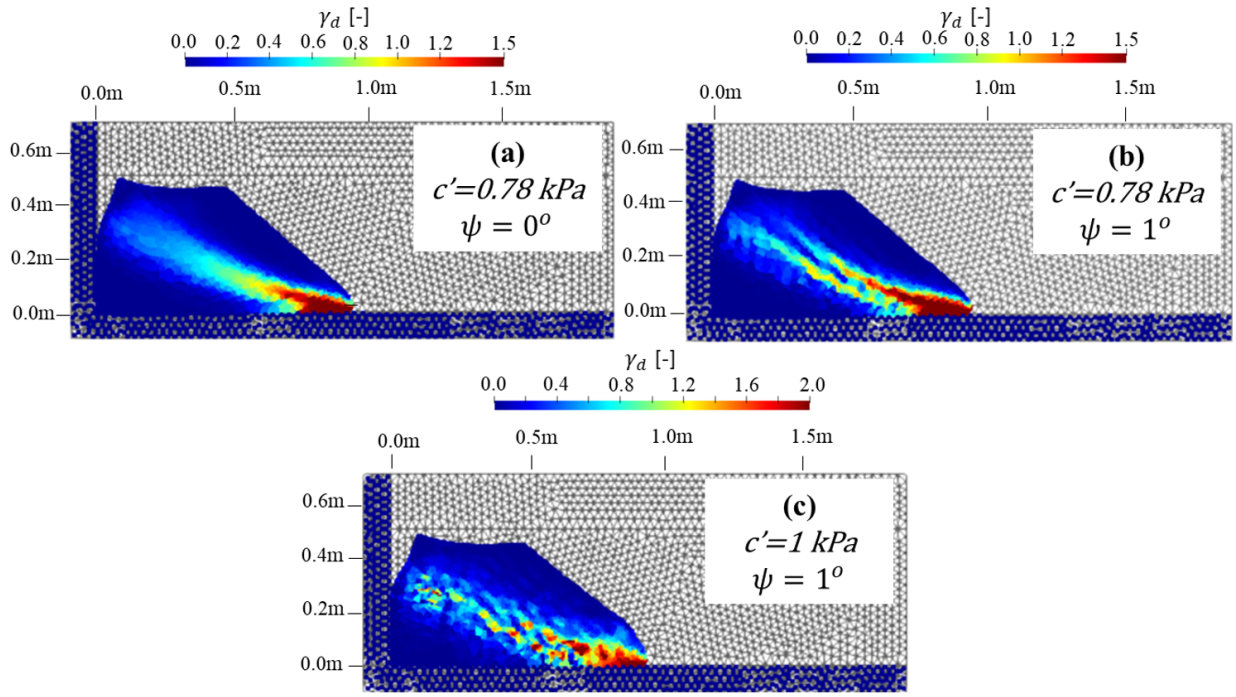

Figure A.7: Deviatoric strain at 10 seconds.

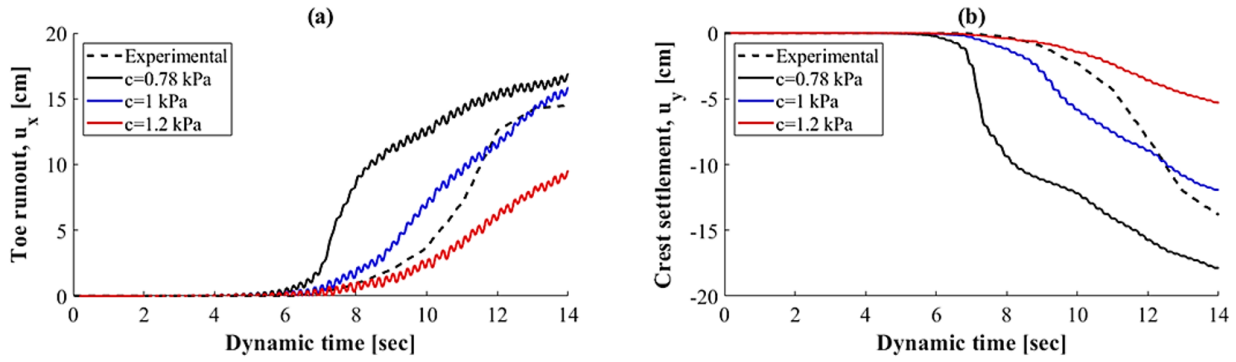

Figure A.8: Parametric analysis for different apparent cohesions with $=1^o$. (a) toe runout and (b) crest settlement.

A.6 Conclusions

This paper presented the capabilities of the MPM in modeling the large-strain runouts induced during landslides triggered by earthquakes. A non-zero kinematic boundary condition imposed at the nodes, employed together with a moving mesh technique is proposed to accurately apply the dynamic loading. A slope instability problem based on a shaking table experiment is modeled with MPM, FEM, and FDM. By comparing the displacement kinematics of the slope toe and crest to the experimental results, it was confirmed that Lagrangian mesh-based methods such as FEM and FDM are not accurate when large deformations are accumulated in the mesh. In contrast, particle-based techniques, such as MPM or SPH, are very promising. Finally, a parametric investigation performed to better understand the evolution of dilatancy and apparent cohesion highlights the complexities of predicting the behavior of partially saturated soils under dynamic loading. The application of multi-phase formulations and advanced constitutive models are required to better understand the dynamics of realistic landslides in earthquake events.

Appendix B

Comparison of the material point method with one-dimensional site response solution

Published in 12th National Conference in Earthquake Engineering proceedings, with the following reference: Alsardi, A. and Yerro, A., 2022. Comparison of the material point method with one-dimensional site response solution. In Proceedings of the 12th National Conference in Earthquake Engineering, Earthquake Engineering Research Institute, Salt Lake City, UT. 2022.

The following authors contributed to this manuscript, as follows:

- Abdelrahman Alsardi
  - Developed and implemented periodic boundary conditions for simulating site response in a level-ground soil column.
  - Performed all numerical simulations from pre-processing to post-processing and analysis.
  - Prepared all figures and wrote the original draft of the manuscript.
  - Addressed conference peer-review comments.
- Dr. Alba Yerro
  - Provided invaluable feedback throughout the implementation of the framework.
  - Discussed results and troubleshooting strategies to perform successful numerical simulations.
  - Obtained research funds to enable the deployment of the framework.
  - Edited and revised the manuscript.

B.1 Introduction

Numerical methods are often employed in geotechnical engineering to simulate seismic site response. Advancements in numerical mesh-based techniques incorporate nonlinear soil behavior that can successfully model small-strain boundary value problems associated with site response. However, these methods are incapable of simulating the large strains associated with post-failure deformations induced by strong-motion shaking due to excessive mesh distortion. Examples of such large strain applications include coseismic landslides, tunnel collapses, and liquefaction. To address large deformation in multi-phase problems, in the last decade, the geotechnical engineering community has widely adopted the material point method (MPM) (e.g., [56, 121, 139, 171, 252]). However, MPM has been rarely used for the study of earthquake-triggered failures, and most of the current state-of-the-art modeling technique relies on simulating small-scale shaking table experiments where fully reflective boundaries are generally accepted (e.g., [57, 78]). Based on the authors' knowledge, the MPM framework has never been verified for site response, which is a crucial step to simulate full-scale earthquake engineering problems accurately. The goal of this paper is to present the performance of the MPM while using tied-degree-of-freedom (TDOF) boundary conditions to simulate a one-dimensional small-strain site response analysis. First, the MPM computational cycle and the implementation of TDOF boundaries in MPM are briefly presented. Then, the response of a soil column using MPM and FEM is compared to validate our TDOF implementation in the MPM framework. Finally, the performance of the MPM model is discussed in terms of the frequency harmonics and the effect of the natural period on the Fourier amplitude response.

B.2 Material Point Method

The MPM is a particle-based numerical tool whereby a continuum is discretized into a set of Lagrangian points, each so-called a material point (MP), that move within an Eulerian computational mesh and represent the deformation of the continuum. Figure B.1 summarizes the MPM computational cycle, which is usually integrated explicitly in time and involves (a) interpolating state variables from MPs to nodes, (b) solving the governing dynamic momentum balance equation, (c) remapping the nodal solution back to the MPs, and (d) updating final MPs positions. The computational mesh does not store any information and can be regenerated after each time step. In the MPM framework, the boundary conditions can be applied on the nodes or on the MPs. In particular, recent developments for earthquake-induced shaking include the advancement of boundary conditions to prescribe seismic action in terms of acceleration, velocity, displacement (e.g., [57, 78, 79, 80]) or traction (e.g., [81]) on the nodes and the MPs . In particular, for this research, an in-house version of the Anura3D opensource research software is used ([149]). More details on the MPM formulation implemented in Anura3D can be found in Fern et al. [59].

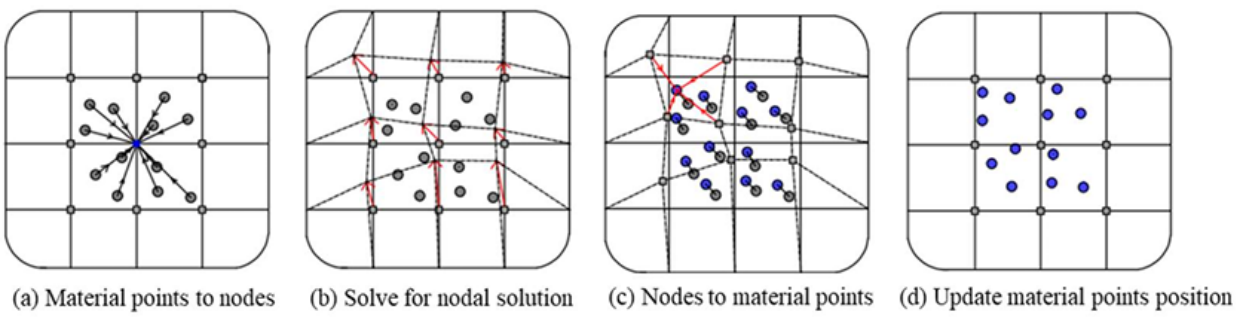

Figure B.1: Computational cycle of the Material Point Method [197].

B.3 Tied Boundary Implementation in MPM

One-dimensional analysis of seismic wave propagation in a soil column is commonly accepted to understand the soil amplification response. This analysis is generally conducted using time-domain integration schemes. They can include history-dependent materials using rigorous bounding surface constitutive models that capture accurate material hysteresis. In this paper, TDOF boundary conditions are implemented in the MPM framework to simulate one-dimensional seismic wave propagation in a two-dimensional problem. The main objective of the TDOF condition is to ensure that identical displacement solution (i.e., nodal solution in Figure B.1(b)) for the nodes at the same spatial level from both lateral sides of the model so that a constrained free-field domain is simulated through the periodic effect. Similar to mesh-based methods, TDOF can be implemented by overwriting the degrees of freedom of the corresponding nodes to obtain the same nodal solution. The implementation effectively lumps the mass and the forces of these tied nodes so that they are identical, whereby a single acceleration, velocity, and ultimately displacement value is obtained for each set of nodes. The nodal solution is later mapped to the MPs located in the elements containing these nodes (Figure B.1(c)).

B.4 Verification of Tied Boundaries in the MPM

For verification purposes, a 10-meter soil column boundary value problem is subjected to a ground motion. The shaking is applied in terms of acceleration at the base of the model (Figure B.2(a)), similar to the approach described in Alsardi et al. [57]. The MPM results are compared to the FEM results obtained with the Plaxis software. The geometry and boundary conditions are identical in MPM and FEM (Figure B.2(b)). The MPM model employs linear

triangular elements, and the FEM model employs quadratic triangular elements. The effect of the basis function order should not be significant in this problem since a linear elastic model is used. Also, note that the MPs do not move across different elements because the selected applied ground motion has a low Arias intensity equal to $5.51\text{x}10^{-2}$ m/s (i.e., no cell-crossing). The applied ground motion accelerogram (M_w 6.61 San Fernando February 9, 1971, Maricopa array 2, H1 component, source-to-site distance R_{jb}=109 km) was obtained from the PEER database [156] and was applied as a vertically propagating shear (SV) wave. This record was selected because of its rich frequency content, which is expected to engage a range of modes of the problem. The MPM algorithm employs the conditionally stable Euler-Cromer explicit time integration scheme. The time step is chosen to satisfy the domain of dependence and information propagation of the momentum balance governing equation using the Courant-Friedrichs-Levy condition. For the linear elastic constitutive model, Young's modulus (E) was selected as 10 MPa, and the Poisson ratio as 0.33, consistent with well-graded sands. This corresponds to shear modulus (G) equal to 3.76 MPa. Unit weight of the soil was assumed equal to 18.6 kN/m^3. No material or numerical damping is considered in this study.

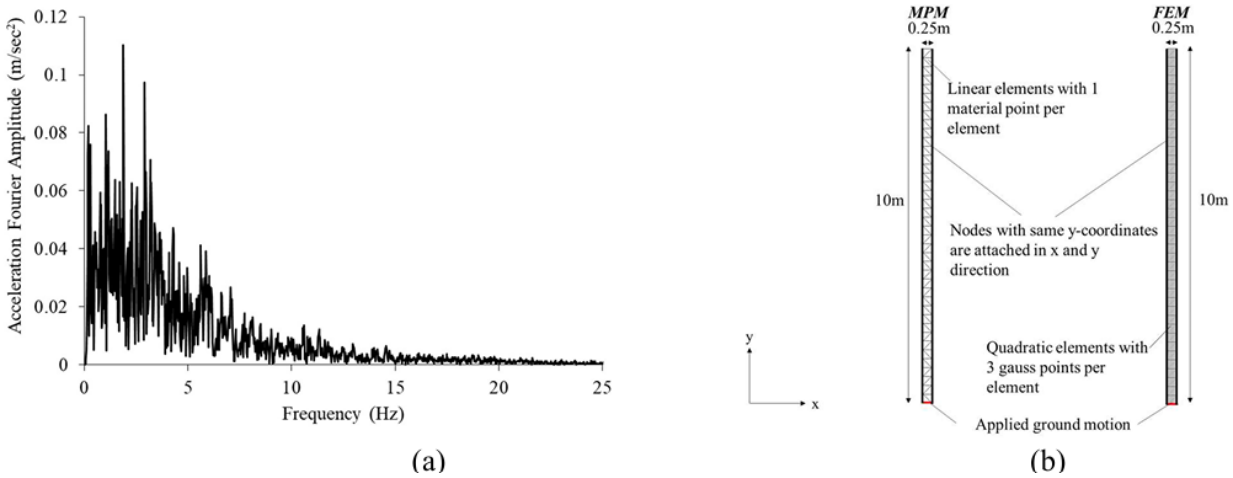

Figure B.2: Details of the boundary value problem used for verifying MPM: (a) Fourier Amplitude of the applied ground motion, and (b) Spatial discretization of MPM and FEM model.

B.5 Comparison of tied boundaries in MPM with FEM and analytical solution

The displacement solution at the center of the soil column at y=5m is plotted for FEM and MPM in Figure B.3. An identical match is seen in the numerical solutions throughout the soil column, which successfully confirms the verification of the TDOF boundary conditions implementation in MPM. This match between FEM and MPM was also seen at different depths throughout the soil column. Additionally, the acceleration Fourier amplitude spectrum is plotted for the MP at the top of the soil column, as shown in Figure B.4. It is seen that the accelerations having frequencies close to natural frequency harmonics to the soil column are significantly amplified, which is consistent with the one-dimensional analytical solution for a homogeneous soil column.

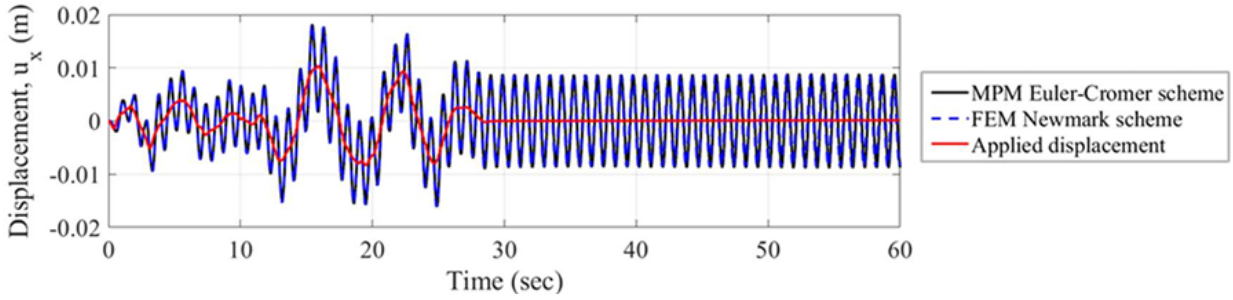

Figure B.3: Displacement-time history comparison of the MPM and FEM node in the middle of the soil column. Both numerical solutions were consistent throughout the soil column.

To assess the effect of the variation of the soil column natural frequency, a parametric analysis was conducted by varying the E value of the linear-elastic model. It is well-known analytically that increasing E by a factor results in the increase of the column's natural frequency by the square root of that factor (e.g., if E is increased by a factor of four, the natural frequency increases by a factor of two). This indicates that a higher E value will tend to amplify higher frequency amplitudes. This response is depicted in Figure B.4, in which a soil column with $E = 40$ MPa exhibited significant amplification for frequencies that are double to what was observed in the baseline verification simulation (E=10 MPa). Note that the amplitude value of the peaks in Figure B.4 depends on the amplitude of the applied ground motion at the natural frequency. In that sense, if the applied ground motion has a higher amplitude at that frequency (Figure B.2(a)), a larger value peak will be observed in Figure 4. This effect on the displacement-time history is presented in Figure B.5, where the frequency of the oscillations increases with an increase in E value.

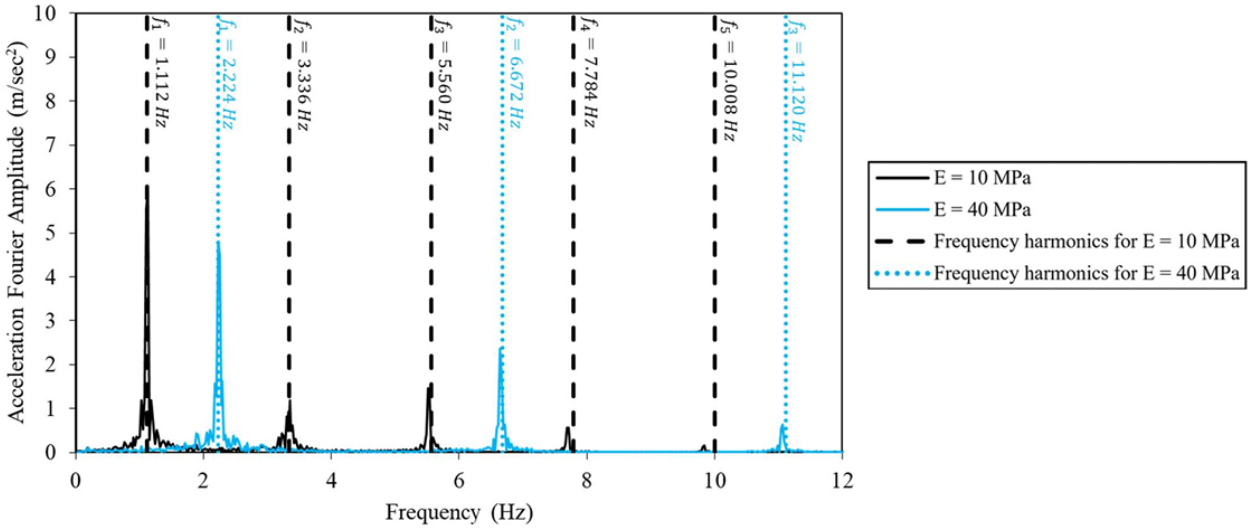

Figure B.4: Fourier amplitude spectrum of the material point in the upper-most element.

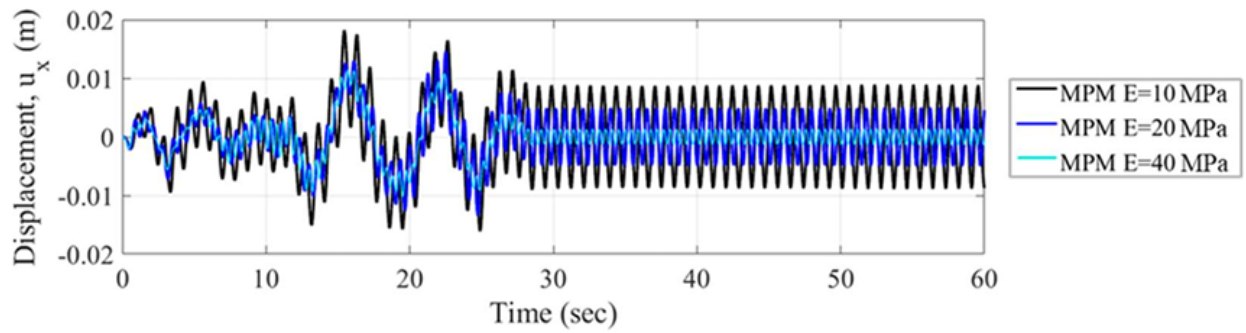

Figure B.5: Effect of changing the natural frequency of the soil column (by changing Young's modulus, E, value) on the displacement-time history results.

B.6 Conclusions

The MPM framework has been verified for earthquake site response analysis by means of the implementation of tied-degree-of-freedom (TDOF) boundary conditions. A soil column boundary value problem was used to compare the results from MPM and FEM simulations. It was seen that the MPM solution was consistent with FEM and captured the natural frequency harmonics from the analytical solution. The MPM is shown as a promising numerical

framework that is compatible with the current state-of-practice FEM approach while also capable of simulating large deformation problems in geotechnical engineering. Future work of this research will consider more advanced constitutive models.

Appendix C

Impact of Fluid Column Collapse on Structures using Higher-Order MPM.

Published in GeoCongress 2026 proceedings, with the following reference: Alsardi, A. and Yerro, A., 2022. Impact of Fluid Column Collapse on Structures using Higher-Order MPM. In GeoCongress 2026, Salt Lake City, UT. 2026 (In Press).

The following authors contributed to this manuscript, as follows:

- Abdelrahman Alsardi
  - Developed and implemented volumetric strain smoothing algorithm in MPM.
  - Performed all numerical simulations from pre-processing to post-processing and analysis.
  - Prepared all figures and wrote the original draft of the manuscript.
  - Addressed conference peer-review comments.
- Dr. Alba Yerro
  - Provided invaluable feedback throughout the implementation of the framework.
  - Discussed results and troubleshooting strategies to perform successful numerical simulations.
  - Obtained research funds to enable the deployment of the framework.
  - Edited and revised the conference manuscript.

C.1 Introduction

Geotechnical engineering problems often involve large deformations of the soil. Within the last decade, the Material Point Method (MPM) [58] has garnered lots of attention from the geotechnical community due to its ability to deal with large deformations at the same time that has a close resemblance to the Finite Element Method. Key characteristics of the conventional MPM framework include the fact that it can simulate large deformations by virtue of mobile Lagrangian integration points, so-called material points (MP), which move within an Eulerian nodal background grid and represent the continuum. The governing momentum balance equation is solved on the nodes, and the solution is then transferred back to the integration points. The numerical framework avoids mesh entanglement as the background grid remains undeformed. Additionally, the MPM naturally prevents multi-body interpenetration, without the need for additional contact algorithms. However, there still exist fundamental challenges that show up as numerical instabilities and stress oscillations that hinder the MPM from fully achieving its full potential in simulating large deformations in practical applications. This is particularly important when advanced constitutive models with history-dependent state variables are required for the analysis. A main source of this numerical noise is attributed to the ringing instability known as the cell-crossing instability that occurs when using lower-order interpolation functions [60]. Moreover, simulating constant-volume deformation processes, such as those in undrained soils, nearly incompressible fluids (e.g., free water or fluidized soil), or critical state conditions, is also extremely challenging due to numerical artifacts associated with volumetric locking.

Variants of MPM that have been developed to tackle these challenges with particular emphasis on solving the cell-crossing error and the dynamic ringing instability. The Generalized Interpolation Material Point (GIMP) type approaches tend to smooth interpolation func-

tions and their derivatives, while also giving the integration points a tributary volume upon which the domain is performed [60]. These types of approaches use a structured mesh and require neighbor search algorithms. The GIMP-type approaches exhibit severe cases of particle separation under large deformations, which result in non-physical continuum behavior [147]. Other remedied variants include Dual Domain Material Point (DDMP), although the implementation can be cumbersome. Steffen et al. [66] was the first to show that higher-order frameworks using B-splines present significant stabilization in the MPM with minimal alteration to the standard computational cycle proposed by Sulsky et al. [58]. Concerning the mitigation of volumetric locking in higher-order frameworks, the existing techniques can be separated into (i) volumetric strain smoothing techniques (ii) volumetric stress smoothing techniques (e.g., [188]), and (iii) displacement-stress field decoupling methods (e.g., [76]). The volumetric stress smoothing is generally effective. However, updating stress state might result in the violation of consistency in advanced constitutive frameworks. Field decoupling methods can be challenging to implement and often require significant reformulation of the time discretization scheme.

This paper aims to benchmark a new MPM formulation as part of an isogeometric framework where the cell-crossing problem is intrinsically solved using cubic interpolation functions. Volumetric locking is mitigated using a volumetric strain smoothing technique, allowing further implementation of advanced constitutive models. This is achieved with minimal changes to the standard MPM computational cycle. Such a volumetric strain smoothing algorithm has not been tested in higher order MPM, with stabilization techniques often relying on pressure smoothing and artificial viscous damping [188]. Column collapse problems, where the material is allowed to flow freely under gravity until it stops or eventually interacts with a wall, are common benchmarks used in the assessment of numerical frameworks (e.g., [188, 200]. The material is simulated as a Newtonian fluid with a high bulk modulus con-

sistent with a nearly incompressible soil material at its fluidized state, with minimal density variation. The goal is to provide a qualitative insight into the numerical stability of the newly stabilized MPM framework, looking at the effect of interpolation function order and volumetric strain stabilization. Additionally, the interaction of the fluid with downstream boundaries is also assessed considering fully rigid and linear-elastic behaviors. The numerical framework is validated by comparison against benchmark numerical and experimental data, when available.

This paper is organized as follows. Firstly, the higher-order B-spline MPM numerical framework is presented, followed by the description of the volumetric smoothing algorithm. Secondly, fluid column collapse is simulated with a height-to-width aspect ratio of 1 (square) and 2 (rectangle). This is compared to the benchmark experiment and existing MPM results in the literature. Thirdly, the column collapse problem is simulated with a downstream fully reflective rigid boundary. Fourthly, an elastic boundary wall is considered as a barrier, and the wall deflection is measured for comparison against a numerical benchmark. Next, a theoretical variation of the last simulation is considered to assess the effect of the basal boundary of the wall. The final conclusions are summarized in the end.

C.2 Stabilized Higher-Order MPM Numerical Framework

A novel MPM formulation is proposed herein to mitigate numerical noise triggered by cell-crossing instability and volumetric locking. The conventional MPM framework is modified by using a recursive higher-order B-Splines as interpolation functions which enables the user to select the order arbitrarily. A simple strain smoothing procedure is also used to stabilize

the volumetric strain. This framework benefits from retaining the standard MP spatial integration and prevents state variable and mean stress averaging compared to other stress smoothing techniques. More details of the current framework are described in Alsardi at el. [192].

Higher Order Extended B-Splines: Linear interpolation functions employed in the standard MPM have discontinuous derivatives, which result in cell-crossing error, incrementally destroying the solutions during large deformations [60]. The discontinuity specifically affects the internal force, strain, and stress calculations. As such, the use of B-spline functions in MPM serves to provide smooth derivatives, which prevent this error in MPM. Additionally, the nearby higher order elements share more active nodes in comparison with the standard linear elements. This prevents sudden erroneous jumps in the interpolated numerical values and provides a gradual element-to-element transition which reduces the MPM ringing error. As part of the newly developed isogeometric approach, the interpolation functions and corresponding derivatives are generated using the recursive Cox de-Boor equation [191]. The interpolation function derivatives are first calculated in the parameter space. The chain rule and the element Jacobian are then used to obtain the function derivatives in the physical space.

Volumetric locking mitigation: The use of higher-order B-Splines does not prevent volumetric locking. Therefore, the proposed formulation is enhanced with a smoothing algorithm of the volumetric strains to alleviate the 'checkerboarding' error that occurs when simulating nearly incompressible media. Specifically, the strain tensor for each MP is split into its volumetric and deviatoric portions. The volumetric portion of the strain is smoothed by the mapping to the background grid and remapped back to the MPs to smooth the volumetric strain field. The smoothed volumetric strain is added to the diagonal of the unaltered deviatoric portion of the strain tensor. The smoothed strain field is then used as an input

to the constitutive model. This approach is a simple numerical projection that minimally modifies the computational cycle of the MPM to reduce the restriction on the volumetric deformation.

C.3 Column Collapse Simulations

The column collapse simulations are performed with a normally fixed base and lateral sides to allow free sliding. The complexity of the models is progressively increased by including downstream barriers. The selected free flow benchmarks were previously explored by other researchers using different variations of the MPM formulation. This study performs further parametric analyses of B-Spline interpolation functions to assess the efficacy of the implemented framework as a tool to study dam break problems. All simulations in this paper are performed at 2D plane-strain, where the out-of-plane strain is always zero.

Fluid constitutive model: The strain-stress behavior of the fluid is simulated using the Newtonian constitutive model characterized by the bulk modulus, K_w, and dynamic viscosity, . The strain-stress relationship is presented in Equation C.1, where the MP stress, ^{MP}, is calculated using the volumetric strain, $^{MP}_{vol}$, and the deviatoric strain rate, v^{MP}_{dev}, where $\vec{I}$ is the identity matrix. A cavitation limit is applied as a tension cutoff to prevent the accumulation of tensile stress during deformation. The employed material parameters are K_w=2.2x104 kPa and =$1x10^{-6}$ kPa/s with density, $_w$=1000 kg/m^3, unless otherwise noted. The value of K_w was reduced by two orders of magnitude relative to that of water to reduce the computational cost for practical purposes. This increases the critical time step and makes the calculation computationally more efficient.

$$\sigma^{MP} = \varepsilon^{MP}_{vol} K_w \vec{I} + 2\mu \nabla v^{MP}_{dev} \tag{C.1}$$

Column collapse with no downstream barrier: Two aspect ratios (AR) of 1.0 (square) and 2.0 (rectangle) are considered to study the column collapse problem under the given framework with square elements of 5x5 cm^2. The stresses are initialized assuming a lateral earth pressure coefficient, K_0=0.5. Figures C.1 and C.2 depict the pressure contour plots for the AR=1 and AR=2, respectively, considering B-Spline interpolation function orders linear to cubic. Note that linear order is equivalent to the standard MPM with quadrilateral elements. The effect of volumetric strain smoothing to mitigate volumetric locking is also presented for comparison.

Results show that volumetric locking is extremely detrimental to the progression of the column collapse, where the flow is restricted and greatly underestimated due to the 'checker-boarding' error (Figures C.1 and C.2, (a-c)). Note that the sole use of higher-order interpolation functions can slightly mitigate volumetric locking, but that is not enough to ensure a stable simulation. The pressure fields are greatly enhanced when volumetric smoothing is performed (Figures C.1(d-f) and C.2(d-f)), and the behavior of the fluid in terms of geometry and runout is very similar for all orders of shape functions.

A quantitative validation between the new MPM formulation and existing benchmarks in terms of normalized runout and crest settlement is presented in Figure C.3. The normalized values of time, T, height, H, and length, L, are calculated using the initial column length, L_0, height, H_0, and gravitational acceleration, g=9.81 m/s^2, as shown in Equation C.2. The experimental benchmark by Martin and Moyce [255] is used for reference, and two numerical solutions are also considered, both using variations of the standard linear MPM; Mast et al. [201] used multi-field variational principle to filter noise in the volumetric portions of the strain and stress, while Martinelli and Galavi [196] uses linear shape functions with Gauss point integration and $\bar{B}$ approach to reduce the number of integration points used to calculate the volumetric strain. Note that Martinelli and Galavi [196] enforces an average

constant pressure field throughout the element to achieve a more stable solution as part of a mixed MP-gauss point spatial integration scheme. From Figure C.2, it is clear that the new MPM framework matches well with the previous numerical solutions and follows the experimental trends very well.

$$T = t\sqrt{\frac{H_0 g}{L_0^2}}; H = \frac{h(t)}{H_0}; L = \frac{l(t)}{L_0} \tag{C.2}$$

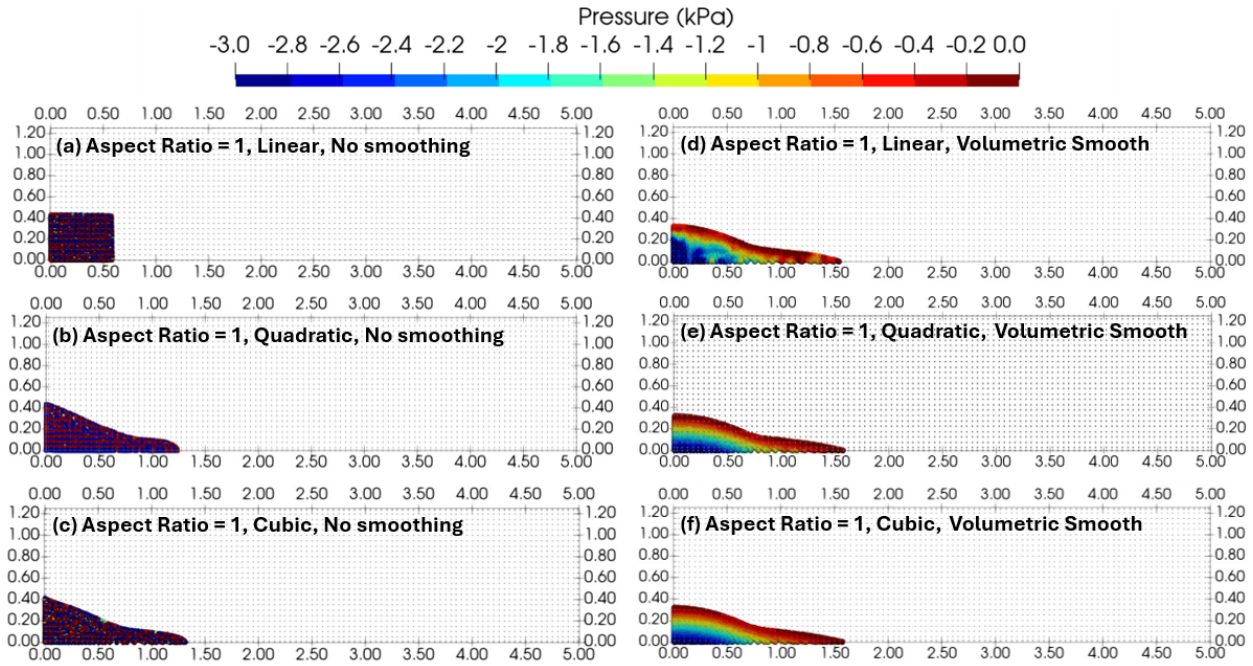

Figure C.1: Pressure field considering a column collapse problem with AR=1 for linear to cubic interpolation functions. (a-c) with no volumetric smoothing; (d-f) with volumetric smoothing.

Despite the similarity between the linear vs higher-order B-splines solutions in terms of runout and crest settlement, the results with linear shape functions show important numerical instabilities when analyzing the pressure field (Figures C.3(d) and C.4(d)). The reason for this noise can be attributed to cell-crossing instability. Looking at the deformed profile in

Figure C.1, it is also clear to see that cell-crossing error contributes to an increased restriction of the fluid flow (Figures C.1(a) vs C.1(b)). Quadratic and cubic interpolation functions in the new MPM framework are effective in preventing cell-crossing instability, leading to the most accurate solutions (Figures C.3(e-f) and C.4(e-f)). It is expected that the mitigation of artificial stress oscillations becomes more relevant when using advanced constitutive models with history-dependent parameters. All further analyses in this paper will be performed using cubic interpolation functions.

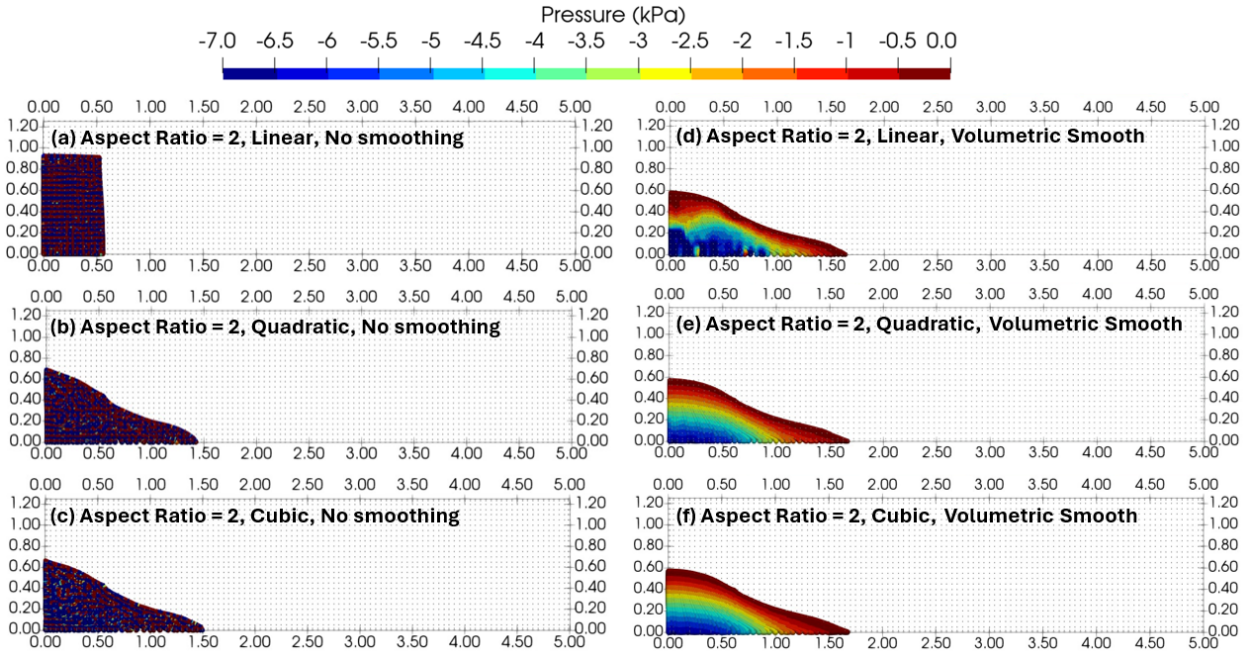

Figure C.2: Pressure field considering a column collapse problem with AR=2 for linear to cubic interpolation functions. (a-c) with no volumetric smoothing; (d-f) with volumetric smoothing.

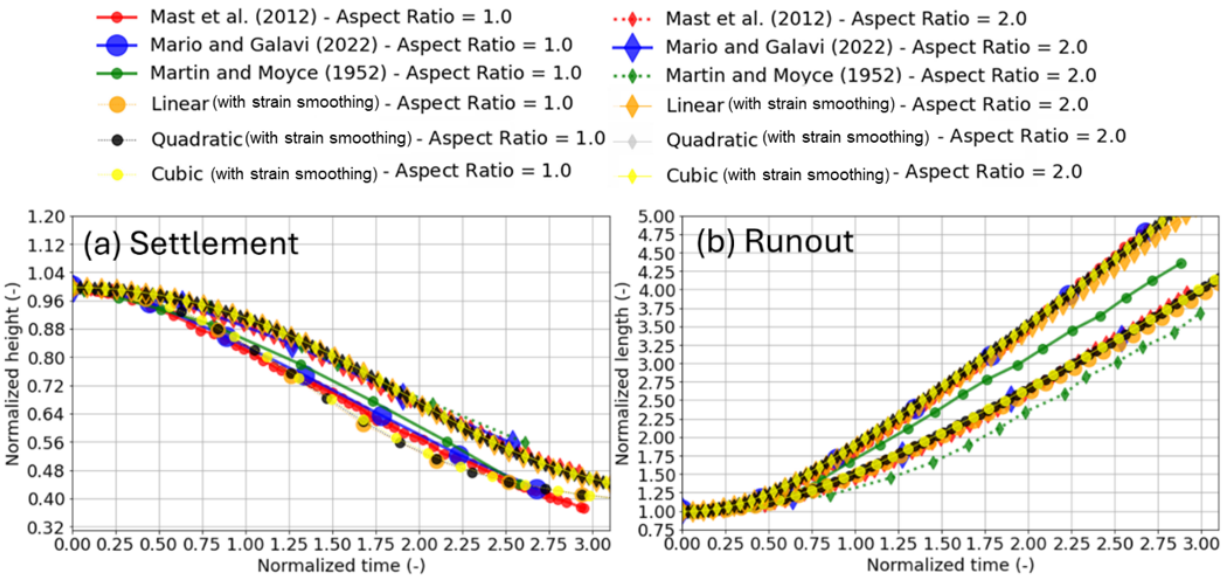

Figure C.3: Comparison between the new MPM formulation (considering different B-spline orders) and previous experimental and numerical solutions. Results are presented in terms of (a) normalized vertical settlement and (b) normalized runout.

Water column collapse with a rigid downstream barrier: The initial geometry is presented in Figure C.4(a) for the commonly adopted benchmark problem [76, 188, 200]. The background grid is discretized by 3.2x1.6 cm^2 rectangular elements. Figure C.4(b) shows the evolution of the water-structure interaction at three different times. The column breaks to flow freely until it reaches the rigid barrier which causes the fluid to reflect to generate a wave in the upstream direction. The results are generally consistent with numerical trends of Chandra et al. [200], Telikicherla and Moutsanidis [188] and Kularathna and Soga [76], and experimental photos in Cruchaga et al. [256]. The results are numerically stable, ultimately reaching a quasistatic water level (Figure C.4(b-iv)).

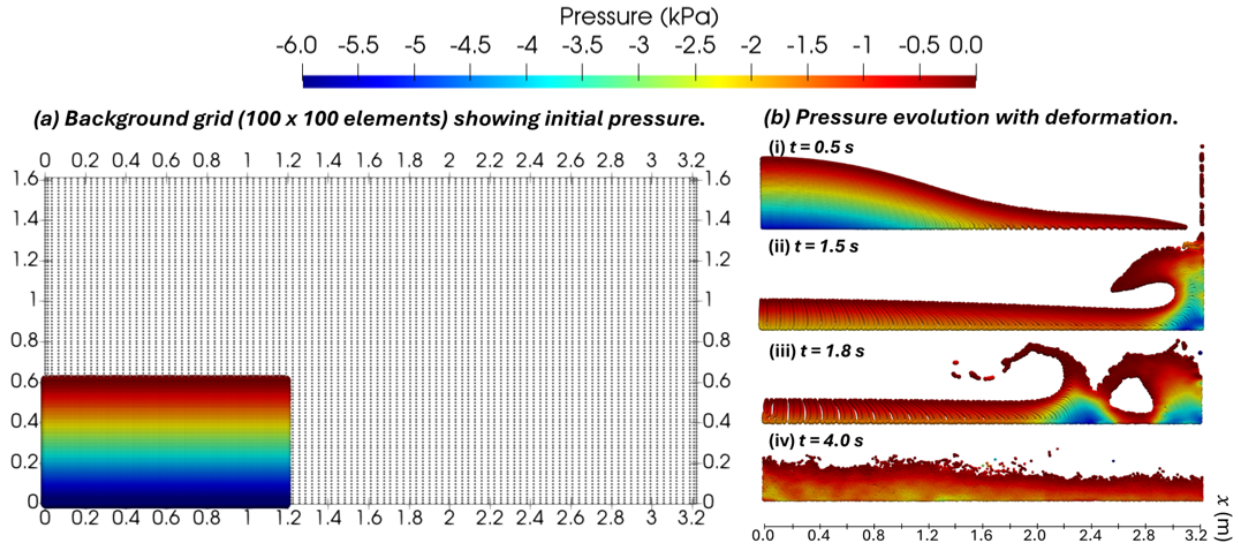

Figure C.4: Initial geometry subsequent wave evolution due to interaction with rigid barrier.

Water column collapse with an elastic downstream barrier: The downstream barrier is formally simulated as an elastic barrier with Young's Modulus, E=1 MPa, and Poisson ratio, =0.2, following a geometry that is consistent with Telikicherla and Moutsanidis [188]. We discretize the 58.4x43.8 cm^2 geometry into 100x100 elements. The evolution of the water pressure is presented in Figure C.5. It is observed that a smooth pressure distribution is maintained throughout the calculation. The water pressure increases upon impacting the elastic barrier (Figure C.5(a)), with subsequent pressure alleviation as the momentum is transferred to the elastic barrier (Figure C.5(b)). The pressure builds up further as it interacts with the downstream rigid wall due to its tendency to compress.

The result of this problem is heavily dependent on the input K_w parameter for the water material. Figure C.6 compares the wall deflection trends for K_w=2.2x103 kPa and K_w=2.2x104 kPa with the numerical benchmark from Walhorn et al. [257] as a reference case. Walhorn et al. [257] uses a free surface flow simulation from a monolithic fully incompressible model in an Eulerian finite element analysis incorporated with a level set method to track free surface flows. This case is often used as a benchmark that incorporates full incompressibility. It is

seen that the wall deflection rebound is closer to the incompressible reference when using a higher value for K_w.

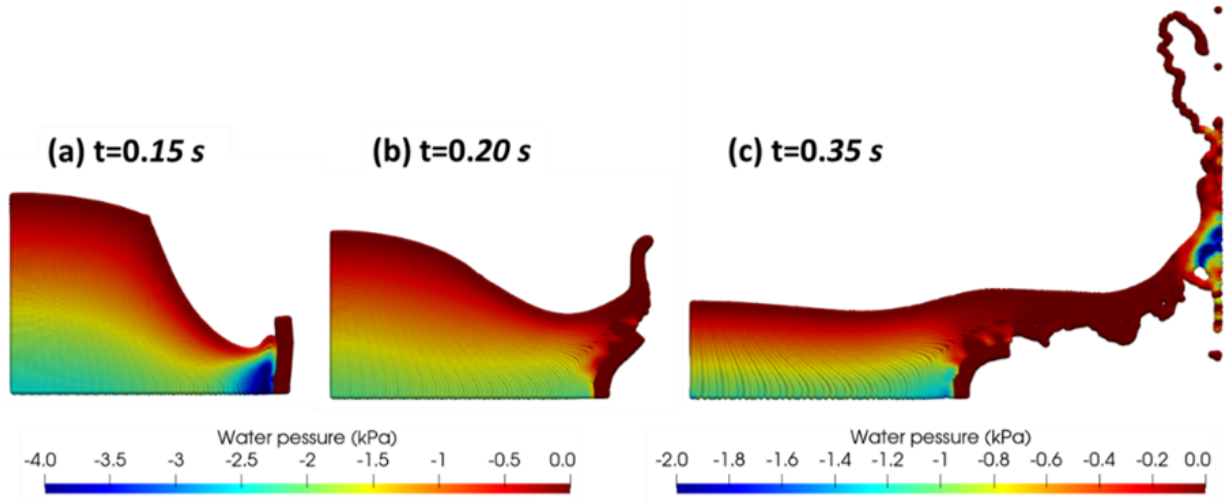

Figure C.5: Water pressure evolution as it impacts elastic barrier and interacts with rigid wall.

Finally, a variation of the previous model is considered with a wall that is not fixed to the underlying base. This could be the first step to mimic a prevalent failure mechanism that might occur when the wall is not well restrained (e.g, not laterally confined), triggering the failure of the wall foundation. Figure C.7 shows the water velocity and wall deflection considering a (a) fixed base and (b) free base at t=0.33 s. It is seen that the water velocity is reduced by about 30% when the wall is allowed to slide by means of a free base. The wall deflection also halves but incurs an absolute sliding displacement of 0.15 m. Enabling the wall to slide reduces the water volume that overrides the elastic barrier. This simulation presents a promising application of MPM in investigating flood defense designs against coastal surges incorporating fluid-structure interaction features.

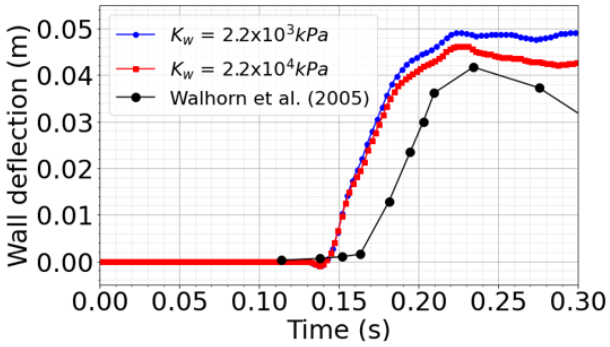

Figure C.6: Wall deflection versus time considering different bulk water modulus, K_w.

C.4 Conclusions

This paper presents a study for benchmarking a B-spline MPM with volumetric smoothening to solve problems associated with water-soil-structure interaction. The following are conclusions obtained from this study: (1) The use of higher-order interpolation alleviates locking but is not sufficient to obtain a stable stress solution. Volumetric locking mitigation is necessary to simulate fluid flows to prevent artifacts from the 'checkerboarding' errors. (2) Fluid interaction trends with rigid and elastic walls are captured in the framework with acceptable accuracy. A bulk modulus that is realistic to water is necessary to capture momentum transfer from the fluid to the structure and hence capture wall rebound. (3) The sliding mechanism of the elastic wall manifests in less deflection and overriding water volume. (4) Overall, cubic B-spline MPM presents a promising framework for fluid-structure interaction. This results in a smooth stress field that is numerically stable by intrinsically eliminating cell-crossing error and mitigating volumetric locking.

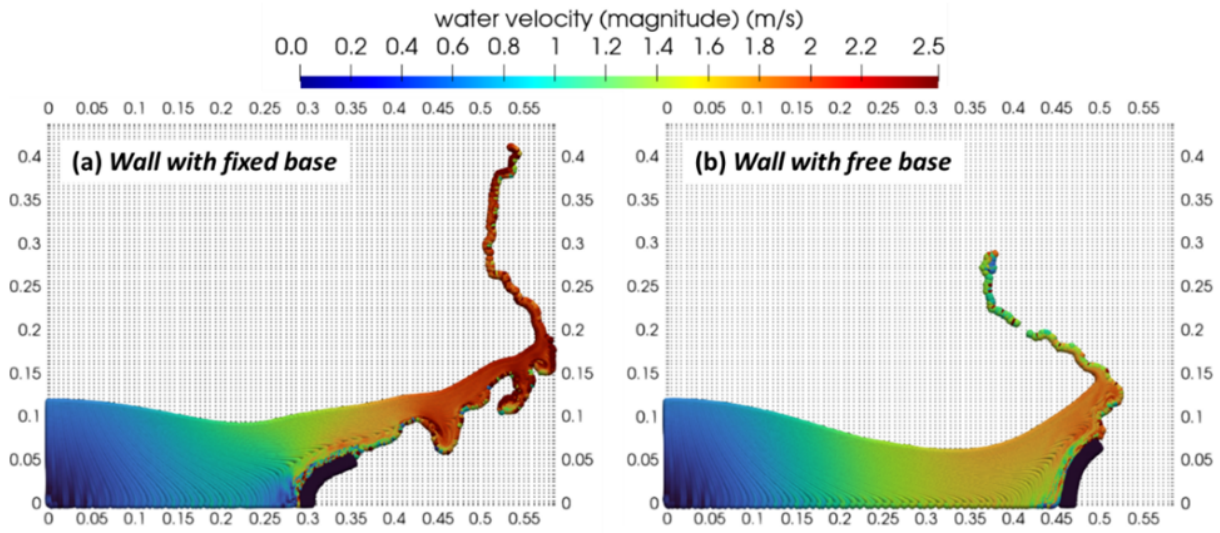

Figure C.7: Variation to assess the effect of the basal boundary condition at t=0.33s.

Appendix D

Implementation of Higher-Order MPM

D.1 Implementation details of the MPM

This section aims to outline implementation details of the MPM used in this paper. Throughout this section, the subscripts S and L are used to represent the quantities for the solid and liquid phases. When the water and solid phase co-exist in each MP, the MP volume is partitioned into the solid and liquid phase, V_S^{MP} and V_L^{MP} respectively, using the porosity n_L^{MP} (Equation D.1). The corresponding masses for each phase, m_S^{MP} and m_L^{MP}, are calculated using the densities of the phases, ρ_S and ρ_L, to obtain the mass of the mixture, m_m^{MP}, for each MP (Equation D.2). When solving the momentum balance of the liquid phase, it is also necessary to calculate the mass of MP, $\tilde{m}_L^{MP}$, assuming the full volume is occupied by the liquid (Equation D.3).

$$V_{MP} = V_S^{MP} + V_L^{MP} = (1 - n_L^{MP})V_{MP} + n_L^{MP}V_{MP} \tag{D.1}$$

$$\begin{cases} m_S^{MP} = \rho_S V_{MP}^S \\ m_L^{MP} = \rho_L V_L^{MP} \\ m_m^{MP} = m_S^{MP} + m_L^{MP} \end{cases} \tag{D.2}$$

$$\tilde{m}_L^{MP} = \rho_L V_{MP} \tag{D.3}$$

Herein, the computational cycle of the MPM is detailed, highlighting the 2-phase velocity formulation to simulate porous media behavior. The fully-coupled MPM with two velocity fields used to represent the solid and liquid phases in saturated porous media is also described. The modified fully-coupled two-phase MPM to simulate unsaturated porous media is also described.

D.1.1 Computational cycle

The momentum balance equation is discretized in space using nodal interpolation functions, N_i, as per the Galerkin discretization. An explicit Euler-Cromer integration scheme is adopted herein to update the set of MPs consisting of a total number of n_{MP}. The mass and force values at step k are used to obtain the velocity solution at step $k+1$. Note that the duration of the time step, Δt, is consistent with the Courant–Friedrichs–Lewy (CFL) condition with a Courant number of 0.75 to ensure stability of the explicit time integration. In this subsection, curly brackets will be used to highlight sub-steps taken to simulate 2-phase porous media in a coupled manner. The computational cycle consists of the following steps:

- Lumped nodal mass, M_i^k, is calculated by looping across the total number of MPs, n_{MP}, and mapping m_{MP} using the nodal basis functions, N_i evaluated at the parent

coordinates $\vec{\xi}^k_{MP}$ (Equation D.4). In the 2-phase formulation, Equations D.5 and D.6 are used to find the phase mass and drag lumped matrices. Lumped nodal liquid mass of the water phase, $\tilde{M}^k_{i,L}$, is calculated using $\tilde{m}^{MP}_L$ assuming the entire volume of the MP is occupied by the water phase. Drag force matrix, Q^k_L is calculated using the viscosity, ν^{MP}_L, and the intrinsic permeability, κ^{MP}_L consistent with Darcy's law.

$$M^k_i = \sum_{MP=1}^{n_{MP}} m_{MP} N_i(\vec{\xi}^k_{MP}) \tag{D.4}$$

$$\begin{cases} \tilde{M}^k_{i,L} = \sum\limits_{MP=1}^{n_{MP}} \tilde{m}^{MP}_L N_i(\vec{\xi}^k_{MP}) \\ Q^k_{i,L} = -\sum\limits_{MP=1}^{n_{MP}} N_i(\vec{\xi}^k_{MP}) \dfrac{n^{MP}_L \mu^{MP}_L}{\kappa^{MP}_L} N_i(\vec{\xi}^k_{MP})\ V_{MP} \end{cases} \tag{D.5}$$

$$\begin{cases} M_{i,L} = \sum\limits_{MP=1}^{n_{MP}} m^{MP}_L N_i(\vec{\xi}^k_{MP}) \\ M_{i,S} = \sum\limits_{MP=1}^{n_{MP}} m^{MP}_S N_i(\vec{\xi}^k_{MP}) \end{cases} \tag{D.6}$$

- Nodal external traction forces, $\vec{f}^{k,trac}_i$, are calculated across each element with size S_{el} whereby the integration is performed across boundary Gauss points, $n_{b,MP}$, under a traction vector, $\vec{\tau}$. The $n_{b,MP}$ boundary Gauss points are located in the parent and physical domains at $\vec{\xi}_{b,MP}$ and $\vec{x}_{b,MP}$, respectively (Equations D.7 and D.8). External forces, $\vec{f}^{ext}_{i,L}$ and $\vec{f}^{ext}_{i,S}$, are calculated for the liquid phase and the soil mixture (Equations D.9). The liquid phase traction vector, $\vec{\hat{p}}_L$, is applied in the normal directions. The traction vector on the soil mixture, $\vec{\tau}_m$, can be applied in an arbitrary direction.

$$\vec{\tau}(\vec{x}_{b,MP}) = \sum_{i=1}^{n_{n,bel}} N_i(\vec{\xi}_{b,MP}) \vec{\tau}(\vec{x}_i) \tag{D.7}$$

$$\vec{f}_i^{k,trac} = \sum_{bMP=1}^{n_{b,MP}} \frac{S_{el}}{n_{bMP}} N_i^k(\vec{\xi}_{MP}^k)\vec{\tau}(\vec{x}_{b,MP}) \tag{D.8}$$

$$\begin{cases} \vec{f}_{i,L}^{trac} = \sum_{bMP=1}^{n_{MP}} \frac{S_{el}}{n_{bMP}} N_i(\vec{\xi}_{bMP}^k)\vec{\hat{p}}_L \\ \vec{f}_{i,S}^{trac} = \sum_{bMP=1}^{n_{MP}} \frac{S_{el}}{n_{bMP}} N_i(\vec{\xi}_{bMP}^k)\vec{\tau}_m \end{cases} \tag{D.9}$$

- Nodal gravity forces, $\vec{f}_i^{k,grav}$, are calculated under the gravitational acceleration vector, $\vec{g}$ (Equation D.10). For the 2-phase formulation, the gravity forces, $\vec{f}_{i,L}^{grav}$ and $\vec{f}_{i,S}^{grav}$ are calculated for the liquid phase and the soil mixture respectively (Equation D.11).

$$\vec{f}_i^{k,grav} = \sum_{MP=1}^{n_{MP}} m_{MP} N_i(\vec{\xi}_{MP}^k)\vec{g} \tag{D.10}$$

$$\begin{cases} \vec{f}_{i,L}^{grav} = \sum_{MP=1}^{n_{MP}} m_L^{MP} N_i(\vec{\xi}_{MP}^k)\vec{g} \\ \vec{f}_{i,S}^{grav} = \sum_{MP=1}^{n_{MP}} m_m^{MP} N_i(\vec{\xi}_{MP}^k)\vec{g} \end{cases} \tag{D.11}$$

- Nodal internal forces, $\vec{f}_k^{k,int}$, are calculated using the derivatives of the interpolation functions in the physical domain, $B_i = \frac{dN}{d\vec{x}}$, and the stress, $\vec{\sigma}_{MP}$, evaluated at the parent domain, $\vec{\xi}_{MP}^k$ (Equation D.12). Internal forces, $\vec{f}_{i,L}^{int}$ and $\vec{f}_{i,S}^{int}$, are calculated using the pore pressure, p_L^{MP}, and the effective stress, $\vec{\sigma}'_{MP}$ (Equation D.13).

$$\vec{f}_i^{k,int} = -\sum_{MP=1}^{n_{MP}} V_{MP} B_i(\vec{\xi}_{MP}^k)\vec{\sigma}_{MP} \tag{D.12}$$

$$\begin{cases} \vec{f}_{i,L}^{k,int} = -\sum_{MP=1}^{n_{MP}} B_i(\vec{\xi}_{MP}^k) p_L^{MP} \vec{m} V_{MP} \\ \vec{f}_{i,S}^{k,int} = -\sum_{MP=1}^{n_{MP}} B_i(\vec{\xi}_{MP}^k) \vec{\sigma}'_{MP} V_{MP} \end{cases} \tag{D.13}$$

- Nodal acceleration field, $\vec{a}_i^k$, is calculated by dividing the resultant for the nodal forces with the nodal mass, M_i^k (Equation D.14). Two acceleration fields are calculated when using the 2-phase formulation as shown in Equation D.15: (i) Liquid nodal acceleration, $\vec{a}_{i,L}$, is calculated by dividing the liquid resultant forces with the liquid mass assuming the entire volume is occupied by the liquid phase. (ii) Acceleration of the solid phase, $\vec{a}_{i,S}$, is back-calculated from the momentum balance of the mixture using $\vec{a}_{i,L}$.

$$\vec{a}_i^k = \frac{\vec{f}_i^{k,trac} + \vec{f}_i^{k,grav} + \vec{f}_i^{int,k}}{M_i^k} \tag{D.14}$$

$$\begin{cases} \vec{a}_{i,L}^k = \dfrac{\vec{f}_{i,L}^{k,trac} + \vec{f}_{i,L}^{k,grav} + \vec{f}_{i,L}^{k,int} + Q_{i,L}^k(\vec{v}_{i,L}^k - \vec{v}_{i,S}^k)}{\tilde{M}_{i,L}^k} \\ \vec{a}_{i,S}^k = \dfrac{\vec{f}_{i,S}^{k,trac} + \vec{f}_{i,S}^{k,grav} + \vec{f}_{i,S}^{k,int} - M_{i,L}^k \, \vec{a}_{i,L}^k}{M_{i,S}^k} \end{cases} \tag{D.15}$$

- MP velocity, $\vec{v}_{MP}^{k+1}$, is calculated through forward Euler integration across time step duration, Δt, using the nodal acceleration, $\vec{a}_i^k$. In a similar manner, this is calculation is performed in each phase to obtain the MP velocities, $\vec{v}_{MP,L}^{k+1}$ and $\vec{v}_{MP,S}^{k+1}$, for the liquid and solid phases.

$$\vec{v}_{MP}^{k+1} = \vec{v}_{MP}^k + \Delta t \sum_{i=1}^{n_{n,el}} N_i(\vec{\xi}_{MP}^k) \vec{a}_i^k \tag{D.16}$$

$$\begin{cases} \vec{v}_{MP,L}^{k+1} = \vec{v}_{MP,L}^{k} + \Delta t \sum_{i=1}^{n_{n,el}} N_i(\vec{\xi}_{MP}^{k}) \vec{a}_{i,L}^{k} \\ \vec{v}_{MP,S}^{k+1} = \vec{v}_{MP,S}^{k} + \Delta t \sum_{i=1}^{n_{n,el}} N_i(\vec{\xi}_{MP}^{k}) \vec{a}_{i,S}^{k} \end{cases} \tag{D.17}$$

- Nodal momentum, $\vec{P}_i^{k+1}$, is calculated by mapping the product of the momentum of each MP (i.e., $m_{MP}\vec{v}_{MP}^{k+1}$) back to the nodes, where $n_{el,i}$ is the number of nodes in an element (Equation D.18). Nodal velocity, $\vec{v}_i^{k+1}$, is calculated by dividing the nodal momentum, $\vec{P}_i^{k+1}$, by the nodal mass, M_i^k (Equation D.19). When using the 2-phase formulation, the nodal velocities for the liquid and solid phases, $\vec{v}_{i,L}^{k+1}$ and $\vec{v}_{i,S}^{k+1}$, are updated in the same manner (Equation D.20).

$$\vec{P}_i^{k+1} = \sum_{el=1}^{n_{el,i}} \sum_{MP=1}^{n_{MP}} m_{MP} N_i(\vec{\xi}_{MP}^{k}) \vec{v}_{MP}^{k+1} \tag{D.18}$$

$$\vec{v}_i^{k+1} = \frac{\vec{P}_i^{k+1}}{M_i^k} \tag{D.19}$$

$$\begin{cases} \vec{v}_{i,L}^{k+1} = \dfrac{\sum_{el=1}^{n_{el,i}} \sum_{MP=1}^{n_{MP}} m_L^{MP} N_i(\vec{\xi}_{MP}^{k}) \vec{v}_{L,MP}^{k+1}}{M_{i,L}} \\ \vec{v}_{i,S}^{k+1} = \dfrac{\sum_{el=1}^{n_{el,i}} \sum_{MP=1}^{n_{MP}} m_S^{MP} N_i(\vec{\xi}_{MP}^{k}) \vec{v}_{S,MP}^{k+1}}{M_{i,S}} \end{cases} \tag{D.20}$$

- Nodal incremental displacement field, $\Delta\vec{u}_i^{k+1}$ is calculated by multiplying the velocity field, $\vec{v}_i^{k+1}$, by the time increment, Δt. Incremental displacement fields for the liquid and solid phase, $\Delta\vec{u}_{i,L}^{k+1}$ and $\Delta\vec{u}_{i,S}^{k+1}$, is calculated by multiplying the corresponding velocity fields by Δt.

$$\Delta\vec{u}_i^{k+1} = \Delta t \vec{v}_i^{k+1} \tag{D.21}$$

$$\begin{cases} \Delta\vec{u}_{i,L}^{k+1} = \Delta t \ \vec{v}_{i,L}^{k+1} \\ \Delta\vec{u}_{i,S}^{k+1} = \Delta t \ \vec{v}_{i,S}^{k+1} \end{cases} \tag{D.22}$$

- Incremental MP strain, $\Delta\vec{\varepsilon}_{MP}^{k+1}$, is calculated using the derivative of the interpolation function in the physical domain, B_i, and the incremental nodal displacement field, $\Delta\vec{u}_i^{k+1}$ (Equation D.23). When using the 2-phase formulation, the incremental MP strains for the liquid and solid phase, $\Delta\vec{\varepsilon}_{L,MP}^{k+1}$ and $\Delta\vec{\varepsilon}_{S,MP}^{k+1}$ respectively, are evaluated using the incremental displacement fields, $\Delta\vec{\varepsilon}_{MP,L}^{k+1}$ and $\Delta\vec{\varepsilon}_{MP,S}^{k+1}$, and B_i (Equation D.24).

$$\Delta\vec{\varepsilon}_{MP}^{k+1} = B_i(\vec{\xi}_{MP}^{k})\Delta\vec{u}_i^{k+1} \tag{D.23}$$

$$\begin{cases} \Delta\vec{\varepsilon}_{MP,L}^{k+1} = B_i(\vec{\xi}_{MP}^{k})\Delta\vec{u}_{i,L}^{k+1} \\ \Delta\vec{\varepsilon}_{MP,S}^{k+1} = B_i(\vec{\xi}_{MP}^{k})\Delta\vec{u}_{i,S}^{k+1} \end{cases} \tag{D.24}$$

- Constitutive model is deployed to evaluate effective stress increment for each MP, $\Delta\vec{\sigma}'^{k+1}_{MP}$, using $\Delta\vec{\varepsilon}_{MP}^{k+1}$, state variables, SV, and the tangent stiffness matrix, D (Equation D.25). Increment of excess pore pressure and effective stress are calculated using constitutive laws of liquid and soil. In this research, the liquid is assumed to be Newtonian where the pressure is calculated using the volumetric strains of the liquid and solid phase, $\Delta\varepsilon_{MP,L,vol}$ and $\Delta\varepsilon_{MP,S,vol}$, and the liquid porosity, n_L, and the bulk water modulus, K_w (Equation D.26).

$$\Delta\vec{\sigma}'^{k+1}_{MP} = D(SV)\cdot\Delta\vec{\varepsilon}_{MP}^{k+1} \tag{D.25}$$

$$\begin{cases} \Delta\varepsilon_{MP,S,vol} = \mathrm{tr}(\Delta\vec{\varepsilon}^{k+1}_{MP,S}) \\ \Delta\varepsilon_{MP,L,vol} = \mathrm{tr}(\Delta\vec{\varepsilon}^{k+1}_{MP,L}) \\ \Delta p_L = \dfrac{K_w}{n_L}(n_L\nabla\cdot\vec{v}_L + (1-n_L)\nabla\cdot\vec{v}_S) \\ \qquad = K_w\left(\Delta\varepsilon_{MP,L,vol} + \dfrac{1-n_L}{n_L}\Delta\varepsilon_{MP,S,vol}\right) \end{cases} \tag{D.26}$$

- The MP volume (Equation D.27), density (Equation D.28), and liquid porosity (Equation D.29) of each MP is updated according to the volumetric strain, $\Delta\vec{\varepsilon}^{k+1}_{MP,S}$, of the solid skeleton.

$$V^{k+1}_{MP} = (1+\Delta\varepsilon^{k+1}_{MP,S,vol})V^k_{MP} \tag{D.27}$$

$$\rho^{k+1}_{MP} = \frac{\rho^k_{MP}}{(1+\Delta\varepsilon^{k+1}_{MP,S,vol})} \tag{D.28}$$

$$\{n_L = n_L + (1-n_L)\Delta\varepsilon_{MP,S,vol} \tag{D.29}$$

- Update MP displacement, $\vec{u}^{k+1}_{MP}$, and position, $\vec{x}^{k+1}_{MP}$, according to the incremental displacement field, $\Delta\vec{u}^{k+1}_i$. When using the 2-phase formulation, the MP locations are updated according to $\Delta\vec{u}^{k+1}_{i,S}$ as they are Lagrangian with respect to the solid phase.

$$\vec{u}^{k+1}_{MP} = \vec{u}^k_{MP} + \sum_{i=1}^{n_{n,el}} N_i(\vec{\xi}^k_{MP})\Delta\vec{u}^{k+1}_i \tag{D.30}$$

$$\vec{x}^{k+1}_{MP} = \vec{x}^k_{MP} + \sum_{i=1}^{n_{n,el}} N_i(\vec{\xi}^k_{MP})\Delta\vec{u}^{k+1}_i \tag{D.31}$$

D.2 NURBS interpolation function algorithms

An outline of the algorithms used to generate NURBS interpolation functions are presented in this appendix. Algorithm 1 presents the pseudocode used to generate the NURBS functions and their derivatives in 3D using the Cox de-Boor recursive equation in each direction and their tensor product. The IEN matrix is a connectivity array that relates the local interpolation function numbers for a given element number to their corresponding global interpolation function numbers. The INN matrix is referred to as the 'NURBS coordinates' which connects the global element numbering in the physical domain to the parameter domain, and provides the knot vector indices corresponding to the element. The pseudocode in Algorithm 1 shows (i) the coordinate transformation from the parameter space to the parent space (i.e., $\vec{\tilde{\xi}}$ to $\vec{\xi}$) for each MP, (ii) the use of Cox de-Boor equation using the coordinates in the parameter space to evaluate the univariate interpolation functions and their derivatives, (iii) the tensor product of the univariate interpolation functions and their derivatives to obtain the interpolation function derivatives in 3D. Algorithm 2 presents the normalization procedure for the NURBS interpolation functions and their derivatives to ensure mass conservation. Algorithm 3 presents the pseudocode to calculate the Jacobian that interconnects physical, parameter, and parent spaces. These aforementioned algorithms represent the main modifications performed to the MPM to calculate the spatial interpolation functions in an IGA framework.

Algorithm 1 Evaluation of interpolation functions and their derivatives for 3D NURBS.

Require: Local position in parent domain ($\tilde{\xi}$), Connectivity array (IEN), Element number (IEl), Patch number (IP), NURBS coordinates, (INN), Knot vectors (Ξ, $\mathcal{H}$, $\mathcal{Z}$), Shape function univariate orders (p, q, r)

Ensure: shape function value (N_i), and shape function derivative value w.r.t. parameter domain ($\frac{dN_i}{d\xi}$)

Part A: Obtain NURBS coordinates using connectivity array.

ni $\leftarrow$ INN(IEN(1, IEl, IP), 1, IP)
nj $\leftarrow$ INN(IEN(1, IEl, IP), 2, IP)
nk $\leftarrow$ INN(IEN(1, IEl, IP), 3, IP)

Part B: Obtain location in parameter space.

$\xi \leftarrow \frac{1}{2}((\Xi(\text{ni+1, IP}) - \Xi(\text{ni, IP}))\tilde{\xi}(1) + (\Xi(\text{ni+1, IP}) + \Xi(\text{ni, IP})))$
$\eta \leftarrow \frac{1}{2}((\mathcal{H}(\text{nj+1, IP}) - \mathcal{H}(\text{nj, IP}))\tilde{\xi}(2) + (\mathcal{H}(\text{nj+1, IP}) + \mathcal{H}(\text{nj, IP})))$
$\zeta \leftarrow \frac{1}{2}((\mathcal{Z}(\text{nk+1, IP}) - \mathcal{Z}(\text{nk, IP}))\tilde{\xi}(3) + (\mathcal{Z}(\text{nk+1, IP}) + \mathcal{Z}(\text{nk, IP})))$

Part C: Obtain univariate shape function values in each direction.

$[N_i, \frac{dN_i}{d\xi}] \leftarrow$ Cox de Boor(ξ, p, Ξ)
$[M_i, \frac{dM_i}{d\eta}] \leftarrow$ Cox de Boor(η, q, $\mathcal{H}$)
$[L_i, \frac{dL_i}{d\zeta}] \leftarrow$ Cox de Boor(ζ, r, $\mathcal{Z}$)

Part D: Perform tensor product multiplication to obtain 3D shape functions and derivatives.

for orders $0 \rightarrow p$ in ζ direction **do**
  for orders $0 \rightarrow q$ in η direction **do**
    for orders $0 \rightarrow r$ in ξ direction **do**
      $n_{loc} \leftarrow n_{loc} + 1$
      Obtain control point weight, $W_i \leftarrow$IEN(n_{loc}, IEl, IP)
      $R(n_{loc}) = N_i M_i L_i W_i$
      $\frac{dR}{d\xi}(n_{loc}, 1) = \frac{N_i}{d\xi} M_i L_i W_i$
      $\frac{dR}{d\xi}(n_{loc}, 2) = N_i \frac{dM_i}{d\eta} L_i W_i$
      $\frac{dR}{d\xi}(n_{loc}, 3) = N_i dM_i \frac{dL_i}{d\zeta} W_i$
    end for
  end for
end for

Algorithm 2 Normalization of interpolation functions and their derivatives for 3D NURBS.

Require: Shape function univariate orders (p, q, r), Shape function values (R), Shape function derivative w.r.t. parameter domain $(\frac{dR_i}{d\xi})$

Ensure: Normalized shape function values (R), Normalized shape function derivative w.r.t. parameter domain $(\frac{dR_i}{d\xi})$, Number of nodes in an element (n_{el})

Part A: Sum shape functions and their derivatives.

for orders $i = 0$ **to** p in ζ direction **do**
  for orders $j = 0$ **to** q in η direction **do**
    for orders $k = 0$ **to** r in ξ direction **do**
      $n_{loc} \leftarrow n_{loc} + 1$
      $\sum_{total} \leftarrow \sum_{total} + R(n_{loc})$
      $\sum_{\xi} \leftarrow \sum_{\xi} + \frac{dR}{d\xi}(n_{loc}, 1)$
      $\sum_{\eta} \leftarrow \sum_{\eta} + \frac{dR}{d\xi}(n_{loc}, 2)$
      $\sum_{\zeta} \leftarrow \sum_{\zeta} + \frac{dR}{d\xi}(n_{loc}, 3)$
    end for
  end for
end for

Part B: Normalize shape functions and derivatives.

$n_{el} = (p+1)(q+1)(r+1)$
for $n_{loc} = 1$ **to** n_{el} **do**
  $R(n_{loc}) \leftarrow \frac{R(n_{loc})}{\sum_{total}}$
  $\frac{dR}{d\xi}(n_{loc}, 1) \leftarrow \frac{\frac{dR}{d\xi}(n_{loc},1) \cdot \sum_{total} - R(n_{loc}) \cdot \sum_{\xi}}{\sum_{total}^2}$
  $\frac{dR}{d\xi}(n_{loc}, 2) \leftarrow \frac{\frac{dR}{d\xi}(n_{loc},2) \cdot \sum_{total} - R(n_{loc}) \cdot \sum_{\eta}}{\sum_{total}^2}$
  $\frac{dR}{d\xi}(n_{loc}, 3) \leftarrow \frac{\frac{dR}{d\xi}(n_{loc},3) \cdot \sum_{total} - R(n_{loc}) \cdot \sum_{\zeta}}{\sum_{total}^2}$
end for

Algorithm 3 Jacobian calculation for 3D NURBS element.

Require: Connectivity array (IEN), Element number (IEl), Patch number (IP), NURBS coordinates, (INN), Knot vectors (Ξ, $\mathcal{H}$, $\mathcal{Z}$), Number of nodes in an element (n_{el}), Shape function derivative w.r.t. parameter domain ($\frac{dR_i}{d\xi}$), Nodal coordinates, (Co).

Ensure: Shape function derivative w.r.t. physical space ($\frac{dR_i}{dx}$), Jacobian matrix ($\frac{dx}{d\xi}$), Jacobian determinant J.

Part A: Obtain physical-to-parameter space Jacobian.

for $nn = 1, n_{el}$ **do**
  NodeID = IEN(nn, IEl, IP)
  for orders $i = 1$ **to** 3 **do**
    for orders $j = 1$ **to** 3 **do**
      $\frac{dx}{d\xi}(i,j) \leftarrow \frac{dx}{d\xi}(i,j) + \frac{dR}{d\xi}(n_{loc},j)$ Co(NodeID, j, IP)
    end for
  end for
end for
$\frac{d\xi}{dx} = \frac{dx}{d\xi}^{-1}$

Part B: Use chain rule to find derivatives w.r.t physical space.

for $n_{loc} = 1$ **to** nen **do**
  for orders $i = 1$ **to** 3 **do**
    for orders $j = 1$ **to** 3 **do**
      $\frac{dR}{dx}(n_{loc},i) \leftarrow \frac{dR}{dx}(n_{loc},i) + \frac{dR}{d\xi}(n_{loc},j)\frac{d\xi}{dx}(j,i)$
    end for
  end for
end for

Part C: Obtain NURBS coordinates using connectivity array.

ni $\leftarrow$ INN(IEN(1, IEl, IP), 1, IP); $\frac{d\xi}{d\tilde{\xi}}(1,1) = \frac{1}{2}(\Xi(ni+1) - \Xi(ni))$
nj $\leftarrow$ INN(IEN(1, IEl, IP), 2, IP); $\frac{d\xi}{d\tilde{\xi}}(2,2) = \frac{1}{2}(\mathcal{H}(nj+1) - \mathcal{H}(nj))$
nk $\leftarrow$ INN(IEN(1, IEl, IP), 3, IP); $\frac{d\xi}{d\tilde{\xi}}(3,3) = \frac{1}{2}(\mathcal{Z}(nk+1) - \mathcal{Z}(nk))$

Part D: Obtain physical-to-parent space Jacobian and its determinant.

for orders $i = 1$ **to** 3 **do**
  for orders $j = 1$ **to** 3 **do**
    for orders $k = 1$ **to** 3 **do**
      $\frac{dx}{d\tilde{\xi}}(i,j) \leftarrow \frac{dx}{d\tilde{\xi}}(i,j) + \frac{dx}{d\xi}(i,k)\frac{d\xi}{d\tilde{\xi}}(k,j)$
    end for
  end for
end for
$J = |\frac{dx}{d\tilde{\xi}}|$

D.3 Determining local position in parent domain from global position

The local position in a parent domain of an MP can be calculated analytically when using B-splines because the mesh is structured grid that uses B-splines. There is a direct one-to-one relationship between the physical, parameter, and parent spaces. In this approach, the NURBS coordinates in the parameter space are scaled to match the boundaries of the elements in the physical space. The minimum and maximum scaled NURBS coordinates, k_i and k_{i+1} respectively, in each direction are used to obtain the coordinates in the parent domain as shown in Equation D.32. This coordinate in the parent space can be directly linked to the parameter space using the NURBS minimum and maximum coordinates, ξ_i and ξ_{i+1} respectively, as shown in Equation D.33.

$$\tilde{\xi} = 2\left(\frac{\mathrm{x} - k_i}{k_{i+1} - k_i}\right) - 1 \tag{D.32}$$

$$\xi = \frac{(\xi_{i+1} - \xi_i)\tilde{\xi} + (\xi_{i+1} + \xi_i)}{2} \tag{D.33}$$

However, if NURBS are to be used, the physical space geometry is governed by the weights of each node. As such, the direct relationship between the spaces no longer holds. It is argued that when using NURBS, the treatment of the mesh becomes similar to that of an unstructured mesh. The value of accurate geometry representation is added, as is the case, with greater computational expense. However, this is necessary for the numerical stability of certain physical systems. First, a guess is projected in the parent domain, whereby the coordinates in the parameter domain are then calculated ($\xi^{\mathcal{I}}$, $\eta^{\mathcal{I}}$, $\zeta^{\mathcal{I}}$). The corresponding global

coordinate is then calculated and is compared to the global coordinate solution, $\vec{\mathrm{x}}^{\text{solution}}$, as shown in Equation D.34. The calculated residual, $\vec{\mathrm{r}}$, is used in tandem with the inverse Jacobain, $\frac{d\tilde{\xi}}{dx}$, to iteratively calculate the solution in the parent space as shown in Equation D.35. The global coordinates for the iteration, $\vec{\mathrm{x}}^{\mathcal{I}+1}$, and $\vec{\mathrm{r}}$ are subsequently recalculated. The Newton iteration $\mathcal{I} \leftarrow \mathcal{I}+1$ until convergence is achieved within the element according to a specificed tolerance (i.e, $|\vec{\mathrm{r}}| < \text{TOL}$). Otherwise, when cell-crossing occurs, a search is initiated against neighboring elements and patches depending on which side was crossed until convergence is finally achieved.

$$\vec{\mathrm{r}}(\xi^{\mathcal{I}}, \eta^{\mathcal{I}}, \zeta^{\mathcal{I}}) = \left(\sum_{i=1}^{n_{el}} N_i(\xi^{\mathcal{I}}, \eta^{\mathcal{I}}, \zeta^{\mathcal{I}}) \mathrm{Co}_{i,j,k} \right) - \vec{\mathrm{x}}^{\text{solution}} \tag{D.34}$$

$$\tilde{\xi}^{\mathcal{I}+1} = \tilde{\xi}^{\mathcal{I}} + \left(\frac{d\tilde{\xi}}{dx}(\xi^{\mathcal{I}}, \eta^{\mathcal{I}}, \zeta^{\mathcal{I}}) \cdot \vec{\mathrm{r}} \right) \tag{D.35}$$

D.4 Benchmark for simulating near incompressibility and circular geometries

The efficacy of the strain smoothing implementation is assessed in this section when using B-splines as interpolation functions in the MPM. This serves as a necessary step to ensure compatibility with standard benchmark techniques in the literature prior to deploying the IGA-MPM algorithm to solve novel geotechnical engineering problems. We also assess the stability of IGA-MPM in simulating circular geometries. The commonly adopted Cook's membrane problem is considered herein. This is performed to ensure compatibility with results in the literature using a fine mesh discretization. A quadrant geometry is then considered.

D.4.1 Cook's Membrane problem

The Cook's membrane problem has been extensively adopted to investigate the performance of volumetric locking mitigation techniques [171, 174, 186, 189, 258, 259, 260, 261]. Trapezoidal-shaped solid is sheared under upward vertical traction loading applied at at the thin rightmost lateral edge. The left edge is fully fixed. It is considered as a small-strain problem which is usually considered as a fundamental check in insuring volumetric locking mitigation. Cubic B-splines are considered herein. The trapezoidal geometry is specifically adopted to incorporate triangular geometric features which are often known to be challenging when simulating nearly incompressible media. The geometry adopted herein is consistent with [186] with linear-elastic material parameters E=1000 kPa and ν=0.499, and density, ρ=1000 kg/m^3. The applied traction has a value of 0.25 N/m. The plane-strain formulation is used with the background grid discretized as 50 by 50 elements in the x and y directions. Each element in the structured mesh is filled with 4 MPs per coordinate direction. Figure D.1(a) and D.1(b) illustrate the numerical solution with and without strain-smoothing. The background mesh is also presented in the background in Figure D.1. The mean stress solution 'checkerboards' when smoothing is not used as shown in Figure D.1(b), resulting in an unstable simulation. However, volumetric locking is remedied through strain smoothing presenting an improved mean stress distribution as consistent with other implementations in the literature [174, 186]. The vertical displacement profile for the stabilized simulation is shown in Figure D.1(b). This presents a displacement of approximately 7 cm as consistent with the convergent solution of [186].

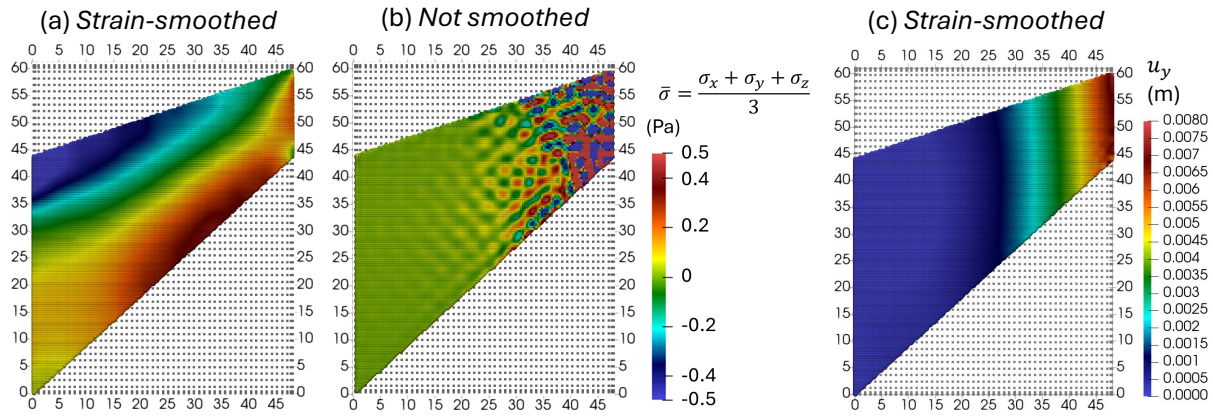

Figure D.1: Effect of strain-smoothing on the cook's membrane problem with a fine mesh refinement. (a) Mean effective stress with strain-smoothing. (b) Mean effective stress with no smoothing. (c) Vertical displacement profile with strain-smoothing.

D.4.2 Compression of a plane-strain quadrant under gravity

This example is analogous in concept to the 1D stresses generated in the regular column albeit with a circular geometry. The compression of a plane-strain quadrant, with radius = 1 m, under gravity is investigated here under quadratic and cubic interpolation functions. The material is linear-elastic with Young's modulus, E=1000 kPa, Poisson ratio, ν=0, and density, ρ=1000 kg/m^3. Each element contains 16 MPs corresponding to 4 MPs in each direction. The bottom boundary is fully fixed, and the lateral edge is normally fixed (i.e., rollers). The gravitational field, g, is set to 8 m/s^2, and the deformation is induced by linearly increasing the gravitational field from 0 to 12.5g consistent with [64] and [60]. Analytically, a maximum of 100 kPa is expected at the base of the quadrant under gravitational loading. Figure D.2 shows the vertical stress profiles for the quadrants using quadratic (a(i-iv)) and cubic (b(i-iv)) interpolation functions. In this simple example, it is seen that convergent stress profiles are achieved even at coarse discretizations. With refinement, very smooth stress profiles are achieved with a band of high stress at the base and a maximum vertical displacement of 0.37 m.

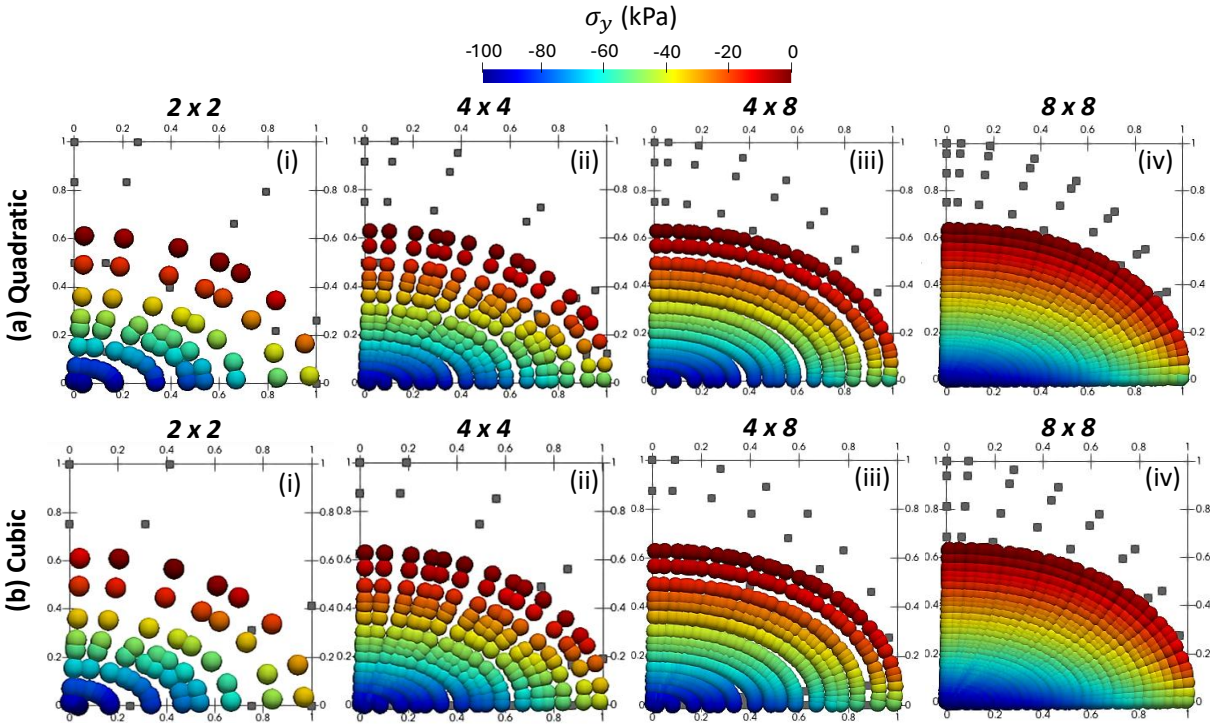

Figure D.2: Quadrant compression under $12.5g$, where g=8 m/s^2, for various mesh refinements using quadratic and cubic interpolation functions. Nodes are presented as gray squares, and MPs are represented as circles.

Appendix E

Formulation details of the PM4Sand model

The following sections describe the pertaining details of the PM4Sand constitutive model. The model is formulated in terms of stress ratio, r (Equation E.1). The value of r is calculated using the deviatoric stress tensor, s, normalized by the mean effective stress, p. Note that all stresses in this constitutive model are effective stresses, and the conventional prime symbol is dropped in the following subsections for simplification.

$$\boldsymbol{r} = \frac{\boldsymbol{s}}{p} = \begin{bmatrix} \frac{\sigma_{xx}-p}{p} & \frac{\sigma_{xy}}{p} \\ \frac{\sigma_{xy}}{p} & \frac{\sigma_{yy}-p}{p} \end{bmatrix} \tag{E.1}$$

E.1 Critical state surface

The framework of the PM4Sand model uses relative density, D_R, as opposed to void ratio, e_v. The critical state relative density, $D_{R,cs}$, is used as presented by Bolton [21] to define the critical state line. The relative state parameter index, ξ_R, is used as per Boulanger [262] to incorporate critical state theory within the PM4Sand model as shown in Equations E.2-E.3. The fitting parameters Q and R were shown by Bolton [21] to be 10 and 1 for quartz sand, which are used as secondary parameters in the PM4Sand model. These secondary parameters

may be modified by the user if there is interest in better capturing the critical state line. The value of ξ_R represents whether the material is loose or dense. Specifically, $\xi_R > 0$ for loose of critical soils ($D_{R,cs} > D_R$), and $\xi_R < 0$ for dense of critical soils ($D_{R,cs} < D_R$).

$$\xi_R = D_{R,cs} - D_R \tag{E.2}$$

$$D_{R,cs} = \frac{R}{Q - \ln(100\frac{p}{p_A})} \tag{E.3}$$

E.2 Bounding, dilatancy (phase transition), critical state surfaces

All surfaces used within the model are described herein, except the yield surface, which will be described in the next subsection. Surfaces look like a line in the $p - q$ space, and circles on a stress ratio graph of r_{yy} versus r_{xy}. The surfaces are tracked more easily when using the stress ratio approach, as initially proposed by Dafalias and Manzari [32]. The critical state stress ratio is defined by $M = \frac{q_c}{p_c}$. The ratio M can be related to the critical state effective stress friction angle, ϕ_{cv}, as shown in Equation E.4.

$$M = 2\sin(\phi_{cv}) \tag{E.4}$$

Similarly, the ratios M^b and M^d are the stress ratios that define bounding and dilatancy surfaces as related to the critical state ratio, as shown in Equations E.5 and E.6. The n^b and n^d factors are model parameters for calculating M^b and M^d, respectively. The default value of n^b is 0.5 for dense of critical, and a reduced value of $n^b/4$ is used to compute M^b

for loose of critical state soils. The default value of n^d is 0.1, and a higher value of $4n^d$ is used to compute M^d for dense of critical state soils. This model enables the flexibility in separately calibrating the behavior for contractive versus dilative behavior.

$$M^b = M \exp(-n^b \xi_R) \tag{E.5}$$

$$M^d = M \exp(n^d \xi_R) \tag{E.6}$$

E.3 Yield surface and image back-stress ratio tensors

The yield surface function, f, is defined in Equation E.7 as a function of the deviatoric stress tensor, s, back-stress ratio, α, that defines the yield surface cone center and mean effective stress, p. The parameter, m, defines the radius of the cone, which is often fixed at a value of 0.01. The yield surface function is normalized to be cast as a function of the stress ratio, $r = \frac{s}{p}$ (Equation E.8).

$$f = [(\mathbf{s} - p\boldsymbol{\alpha}) : (\mathbf{s} - p\boldsymbol{\alpha})]^{\frac{1}{2}} - \sqrt{\frac{1}{2}} pm = 0 \tag{E.7}$$

$$f = [(\mathbf{r} - \boldsymbol{\alpha}) : (\mathbf{r} - \boldsymbol{\alpha})]^{\frac{1}{2}} - \sqrt{\frac{1}{2}} m = 0 \tag{E.8}$$

The image back-stress ratio tensors, $\boldsymbol{\alpha}^b$ and $\boldsymbol{\alpha}^d$, at the bounding and dilatancy surfaces are defined to track the evolution of these surfaces (Equation E.9 and E.10. The term $\mathbf{n}$ is a second-order tensor used to represent the normal to the yield surface cone.

$$\boldsymbol{\alpha}^b = \sqrt{\frac{1}{2}}[M^b - m]\mathbf{n} \tag{E.9}$$

$$\boldsymbol{\alpha}^d = \sqrt{\frac{1}{2}}[M^d - m]\mathbf{n} \tag{E.10}$$

E.4 Stress reversal and initial back-stress ratio tensors

The value of α_{in} is updated at each loading reversal. A reversal is detected when Equation E.11 is true, where α_{in} is the initial back-stress ratio and $\mathbf{n}_{trial}$ is the trial norm to the yield surface in the stress ratio space. When a load reversal occurs, the value of α_{in} is updated to the current stress ratio.

$$(\boldsymbol{\alpha} - \boldsymbol{\alpha}_{in}) : \mathbf{n}_{trail} < 0 \tag{E.11}$$

Bounding surface plasticity models are prone to overshooting errors when load reversals occur [263]. These overshooting errors would produce a higher value of plastic modulus, K_p, upon reversals, which manifests in an over-stiffening effect. This is undesirable and does not reflect realistic cyclic soil behavior. In the present PM4Sand model (XX), an apparent initial back stress ratio, α_{in}^{app}, and a previous (apparent) initial back stress ratio, α_{in}, are introduced and tracked to remedy the overshooting problem. The components of α_{in} are taken as:

- the minimum (positive) value they have ever had, α_{in}^{min}, but smaller than zero, for positive loading directions
- the maximum (negative) value they have ever had, α_{in}^{max}, but no smaller than zero for

negative loading directions.

In this context, α_{in}^{max} (which is negative) and α_{in}^{min} (which is positive) are also tracked during loading. The parameter α_{in} from the Sanisand model is named α_{in}^{true} in PM4Sand, which is the true reversal back-stress ratio. The α_{in} value is updated according to Equation E.12 for use to calculate K_p to prevent the aforementioned stiffening effect.

$$\boldsymbol{\alpha}_{in} = \begin{cases} \boldsymbol{\alpha}_{in}^{true}, & \text{if } (\boldsymbol{\alpha} - \boldsymbol{\alpha}_{in}) : \mathbf{n} < 0, \\ \boldsymbol{\alpha}_{in}^{app}, & otherwise. \end{cases} \tag{E.12}$$

E.5 Elastic strains and moduli

Elastic deviatoric strain increment, $d\boldsymbol{e}^{el}$, and elastic volumetric strain increment, $d\varepsilon_{vol}^{el}$, are calculated as a function of the shear modulus, G, and bulk modulus, K, respectively. Prior to including the fabric effects, the value of G is a function of the small-strain shear modulus coefficient, G_0, and p. The factor C_{SR} accounts for the stress ratio effect in the G calculation. $C_{SR,0}$ and m_{SR} are constants. The current stress ratio, η, is calculated as the ratio of deviatoric stress magnitude, q, to the mean effective stress, p. The values of $C_{SR,0}$=0.5 and m_{SR}=4 are set as per the calibration by Boulanger and Ziotopoulou [111]. Bulk elastic modulus, K, is back-calculated from G as shown in Equation E.17. The value of p_A is set to atmospheric pressure equal to 101.3 kPa.

$$d\boldsymbol{e}^{el} = \frac{d\boldsymbol{s}}{2G} \tag{E.13}$$

$$d\varepsilon_{vol}^{el} = \frac{dp}{K} \tag{E.14}$$

$$G = G_0 p_A (\frac{p}{p_A})^{\frac{1}{2}} C_{SR} \tag{E.15}$$

$$C_{SR} = 1 - C_{SR,0} (\frac{\eta}{M^b})^{m_{SR}} \tag{E.16}$$

$$K = \frac{2(1+\nu)}{3(1-2\nu)} G \tag{E.17}$$

E.6 Plastic components without fabric effects (flow rule)

This section aims to summarize the main components of the plasticity framework. This includes the loading index for calculation of the plastic strains, back-stress ratio hardening, plastic modulus, and dilation.

E.6.1 Loading index

The loading index, L, is used to compute the plastic component of volumetric strain, $d\varepsilon_{vol}^{pl}$, and deviatoric strain, $d\boldsymbol{e}^{pl}$, increments (Equation E.18 and E.19) based on an associative flow rule.

$$d\varepsilon_{vol}^{pl} = \langle L \rangle D \tag{E.18}$$

$$d\boldsymbol{e}^{pl} = \langle L \rangle \boldsymbol{R}' \tag{E.19}$$

Parameter D represents the sand's dilatancy value. Tensor $\boldsymbol{R}$ is the direction of plastic strain increment, $d\varepsilon^{pl}$. Tensor $\boldsymbol{R}'$ is the deviatoric component of R (Equation E.21) as consistent with the associative flow rule. Note $\langle\rangle$ are MacCauley brackets, which maintain positive values for terms inside the brackets. The tensor R is shown in Equation E.20 for the assumption of no Lode angle dependency, as the model is formulated in 2D plane-strain.

$$\boldsymbol{R} = \mathbf{n} + \frac{1}{3} D \boldsymbol{I} \tag{E.20}$$

$$\boldsymbol{R}' = \mathbf{n} \tag{E.21}$$

The dilatancy parameter, D, relates the plastic volumetric strain increment, $d\varepsilon^{pl}$, to the magnitude of the plastic deviatoric strain increment, $d\boldsymbol{e}^{pl}$ (Equation E.22).

$$D = \frac{d\varepsilon^{pl}_{vol}}{|d\boldsymbol{e}^{pl}|} = \frac{d\varepsilon^{pl}_{vol}}{\sqrt{\frac{1}{2}}|d\gamma^{pl}|} \tag{E.22}$$

The loading index is identical to that presented in Dafalias and Manzari [32] (Equation E.23).

$$L = \frac{2G\mathbf{n} : d\boldsymbol{e} - \mathbf{n} : \mathbf{r} K d\varepsilon_{vol}}{K_p + 2G - KD\mathbf{n} : r} \tag{E.23}$$

The stress increment, $d\sigma$, for an imposed strain increment can be computed as shown in Equation E.24 where $d\boldsymbol{e}$ is the deviatoric strain. This expression will be enhanced with fabric considerations later on in this section to capture anisotropy as deformations occur.

$$d\sigma = 2Gd\boldsymbol{e} + Kd\varepsilon_{vol}\boldsymbol{I} - \langle L\rangle(2G\mathbf{n} + KD\mathbf{I}) \tag{E.24}$$

E.6.2 Hardening and the update of the back-stress ratio

The plastic modulus, K_p, is related to the kinematic hardening rule as shown in Dafalias and Manzari [32], whereby the back-stress ratio increment is updated as per Equation E.25.

$$d\boldsymbol{\alpha} = \langle L\rangle(\frac{2}{3})h(\alpha^b - \alpha) \tag{E.25}$$

Parameter h is referred to as the hardening coefficient. Expression $(\alpha^b - \alpha)$ is the distance between the bounding and current back-stress ratio tensors. When consistency is enforced (i.e., $df = 0$), Equation E.26 is derived to update the value of K_p.

$$K_p = \frac{2}{3}ph(\boldsymbol{\alpha}^b - \boldsymbol{\alpha}) : \mathbf{n} = \frac{2}{3}ph\mathbf{b} : \mathbf{n} \tag{E.26}$$

The consistency condition can be satisfied by expressing the hardening coefficient, h, as shown in Equation E.27.

$$h = \frac{3}{2}\frac{K_p}{p(\boldsymbol{\alpha}^b - \boldsymbol{\alpha}) : \mathbf{n}} \tag{E.27}$$

E.6.3 Plastic modulus

The equation for K_p is expressed in Equation E.28. A factor C_{rev} is introduced in K_p to soften the stress-strain response upon reversal when α does not exceed α_{in}^{app} (i.e., $(\alpha - \alpha_{in}^p) : \mathbf{n} \leq 0$). The expression in Equation E.30 defines C_{rev}. The factor, $C_{\gamma 1}$, is added to prevent the

denominator from becoming zero and render an unstable solution. Factor $C_{\gamma 1}$ also generates non-linearity even when $(\alpha - \alpha_{in}^{app}) : \mathbf{n}$ is small. Boulanger and Ziotopoulou [111] presented the calibration as per Equation E.29. For a state with a stress ratio outside the bounding surface ($(\alpha^b - \alpha) : \mathbf{n} < 0$) and loose than critical ($\xi_R < 0$) condition, K_p is set to zero instead of allowing negative values, which can generate numerical instabilities.

$$K_p = Gh_0 \frac{[(\boldsymbol{\alpha}^b - \boldsymbol{\alpha}) : \mathbf{n}]^{0.5}}{[\exp[(\boldsymbol{\alpha} - \boldsymbol{\alpha}_{\boldsymbol{in}}^{\boldsymbol{app}}) : \mathbf{n}] - 1] + C_{\gamma 1}} C_{rev} \tag{E.28}$$

$$C_{\gamma 1} = \frac{h_0}{200} \tag{E.29}$$

$$C_{rev} = \begin{cases} \frac{(\boldsymbol{\alpha} - \boldsymbol{\alpha}_{in}^{app}) : \mathbf{n}}{(\boldsymbol{\alpha} - \boldsymbol{\alpha}_{in}^{true}) : \mathbf{n}}, & \text{if } (\boldsymbol{\alpha} - \boldsymbol{\alpha}_{in}^{p}) : \mathbf{n} \leq 0, \\ 1, & otherwise. \end{cases} \tag{E.30}$$

E.6.4 Plastic volumetric strains - Dilation

Dilation occurs whenever the term $[(\boldsymbol{\alpha}^d - \boldsymbol{\alpha}) : \mathbf{n}]$ is negative, whereas contraction occurs when it is positive. The dilation parameter, D, is made proportional to the difference between the current stress ratio and the dilatancy surface stress ratio, $(\boldsymbol{\alpha}^d - \boldsymbol{\alpha})$. Depending on $(\alpha^d - \alpha) : \mathbf{n} \lessgtr 0$, contraction ($D > 0$), dilation ($D < 0$), or zero volumetric rate ($D = 0$) can be obtained. Following the original Manzari and Dafalias [264] formulation, Equation E.31 can be written. Parameter, A_{d0}, can be related to the dilatancy relationship proposed by Bolton [21] as shown in Equation E.32.

$$D = A_{d0}[(\boldsymbol{\alpha}^d - \boldsymbol{\alpha}) : \mathbf{n}] \tag{E.31}$$

$$A_{d0} = \frac{1}{0.4} \frac{\sin^{-1}(\frac{M^b}{2}) - \sin^{-1}(\frac{M}{2})}{M^b - M^d} \tag{E.32}$$

E.6.5 Plastic volumetric strains - Contraction

The dilation, D, during contraction is calculated using Equation E.33.

$$D = A_{dc}[(\alpha - \alpha_{in}) : n + C_{in}]^2 \frac{(\alpha^d - \alpha) : n}{(\alpha^d - \alpha) : n + C_D} \tag{E.33}$$

The parameter A_{dc} is used for contraction as opposed to A_{d0} for dilation, whereby A_{d0} is divided by the contraction rate parameter h_p (E.34). The value of h_p needs to be calibrated to obtain desired desired cyclic resistance ratio (CRR). The effect of confining stress on cyclic loading behavior was then conveniently incorporated by making h_p depend on ξ_R, so that the model produces results consistent with the design K_σ.

$$A_{dc} = \frac{A_{d0}}{h_p} \tag{E.34}$$

The term C_{in} is a function of fabric parameters, and C_D is a calibration parameter which is equal to 0.16 as calibrated by Chen [113] in Opensees [114]. The term C_D was often altered in different implementations (0.1 in FLAC [111] and 0.16 in Opensees [113]). The factor $\frac{(\alpha^d - \alpha):n}{(\alpha^d - \alpha):n + C_D}$ ensures that dilatancy, D, goes to zero smoothly as α approaches α^d. The factor, h_p, is a function of the state parameter, ξ_R, as shown in Equation E.35. There is an upper limit on the contraction rate as shown in Equation E.36.

$$h_p = \begin{cases} h_{p0} \exp[-0.7 + 7.0(0.5 - \xi_R)^{2.5}], & \text{if } \xi_R \leq 0.5, \\ h_{p0} \exp[-0.7], & otherwise. \end{cases} \tag{E.35}$$

$$D \leq 1.5 A_{d0} \frac{(\alpha^d - \alpha) : n}{(\alpha^d - \alpha) : n + C_D} \tag{E.36}$$

E.7 Fabric effects

In Manzari and Dafalias [264] model, the fabric-dilatancy tensor, z, was first introduced to account for the effects of prior straining and the corresponding induced anisotropy. The fabric tensor, z, evolved in response to plastic volumetric dilation strains as shown in Equation E.37. The parameter c_z controls the rate of evolution, and z_{max} is the maximum value that the components of the fabric-dilatancy tensor, z, can have.

$$dz = -c_z \langle -d\varepsilon_{vol}^{pl} \rangle (z_{max}\mathbf{n} + \boldsymbol{z}) \tag{E.37}$$

Parameter c_z controls the rate of evolution, and z_{max} is the maximum value that z can attain. The fabric-dilatancy tensor, z, was modified for the PM4Sand model as presented in Equation E.38. The tensor, z, evolves in response to plastic deviatoric strains that occur during dilation only (i.e., dividing the plastic volumetric strain by the dilatancy gives shear strain).

$$dz = -\frac{c_z}{1 + \langle \frac{z_{cum}}{2 z_{max} - 1} \rangle} \frac{\langle -d\varepsilon_{vol}^{pl} \rangle}{D} (z_{max}\mathbf{n} + \boldsymbol{z}) \tag{E.38}$$

The evolution of fabric, z, is restricted to only occur when $(\alpha^d - \alpha) : \mathbf{n} < 0$ (i.e., when dilation

occurs). This additional constraint prevents fabric accumulation during dilation above the rotated dilatancy surface but below the non-rotated dilatancy surface. The parameter z_{cum} is the cumulative value of absolute changes in z computed according to Equation E.39.

$$dz_{cum} = |dz| \tag{E.39}$$

The rate of evolution for z therefore decreases with increasing values of z_{cum}, which enables the undrained cyclic stress-strain response to progressively accumulate shear strain rather than lock-up into a repeating stress-strain loop, as is usually observed in the Manzari and Dafalias [264] model. In addition, the greatest past peak value (scalar amplitude) for z during its loading history is also tracked as shown in Equation E.40.

$$z_{peak} = \max(\sqrt{\frac{z : z}{2}}, z_{peak}) \tag{E.40}$$

The values of z, z_{peak}, and z_{cum} are later used to facilitate the accumulation of shear strains under symmetric loading through their effects on the plastic modulus and dilatancy relationships. Fabric terms do not grow until the soil reaches the dilatancy surface, and the stress ratios are limited by the bounding stress ratio. If there is no horizontal shear stress reversal, neither the back-stress ratio nor the fabric terms reverse.

E.7.1 Effect of fabric on plastic modulus

The effect of fabric was incorporated in the plastic modulus, K_p, by reducing K_p as the fabric tensor increases in peak amplitude, as shown in Equation E.41. The factors, $C_{k\alpha}$, C_{zpk1}, C_{zpk2}, and C_{pzp2} are presented in Equations E.42, E.44, E.44, and E.45. The factor, C_{rev}, has been defined in Equation E.30.

$$K_p = Gh_0 \frac{[(\alpha^b - \alpha) : n]^{0.5}}{[\exp((\boldsymbol{\alpha} - \boldsymbol{\alpha}_{in}) : \mathbf{n})] + C_{\gamma 1}} C_{rev} \frac{C_{k\alpha}}{1 + C_{K_p}(\frac{z_{peak}}{z_{max}})\langle(\boldsymbol{\alpha}^b - \boldsymbol{\alpha}) : \mathbf{n}\rangle\sqrt{1 - C_{zpk2}}} \tag{E.41}$$

$$C_{k\alpha} = 1 + \frac{C_{K\alpha f}}{1 + (2.5\langle(\alpha - \alpha_{in}^{true})\rangle)^2} C_{pzp} C_{zpk1} \tag{E.42}$$

$$C_{zpk1} = \frac{z_{peak}}{z_{cum} + \frac{z_{max}}{5}} \tag{E.43}$$

$$C_{zpk2} = \frac{-\langle -(p_{zp} - p)\rangle}{-\langle -(p_{zp} - p)\rangle + p_{min}} \tag{E.44}$$

$$C_{pzp2} = \frac{-\langle -(p_{zp} - p)\rangle}{-\langle -(p_{zp} - p)\rangle + p_{min}} \tag{E.45}$$

The expression in Equation E.41 results in a reduction in plastic modulus, K_p, when fabric is favorable (i.e., $z : n \geq 0$) and with increasing plastic shear strains (which conceptually represents the breakage of cementation). This reduces both the plastic modulus, K_p, and the hysteretic damping at larger shear strains. The goal of doing this in PM4Sand is to improve the path in undrained cyclic loading.

The terms $C_{k\alpha}$ and $\sqrt{1 - C_{zpk2}}$ both serve to increase K_p during non-reversal loading by amounts that depend on the fabric memory and stress history. Factors, C_{zpk1} and C_{zpk2}, are terms that start from zero and grow to unity for uni-directional growth of fabric, which is the case during non-reversing loading conditions. These terms differ in the rate at which they approach unity, using a constant $z_{max}/5$ or $z_{max}/100$, with these respective values chosen

for their ability to better approximate the engineering behaviors of interest and correlations. For full reversal loading, where the fabric alternates between positive and negative values, both terms will go to zero. Term C_{pzp} starts initially at zero and stays equal to zero until fabric is formed. After fabric is formed, this term quickly transitions to unity for values of mean effective stress p that are less than the value that p had when the maximum fabric was formed (p_{zp}). Setting C_{K_p} to a default value of 2.0 as per the calibration by BZ was found to produce reasonable responses with particular emphasis on improving (reducing) the equivalent damping ratios at shear strains of 1 to 3 % in drained cyclic loading. Term $C_{K\alpha f}$ is particularly useful for adjusting the undrained cyclic loading response with sustained static shear stresses.

E.7.2 Effect of fabric on plastic volumetric dilation

A rotated dilatancy surface with slope M^{dR} is introduced in the PM4Sand formulation, which evolves in response to the history of the fabric tensor z. This was added to the framework of the PM4Sand model to facilitate earlier dilation at low stress ratios under certain loading paths [111]. The rotated surface is equal to the original dilatancy surface divided by a factor C_{rot1}. This scales down the original dilatancy surface. Thus, the scaling factor that defines the rotated dilatancy surface was made dependent on whether fabric is favorable ($\boldsymbol{z} : \mathbf{n} > 0$) or unfavorable ($\boldsymbol{z} : \mathbf{n} < 0$) and on the factor C_{zin1} which is an indirect measure of whether there are reversals or not (Equation E.48). M^d is the slope of the unrotated dilatancy surface.

$$M^{dR} = \frac{M^d}{C_{rot1}} \tag{E.46}$$

$$C_{rot1} = 1 + \frac{2\langle -\boldsymbol{z} : \boldsymbol{n} \rangle}{\sqrt{2} z_{max}} (1 - C_{zin1}) \geq 1 \tag{E.47}$$

$$C_{zin1} = \langle 1 - \exp(-2.0 | \frac{z_{in} : n - z : n}{z_{max}} |) \rangle \tag{E.48}$$

Term z_{in} is the fabric tensor at the beginning of the current loading branch. Term C_{zin1} can take values ranging from 0, when there are no reversals, to 1 when there are reversals. The rotated dilatancy surface operates only for loading with an unfavorable fabric since the factor C_{rot1} becomes 1 when the fabric is favorable (i.e., $\langle -\boldsymbol{z} : \mathbf{n} \rangle = 0$). A back-stress ratio tensor for the rotated dilatancy surface (α^{dR}) was introduced as shown in Equation E.49.

$$\alpha^{dR} = \frac{1}{\sqrt{2}} (M^{dR} - m)\mathbf{n} \tag{E.49}$$

Dilation occurs whenever the term $(\alpha^{dR} - \alpha) : \mathbf{n}$ is negative, whereas contraction occurs when it is positive. The calculation of D is still treated separately during dilation and contraction. The D value during dilation is now calculated according to the expression in Equation E.50. The value for D is calculated from the rotated dilatancy surface in Equation E.50.

$$D_{rot} = A_d \frac{\langle -\boldsymbol{z} : \mathbf{n} \rangle}{\sqrt{2} z_{max}} \frac{(\boldsymbol{\alpha}^{dR} - \boldsymbol{\alpha}) : \mathbf{n}}{C_{DR}} \tag{E.50}$$

The C_{DR} factor is applied to reduce the rate at which dilatancy is increasing. Another value for D is computed that would be obtained from the non-rotated dilatancy surface in Equation E.51.

$$D_{non-rot} = A_d(-\langle -(\alpha^d - \alpha) : \mathbf{n} \rangle) \tag{E.51}$$

Lastly, the operating value of D is selected from the above two values as shown in Equation E.52.

$$D = \begin{cases} D_{non-rot}, & \text{if } D_{non-rot} \leq D_{rot}, \\ D_{non-rot} + (D_{rot} - D_{non-rot}) \frac{\langle M^b - M^{cur} \rangle}{\langle M^b - M^{cur} + 0.01 \rangle}, & otherwise. \end{cases} \tag{E.52}$$

Parameter A_d for both D_{rot} and $D_{non-rot}$ is expressed in Equation E.53.

$$A_d = \frac{A_{d0}(C_{zin2})}{(\frac{z_{cum}^2}{z_{max}})(1 - \frac{\langle -\mathbf{z}:\mathbf{n} \rangle}{\sqrt{2} z_{peak}})^3 (C_\varepsilon)^2 (C_{pzp})(C_{pmin})(C_{zin1}) + 1} \tag{E.53}$$

Term C_ε is a calibration constant that can be used to modify the rate of plastic shear strain evolution. Term C_{pzp} causes the effects of fabric on dilation to be reduced whenever the current value of p is near the value of p_{zp}. Term C_{pmin} provides a minimum amount of shear resistance for a soil after it has temporarily reached an excess pore pressure of 100%. The parameter p_{min2} is currently set to become equal to 5% of the value of p' at consolidation. Term C_{zin1} facilitates strain-hardening when stress reversals are not causing fabric changes. Lastly, C_{zin2} causes the dilatancy to be decreased by up to a factor of 3 under conditions of large strains and full stress (and fabric) reversals, which improves the prediction of cyclic strain accumulation during undrained cyclic loading.

$$C_{pzp} = \frac{1}{1 + (2.5 \frac{p}{p_{zp}})^5} \tag{E.54}$$

$$C_{pmin} = \frac{1}{1 + (\frac{p_{min}}{p})^2} \tag{E.55}$$

$$C_{zin1} = 1.0 - \exp\left(-2.0|\frac{\boldsymbol{z}_{in} : \mathbf{n} - \boldsymbol{z} : \mathbf{n}}{z_{max}}|\right) \tag{E.56}$$

$$C_{zin2} = \frac{1 + C_{zin1}\frac{z_{cum} - z_{peak}}{3z_{max}}}{1 + 3C_{zin1}\frac{z_{cum} - z_{peak}}{3z_{peak}}} \tag{E.57}$$

E.7.3 Effect of fabric on plastic volumetric contraction

In the Manzari and Dafalias [264] model, the fabric tensor was used to modify the dilatancy during contraction ($D > 0$) as shown in Equation E.58. The relationship enhances the volumetric contraction whenever the fabric is favorable ($z : n \geq 0$), based on the term $1 + \langle z : n \rangle$.

$$D = A_d[(\alpha^d - \alpha) : \mathbf{n}](1 + \langle z : n \rangle) \tag{E.58}$$

In PM4Sand, the relationship was modified as shown in Equation E.59.

$$D = A_d[(\boldsymbol{\alpha}^d - \boldsymbol{\alpha}) : \mathbf{n} + C_{in}]^2 \frac{(\boldsymbol{\alpha}^d - \boldsymbol{\alpha}) : \mathbf{n}}{(\boldsymbol{\alpha}^d - \boldsymbol{\alpha}) : \mathbf{n} + C_D} C_{pmin2} \tag{E.59}$$

$$A_{dc} = \frac{A_{d0}(1 + \langle \boldsymbol{z} : \mathbf{n} \rangle)}{h_p C_{dz}} \tag{E.60}$$

The term, C_{dz}, serves to increase the rate of contraction as z_{peak} nears z_{max} or as a large amount of cumulative fabric formation/destruction has taken place (Equation E.63). This term was developed to improve the modeling of the cyclic strength of denser sand. The degradation of the denominator as z_{peak} or z_{cum} increases enables the generation of high

excess pore pressure at higher loading levels, and controls the slope of the CRR versus number of uniform loading cycles relationship obtained for undrained element loading. Term C_{rot} was introduced into the factor C_{dz} to provide better control over the rate of contraction as z_{peak} nears z_{max} or as a large amount of cumulative fabric formation/destruction has taken place. Term C_{rot2} takes values that range from 1 for loading with zero fabric or cyclic loading that causes reversals of fabric (since z_{cum} will become much larger than z_{peak}), to 0 for loading that causes fabric to grow monotonically in one direction such as in non-reversal cyclic loading (since z_{cum} will equal z_{peak}) (Equation E.64). The limit on the minimum value of C_{dz} is required for avoiding division by zero and to avoid over-estimating contraction rates (i.e., small values of h_p and large values of z_{peak} or z_{cum}). The term C_{pmin2} slows the rate of contraction when p is approaching its minimum allowable value, and stops further contraction when p is less than twice the minimum allowable p (Equation E.65).

$$C_D = 0.16 \tag{E.61}$$

$$C_{in} = \frac{2\langle \boldsymbol{z} : \mathbf{n} \rangle}{\sqrt{2} z_{max}} \tag{E.62}$$

$$C_{dz} = (1 - C_{rot2}\frac{\sqrt{2}z_{peak}}{z_{max}})(\frac{z_{max}}{z_{max} + C_{rot2} z_{cum}}) \geq \frac{1}{1 + \frac{z_{max}}{2}} \tag{E.63}$$

$$C_{rot2} = 1 - \frac{z_{peak}}{z_{cum} + \frac{z_{max}}{100}} = 1 - C_{zpk2} \tag{E.64}$$

$$C_{pmin2} = \begin{cases} 0, & \text{if } p \leq 2p_{min}, \\ 1, & \text{if } p \geq 18p_{min}, \\ \frac{p-2p_{min}}{16p_{min}}, & otherwise. \end{cases} \tag{E.65}$$

E.7.4 Effect of fabric on the elastic modulus

The elastic shear modulus and elastic bulk modulus may degrade with increasing values of the cumulative plastic deviatoric strain term, z_{cum}. This accounts for the progressive destruction with increasing plastic shear strains of any minor cementation bonds or other ageing or strain history-related phenomena that produced an increase in small-strain shear modulus. Equation E.66 presents the degradation of the elastic shear modulus. Term C_{GD} is a factor by which the shear modulus is degraded at very large values of z_{cum}. This change in G causes the bulk modulus K to progressively decrease with increasing z_{cum}. The change in K improves the model's ability to track the stress-strain response of liquefying sand. In particular, decreasing K with increasing z_{cum} reduces the rate of strain-hardening after phase transformation at larger shear strain levels, and improves the ability to approximate the hysteretic stress-strain response of a soil as it liquefies.

$$G = G_0 p_A (\frac{p}{p_A})^{\frac{1}{2}} C_{SR} (\frac{1 + \frac{z_{cum}}{z_{max}}}{1 + \frac{z_{cum}}{z_{max}} C_{GD}}) \tag{E.66}$$

E.8 Post-shaking reconsolidation

The conventional elastic modulus is multiplied by a reduction factor, F_{sed}, to reduce the value of G to better estimate post-liquefaction strains (Equation E.67).

$$G_{post-shaking} = F_{sed} G \tag{E.67}$$

Term F_{sed} is calculated as shown in Equation E.69. Term $F_{sed,min}$ represents the smallest value that F_{sed} can attain. $p_{sed,0}$ is the mean effective stress up to which reconsolidation strains are enhanced (Equation E.71). The value of F_{sed} progressively reduces from unity toward the value of $F_{sed,min}$ as z_{cum} progressively increases, and provided that M^{cur} is less than M^d.

$$K_{post-shaking} = F_{sed} K \tag{E.68}$$

$$F_{sed} = F_{sed,min} + (1 - F_{sed,min})(\frac{p}{20 p_{sed}}) \leq 1 \tag{E.69}$$

$$p_{sed} = p_{sed,0}(\frac{z_{cum}}{z_{cum} + z_{max}})\langle 1 - \frac{M^{cur}}{M^d}\rangle^{0.25} \tag{E.70}$$

$$p_{sed,0} = -\frac{P_{atm}}{5} \tag{E.71}$$

E.9 General trends in PM4Sand considering level and sloping grounds

Loose sand material with relative density, D_R of 35% with parameters consistent with the calibration in Boulanger and Ziotopoulou [111]. The simulations consist of two sets of 2D

plane-strain stress-controlled cyclic simple shear tests where a cyclic single amplitude shear stress, τ, for a stress point under a vertical effective stress, σ'_{vc}, with K_0=0.5 conditions with the ratio, $\alpha = \tau/\sigma'_{vc}$=0 (no initial static shear stress) and 0.2 (with initial static shear stress) to simulate level and sloping ground, respectively. Figure E.1 presents a summary of the first set of results showing key features that PM4Sand is able to capture in level-ground conditions (cyclic simple shear without initial static shear stress). This includes the (a) stress-strain functional form, (b) undrained stress path with reducing effective stresses with liquefaction triggering and subsequent post-triggering "butterfly" shape that arises from the repeated loading and unloading cycles after initial liquefaction, (c) back-stress ratio tensor evolution, and (d) fabric tensor evolution. The results from the second element-level simulation is shown in Figure E.2. Similarly, the trends under an initial static shear stress are consistent with Boulanger and Ziotopoulou [111].

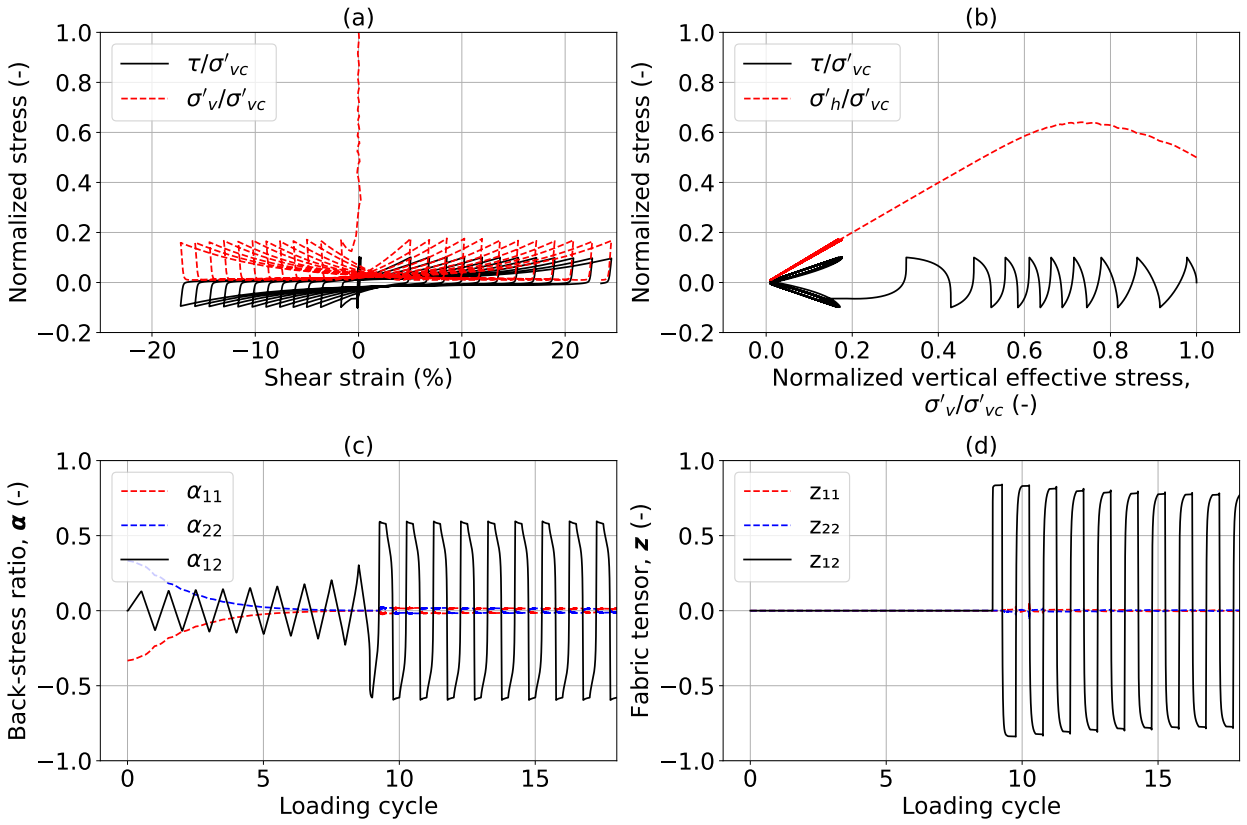

Figure E.1: Trends of PM4Sand in an undrained cyclic simple shear test in level-grounds considering (a) stress-strain, (b) stress paths, (c) back-stress ratio, and (d) fabric evolution. This material calibration is for loose sand material with relative density, $D_R = 35\%$ (loose), consistent with Boulanger and Ziotopoulou [111], and normal stress, σ_{vc}=100 kPa under K_0=0.5 conditions.

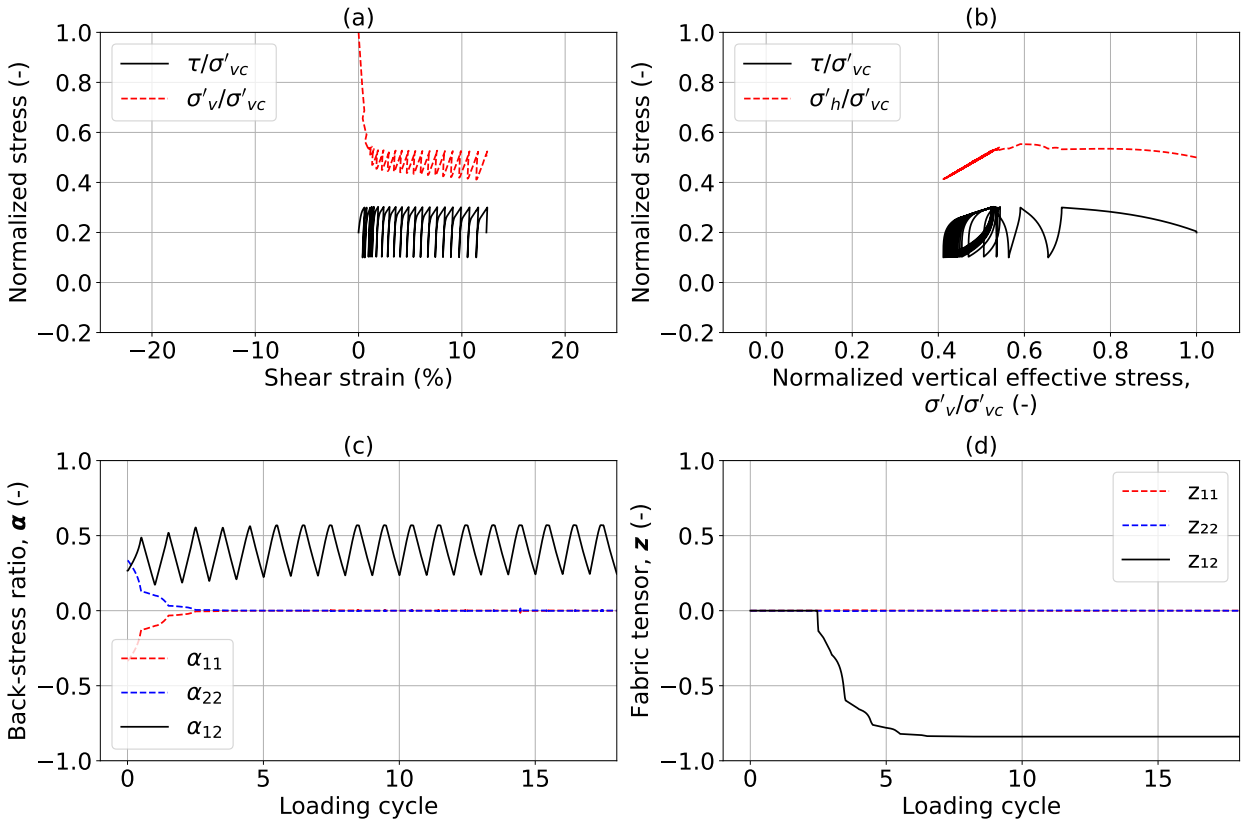

Figure E.2: Trends of PM4Sand in an undrained cyclic simple shear test in sloping ground conditions considering (a) stress-strain, (b) stress paths, (c) back-stress ratio, and (d) fabric evolution. This material calibration is for loose sand material with relative density, D_R = 35% (loose), consistent with Boulanger and Ziotopoulou [111], and normal stress, σ_{vc}=100 kPa under K_0=0.5 conditions and initial static shear stress ratio, α=0.2.

Bibliography

[1] R. Popescu and J. H. Prevost, "Comparison between velacs numerical 'class a'predictions and centrifuge experimental soil test results," *Soil Dynamics and Earthquake Engineering*, vol. 14, no. 2, pp. 79–92, 1995.

[2] J. Wartman, "Physical model studies of seismically induced deformations in slopes," *Ph. D. Thesis*, 1999.

[3] E. J. Malvick, B. L. Kutter, and R. W. Boulanger, "Postshaking shear strain localization in a centrifuge model of a saturated sand slope," *Journal of Geotechnical and Geoenvironmental Engineering*, vol. 134, no. 2, pp. 164–174, 2008.

[4] S. Nikolaou, X. Vera-Grunauer, R. Gilsanz, R. Luque, T. Kishida, G. Diaz-Fanas, and S. Lopez, "Geer-atc mw7. 8 ecuador4/16/16 earthqueake reconnaissanc part i: Seismilogical & ground motion aspects," in *Santiago: 16th World Conference on Earthquake Engineering*, 2017.

[5] GeologyIn, "Geologists reveal correlation between earthquakes and landslides," 2021.

[6] Nature Editorial Board, "Landslide-triggered earthquakes," 2014.

[7] D. Jacobson, "Big sur landslide highlights earthquake vulnerability of magnificent california coast," 2017.

[8] T. L. Youd, "Liquefaction, flow, and associated ground failure," tech. rep., US Geological Survey, 1973.

[9] M. Hamada and T. O'Rourke, "Case studies of liquefaction and lifeline performance

during past earthquakes. volume 1, japanese case studies," *Technical Rep. NCEER-92*, vol. 1, pp. 1–28, 1992.

[10] Y. Bozorgnia and V. V. Bertero, *Earthquake engineering: from engineering seismology to performance-based engineering*. CRC press, 2004.

[11] J. Moehle and G. G. Deierlein, "A framework methodology for performance-based earthquake engineering," in *13th World Conference on Earthquake Engineering*, vol. 679, 2004.

[12] S. L. Kramer, "Performance-based design methodologies for geotechnical earthquake engineering," *Bulletin of Earthquake Engineering*, vol. 12, no. 3, pp. 1049–1070, 2014.

[13] J. F. Bird and J. J. Bommer, "Earthquake losses due to ground failure," *Engineering geology*, vol. 75, no. 2, pp. 147–179, 2004.

[14] United Research Services, "Phase 1 technical memorandum - seismology: Delta risk management strategy (california district of water resources)," 2007.

[15] Z. Lyu, J. Chai, Z. Xu, Y. Qin, and J. Cao, "A comprehensive review on reasons for tailings dam failures based on case history," *Advances in Civil Engineering*, vol. 2019, 2019.

[16] G. Villavicencio, R. Espinace, J. Palma, A. Fourie, and P. Valenzuela, "Failures of sand tailings dams in a highly seismic country," *Canadian geotechnical journal*, vol. 51, no. 4, pp. 449–464, 2014.

[17] K. Ishihara, K. Ueno, S. Yamada, S. Yasuda, and T. Yoneoka, "Breach of a tailings dam in the 2011 earthquake in japan," *Soil Dynamics and Earthquake Engineering*, vol. 68, pp. 3–22, 2015.

[18] M. Jefferies, D. Shuttle, and K. Been, "Principal stress rotation as cause of cyclic mobility," *Geotechnical Research*, vol. 2, no. 2, pp. 66–96, 2015.

[19] A. N. Schofield and P. Wroth, *Critical state soil mechanics*, vol. 310. McGraw-hill London, 1968.

[20] K. Been and M. G. Jefferies, "A state parameter for sands," *Géotechnique*, vol. 35, no. 2, pp. 99–112, 1985.

[21] M. Bolton, "The strength and dilatancy of sands," *Geotechnique*, vol. 36, no. 1, pp. 65–78, 1986.

[22] K. Been, M. Jefferies, and J. Hachey, "The critical state of sands," *Géotechnique*, vol. 41, no. 3, pp. 365–381, 1991.

[23] S. L. Kramer, *Geotechnical earthquake engineering*. Pearson Education, 1996.

[24] M. Vucetic and R. Dobry, "Effect of soil plasticity on cyclic response," *Journal of geotechnical engineering*, vol. 117, no. 1, pp. 89–107, 1991.

[25] M. B. Darendeli, *Development of a new family of normalized modulus reduction and material damping curves*. The university of Texas at Austin, 2001.

[26] J. Wartman, R. B. Seed, and J. D. Bray, "Shaking table modeling of seismically induced deformations in slopes," *Journal of Geotechnical and Geoenvironmental Engineering*, vol. 131, no. 5, pp. 610–622, 2005.

[27] T. L. Youd, "Compaction of sands by repeated shear straining," *Journal of the Soil Mechanics and Foundations Division*, vol. 98, no. 7, pp. 709–725, 1972.

[28] G. R. Martin, H. B. Seed, and W. L. Finn, "Fundamentals of liquefaction under cyclic loading," *Journal of the Geotechnical Engineering Division*, vol. 101, no. 5, pp. 423–438, 1975.

[29] M. Jefferies and K. Been, *Soil liquefaction: a critical state approach*. CRC press, 2019.

[30] M. Yoshimine, K. Ishihara, and W. Vargas, "Effects of principal stress direction and intermediate principal stress on undrained shear behavior of sand," *Soils and Foundations*, vol. 38, no. 3, pp. 179–188, 1998.

[31] Y. Nakata, M. Hyodo, H. Murata, and N. Yasufuku, "Flow deformation of sands subjected to principal stress rotation," *Soils and Foundations*, vol. 38, no. 2, pp. 115–128, 1998.

[32] Y. F. Dafalias, A. G. Papadimitriou, and X. S. Li, "Sand plasticity model accounting for inherent fabric anisotropy," *Journal of Engineering Mechanics*, vol. 130, no. 11, pp. 1319–1333, 2004.

[33] K. Terzaghi, "Mechanism of landslides. application of geology to engineering practice (berkey volume)," *Paige, Chairman, Geological Society of America*, p. 83, 1950.

[34] N. M. Newmark, "Effects of earthquakes on dams and embankments," *Géotechnique*, vol. 15, no. 2, pp. 139–160, 1965.

[35] J. M. Duncan, S. G. Wright, and T. L. Brandon, *Soil strength and slope stability*. John Wiley & Sons, 2014.

[36] R. W. Jibson, "Regression models for estimating coseismic landslide displacement," *Engineering geology*, vol. 91, no. 2-4, pp. 209–218, 2007.

[37] G. Saygili and E. M. Rathje, "Empirical predictive models for earthquake-induced sliding displacements of slopes," *Journal of Geotechnical and Geoenvironmental Engineering*, vol. 134, no. 6, pp. 790–803, 2008.

[38] S.-Y. Hsieh and C.-T. Lee, "Empirical estimation of the newmark displacement from the arias intensity and critical acceleration," *Engineering Geology*, vol. 122, no. 1-2, pp. 34–42, 2011.

[39] J. Lee and R. Green, "Empirical predictive relationship for seismic lateral displacement of slopes," *Géotechnique*, vol. 65, no. 5, pp. 374–390, 2015.

[40] F. I. Makdisi and H. B. Seed, "Simplified procedure for estimating dam and embankment earthquake-induced deformations," *Journal of the Geotechnical Engineering Division*, vol. 104, no. 7, pp. 849–867, 1978.

[41] J.-S. Lin and R. V. Whitman, "Decoupling approximation to the evaluation of earthquake-induced plastic slip in earth dams," *Earthquake engineering & structural dynamics*, vol. 11, no. 5, pp. 667–678, 1983.

[42] R. W. Jibson, "Predicting earthquake-induced landslide displacements using newmark's sliding block analysis," *Transportation research record*, vol. 1411, pp. 9–17, 1993.

[43] J. D. Bray and E. M. Rathje, "Earthquake-induced displacements of solid-waste landfills," *Journal of Geotechnical and Geoenvironmental Engineering*, vol. 124, no. 3, pp. 242–253, 1998.

[44] J. D. Bray and T. Travasarou, "Simplified procedure for estimating earthquake-induced deviatoric slope displacements," *Journal of geotechnical and geoenvironmental engineering*, vol. 133, no. 4, pp. 381–392, 2007.

[45] E. M. Rathje and G. Antonakos, "A unified model for predicting earthquake-induced sliding displacements of rigid and flexible slopes," *Engineering Geology*, vol. 122, no. 1-2, pp. 51–60, 2011.

[46] J. D. Bray, J. Macedo, and T. Travasarou, "Simplified procedure for estimating seismic slope displacements for subduction zone earthquakes," *Journal of Geotechnical and Geoenvironmental Engineering*, vol. 144, no. 3, p. 04017124, 2018.

[47] E. M. Rathje and J. D. Bray, "Nonlinear coupled seismic sliding analysis of earth structures," *Journal of Geotechnical and Geoenvironmental Engineering*, vol. 126, no. 11, pp. 1002–1014, 2000.

[48] P. Lane and D. Griffiths, "Assessment of stability of slopes under drawdown conditions," *Journal of Geotechnical and Geoenvironmental Engineering*, vol. 126, no. 5, pp. 443–450, 2000.

[49] R. Tripe, S. Kontoe, and T. Wong, "Slope topography effects on ground motion in the presence of deep soil layers," *Soil Dynamics and Earthquake Engineering*, vol. 50, pp. 72–84, 2013.

[50] L. Pelecanos, S. Kontoe, and L. Zdravković, "A case study on the seismic performance of earth dams," *Géotechnique*, vol. 65, no. 11, pp. 923–935, 2015.

[51] D. Taborda, D. Potts, and L. Zdravković, "On the assessment of energy dissipated through hysteresis in finite element analysis," *Computers and Geotechnics*, vol. 71, pp. 180–194, 2016.

[52] R. A. Green, C. G. Olgun, and W. I. Cameron, "Response and modeling of cantilever retaining walls subjected to seismic motions," *Computer-Aided Civil and Infrastructure Engineering*, vol. 23, no. 4, pp. 309–322, 2008.

[53] R. W. Boulanger, R. Kamai, and K. Ziotopoulou, "Liquefaction induced strength loss and deformation: simulation and design," *Bulletin of Earthquake Engineering*, vol. 12, no. 3, pp. 1107–1128, 2014.

[54] J. Macedo and J. D. Bray, "Key trends in liquefaction-induced building settlement," *Journal of Geotechnical and Geoenvironmental Engineering*, vol. 144, no. 11, p. 04018076, 2018.

[55] X. Zhang, Z. Chen, and Y. Liu, *The material point method: a continuum-based particle method for extreme loading cases*. Academic Press, 2016.

[56] K. Soga, E. Alonso, A. Yerro, K. Kumar, and S. Bandara, "Trends in large-deformation analysis of landslide mass movements with particular emphasis on the material point method," *Géotechnique*, vol. 66, no. 3, pp. 248–273, 2016.

[57] A. Alsardi, J. Copana, and A. Yerro, "Modelling earthquake-triggered landslide runout with the material point method," *Proceedings of the Institution of Civil Engineers - Geotechnical Engineering*, p. 1–14, 2021.

[58] D. Sulsky, Z. Chen, and H. L. Schreyer, "A particle method for history-dependent materials," *Computer methods in applied mechanics and engineering*, vol. 118, no. 1-2, pp. 179–196, 1994.

[59] J. Fern, A. Rohe, K. Soga, and E. Alonso, *The material point method for geotechnical engineering: a practical guide*. CRC Press, 2019.

[60] S. G. Bardenhagen and E. M. Kober, "The generalized interpolation material point method," *Computer Modeling in Engineering and Sciences*, vol. 5, no. 6, pp. 477–496, 2004.

[61] I. Kafaji, *Formulation of a dynamic material point method (MPM) for geomechanical problems*. 2013.

[62] Q.-A. Tran and W. Sołowski, "Generalized interpolation material point method modelling of large deformation problems including strain-rate effects–application to penetration and progressive failure problems," *Computers and Geotechnics*, vol. 106, pp. 249–265, 2019.

[63] A. Sadeghirad, R. M. Brannon, and J. Burghardt, "A convected particle domain interpolation technique to extend applicability of the material point method for problems involving massive deformations," *International Journal for numerical methods in Engineering*, vol. 86, no. 12, pp. 1435–1456, 2011.

[64] D. Z. Zhang, X. Ma, and P. T. Giguere, "Material point method enhanced by modified gradient of shape function," *Journal of Computational Physics*, vol. 230, no. 16, pp. 6379–6398, 2011.

[65] K. A. Perez, P. L. Barclay, and D. Z. Zhang, "Nodal force error and its reduction for material point methods," *Journal of Computational Physics*, vol. 498, p. 112681, 2024.

[66] M. Steffen, R. M. Kirby, and M. Berzins, "Analysis and reduction of quadrature errors in the material point method (mpm)," *International journal for numerical methods in engineering*, vol. 76, no. 6, pp. 922–948, 2008.

[67] R. Tielen, E. Wobbes, M. Möller, and L. Beuth, "A high order material point method," *Procedia Engineering*, vol. 175, pp. 265–272, 2017.

[68] G. Moutsanidis, C. C. Long, and Y. Bazilevs, "Iga-mpm: the isogeometric material point method," *Computer Methods in Applied Mechanics and Engineering*, vol. 372, p. 113346, 2020.

[69] J. Chung and G. Hulbert, "A time integration algorithm for structural dynamics with improved numerical dissipation: The generalized-α method," *Journal of Applied Mechanics*, vol. 60, no. 2, p. 371, 1993.

[70] J. E. Guilkey and J. A. Weiss, "Implicit time integration for the material point method: Quantitative and algorithmic comparisons with the finite element method," *International Journal for Numerical Methods in Engineering*, vol. 57, no. 9, pp. 1323–1338, 2003.

[71] S. Kontoe, *Development of time integration schemes and advanced boundary conditions for dynamic geotechnical analysis*. PhD thesis, Imperial College London, 2006.

[72] S. Kontoe, L. Zdravkovic, and D. M. Potts, "An assessment of time integration schemes for dynamic geotechnical problems," *Computers and Geotechnics*, vol. 35, no. 2, pp. 253–264, 2008.

[73] B. Han, L. Zdravkovic, and S. Kontoe, "Stability investigation of the generalised-α time integration method for dynamic coupled consolidation analysis," *Computers and Geotechnics*, vol. 64, pp. 83–95, 2015.

[74] Q.-A. Tran and W. Sołowski, "Temporal and null-space filter for the material point method," *International Journal for Numerical Methods in Engineering*, vol. 120, no. 3, pp. 328–360, 2019.

[75] S. Kularathna and K. Soga, "Implicit formulation of material point method for analysis of incompressible materials," *Computer Methods in Applied Mechanics and Engineering*, vol. 313, pp. 673–686, 2017.

[76] S. Kularathna and K.Soga, "Comparison of two projection methods for modeling in-

compressible flows in mpm," *Journal of Hydrodynamics*, vol. 29, no. 3, pp. 405–412, 2017.

[77] S. Kularathna, W. Liang, T. Zhao, B. Chandra, J. Zhao, and K. Soga, "A semi-implicit material point method based on fractional-step method for saturated soil," *International Journal for Numerical and Analytical Methods in Geomechanics*, vol. 45, no. 10, pp. 1405–1436, 2021.

[78] T. Bhandari, F. Hamad, C. Moormann, K. Sharma, and B. Westrich, "Numerical modelling of seismic slope failure using mpm," *Computers and Geotechnics*, vol. 75, pp. 126–134, 2016.

[79] P. Ering and G. S. Babu, "Probabilistic back analysis of rainfall induced landslide-a case study of malin landslide, india," *Engineering Geology*, vol. 208, pp. 154–164, 2016.

[80] A. Alsardi and A. Yerro, "Runout modeling of earthquake-triggered landslides with the material point method," in *IFCEE 2021*, pp. 21–31.

[81] K. Feng, G. Wang, D. Huang, and F. Jin, "Material point method for large-deformation modeling of coseismic landslide and liquefaction-induced dam failure," *Soil Dynamics and Earthquake Engineering*, vol. 150, p. 106907, 2021.

[82] M. Kohler, A. Stoecklin, and A. M. Puzrin, "A mpm framework for large-deformation seismic response analysis," *Canadian Geotechnical Journal*, vol. 59, no. 6, pp. 1046–1060, 2022.

[83] O. Zienkiewicz, N. Bicanic, and F. Shen, "Earthquake input definition and the trasmitting boundary conditions," in *Advances in computational nonlinear mechanics*, pp. 109–138, Springer, 1989.

[84] P. J. Stafford, A. Rodriguez-Marek, B. Edwards, P. P. Kruiver, and J. J. Bommer, "Scenario dependence of linear site-effect factors for short-period response spectral ordinates," *Bulletin of the Seismological Society of America*, vol. 107, no. 6, pp. 2859–2872, 2017.

[85] P. Schnabel, H. B. Seed, and J. Lysmer, "Modification of seismograph records for effects of local soil conditions," *Bulletin of the Seismological Society of America*, vol. 62, no. 6, pp. 1649–1664, 1972.

[86] I. M. Idriss and H. B. Seed, "Seismic response of horizontal soil layers," *Journal of the Soil Mechanics and Foundations Division*, vol. 94, no. 4, pp. 1003–1031, 1968.

[87] D. Assimaki and E. Kausel, "An equivalent linear algorithm with frequency-and pressure-dependent moduli and damping for the seismic analysis of deep sites," *Soil Dynamics and Earthquake Engineering*, vol. 22, no. 9-12, pp. 959–965, 2002.

[88] G. Masing, "Self-stretching and hardening for brass," in *Proceedings of the 2nd International Congress for Applied Mechanics*, pp. 332–335, 1926.

[89] C. Phillips and Y. M. Hashash, "Damping formulation for nonlinear 1d site response analyses," *Soil Dynamics and Earthquake Engineering*, vol. 29, no. 7, pp. 1143–1158, 2009.

[90] R. M. Pyke, "Nonlinear soil models for irregular cyclic loadings," *Journal of the Geotechnical Engineering Division*, vol. 105, no. 6, pp. 715–726, 1979.

[91] M. Vucetic, "Normalized behavior of clay under irregular cyclic loading," *Canadian Geotechnical Journal*, vol. 27, no. 1, pp. 29–46, 1990.

[92] H. B. Seed, P. P. Martin, and J. Lysmer, *The generation and dissipation of pore water*

pressures during soil liquefaction. College of Engineering, University of California, 1975.

[93] W. L. Finn, K. W. Lee, and G. R. Martin, "An effective stress model for liquefaction," *Journal of the Geotechnical Engineering Division*, vol. 103, no. 6, pp. 517–533, 1977.

[94] R. Green, J. Mitchell, and C. Polito, "An energy-based excess pore pressure generation model for cohesionless soils,"

[95] C. P. Polito, R. A. Green, and J. Lee, "Pore pressure generation models for sands and silty soils subjected to cyclic loading," *Journal of Geotechnical and Geoenvironmental Engineering*, vol. 134, no. 10, pp. 1490–1500, 2008.

[96] N. Matasović and M. Vucetic, "Cyclic characterization of liquefiable sands," *Journal of Geotechnical Engineering*, vol. 119, no. 11, pp. 1805–1822, 1993.

[97] K. Ishihara, "Soil behaviour in earthquake geotechnics," 1996.

[98] E. E. Alonso, "Triggering and motion of landslides," *Géotechnique*, vol. 71, no. 1, pp. 3–59, 2021.

[99] V. Tsaparli, S. Kontoe, D. M. Taborda, and D. M. Potts, "A case study of liquefaction: demonstrating the application of an advanced model and understanding the pitfalls of the simplified procedure," *Géotechnique*, vol. 70, no. 6, pp. 538–558, 2020.

[100] R. Jardine, D. Potts, A. Fourie, and J. Burland, "Studies of the influence of non-linear stress–strain characteristics in soil–structure interaction," *Géotechnique*, vol. 36, no. 3, pp. 377–396, 1986.

[101] R. A. Green and G. A. Terri, "Number of equivalent cycles concept for liquefaction evaluations—revisited," *Journal of Geotechnical and Geoenvironmental Engineering*, vol. 131, no. 4, pp. 477–488, 2005.

[102] D. C. Serafini and V. Perlea, "Comparison of liquefaction triggering analysis approaches for an embankment dam and foundation," in *Proceedings of the 5th International Conference on Recent Advances in Geotechnical Earthquake Engineering and Soil Dynamics, San Diego, California*, pp. 1–11, 2010.

[103] R. W. Boulanger and K. Ziotopoulou, "On nda practices for evaluating liquefaction effects," in *Geotechnical Earthquake Engineering and Soil Dynamics V: Liquefaction Triggering, Consequences, and Mitigation*, pp. 1–20, American Society of Civil Engineers Reston, VA, 2018.

[104] Z. Yang and A. Elgamal, "Multi-surface cyclic plasticity sand model with lode angle effect," *Geotechnical and Geological Engineering*, vol. 26, no. 3, pp. 335–348, 2008.

[105] P. M. Byrne, S.-S. Park, M. Beaty, M. Sharp, L. Gonzalez, and T. Abdoun, "Numerical modeling of liquefaction and comparison with centrifuge tests," *Canadian Geotechnical Journal*, vol. 41, no. 2, pp. 193–211, 2004.

[106] H. I. Ling and S. Yang, "Unified sand model based on the critical state and generalized plasticity," *Journal of Engineering Mechanics*, vol. 132, no. 12, pp. 1380–1391, 2006.

[107] M. H. Beaty and P. M. Byrne, "Ubcsand constitutive model version 904ar," *Itasca UDM Web Site*, vol. 69, 2011.

[108] A. G. Papadimitriou and G. D. Bouckovalas, "Plasticity model for sand under small and large cyclic strains: a multiaxial formulation," *Soil Dynamics and Earthquake Engineering*, vol. 22, no. 3, pp. 191–204, 2002.

[109] D. Loukidis and R. Salgado, "Modeling sand response using two-surface plasticity," *Computers and Geotechnics*, vol. 36, no. 1-2, pp. 166–186, 2009.

[110] R. Boulanger and K. Ziotopoulou, "Formulation of a sand plasticity plane-strain model for earthquake engineering applications," *Soil Dynamics and Earthquake Engineering*, vol. 53, pp. 254–267, 2013.

[111] R. W. Boulanger and K. Ziotopoulou, "Pm4sand (version 3): A sand plasticity model for earthquake engineering applications," *Report No. UCD/CGM-15/01, Center for Geotechnical Modeling, Department of Civil and Environmental Engineering, University of California, Davis, CA, 108 pp.*, 2015.

[112] R. W. Boulanger and K.Ziotopoulou, "Pm4silt (version 1): A silt plasticity model for earthquake engineering applications," *Report No. UCD/CGM-18/01, Center for Geotechnical Modeling, Department of Civil and Environmental Engineering, University of California, Davis, CA, 104 pp.*, 2018.

[113] L. Chen, *Implementation, Verification, Validation, and Application of Two Constitutive Models for Earthquake Engineering Applications.* Ph.D. thesis, University of Washington, 2020.

[114] F. McKenna, "Opensees: a framework for earthquake engineering simulation," *Computing in Science & Engineering*, vol. 13, no. 4, pp. 58–66, 2011.

[115] N. Hiraoka, A. Oya, H. H. Bui, P. Rajeev, and R. Fukagawa, "Seismic slope failure modelling using the mesh-free sph method," *Int J Geomate*, vol. 5, no. 1, pp. 660–665, 2013.

[116] N. N. Aeronautics and S. Administration), "Arcgis: Preliminary map of 1/7/2020 puerto rico co-seismic landslides. nasa, washington, dc, usa," 2020.

[117] U. G. S. (USGS), "Geologic map of the san francisco bay region," 2006.

[118] H. B. Seed, "Considerations in the earthquake-resistant design of earth and rockfill dams," *Geotechnique*, vol. 29, no. 3, pp. 215–263, 1979.

[119] I. K. Al-Kafaji, *Formulation of a dynamic material point method (MPM) for geomechanical problems*. PhD thesis, Universitätsbibliothek der Universität Stuttgart, 2013.

[120] A. Yerro Colom, "Mpm modelling of landslides in brittle and unsaturated soils," *Ph.D. Thesis*, 2015.

[121] A. Yerro, E. Alonso, and N. Pinyol, "The material point method for unsaturated soils," *Géotechnique*, vol. 65, no. 3, pp. 201–217, 2015.

[122] S. Bandara, A. Ferrari, and L. Laloui, "Modelling landslides in unsaturated slopes subjected to rainfall infiltration using material point method," *International Journal for Numerical and Analytical Methods in Geomechanics*, vol. 40, no. 9, pp. 1358–1380, 2016.

[123] D. Sulsky, S.-J. Zhou, and H. L. Schreyer, "Application of a particle-in-cell method to solid mechanics," *Computer physics communications*, vol. 87, no. 1-2, pp. 236–252, 1995.

[124] M. He, L. R. e Sousa, A. Müller, E. Vargas Jr, R. Sousa, C. S. Oliveira, and W. Gong, "Numerical and safety considerations about the daguangbao landslide induced by the 2008 wenchuan earthquake," *Journal of Rock Mechanics and Geotechnical Engineering*, vol. 11, no. 5, pp. 1019–1035, 2019.

[125] P. Ering and G. S. Babu, "Effect of spatial variability of earthquake ground motions on the reliability of road system," *Soil Dynamics and Earthquake Engineering*, vol. 136, p. 106207, 2020.

[126] G. Biscontin and J. M. Pestana, "Influence of peripheral velocity on vane shear strength of an artificial clay," *Geotechnical Testing Journal*, vol. 24, no. 4, pp. 423–429, 2001.

[127] T. Travasarou, *Optimal ground motion intensity measures for probabilistic assessment of seismic slope displacements*. University of California, Berkeley, 2003.

[128] W. Chen and T. Qiu, "Numerical simulations for large deformation of granular materials using smoothed particle hydrodynamics method," *International Journal of Geomechanics*, vol. 12, no. 2, pp. 127–135, 2012.

[129] M. Beyreuther, R. Barsch, L. Krischer, T. Megies, Y. Behr, and J. Wassermann, "Obspy: A python toolbox for seismology," *Seismological Research Letters*, vol. 81, no. 3, pp. 530–533, 2010.

[130] J. Oliver and A. E. Huespe, "Continuum approach to material failure in strong discontinuity settings," *Computer methods in applied mechanics and engineering*, vol. 193, no. 30-32, pp. 3195–3220, 2004.

[131] C. Wroth, "The interpretation of in situ soil tests," *Geotechnique*, vol. 34, no. 4, pp. 449–489, 1984.

[132] P. H. Morris and D. J. Williams, "A new model of vane shear strength testing in soils," *Géotechnique*, vol. 43, no. 3, pp. 489–500, 1993.

[133] Y. Bozorgnia, N. A. Abrahamson, L. A. Atik, T. D. Ancheta, G. M. Atkinson, J. W. Baker, A. Baltay, D. M. Boore, K. W. Campbell, B. S.-J. Chiou, *et al.*, "Nga-west2 research project," *Earthquake Spectra*, vol. 30, no. 3, pp. 973–987, 2014.

[134] A. Arias, "Measure of earthquake intensity.," tech. rep., Massachusetts Inst. of Tech., Cambridge. Univ. of Chile, Santiago de Chile, 1970.

[135] E. M. Rathje and J. D. Bray, "One-and two-dimensional seismic analysis of solid-waste landfills," *Canadian Geotechnical Journal*, vol. 38, no. 4, pp. 850–862, 2001.

[136] S. Fotopoulou and K. Pitilakis, "Predictive relationships for seismically induced slope displacements using numerical analysis results," *Bulletin of Earthquake Engineering*, vol. 13, no. 11, pp. 3207–3238, 2015.

[137] S. Hsieh and C. Lee, "Empirical estimation of the newmark displacement from the arias intensity and critical acceleration," *Engineering Geology*, vol. 122, no. 1-2, pp. 34–42, 2011.

[138] E. Spencer, "A method of analysis of the stability of embankments assuming parallel inter-slice forces," *Géotechnique*, vol. 17, no. 1, pp. 11–26, 1967.

[139] S. Bandara and K. Soga, "Coupling of soil deformation and pore fluid flow using material point method," *Computers and geotechnics*, vol. 63, pp. 199–214, 2015.

[140] R. Salgado and V. Bisht, "Advances in the solution of geotechnical boundary-value problems," *Computers and Geotechnics*, vol. 138, p. 104183, 2021.

[141] K. Feng, D. Huang, and G. Wang, "Two-layer material point method for modeling soil–water interaction in unsaturated soils and rainfall-induced slope failure," *Acta Geotechnica*, vol. 16, no. 8, pp. 2529–2551, 2021.

[142] A. H. Nielsen, "Absorbing boundary conditions for seismic analysis in abaqus," in *ABAQUS users' conference*, pp. 359–376, 2006.

[143] G. M. Hulbert and J. Chung, "Explicit time integration algorithms for structural dynamics with optimal numerical dissipation," *Computer Methods in Applied Mechanics and Engineering*, vol. 137, no. 2, pp. 175–188, 1996.

[144] A. K. Chopra, *Dynamics of structures*. Pearson Education, 2007.

[145] R. Brinkgreve, S. Kumarswamy, W. Swolfs, D. Waterman, A. Chesaru, P. Bonnier, *et al.*, "Plaxis 2016," *PLAXIS bv, the Netherlands*, 2016.

[146] T. R. Dhakal and D. Z. Zhang, "Material point methods applied to one-dimensional shock waves and dual domain material point method with sub-points," *Journal of Computational Physics*, vol. 325, pp. 301–313, 2016.

[147] A. Sadeghirad, R. M. Brannon, and J. Burghardt, "A convected particle domain interpolation technique to extend applicability of the material point method for problems involving massive deformations," *International Journal for Numerical Methods in Engineering*, vol. 86, no. 12, pp. 1435–1456, 2011.

[148] I. Jassim, *Formulation of a dynamic material point method (MPM) for geomechanical problems*. PhD thesis, Institute of Geotechnical Engineering, University of Stuttgart, 2013.

[149] Anura3D MPM Research Community, "Anura3d," 2021.

[150] D. M. Taborda, *Development of constitutive models for application in soil dynamics*. PhD thesis, Imperial College London, 2011.

[151] P. Toloza Barría, "Liquefaction modelling using the pm4sand soil constitutive model in plaxis 2d," 2018.

[152] R. L. Kuhlemeyer and J. Lysmer, "Finite element method accuracy for wave propagation problems," *Journal of the Soil Mechanics and Foundations Division*, vol. 99, no. 5, pp. 421–427, 1973.

[153] A. Yerro, V. Girardi, M. Martinelli, and F. Ceccato, "Modelling unsaturated soils with the material point method. a discussion of the state-of-the-art," *Geomechanics for Energy and the Environment*, vol. 32, p. 100343, 2022.

[154] J. Chung, *Numerically dissipative time integration algorithms for structural dynamics*. PhD thesis, University of Michigan, 1992.

[155] J. U. Brackbill, D. B. Kothe, and H. M. Ruppel, "Flip: a low-dissipation, particle-in-cell method for fluid flow," *Computer Physics Communications*, vol. 48, no. 1, pp. 25–38, 1988.

[156] T. D. Ancheta, R. B. Darragh, J. P. Stewart, E. Seyhan, W. J. Silva, B. S. Chiou, K. E. Wooddell, R. W. Graves, A. R. Kottke, D. M. Boore, *et al.*, "Peer nga-west 2 database," 2013.

[157] D. Gabor, "Theory of communication. part 1: The analysis of information," *Journal of the Institution of Electrical Engineers-Part III: Radio and Communication Engineering*, vol. 93, no. 26, pp. 429–441, 1946.

[158] J. Lysmer and R. L. Kuhlemeyer, "Finite dynamic model for infinite media," *Journal of the Engineering Mechanics Division*, vol. 95, no. 4, pp. 859–877, 1969.

[159] G. Zalachoris, D. Zekkos, A. Athanasopoulos-Zekkos, and N. Gerolymos, "The role of liquefaction on the seismic response of quay walls during the 2014 cephalonia, greece, earthquakes," *Journal of Geotechnical and Geoenvironmental Engineering*, vol. 147, no. 12, p. 04021137, 2021.

[160] C. Visone, E. Bilotta, and F. Santucci De Magistris, "Remarks on site response analysis by using plaxis dynamic module," 2008.

[161] D. K. Karamitros, G. D. Bouckovalas, and Y. K. Chaloulos, "Insight into the seismic liquefaction performance of shallow foundations," *Journal of Geotechnical and Geoenvironmental Engineering*, vol. 139, no. 4, pp. 599–607, 2013.

[162] S. Kontoe, L. Zdravkovic, D. M. Potts, and C. O. Menkiti, "Case study on seismic tunnel response," *Canadian Geotechnical Journal*, vol. 45, no. 12, pp. 1743–1764, 2008.

[163] V. Galavi, A. Petalas, and R. Brinkgreve, "Finite element modelling of seismic liquefaction in soils," *Geotechnical Engineering Journal of the SEAGS & AGSSEA, 44 (3), 2013*, 2013.

[164] R. Pretell, K. Ziotopoulou, and C. A. Davis, "Liquefaction and cyclic softening at balboa boulevard during the 1994 northridge earthquake," *Journal of Geotechnical and Geoenvironmental Engineering*, vol. 147, no. 2, p. 05020014, 2021.

[165] A. Yerro, E. Alonso, and N. Pinyol, "Run-out of landslides in brittle soils," *Computers and Geotechnics*, vol. 80, pp. 427–439, 2016.

[166] E. Conte, L. Pugliese, and A. Troncone, "Post-failure stage simulation of a landslide using the material point method," *Engineering Geology*, vol. 253, pp. 149–159, 2019.

[167] J. G. Rots, P. Nauta, G. Kuster, and J. Blaauwendraad, "Smeared crack approach and fracture localization in concrete," *HERON, 30 (1), 1985*, 1985.

[168] Y. Cho, F. Khosravikia, and E. M. Rathje, "A comparison of artificial neural network and classical regression models for earthquake-induced slope displacements," *Soil Dynamics and Earthquake Engineering*, vol. 152, p. 107024, 2022.

[169] R. W. Jibson, E. M. Rathje, M. W. Jibson, and Y. W. Lee, "Slammer: Seismic landslide movement modeled using earthquake records," tech. rep., US Geological Survey, 2013.

[170] J. Krahn, "User manual of geostudio software," 2012.

[171] V. Bisht, *Cone penetration analysis using the Material Point Method*. PhD thesis, Purdue University Graduate School, 2021.

[172] K. M. Yost, M. Martinelli, A. Yerro, R. A. Green, and D. A. De Lange, "Addressing complexities in mpm modeling of calibration chamber cone penetrometer tests in homogenous and highly interlayered soils," *Computers and Geotechnics*, vol. 158, p. 105378, 2023.

[173] G. Di Carluccio, N. M. Pinyol, E. E. Alonso, and M. Hürlimann, "Liquefaction-induced flow-like landslides: the case of valarties (spain)," *Géotechnique*, vol. 74, no. 4, pp. 307–324, 2022.

[174] Y. Zhao, C. Jiang, and J. Choo, "Circumventing volumetric locking in explicit material point methods: A simple, efficient, and general approach," *International Journal for Numerical Methods in Engineering*, vol. 124, no. 23, pp. 5334–5355, 2023.

[175] B. Schott, C. Ager, and W. A. Wall, "Monolithic cut finite element–based approaches for fluid-structure interaction," *International Journal for Numerical Methods in Engineering*, vol. 119, no. 8, pp. 757–796, 2019.

[176] C. Wilkes, K. Kumar, and G. Biscontin, "Investigating the thixotropic behaviour of tremie concrete using the slump-flow test and the material point method," *Cement and Concrete Composites*, vol. 143, p. 105222, 2023.

[177] W. T. Sołowski, M. Berzins, W. M. Coombs, J. E. Guilkey, M. Möller, Q. A. Tran, T. Adibaskoro, S. Seyedan, R. Tielen, and K. Soga, "Material point method: overview and challenges ahead," *Advances in Applied Mechanics*, vol. 54, pp. 113–204, 2021.

[178] Y. Gan, Z. Sun, Z. Chen, X. Zhang, and Y. Liu, "Enhancement of the material point method using b-spline basis functions," *International Journal for numerical methods in engineering*, vol. 113, no. 3, pp. 411–431, 2018.

[179] E. Wobbes, M. Möller, V. Galavi, and C. Vuik, "Conservative taylor least squares reconstruction with application to material point methods," *International Journal for Numerical Methods in Engineering*, vol. 117, no. 3, pp. 271–290, 2019.

[180] Y. Yamaguchi, S. Moriguchi, and K. Terada, "Extended b-spline-based implicit material point method," *International Journal for Numerical Methods in Engineering*, vol. 122, no. 7, pp. 1746–1769, 2021.

[181] K. Zhang, S.-L. Shen, A. Zhou, and D. Balzani, "Truncated hierarchical b-spline material point method for large deformation geotechnical problems," *Computers and Geotechnics*, vol. 134, p. 104097, 2021.

[182] Z. Sun, K. Liu, J. Wang, and X. Zhou, "Hydro-mechanical coupled b-spline material point method for large deformation simulation of saturated soils," *Engineering Analysis with Boundary Elements*, vol. 133, pp. 330–340, 2021.

[183] R. Sugai, J. Han, Y. Yamaguchi, S. Moriguchi, and K. Terada, "Extended b-spline-based implicit material point method enhanced by f-bar projection method to suppress pressure oscillation," *International Journal for Numerical Methods in Engineering*, vol. 124, no. 11, pp. 2423–2448, 2023.

[184] M. Xie, P. Navas, and S. López-Querol, "An implicit locking-free b-spline material point method for large strain geotechnical modelling," *International Journal for Numerical and Analytical Methods in Geomechanics*, vol. 47, no. 15, pp. 2741–2761, 2023.

[185] Y. Yamaguchi, S. Moriguchi, and K. Terada, "Extended b-spline-based implicit material point method for saturated porous media," *International Journal for Numerical and Analytical Methods in Geomechanics*, vol. 48, no. 16, pp. 4057–4085, 2024.

[186] R. M. Telikicherla and G. Moutsanidis, "Treatment of near-incompressibility and volumetric locking in higher order material point methods," *Computer Methods in Applied Mechanics and Engineering*, vol. 395, p. 114985, 2023.

[187] R. M. Telikicherla and G. Moutsanidis, "An assessment of the total lagrangian material point method: comparison to conventional mpm, higher order basis, and treatment of near-incompressibility," *Computer Methods in Applied Mechanics and Engineering*, vol. 414, p. 116135, 2023.

[188] R. M. Telikicherla and G. Moutsanidis, "A displacement-based material point method for weakly compressible free-surface flows," *Computational Mechanics*, pp. 1–17, 2025.

[189] A. A. Madadi and B. Dortdivanlioglu, "A subdivision-stabilized b-spline mixed material point method," *Computer Methods in Applied Mechanics and Engineering*, vol. 418, p. 116567, 2024.

[190] S. Hidano, S. Pan, K. Yoshida, R. Nomura, Y. Miki, M. Kawai, S. Moriguchi, K. Nakajima, and K. Terada, "B-spline-based material point method with dynamic load balancing technique for large-scale simulation," *Engineering with Computers*, pp. 1–18, 2025.

[191] C. De Boor, "On calculating with b-splines," *Journal of Approximation theory*, vol. 6, no. 1, pp. 50–62, 1972.

[192] A. Alsardi, A. Yerro, and C. C. Long, "Enhanced mpm framework with multipatch

isogeometric analysis for geotechnical applications," *Computers and Geotechnics*, 2025 (under review) Available at SSRN 5358326.

[193] J. A. Cottrell, T. J. Hughes, and Y. Bazilevs, *Isogeometric analysis: toward integration of CAD and FEA*. John Wiley & Sons, 2009.

[194] A. Apostolatos, R. Schmidt, R. Wüchner, and K.-U. Bletzinger, "A nitsche-type formulation and comparison of the most common domain decomposition methods in isogeometric analysis," *International Journal for Numerical Methods in Engineering*, vol. 97, no. 7, pp. 473–504, 2014.

[195] R. Ribó, M. Pasenau, E. Escolano, J. Ronda, and L. González, "Gid reference manual," *CIMNE, Barcelona*, vol. 27, p. 25, 1998.

[196] M. Martinelli and V. Galavi, "An explicit coupled mpm formulation to simulate penetration problems in soils using quadrilateral elements," *Computers and Geotechnics*, vol. 145, p. 104697, 2022.

[197] A. Alsardi and A. Yerro, "Coseismic site response and slope instability using periodic boundary conditions in the material point method," *Journal of Rock Mechanics and Geotechnical Engineering*, vol. 15, no. 3, pp. 641–658, 2023.

[198] I. Jassim, D. Stolle, and P. Vermeer, "Two-phase dynamic analysis by material point method," *International journal for numerical and analytical methods in geomechanics*, vol. 37, no. 15, pp. 2502–2522, 2013.

[199] V. Bisht, R. Salgado, and M. Prezzi, "Simulating penetration problems in incompressible materials using the material point method," *Computers and Geotechnics*, vol. 133, p. 103593, 2021.

[200] B. Chandra, R. Hashimoto, S. Matsumi, K. Kamrin, and K. Soga, "Stabilized mixed material point method for incompressible fluid flow analysis," *Computer Methods in Applied Mechanics and Engineering*, vol. 419, p. 116644, 2024.

[201] C. Mast, P. Mackenzie-Helnwein, P. Arduino, G. R. Miller, and W. Shin, "Mitigating kinematic locking in the material point method," *Journal of Computational Physics*, vol. 231, no. 16, pp. 5351–5373, 2012.

[202] A. Chmelnizkij, F. Ceccato, J. Grabe, and P. Simonini, "1d wave propagation in saturated soils: verification of two-phase mpm," in *2nd International conference on the material point method for modelling soil-water-structure interaction. Cambridge, UK*, 2019.

[203] M. Jamnia and J. Jackson, "Explicit vs. implicit time integration for nonlinear hydrodynamic shock wave propagation," in *1st National Fluid Dynamics Conference*, p. 3709, 1988.

[204] G. Remmerswaal, P. J. Vardon, and M. A. Hicks, "Inhomogeneous neumann boundary conditions for mpm and gimp," *Computers and Geotechnics*, vol. 173, p. 106494, 2024.

[205] M. Stadler, G. A. Holzapfel, and J. Korelc, "C^n continuous modelling of smooth contact surfaces using nurbs and application to 2d problems," *International Journal for Numerical Methods in Engineering*, vol. 57, no. 15, pp. 2177–2203, 2003.

[206] T. J. Hughes, A. Reali, and G. Sangalli, "Efficient quadrature for nurbs-based isogeometric analysis," *Computer methods in applied mechanics and engineering*, vol. 199, no. 5-8, pp. 301–313, 2010.

[207] F. Scholz, A. Mantzaflaris, and B. Jüttler, "First order error correction for trimmed quadrature in isogeometric analysis," in *Advanced Finite Element Methods with Appli-*

cations: Selected Papers from the 30th Chemnitz Finite Element Symposium 2017 30, pp. 297–321, Springer, 2019.

[208] E. J. Fern, "Modelling tunnel-induced deformations with the material point method," *Computers and Geotechnics*, vol. 111, pp. 202–208, 2019.

[209] J. Given, S. Kularathna, E. Y. Tjung, B. Chandra, K. Soga, H. Wang, S. P. Morgan, H. A. Meier, and J. L. Garzon, "Modeling wellbore erosion using standard and cut-mesh approaches in material point method," in *Geo-Congress 2022*, pp. 618–627, 2022.

[210] S. Timoshenko and S. Woinowsky-Krieger, *Theory of plates and shells (Engineering Societies Monograph), Second Edition*. 1959.

[211] Y. Liang, J. Given, and K. Soga, "The imposition of nonconforming neumann boundary condition in the material point method without boundary representation," *Computer methods in applied mechanics and engineering*, vol. 404, p. 115785, 2023.

[212] L. Prandtl, "On the penetration strength of plastic building materials and slopes," *Proceedings on applied mechanics, hydrodynamics and aerodynamics (in German)*, pp. 104–112, 1921.

[213] S. W. Sloan, A. J. Abbo, and D. Sheng, "Refined explicit integration of elastoplastic models with automatic error control," *Engineering computations*, vol. 18, no. 1/2, pp. 121–194, 2001.

[214] B. M. Das, *Shallow foundations: Bearing capacity and settlement*. CRC press, 2017.

[215] K. Terzaghi, *Theoretical soil mechanics*. 1943.

[216] P. A. Cundall and O. D. Strack, "A discrete numerical model for granular assemblies," *Géotechnique*, vol. 29, no. 1, pp. 47–65, 1979.

[217] C. Kloss, C. Goniva, A. Hager, S. Amberger, and S. Pirker, "Models, algorithms and validation for opensource dem and cfd–dem," *Progress in Computational Fluid Dynamics, an International Journal*, vol. 12, no. 2-3, pp. 140–152, 2012.

[218] S. Farzi Sizkow and U. El Shamy, "A comparison between coupled sph-dem and lbm-dem approaches for soil liquefaction," in *IFCEE 2021*, pp. 53–60, 2021.

[219] P. Fu and Y. F. Dafalias, "Study of anisotropic shear strength of granular materials using dem simulation," *International Journal for Numerical and Analytical Methods in Geomechanics*, vol. 35, no. 10, pp. 1098–1126, 2011.

[220] J. Duriez and S. Bonelli, "Precision and computational costs of level set-discrete element method (ls-dem) with respect to dem," *Computers and Geotechnics*, vol. 134, p. 104033, 2021.

[221] Y. F. Dafalias and M. T. Manzari, "Simple plasticity sand model accounting for fabric change effects," *Journal of Engineering mechanics*, vol. 130, no. 6, pp. 622–634, 2004.

[222] M. Taiebat and Y. F. Dafalias, "Sanisand: Simple anisotropic sand plasticity model," *International Journal for numerical and analytical methods in geomechanics*, vol. 32, no. 8, pp. 915–948, 2008.

[223] D. Griffiths and P. Lane, "Slope stability analysis by finite elements," *Geotechnique*, vol. 49, no. 3, pp. 387–403, 1999.

[224] D. Wang, B. Bienen, M. Nazem, Y. Tian, J. Zheng, T. Pucker, and M. F. Randolph, "Large deformation finite element analyses in geotechnical engineering," *Computers and geotechnics*, vol. 65, pp. 104–114, 2015.

[225] A. Alsardi, J. Copana, and A. Yerro, "Modelling earthquake-triggered landslide runout

with the material point method," *Proceedings of the Institution of Civil Engineers-Geotechnical Engineering*, vol. 174, no. 5, pp. 563–576, 2021.

[226] F. Ceccato, A. Yerro, V. Girardi, and P. Simonini, "Two-phase dynamic mpm formulation for unsaturated soil," *Computers and Geotechnics*, vol. 129, p. 103876, 2021.

[227] K. Kumar, J. Salmond, S. Kularathna, C. Wilkes, E. Tjung, G. Biscontin, and K. Soga, "Scalable and modular material point method for large-scale simulations," *arXiv preprint arXiv:1909.13380*, 2019.

[228] Y. Shi, N. Guo, and Z. Yang, "Geotaichi: A taichi-powered high-performance numerical simulator for multiscale geophysical problems," *Computer Physics Communications*, vol. 301, p. 109219, 2024.

[229] A. Sadeghirad, "B-spline convected particle domain interpolation method," *Engineering Analysis with Boundary Elements*, vol. 160, pp. 106–133, 2024.

[230] X. Zheng, F. Pisano, P. J. Vardon, and M. A. Hicks, "An explicit stabilised material point method for coupled hydromechanical problems in two-phase porous media," *Computers and Geotechnics*, vol. 135, p. 104112, 2021.

[231] K. Xie and C. J. Leo, "Analytical solutions of one-dimensional large strain consolidation of saturated and homogeneous clays," *Computers and geotechnics*, vol. 31, no. 4, pp. 301–314, 2004.

[232] Y.-F. Jin and Z.-Y. Yin, "Two-phase pfem with stable nodal integration for large deformation hydromechanical coupled geotechnical problems," *Computer Methods in Applied Mechanics and Engineering*, vol. 392, p. 114660, 2022.

[233] D. S. Morikawa and M. Asai, "Soil-water strong coupled isph based on u- w- p formula-

tion for large deformation problems," *Computers and Geotechnics*, vol. 142, p. 104570, 2022.

[234] D. S. Morikawa and M. Asai, "A mixed total lagrangian-updated lagrangian smoothed particle hydrodynamics method for geomechanics simulations with discontinuities," *Soils and Foundations*, vol. 65, no. 2, p. 101593, 2025.

[235] M. Cooper, E. Bromhead, D. Petley, and D. Grants, "The selborne cutting stability experiment," *Géotechnique*, vol. 48, no. 1, pp. 83–101, 1998.

[236] C. Tamagnini, G. Viggiani, and R. Chambon, "A review of two different approaches to hypoplasticity," *Constitutive modelling of granular materials*, pp. 107–145, 2000.

[237] L. Zambrano-Cruzatty and A. Yerro, "Numerical simulation of a free fall penetrometer deployment using the material point method," *Soils and Foundations*, vol. 60, no. 3, pp. 668–682, 2020.

[238] K. Adalier, A.-W. Elgamal, and G. R. Martin, "Foundation liquefaction countermeasures for earth embankments," *Journal of Geotechnical and Geoenvironmental Engineering*, vol. 124, no. 6, pp. 500–517, 1998.

[239] B. L. Kutter, T. J. Carey, N. Stone, B. L. Zheng, A. Gavras, M. T. Manzari, M. Zeghal, T. Abdoun, E. Korre, S. Escoffier, *et al.*, "Leap-ucd-2017 comparison of centrifuge test results," in *Model tests and numerical simulations of liquefaction and lateral spreading: LEAP-UCD-2017*, pp. 69–103, Springer, 2019.

[240] K. Arulmoli, "Velacs: Verification of liquefaction analyses by centrifuge studies, laboratory testing program," *Soil data report*, 1992.

[241] T. N. Hoang, T. T. Nguyen, T. V. Nguyen, G. D. Nguyen, and H. H. Bui, "Sph simulation of earthquake-induced liquefaction and large deformation behaviour of granular

materials using sanisand constitutive model," *Computers and Geotechnics*, vol. 174, p. 106617, 2024.

[242] T. N. Hoang, H. H. Bui, T. T. Nguyen, T. V. Nguyen, and G. D. Nguyen, "Development of free-field and compliant base sph boundary conditions for large deformation seismic response analysis of geomechanics problems," *Computer Methods in Applied Mechanics and Engineering*, vol. 432, p. 117370, 2024.

[243] A. Alsardi, A. Yerro, and C. C. Long, "Enhanced mpm framework with multipatch isogeometric analysis for geotechnical applications," *Computers and Geotechnics*, vol. 190, p. 107743, 2026.

[244] A. Alsardi, A. Yerro, and C. C. Long, "Assessment of the hydromechanical higher-order mpm for the simulation of geotechnical problems," *Computational Particle Mechanics (submitted)*, 2026.

[245] A. Niemunis, "Incremental driver, user's manual," *University of Karlsruhe KIT, Germany*, 2008.

[246] J. Montgomery and K. Ziotopoulou, "Numerical simulations of selected leap centrifuge experiments with pm4sand in flac," in *Model Tests and Numerical Simulations of Liquefaction and Lateral Spreading: LEAP-UCD-2017*, pp. 481–497, Springer, 2019.

[247] N. Dinesh, S. Banerjee, and K. Rajagopal, "Performance evaluation of pm4sand model for simulation of the liquefaction remedial measures for embankment," *Soil Dynamics and Earthquake Engineering*, vol. 152, p. 107042, 2022.

[248] Y. Yin, F. Wang, and P. Sun, "Landslide hazards triggered by the 2008 wenchuan earthquake, sichuan, china," *Landslides*, vol. 6, no. 2, pp. 139–152, 2009.

[249] D. K. Keefer, "Landslides caused by earthquakes," *Geological Society of America Bulletin*, vol. 95, no. 4, pp. 406–421, 1984.

[250] R. A. Gingold and J. J. Monaghan, "Smoothed particle hydrodynamics: theory and application to non-spherical stars," *Monthly notices of the royal astronomical society*, vol. 181, no. 3, pp. 375–389, 1977.

[251] S. Bardenhagen, J. E. Guilkey, K. Roessig, J. Brackbill, W. Witzel, and J. Foster, "An improved contact algorithm for the material point method and application to stress propagation in granular material," *Computer Modeling in Engineering & Sciences*, vol. 2, no. 4, p. 509, 2001.

[252] N. Pinyol, M. Alvarado, E. Alonso, and F. Zabala, "Thermal effects in landslide mobility," *Géotechnique*, vol. 68, no. 6, pp. 528–545, 2018.

[253] Itasca, "Flac (fast lagrangian analysis of continua) version 8.0: Software summary," tech. rep., Minneapolis, USA, 2015.

[254] C. W. W. Ng and B. Menzies, *Advanced unsaturated soil mechanics and engineering*. CRC Press, 2014.

[255] J. C. Martin, W. J. Moyce, J. Martin, W. Moyce, W. G. Penney, A. Price, and C. Thornhill, "Part iv. an experimental study of the collapse of liquid columns on a rigid horizontal plane," *Philosophical Transactions of the Royal Society of London. Series A, Mathematical and Physical Sciences*, vol. 244, no. 882, pp. 312–324, 1952.

[256] M. A. Cruchaga, D. J. Celentano, and T. E. Tezduyar, "Collapse of a liquid column: numerical simulation and experimental validation," *Computational Mechanics*, vol. 39, no. 4, pp. 453–476, 2007.

[257] E. Walhorn, A. Kölke, B. Hübner, and D. Dinkler, "Fluid–structure coupling within a monolithic model involving free surface flows," *Computers & structures*, vol. 83, no. 25-26, pp. 2100–2111, 2005.

[258] T. Elguedj, Y. Bazilevs, V. M. Calo, and T. J. Hughes, "B and f projection methods for nearly incompressible linear and non-linear elasticity and plasticity using higher-order nurbs elements," *Computer methods in applied mechanics and engineering*, vol. 197, no. 33-40, pp. 2732–2762, 2008.

[259] G. Moutsanidis, J. J. Koester, M. R. Tupek, J.-S. Chen, and Y. Bazilevs, "Treatment of near-incompressibility in meshfree and immersed-particle methods," *Computational particle mechanics*, vol. 7, no. 2, pp. 309–327, 2020.

[260] L. E. Talbot, J. Given, E. Y. Tjung, Y. Liang, K. Chowdhury, R. Seed, and K. Soga, "Modeling large-deformation features of the lower san fernando dam failure with the material point method," *Computers and Geotechnics*, vol. 165, p. 105881, 2024.

[261] J. Meyer and M. Kaliske, "Mitigation techniques for volumetric locking in the implicit material point method (mpm)," *Proceedings in Applied Mathematics and Mechanics (PAMM)*, vol. 24, no. 4, p. e202400033, 2024.

[262] R. W. Boulanger, "Relating k α to relative state parameter index," *Journal of Geotechnical and Geoenvironmental Engineering*, vol. 129, no. 8, pp. 770–773, 2003.

[263] Y. F. Dafalias, "Bounding surface plasticity. i: Mathematical foundation and hypoplasticity," *Journal of engineering mechanics*, vol. 112, no. 9, pp. 966–987, 1986.

[264] "A critical state two-surface plasticity model for sands," *Géotechnique*, vol. 47, no. 2, pp. 255–272, 1997.